Titre: Title:	Dynamics and Spin-Orbit Coupling Properties of Light Holes Confined in Group-IV Semiconductor Heterostructures
Auteur: Author:	Patrick Del Vecchio
Date:	2024
Type:	Mémoire ou thèse / Dissertation or Thesis
Référence: Citation:	Del Vecchio, P. (2024). Dynamics and Spin-Orbit Coupling Properties of Light Holes Confined in Group-IV Semiconductor Heterostructures [Ph.D. thesis, Polytechnique Montréal]. PolyPublie. https://publications.polymtl.ca/62502/

POLYTECHNIQUE MONTRÉAL
affiliée à l'Université de Montréal

Dynamics and Spin-Orbit Coupling Properties of Light Holes Confined in Group-IV Semiconductor Heterostructures

PATRICK DEL VECCHIO
Département de génie physique

Thèse présentée en vue de l'obtention du diplôme de *Philosophiæ Doctor*
Génie physique

Décembre 2024

POLYTECHNIQUE MONTRÉAL
affiliée à l'Université de Montréal

Cette thèse intitulée :

Dynamics and Spin-Orbit Coupling Properties of Light Holes Confined in Group-IV Semiconductor Heterostructures

présentée par **Patrick DEL VECCHIO**
en vue de l'obtention du diplôme de *Philosophiæ Doctor*
a été dûment acceptée par le jury d'examen constitué de :

Sébastien FRANCOEUR, président
Oussama MOUTANABBIR, membre et directeur de recherche
Hong GUO, membre
Georgios KATSAROS, membre externe

DEDICATION

To my friends and family

ACKNOWLEDGEMENTS

I would like to express my sincere gratitude to my supervisor, Oussama Moutanabbir, for his exceptional support throughout my journey leading to this thesis. I truly appreciated his guidance, which always allowed room for exploring the unexpected. Our many discussions sparked ideas whenever I felt stuck. I also want to thank him for the opportunities he provided, including participation in numerous conferences and supporting my internship in Basel.

I am grateful to all my lab colleagues for their support and the many enjoyable moments we shared in conferences and activities outside of work such as hiking, kayaking, skiing, karting and dining together. A special thanks to everyone I shared office 4047 with over the years. Our complicity made the work environment truly enjoyable and the moments we spent together outside of work will remain precious memories to me.

I would also like to thank all my collaborators, particularly Prof. Giordano Scappucci's and Prof. Daniel Loss' groups. My appreciation extends to Stefano Bosco for his excellent guidance during my internship in Basel and the collaboration that followed.

I gratefully acknowledge the financial support from CRSNG and FRQNT during my Master's, which paved the way for my PhD project. I also want to thank Mitacs for their financial contribution during my internship in the summer and fall of 2023, which has been a wonderful experience.

None of this would have been possible without the support of my long-time friends: Michael, Philippe, Isabelle, Guillaume, Catherine, Claudelle, Laurence et Sébastien. Lastly, I would like to thank my family, especially my mother, which always reminded me that anything is possible. My deepest thanks to my father, sister and grandmother for their love and support.

RÉSUMÉ

Une technologie de pointe particulièrement intéressante depuis quelques décennies est le processeur quantique. Contrairement au processeur classique, opérant sur des bits logiques dont la valeur peut être soit "$\mathbb{0}$" ou "$\mathbb{1}$", un processeur quantique opère sur un bit *quantique*, un qubit, pouvant être dans un état de superposition des valeurs "$\mathbb{0}$" et "$\mathbb{1}$". Un tel processeur exploite le principe de superposition quantique et l'intrication, lui permettant la résolution de problèmes dont la complexité nous est hors de portée, même pour les super-ordinateurs les plus puissants. Une implémentation du qubit prometteuse consiste à utiliser le spin des porteurs de charge dans les nano-structures semiconductrices. L'idée étant de confiner un petit nombre de particules dans une région nanométrique à l'aide de minces couches semiconductrices et des contacts électrostatiques, et d'ensuite manipuler leur spin à l'aide de champs électro-magnétiques alternatifs. L'étude de la physique des porteurs de charge est donc d'importance centrale dans la réalisation des qubits semiconducteurs.

Il existe principalement deux types de porteurs de charge dans les semiconducteurs: les électrons et les trous. Un trou consiste en un état électronique inoccupé par un électron. Sachant qu'un état électronique ne peut accueillir qu'un seul électron à la fois, un trou peut disparaître et réapparaître ailleurs simplement par le mouvement des électrons quittant leur état pour se diriger vers un autre état inoccupé. Le trou peut donc effectivement être traité comme une particule à part entière, de charge positive, et possédant sa propre mobilité, sa propre masse effective, etc... Les trous lourds forment l'une des deux catégories de trous de faible énergie (les autres étant les trous légers) que l'on retrouve dans plusieurs semiconducteurs importants dont le silicium et le germanium. Depuis quelques années, d'immenses progrès ont été réalisés dans la conception de qubits à base de trous (lourds) dans le germanium. Ce système possède plusieurs caractéristiques favorables à l'implémentation d'un qubit. Premièrement, le germanium est compatible avec le silicium, facilitant ainsi la production éventuelle à grande échelle. Le germanium est également un matériau à grand couplage spin-orbite, signifiant que le mouvement des trous est fortement corrélé avec la précession de leur spin. Cela permet de manipuler ce dernier à l'aide de champs électriques plutôt que magnétiques, facilitant la miniaturisation et limitant la surchauffe du dispositif. De plus, le germanium possède des isotopes dont le noyau atomique ne possède aucun spin. Du germanium isotopiquement purifié pour contenir seulement de tels isotopes peut alors être utilisé dans la réalisation du dispositif, ce qui confère au qubit un temps de relaxation et de cohérence beaucoup plus grands. Dans les systèmes à base de germanium, la famille de trous impliquée dans la réalisation du qubit sont les trous lourds. Cela est principalement dû à

une limitation en matériaux disponibles. Le procédé de fabrication standard combine une couche de germanium avec un substrat en alliage silicium-germanium. Cette combinaison de matériaux résulte en une contrainte épitaxiale compressive dans le germanium, favorisant l'apparition de trous lours dans le spectre à basse énergie.

Bien que les trous lourds profitent des avantages mentionnés dans le paragraphe précédent, le niveau de séparation en énergie entre leur deux états de spin, quantifié par le facteur g, est très faible dans la configuration utilisant des champs magnétiques orientés dans le plan des couches semiconductrices. Également, bien que les trous lourds soient assujettis à un grand couplage spin-orbite, la variété de couplage spin-orbite nécessaire à la manipulation du spin y est presque absente. Pour remédier à ce problème, cette thèse propose l'utilisation de trous légers dans l'implémentation de qubits de spin. Tout d'abord, le travail consiste à adapter les théories existantes (la théorie $k \cdot p$) pour l'étude des trous légers et de leur spin lorsqu'ils sont confinés à l'échelle nano-métrique. Ensuite, le modèle est testé contre les résultats d'une étude expérimentale originale, faisant intervenir des trous lourds dans le germanium dont la séparation en énergie entre les deux états de spin s'annule pour des champs magnétiques non-nuls. Ensuite, une nouvelle famille d'hétérostructures à base d'un semiconducteur du groupe IV, l'alliage de germanium et d'étain ($Ge_{1-x}Sn_x$), est introduite. Nous appliquons le modèle dévelopé précédemment afin de montrer que de telles hétérostructures, qui ont déjà été réalisées en laboratoire à l'École Polytechnique de Montréal, sont en mesure d'amener les trous légers à de plus faibles énergies que les trous lourds, ceci grâce à la contrainte épitaxiale en tension que confère le $Ge_{1-x}Sn_x$. De plus, plusieurs propriétés des trous légers y sont évaluées, dont notamment le facteur g et quelques coefficients de couplage spin-orbite. En particulier, ce travail montre que les trous légers ont un facteur g beaucoup plus grand que les trous lours pour des champs magnétiques orientés dans le plan. De plus, la variété de couplage spin-orbite nécessaire à la manipulation y est beaucoup plus grande. Ensuite, le modèle théorique est utilisé afin de modéliser la dynamique du spin d'un trou léger dans les nanostructures semiconductrices, tels que des points quantiques et des canaux quantiques. On y montre notamment qu'une variété de couplage spin-orbite absente dans le cas des trous lourds apporte une riche dynamique au spin, facilitant par exemple le contrôle électrostatique de la force du couplage spin-orbite, ainsi que de très grandes fréquences de manipulation.

Enfin, ce travail approfondit notre compréhension des trous dans les semiconducteurs du groupe IV qui, jusqu'à maintenant, était orientée presque exclusivement au cas des trous lourds. Cette étude introduit et fait l'analyse d'une nouvelle famille de semiconducteurs compatibles avec le silicium qui est prometteuse pour l'implémentation de qubits rapides et efficaces, dont le contrôle peut être réalisé par des méthodes purement électriques, et dont la cohérence est maximisée grâce à la purification isotopique.

ABSTRACT

One of the exciting potential technologies that has attracted significant attention in the last few decades is the quantum processor. In contrast to a classical processing unit, which operates on bits that can be in a state of value $\mathbb{0}$ or $\mathbb{1}$, a quantum processor operates on *quantum* bits, or qubits, which can be in a quantum superposition of the $\mathbb{0}$ and $\mathbb{1}$ states. This quantum superposition, as well as quantum entanglement, are leveraged in a quantum processor to solve specific problems of such complexity that they are out of reach to even the most powerful super-computers. One promising implementation of a qubit device uses the spin degree of freedom of charge carriers confined in semiconductor heterostructures. The idea is to confine a small number of carriers within a very thin layer of a semiconducting material and underneath a set of electrostatic gates, to then manipulate their spin with oscillating electro-magnetic fields. Understanding the spin physics in solid-state devices is thus of central importance in realizing semiconducting spin qubits.

There are two broad categories of charge carriers in semiconductors: electrons and holes. In solid state physics, a hole is an empty, or unoccupied electronic level within the material. Knowing that levels cannot accommodate more than one electron at once, a hole can disappear and reappear elsewhere as a result of an electron hopping from one level to another. In fact, holes are treated as particles (or quasi-particles) as much as solid-state electrons are. Holes are therefore assigned a positive charge, with their own mobility, effective mass, etc... Heavy holes are one of the two categories of low energy holes (the other being light holes) in many important semiconductors, notably silicon and germanium. There has been significant progress in the last few years towards realizing (heavy) hole spin qubits in germanium. This system has many favorable characteristics for qubit devices. Firstly, germanium is silicon-compatible, thus providing great manufacturability. Germanium is also a high spin-orbit coupling material, meaning that the hole's orbital motion is strongly correlated with the precession of its spin. This effect can effectively lead to manipulation schemes where the spin is controlled with oscillating electric fields instead of magnetic fields, reducing heating and vibration issues caused by local magnets and making scaling-up easier. Moreover, germanium has isotopes with spin-free atomic nuclei. An isotopically purified material with zero nuclear spins can therefore provide an ideal environment where hyperfine interactions are eliminated, thus leading to highly coherent and long-lived qubits. State-of-the-art germanium qubit devices use heavy holes as the information carrier. This is mostly a material limitation, since the devices are constructed by growing germanium on a layer of silicon-germanium alloy. This combination of materials leads to a compressive epitaxial strain in

the germanium layer, thus favoring heavy holes to the low energy spectrum.

Despite the aforementioned advantages of heavy holes, the energy difference between their two spin state projections, quantified by the g-factor, is very small when magnetic fields are applied in the plane of the layers. Furthermore, despite the strong spin-orbit coupling, the kind that is dominant in heavy holes does not contribute to the electrical driving of the spin. This thesis therefore proposes novel spin qubits based on light holes. As a first step, existing theories (more specifically, the $k \cdot p$ theory) for describing holes in semiconductors are adapted to the case of light hole ground states confined in semiconductor heterostructures. Next, the theoretical model is benchmarked against the experiment revealing vanishing energy spin splitting at finite magnetic fields in two-dimensional heavy hole gases in germanium. A new family of group IV semiconductors based on germanium-tin alloys ($Ge_{1-x}Sn_x$) is then introduced. The model is employed to show that these new heterostructures, which have already been grown by our group, can bring light holes to the ground state, thanks to the large epitaxial tensile strain caused by the $Ge_{1-x}Sn_x$ layers. Furthermore, the key light hole spin properties are evaluated, such as the g-tensor components and spin-orbit coupling parameters. In particular, this work shows that light holes have a very large in-plane g-factor as well as a strong type of spin-orbit coupling that is relevant to all-electrical driving schemes. Light hole spin dynamics is then evaluated in $Ge_{1-x}Sn_x$-based heterostructures with in-plane confinement, such as in quantum dots and quantum channels. A large spin-orbit coupling linear in momentum that is small in heavy hole systems is reported and shown that it can be leveraged to achieve gate-controlled spin-orbit strength tuning, as well as very large manipulation frequencies compared to heavy holes.

This thesis provides a deeper understanding of light hole spin physics in group IV semiconductors, which so far have been mostly left aside in favor of heavy holes due to the lack of proper material systems. The work presented therein introduces and analyzes a new family of group IV semiconductors that are compatible with silicon. This system is promising for implementing fast and efficient light hole spin-based qubit devices, where manipulation can be performed by all-electrical means and where high coherence times are expected thanks to isotopic purification.

TABLE OF CONTENTS

LIST OF TABLES

LIST OF FIGURES

LIST OF ACRONYMS AND SYMBOLS

CB	Conduction Band
VB	Valence Band
HH	Heavy Hole
LH	Light Hole
SO	Split-Off (hole)
SOI	Spin-orbit Interaction
SOC	Spin-orbit Coupling
SIA	Spatial Inversion Asymmetry
ESR	Electron Spin Resonance
EDSR	Electric-Dipole Spin Resonance
QW	Quantum Well
QC	Quantum Channel
QD	Quantum Dot
SWT	Schrieffer-Wolff Transformation
FBZ	First Brillouin Zone
MOS	Metal-Oxide-Semiconductor
m_0	Free electron mass ($9.109 \cdot 10^{-31}\,\mathrm{kg}$)
g_0	Free electron g-factor
$\hbar$	Reduced Planck constant $h/(2\pi)$
e	Elementary charge (positive)
k_B	Boltzmann constant
$\mathcal{V}$	Volume
α_0	$\alpha_0 = \hbar^2/(2m_0)$
$\mathcal{H}$	Hilbert space
$\mathcal{B}$	Hilbert space basis
$f(z)$	Envelope function
$\mathsf{\eta}$	"eta" level, spin 1/2 CB-LH-SO superposed QW subband
H	"heavy" level, spin 3/2 HH QW subband
j	$\mathsf{\eta}$ level subband index
l	H level subband index
τ	General index for $\mathsf{\eta}$ or H levels
I_i	Orbital angular momentum generators
σ_i	Spin 1/2 Pauli matrices

σ	QW subband pseudo spin index
ς	QC or QD pseudo spin index
E_n	Energy of band n
$\mathcal{E}_\nu$	Energy of band ν (without SOC)
Γ_α	Irreducible representation α
$\mathbf{e}_i$	Unit vector towards direction i
ε	Strain tensor
ε_{ij}	Strain tensor components
ϵ_{ijk}	Levi-Civita tensor
ϵ	Dielectric constant
$\mathbf{f}$	Force vector
$\mathbf{F}$	Electric field vector
$\mathbf{B}$	Magnetic field vector
$\mathbf{A}$	Vector potential
$l_B = \sqrt{\hbar/(eB)}$	Magnetic length
θ	Polar angle
ϕ	Azimuthal angle
$\mathbf{p}$	Momentum
$\mathbf{k}$	Bloch wavevector
$\mathbf{K}$	Mechanical wavevector
$\mathbf{q}$	Phonon wavevector
l_z	QW width
l_x	x-axis in-plane confinement characteristic length
l_y	y-axis in-plane confinement characteristic length
$\perp$	Perpendicular to the QW plane
$\parallel$	In the QW plane
$\mathbb{0}$, $\mathbb{1}$	Qubit levels

LIST OF APPENDICES

CHAPTER 1 INTRODUCTION

Semiconductor heterostructures are widely used in electronics, optoelectronics and spintronics. In the last few decades, many experiments showed promising results towards the implementation of scalable quantum computing devices, by leveraging the rich spin physics of charge carriers in these systems. The physics of solid-state charge carriers is strongly dependent on many of the device properties: the materials used in the heterostructure, the thickness of the layers, the type and concentration of impurities or dopants, the epitaxial strain, the crystal defects such as dislocations or vacancies, the temperature, symmetry effects at interfaces and many more. It is hard to overestimate the formidable complexity of semiconductor physics, which has even been qualified as "physics of dirt" by W. E. Pauli or "squalid state physics" by M. Gell-Mann. Despite all that complexity, decades of research in solid-state physics led to significant progress in knowledge and is still a flourishing area of research today.

In this section, we present basic properties that are important in the field of semiconductors and for this dissertation. It is then followed by a discussion of a few key elements that characterize semiconductor heterostructures, before presenting a quick overview of qubit dynamics, and the influence of spin-orbit coupling. The motivation as well as a list of objectives addressed by this research are then presented, followed by a brief outline of the results presented in this dissertation.

1.1 Basic concepts

1.1.1 Semiconductor heterostructures

A semiconductor is a material that lies somewhat between a conductor and an isolator in terms of its electrical conductivity. Every semiconductor is characterized by its *bandgap* energy, which is a band of energy devoid of any quantum levels that can accommodate electrons. The set of electronic bands that are below the bandgap (lower in energy) are called *valence* bands (VB), while those above the bandgap are called *conduction* bands (CB). At zero temperature, all the valence bands are occupied by an electron, while none of the conduction bands are occupied. In this situation, the semiconductor cannot host any electrical current. If a valence band electron receives enough energy (from thermal excitation or from a photon), it can be promoted to the conduction band, while leaving an empty level behind, a *hole*, in the valence band. Both holes and conduction band electrons can serve as carriers of electrical

current. In general, a charge carrier with crystal momentum $\mathbf{k}$ jumping from one energy level $E_i(\mathbf{k})$ to another level $E_f(\mathbf{k}')$ will involve a phonon of momentum $\mathbf{q} = \mathbf{k} - \mathbf{k}'$. If $\mathbf{k} = \mathbf{k}'$ (no phonon involved), it is called a *direct* transition. Otherwise, any transition involving a phonon is called an *indirect* transition. In group IV semiconductors, the valence band edge (the maximum of the band) is located at $\mathbf{k} = 0$. In contrast, the conduction band edge (the minimum of the band) is away from $\mathbf{k} = 0$ in Si and Ge. Therefore, the smallest energy excitation that moves a carrier across the bandgap involves an indirect transition. Consequently, Si and Ge are referred as *indirect bandgap* semiconductors. On the other hand, some group III-V materials (e.g. GaAs) have their CB minimum at $\mathbf{k} = 0$ and are correspondingly referred as *direct bandgap* semiconductors.

In semiconductors, electrons, and especially holes, are subject to spin-orbit interaction (SOI). SOI is a relativistic effect, and results from the perceived motion of the positive nuclei within the reference frame of a moving electron in the crystal. This apparent motion generates a magnetic field in the electron's frame, which then interacts with the electron's spin. SOI in semiconductors tends to increase with the atomic number Z [1]. Worth mentioning is another source of SOI called Dresselhaus SOI, which arises in inversion asymmetric crystals such as III-V or II-VI semiconductors. However, this type of SOI will not be discussed further, as the main focus of this work is on group IV semiconductors, which lack the crystal asymmetry required for Dresselhaus SOI.

A semiconductor *planar heterostructure* consists of multiple layers of semiconducting materials deposited on top of each other, starting from a semiconducting wafer substrate usually made of Si. An important category of heterostructures for this work is the quantum well (QW) heterostructure. A QW is made by forming a sandwich of semiconductors where the layer in the middle (the QW, usually $\sim 10\,\text{nm}$ thick) has band edge energies lying within the bandgap of the layers surrounding it (the barriers). This configuration promotes the accumulation of charge carriers in the QW as they tend to minimize their energy. There are three types of band alignments in a QW heterostructure (see Fig. 1.1). A type-I QW is such that both holes and electrons accumulate in the QW layer, whereas in a type-II alignment, only one type of carrier accumulates in the well. Type-III alignment occurs if the bandgap region of the QW does not overlap with that of the barriers. If adjacent layers in a heterostructure share the same lattice constant, they are said to be *lattice matched*. Otherwise, they are *lattice mismatched*. A lattice mismatched layer will try to adjust its crystal structure such that its in-plane lattice constant matches that of its underlying material layer. This results in *epitaxial strain*. Epitaxial strain can be either compressive or tensile, depending on the relative size of the lattice constants between the two layers. In the former case, a material A is deposited on a substrate of lattice constant smaller than that of A, while in the latter

case, the substrate's lattice constant is larger than that of A. Strain has profound effects on the electronic band structure, including the tendency of the bandgap to shrink with tensile strain, and to expand with compressive strain. If band structure extrema shift at different rates with respect to strain, an indirect bandgap material can become direct, or vice-versa if strain is large enough. Strain effects will be discussed in more detail in coming sections, as the theoretical framework is presented.

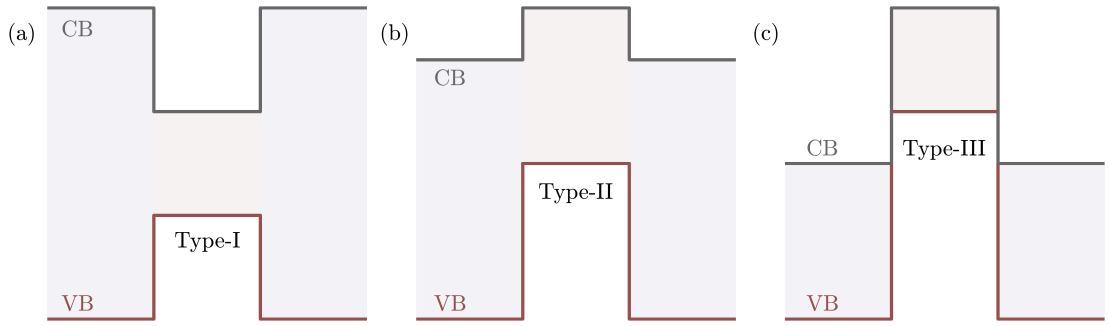

Figure 1.1 (a) Type-I, (b) type-II, and (c) type-III band alignments. Bandgaps in the well (barriers) are indicated by red (blue) areas. Vertical axis is energy and horizontal axis is position (parallel to growth direction). The heterostructures are symmetric in all cases.

If a DC electric field $\mathbf{F} = F_z \mathbf{e}_z$ is applied to the heterostructure towards the growth direction z, the piecewise-constant band alignments as in Fig. 1.1 acquire a slope equal to eF_z, where e is the elementary charge. This field influences the behavior of charge carriers in multiple ways. First, the field pushes positive carriers (holes) towards the surface of the heterostructure and negative carriers (electrons) towards the substrate, thereby increasing the overlap of their wavefunction with the interfaces between the well and the adjacent barrier layers. Secondly, the tilting of the bands removes any structure inversion symmetry that might have been present prior to applying the field. As will be discussed at length in this work, this symmetry breaking, or structure inversion asymmetry (SIA), has profound effects on the dynamics of carriers in the QW. It is enabled by the inherent SOI of the host materials and is referred as Rashba SOI [2].

1.1.2 The diamond crystal structure

The real-space and k-space lattice

Si, Ge and α-Sn (simply Sn from now on) all share the same atomic structure as diamond in their bulk crystal form. Atomic sites in the diamond crystal structure correspond to the lattice points of two inter-penetrating face-centered cubic (fcc) Bravais sub-lattices. This

configuration is displayed in Fig. 1.2a where atomic sites belonging to the first (second) fcc sub-lattice are represented by black (green) spheres. The lattice constant a_0 of the crystal is defined as the distance between two adjacent corners of the fcc lattice (Fig. 1.2b). Each atom in the crystal has four nearest neighbors located $\sqrt{3}a_0/4$ apart. In this arrangement, atoms are able to satisfy their four empty p electronic orbitals via sp^3 bonding with their four nearest neighbors (Fig. 1.2b). The crystal is invariant with respect to any translation by a lattice vector $\mathbf{R}_{lmn} = l\mathbf{a}_1 + m\mathbf{a}_2 + n\mathbf{a}_3$, where l, m and n are integers and where the three primitive vectors $\mathbf{a}_{1,2,3}$ are

$$\mathbf{a}_1 = \frac{a_0}{2}\begin{bmatrix}0\\1\\1\end{bmatrix}, \qquad \mathbf{a}_2 = \frac{a_0}{2}\begin{bmatrix}1\\0\\1\end{bmatrix}, \qquad \mathbf{a}_3 = \frac{a_0}{2}\begin{bmatrix}1\\1\\0\end{bmatrix}. \tag{1.1}$$

The set of $\mathbf{R}_{lmn}$ defines the real-space lattice. The set of points $\mathbf{r}$ that are closer to a given lattice point $\mathbf{R}_{lmn}$ than to any other point $\mathbf{R}_{l'n'm'} \neq \mathbf{R}_{lmn}$ is called a Wigner-Seitz cell (Fig. 1.2c). For the diamond crystal structure, each Wigner-Seitz cell has a volume $\mathcal{V} = \mathbf{a}_1 \cdot (\mathbf{a}_2 \times \mathbf{a}_3) = a_0^3/4$, and each cell contains two atoms (one from each fcc sub-lattice) whose coordinates are

$$\mathbf{c}_1 = \begin{bmatrix}0\\0\\0\end{bmatrix}, \qquad \mathbf{c}_2 = \frac{a_0}{4}\begin{bmatrix}1\\1\\1\end{bmatrix}. \tag{1.2}$$

A reciprocal-space lattice (or $\mathbf{k}$-space lattice) is generated by the set of reciprocal lattice vectors $\mathbf{G}$ such that

$$e^{i\mathbf{G}\cdot\mathbf{R}} = 1. \tag{1.3}$$

Similarly to $\mathbf{R}_{lmn}$, the $\mathbf{k}$-space lattice is invariant with respect to any translations by $\mathbf{G}_{lmn} = l\mathbf{b}_1 + m\mathbf{b}_2 + n\mathbf{b}_3$, with l, m and n integers. The three primitive $\mathbf{k}$-space vectors $\mathbf{b}_i$ are obtained by cyclic permutations of $\mathbf{b}_1 = 2\pi(\mathbf{a}_2 \times \mathbf{a}_3)/\mathcal{V}$:

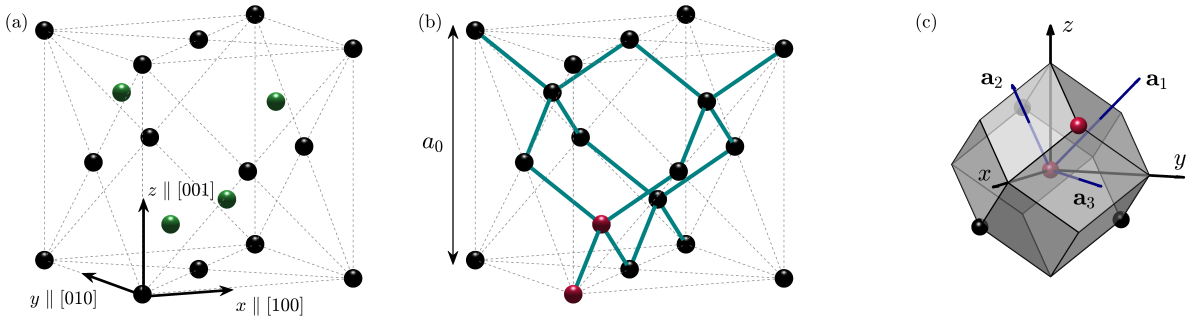

Figure 1.2 Conventional unit cell of a diamond crystal structure. (a) The diamond crystal is equivalent to two inter-penetrating fcc sub-lattices. Black (green) atomic sites belong to the first (second) fcc sub-lattice. Alignment of the Cartesian axes with respect to the crystal directions is also shown. (b) Covalent bonding (teal lines) of atoms with their four nearest neighbors. Each bond is $\sqrt{3}a_0/4$ in length, where a_0 is the lattice constant. (c) Real-space Wigner-Seitz cell. Primitive vectors $\mathbf{a}_{1,2,3}$ (dark blue) and the two atoms (red spheres) contained within are also shown. These two atoms are the same as those marked in red in panel (b). The three other atoms (black) belong to adjacent primitive cells.

$$\mathbf{b}_1 = \frac{2\pi}{a_0}\begin{bmatrix}-1\\1\\1\end{bmatrix}, \qquad \mathbf{b}_2 = \frac{2\pi}{a_0}\begin{bmatrix}1\\-1\\1\end{bmatrix}, \qquad \mathbf{b}_3 = \frac{2\pi}{a_0}\begin{bmatrix}1\\1\\-1\end{bmatrix}. \tag{1.4}$$

The $\mathbf{k}$-space Wigner-Seitz cell centered on $\mathbf{G} = \mathbf{0}$ is called the first Brillouin zone (FBZ). The point lying at the center of the FBZ ($\mathbf{k} = \mathbf{G}_{000} = \mathbf{0}$) is called the Γ point. Other notable high symmetry points lying on the edge of the FBZ are the so-called L and X points:

$$\mathrm{L} = \frac{\pi}{a_0}\begin{bmatrix}1\\1\\1\end{bmatrix}, \qquad \mathrm{X} = \frac{2\pi}{a_0}\begin{bmatrix}1\\0\\0\end{bmatrix}. \tag{1.5}$$

The FBZ totals 8 equivalent L points and 6 equivalent X points. The path connecting Γ to L is called Λ while the path connecting Γ to X is called Δ. The FBZ is displayed in Fig. 1.3 with its symmetry points, primitive vectors and reciprocal space reference frame.

The whole $\mathbf{k}$-space lattice can be constructed by stacking together Wigner-Seitz cells centered on every $\mathbf{G}_{lmn}$. In particular, for any point $\mathbf{k}'$ in $\mathbf{k}$-space, there is a unique $\mathbf{k} \in$ FBZ and a unique $\mathbf{G}_{lmn}$ such that $\mathbf{k}' = \mathbf{k} + \mathbf{G}_{lmn}$.

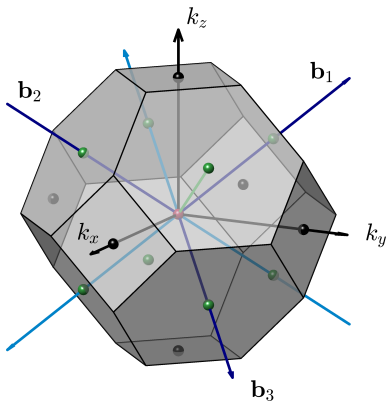

Figure 1.3 First Brillouin zone (FBZ) of the fcc Bravais lattice. The primitive reciprocal vectors $\mathbf{b}_{1,2,3}$ are shown as dark blue arrows, while $-\mathbf{b}_{1,2,3}$ are shown as light blue arrows. The reciprocal space coordinate system $k_{x,y,z}$ is shown as black arrows. Spheres represent high symmetry points of the FBZ: Γ (red), 8 × L (green) and 6 × X (black). The Λ path connecting Γ to L is shown by the green line. Any point within the FBZ is closer to the Γ point than to any other point $\mathbf{G}_{lmn} \neq \mathbf{0}$.

Symmetry of the diamond structure

The space group of the diamond crystal structure is $Fd3m$, or O_h^7. This crystal structure is known to be *nonsymmorphic*, meaning that the subset of symmetry operations on the crystal that are not pure translations contain glide planes or screw axes [3]. In diamond, there are three glide planes, each one containing a translation by $\sqrt{3}a_0/4$ along the diagonal of the unit cell. However, the factor group G over the translation subgroup of a diamond lattice is isomorphic to the point group O_h, the set of operations that leave a cube invariant. Since $G \simeq O_h$, we will simply refer to G as O_h in the following. A wealth of information regarding the energy level structure of an electron in the crystal can be deduced only from symmetry considerations, as we show below.

Ignoring spin for now, the Hamiltonian H of a single electron in the crystal must remain invariant with respect to any operation of the group O_h. If T_R is an operator associated with an operation $R \in O_h$, then the Hamiltonian must commute with T_R: $[T_R, H] = 0$ for every $R \in O_h$. In particular, if $|\varphi\rangle$ is an eigenstate of H with associated energy E, then $T_R|\varphi\rangle$ is also an eigenstate of H with the same energy: $HT_R|\varphi\rangle = T_R H|\varphi\rangle = ET_R|\varphi\rangle$. If the energy E is l-fold degenerate ($l = 1, 2, \dots$), then the set of eigenstates $\{|\varphi_l\rangle\}$ lying in that degenerate subspace provides a basis for an l-dimensional irreducible representation (irrep) of O_h. Since O_h has 48 elements categorized into 10 classes, the group has a total of 10 irreps labeled (according to Reference [4]) $\left\{\Gamma_i^{\pm}\right\}_{i=1}^{5}$ with $\Gamma_{1,2}^{\pm}$ being one-dimensional, $\Gamma_3^{\pm}$ being two-dimensional and $\Gamma_{4,5}^{\pm}$ being three-dimensional. Superscripts ± indicate the parity

with respect to inversion.

In group IV crystals, each atom forms 4 hybridized sp^3 orbitals with four nearest neighbors, where each orbital accommodates at most 2 electrons. An 8-dimensional representation $\Gamma^{(8)}$ of O_h can be constructed by keeping track of the position of the 2 (red) atoms within the primitive cell (Fig. 1.2c) plus their three other nearest neighbors (totaling 8 atoms) upon application of each element of O_h. With the fixed point located halfway between the two red atoms, the character of each group element is obtained by identifying the number of atoms that remain invariant by the transformation. For example, upon performing an element in class $8C_3$, corresponding to the 3-fold rotations along the axis connecting two nearest neighbors (the two red atoms for instance), only these two atoms remain invariant, thus giving $\chi(8C_3) = 2$. The classes $6C_4$, $6C_2'$, i, $8S_6$, and $3\sigma_h$ involve a glide, hence their characters are zero. The four other classes have characters $\chi(E) = 8$, $\chi(3C_2) = 0$, $\chi(6S_4) = 0$ and $\chi(6\sigma_\mathrm{d}) = 4$. This representation decomposes into:

$$\Gamma^{(8)} = \Gamma_1^+ \oplus \Gamma_5^+ \oplus \Gamma_2^- \oplus \Gamma_4^-. \tag{1.6}$$

From this, the low-energy spectrum of the electron at the Γ point is expected to transform according to one of the four irreps in (1.6). For instance, in Si and Ge, the lowest energy at the Γ point transforms according to Γ_1^+, while the second lowest (at the edge of the valence band) transforms according to Γ_5^+ (3-fold degenerate). In Si, the next level (above the bandgap) transforms according to Γ_4^-, while in Ge it transforms according to Γ_2^-.

If electron spin is taken in account, a rotation of 2π along any fixed axis introduces a π-phase to the spinor. The crystal symmetry is therefore expanded to the O_h *double* group, where a full rotation corresponds to 4π. This introduces 6 new irreps, namely $\left\{\Gamma_i^\pm\right\}_{i=6}^8$ with $\Gamma_{6,7}^\pm$ being 2-dimensional and $\Gamma_8^\pm$ being 4-dimensional. A representation including spin for an electron transforming according to one of the four irreps in (1.6) is obtained from a direct product with the 2-dimensional representation $\mathcal{D}_{1/2}^+$ of the full rotation group. These decompose like so:

$$\Gamma_1^+ \otimes \mathcal{D}_{1/2}^+ = \Gamma_6^+, \tag{1.7a}$$

$$\Gamma_5^+ \otimes \mathcal{D}_{1/2}^+ = \Gamma_7^+ \oplus \Gamma_8^+, \tag{1.7b}$$

$$\Gamma_2^- \otimes \mathcal{D}_{1/2}^+ = \Gamma_7^-, \tag{1.7c}$$

$$\Gamma_4^- \otimes \mathcal{D}_{1/2}^+ = \Gamma_6^- \oplus \Gamma_8^-. \tag{1.7d}$$

Hence, with spin effects included in the Hamiltonian (e.g. spin-orbit coupling), low-energy eigenstates of H at the Γ point are either doubly degenerate ($\Gamma_{6,7}^{\pm}$) or 4-fold degenerate ($\Gamma_8^{\pm}$). In particular, the otherwise 6-fold degenerate valence band edge ($\Gamma_5^+ \otimes \mathcal{D}_{1/2}^+$) splits into one 4-fold degenerate level Γ_8^+ and one 2-fold degenerate level Γ_7^+ (the so-called split-off band). The former is compatible with the 4-dimensional irrep $\mathcal{D}_{3/2}^+$ of the full rotation group ($j = 3/2$ matrices), while the latter is compatible with $\mathcal{D}_{1/2}^+$ ($j = 1/2$ matrices).

Away from $\mathbf{k} = \mathbf{0}$ the crystal symmetry is reduced to a subgroup of O_h. For instance, along Δ, the crystal symmetry becomes C_{4v}, for which the double group has no irreps of dimension higher than 2. The 4-fold degeneracy decomposes to $\Gamma_8^+ = \Gamma_6 \oplus \Gamma_7$ where $\Gamma_{6,7}$ are 2-dimensional irreps of the C_{4v} double group. Γ_8^+ therefore splits away from the Γ point into a pair of 2-fold bands called heavy-holes (HH, $m_j = \pm 3/2$) and light-holes (LH, $m_j = \pm 1/2$).

1.1.3 Quantum bits and spin-orbit coupling

A quantum bit, or qubit, is the quantum counterpart of classical bits. In contrast to classical bits, which can either be in a state of value $\mathbb{0}$ or $\mathbb{1}$, a qubit will in general find itself in a quantum superposition between the $\mathbb{0}$ state and the $\mathbb{1}$ state:

$$|\psi\rangle = c_{\mathbb{0}} |\mathbb{0}\rangle + c_{\mathbb{1}} |\mathbb{1}\rangle . \tag{1.8}$$

A qubit is always normalized, meaning that for any qubit $|\psi\rangle$ given by (1.8), the superposition coefficients satisfy $|c_{\mathbb{0}}|^2 + |c_{\mathbb{1}}|^2 = 1$. A qubit is realized by any two-level quantum system that is sufficiently well isolated from its environment, such that the qubit dynamics involves only the states $|\mathbb{0}\rangle$ and $|\mathbb{1}\rangle$. If $E_{\mathbb{0}}$ and $E_{\mathbb{1}}$ are the energies associated with $|\mathbb{0}\rangle$ and $|\mathbb{1}\rangle$ respectively, and $\hbar\omega = E_{\mathbb{1}} - E_{\mathbb{0}} > 0$ is the qubit energy, any excited level $|\mathbb{e}\rangle$ at energy $E_{\mathbb{e}}$ should be far from both $|\mathbb{0}\rangle$ and $|\mathbb{1}\rangle$. In particular, excited levels should not come by $\hbar\omega$-energy steps (as in a harmonic oscillator), since this would suppress the qubit addressability. Two-level systems are fortunately abundant in physics. Among the simplest are the spin 1/2 of an electron or the polarization of a photon. More complex systems also provide useful platforms to implement two-level systems, such as gate-defined semiconductor spin qubits, which are the focus of this thesis. Other implementations also include trapped ion qubits, color center qubits or superconducting qubits.

Once a qubit is defined ($E_{\mathbb{1}} \neq E_{\mathbb{0}}$), its total energy is given by the Hamiltonian

$$H_q = E_{\mathbb{1}} |\mathbb{1}\rangle \langle\mathbb{1}| \tag{1.9a}$$

$$= \hbar\omega\varsigma_+\varsigma_-, \tag{1.9b}$$

where $E_{\mathbb{0}} \equiv 0$ without loss of generality and where the operators $\varsigma_\pm$ are given by

$$\varsigma_+ = |\mathbb{1}\rangle\langle\mathbb{0}|, \qquad \varsigma_- = |\mathbb{0}\rangle\langle\mathbb{1}|, \tag{1.10}$$

with anti-commutation relations $\{\varsigma_\pm, \varsigma_\mp\} = 1$ and $\{\varsigma_\pm, \varsigma_\pm\} = 0$. Driving the qubit is performed by applying an oscillating perturbation W that is off-diagonal with respect to $\{|\mathbb{1}\rangle, |\mathbb{0}\rangle\}$. If the driving is performed at frequency ω', the perturbation Hamiltonian is

$$W = \frac{\hbar\Omega}{2}\left(e^{-i\omega' t}\varsigma_+ + e^{i\omega' t}\varsigma_-\right), \tag{1.11}$$

where $\Omega = 2\,|\langle\mathbb{1}|\,W\,|\mathbb{0}\rangle|\,/\hbar$. Solving the time-dependent Schrödinger equation for (1.8), assuming $\omega' = \omega$, and switching to the rotating frame via the substitution $\tilde{c}_{\mathbb{1}} = e^{i\omega t}c_{\mathbb{1}}$, we find the following differential equations for $c_{\mathbb{0}}(t)$ and $\tilde{c}_{\mathbb{1}}(t)$:

$$\frac{\mathrm{d}}{\mathrm{d}t}\tilde{c}_{\mathbb{1}}(t) = -\frac{i\Omega}{2}c_{\mathbb{0}}(t), \qquad \frac{\mathrm{d}}{\mathrm{d}t}c_{\mathbb{0}}(t) = -\frac{i\Omega}{2}\tilde{c}_{\mathbb{1}}(t). \tag{1.12}$$

For a qubit initially in state $|\mathbb{0}\rangle$, (1.12) solves into

$$\tilde{c}_{\mathbb{1}}(t) = -i\sin\left(\frac{\Omega t}{2}\right), \qquad c_{\mathbb{0}}(t) = \cos\left(\frac{\Omega t}{2}\right), \tag{1.13}$$

indicating that the driving induces oscillations in the probabilities $P_{\mathbb{0}}(t) = |c_{\mathbb{0}}|^2 = \frac{1}{2}(1 - \cos\Omega t)$ and $P_{\mathbb{1}}(t) = |c_{\mathbb{1}}|^2 = \frac{1}{2}(1 + \cos\Omega t)$ with (Rabi) frequency Ω. The Rabi frequency increases if the driving frequency $\omega' \neq \omega$, but at the cost of smaller probability oscillation amplitudes.

A *spin* qubit maps the $\mathbb{0}$ and $\mathbb{1}$ states directly to a particle's spin 1/2 projections $|-\rangle$ and $|+\rangle$ along a given axis, usually specified by a static magnetic field $\mathbf{B}$. Setting this field along the z axis without loss of generality, the two-level system is described by the Zeeman Hamiltonian

$$H_q = g\mu_{\mathrm{B}}B\sigma_+\sigma_-, \tag{1.14}$$

where g is the particle's g factor and $\sigma_\pm$ are Pauli raising and lowering operators. Driving the qubit requires a magnetic field $\tilde{\mathbf{B}}$ that oscillates in the x-y plane. The Hamiltonian of this perturbation is given by

$$W = \frac{g\mu_\mathrm{B}\tilde{B}}{2}\left(\sigma_x \cos\omega t + \sigma_y \sin\omega t\right) \tag{1.15}$$

$$= \frac{g\mu_\mathrm{B}\tilde{B}}{2}\left(e^{-i\omega t}\sigma_+ + e^{i\omega t}\sigma_-\right), \tag{1.16}$$

from which we easily identify $\omega = g\mu_\mathrm{B}B/\hbar$ and $\Omega = g\mu_\mathrm{B}\tilde{B}/\hbar$. Resonant driving of a qubit by means of an oscillating magnetic field is referred as electron spin resonance (ESR).

In semiconductor heterostructures, spin-orbit coupling can be leveraged such that the two-level system consists of the particle's spin-1/2 projections *entangled* with orbital degrees of freedom. In this situation, a static **B**-field is still required to define the two-level system, but driving can surprisingly be performed only with oscillating *electric* fields. This process must involve some intermediate orbital state as the electric field cannot directly couple to the spin degree of freedom. To demonstrate this, let the two-level system be defined by

$$|\mathbb{0}\rangle = |-\rangle\,|0,0\rangle + \beta_\mathbb{0}\,|+\rangle\,|1,0\rangle\,, \tag{1.17a}$$

$$|\mathbb{1}\rangle = |+\rangle\,|0,0\rangle - \beta_\mathbb{1}\,|-\rangle\,|0,1\rangle\,, \tag{1.17b}$$

and with a Hamiltonian given by

$$H_q = g\mu_\mathrm{B}B\varsigma_+\varsigma_-. \tag{1.18}$$

The small parameters $\beta_\mathbb{0}$ and $\beta_\mathbb{1}$ ($\beta^2_{\mathbb{0},\mathbb{1}} \approx 0$) arise from spin-orbit coupling and are such that $\beta_\mathbb{0} = \beta_\mathbb{1}$ if the static $\mathbf{B}$ field is removed. The kets $|n_1, n_2\rangle$ are orbital eigenstates and are acted upon with ladder operators a_1 and a_2 as in the usual harmonic oscillator:

$$a_1 = \frac{x - iy}{2l} + \frac{ilk_-}{2}, \qquad\qquad a_2 = \frac{x + iy}{2l} + \frac{ilk_+}{2}, \tag{1.19}$$

where l is a characteristic length of the device and $k_\pm = k_x \pm ik_y$ with $k_{x,y}$ the particle's wavevector components. Writing x and y in terms of the a_i's:

$$x = \frac{l}{2}\left(a_1 + a_1^\dagger + a_2 + a_2^\dagger\right), \qquad y = \frac{il}{2}\left(a_1 - a_1^\dagger - a_2 + a_2^\dagger\right), \tag{1.20}$$

the perturbation Hamiltonian associated with the oscillating electric field $\tilde{\mathbf{F}}$ is

$$W = e\tilde{F}\left(x\cos\omega t - y\sin\omega t\right) \tag{1.21a}$$

$$= \frac{e\tilde{F}l}{2}\left(a_1 + a_2^\dagger\right)e^{-i\omega t} + \text{H.c.}. \tag{1.21b}$$

Projecting W onto $\{|\mathbb{1}\rangle, |\mathbb{0}\rangle\}$ gives a perturbation Hamiltonian with a structure similar to that of (1.11):

$$W = \frac{e\tilde{F}l}{2}(\beta_{\mathbb{0}} - \beta_{\mathbb{1}})\left(e^{-i\omega t}\varsigma_+ + e^{i\omega t}\varsigma_-\right), \tag{1.22}$$

with the qubit energy and Rabi frequency easily identified as $\omega = g\mu_{\text{B}}B$ and $\Omega = e\tilde{F}l(\beta_{\mathbb{0}} - \beta_{\mathbb{1}})/\hbar$ respectively. Electrical driving of a spin qubit as in the last example is referred as electric-dipole spin resonance (EDSR). EDSR on semiconducting spin qubits is enabled notably by engineering the Rashba spin-orbit coupling arising from the spatial inversion asymmetry of the heterostructure. There are three types of Rashba spin-orbit couplings, one of which is linear in momentum ($\sim k_-$) and two of which are cubic in momentum ($\sim k_+^3$ and $\sim k_-k_+k_-$). Since EDSR relies on electrical dipolar interaction, orbital degrees of freedom that are entangled with the spin degree of freedom must not differ by more than one quantum of energy, as in (1.17). Rashba spin-orbit coupling terms that contribute to EDSR must therefore change $|n_1, n_2\rangle$ by only one quantum, which is the case for the two Rashba terms $\sim k_-$ and $\sim k_-k_+k_-$.

1.2 Motivation

Quantum technologies exploit the quantum properties of nature to perform an operation or a task. Among these technologies, quantum computing has been a very active research field in the last few decades since it was proven that quantum algorithms could solve certain problems much faster than any classical algorithm [5, 6]. A significant scientific and engineering challenge is the physical implementation of qubits that can be manipulated and entangled efficiently with low relaxation and dephasing rates. Electron spins in semiconductor quan-

tum dots attracted a lot of attention after Daniel Loss and David P. DiVincenzo revealed their potential as qubits [7]. This implementation brings many advantages: first, solid-state physics and semiconductor processing have been at the heart of information technologies for multiple decades. This knowledge can be recycled and applied to solid-state quantum computing. Secondly, arrays of interconnected quantum dots enable large scale multi-qubit quantum systems ($> 10^6$ physical qubits) capable of solving practical quantum algorithms [8]. Quantum dots are also convenient to implement two-qubit operations, since tunnel coupling between neighboring dots can be precisely engineered [9–12]. Thirdly, the vast amount of semiconductor elements and their alloys, combined with lattice engineering from epitaxy can be leveraged to create extremely diversified quantum systems.

In the past few years, research in this field was mostly oriented towards devices based on group III-V materials, notably GaAs and InAs [13]. While III-V qubits are notoriously fast [14, 15], thanks to their inherently large spin-orbit interaction, an important issue is the interaction of the electron spin with the surrounding nuclear spin bath. This increases the decoherence rate of the qubit through hyperfine interaction and is only partially alleviated by means of decoupling schemes [16]. Since the late 2000's and early 2010's, a whole new axis of research has sparkled with the experimental demonstration of group IV semiconductor qubits [17, 18]. In contrast to III-V's, group IV elements have nuclear spin-free isotopes. Isotopically enriched nuclear spin-free, nuclear spin-full depleted materials such as ^{28}Si or ^{70}Ge therefore eliminate this decoherence channel. Following that approach, electron spins in Si quantum dots have reached coherence times $T_2 = 28\,\mathrm{ms}$ and dephasing times $T_2^* = 120\,\mu\mathrm{s}$ [19]. However, one drawback of Si-based qubits is the inherently small spin-orbit coupling, which typically requires the fabrication of on-chip magnetic field striplines for qubit manipulation, hindering scaling-up efforts. Recently, there has been a surge of interest towards hole spin-based qubit devices. Holes have many advantages over electrons: the p-type symmetry of their wavefunction reduces hyperfine interactions with the nuclear spin bath [20]. Holes are also more affected by spin-orbit interaction than electrons, enabling all-electrical qubit manipulation schemes such as electric dipole spin resonance (EDSR) and g-tensor modulation resonance (g-TMR). Moreover, holes occupy a single valley (the Γ point valley) which eliminates the complications related to valley splitting. To this end, a shift towards hole spins in Ge has occurred in the past few years, with the first devices already demonstrated in $Si_{1-x}Ge_x$/Ge/$Si_{1-x}Ge_x$ QWs in the late 2010's [21]. This system has all the advantages listed before, plus a few more from the intrinsic properties of Ge: it has a higher intrinsic SOI than Si, it is compatible with Si processing, and it has the highest hole mobility of all standard semiconductors [22, 23].

The coherent growth of Ge onto strain-relaxed $Si_{1-x}Ge_x$ barriers results in compressive epi-

taxial strain in the Ge layer. HHs being typically heavier than LHs towards the growth direction, combined with the effects of strain on the band structure, the ground state in state-of-the-art Ge qubits are HHs. Besides the aforementioned qualities pertaining to holes in Ge, HHs also come with a few drawbacks. First, a sizable Zeeman splitting requires large magnetic fields due to the near-zero in-plane g-factor. HHs also have a negligible linear Rashba SOC and their largest cubic Rashba contribution does not participate in EDSR. Instead, their smaller cubic Rashba parameter that contributes to EDSR is highly dependent on the device geometry through the LH admixture within the HH ground state. Given that LH-HH mixing improves the driving efficiency and increases the in-plane g-factor of HH spin qubits, LH ground states could potentially be promising candidates for spin qubits. Indeed, their g-factor remains finite for in-plane magnetic fields. Secondly, they have a large linear Rashba interaction and their largest contribution to cubic Rashba SOC is compatible with EDSR [24]. Thirdly, the small LH component arising from LH-HH mixing is indispensable in devices relying on proximity induced superconductivity [25]. Therefore, a mostly LH system with a small HH component could potentially be more efficient in such devices. Lastly, LHs are key ingredients for transferring the polarization state of a photon to the spin state of a solid-state qubit [26, 27].

Pushing a LH to the ground state is challenging since the amount of tensile strain required to change the ordering between LHs and HHs must overcome the large out-of-plane mass of HHs. There are only a few material combinations that (a) have a substantial lattice mismatch to induce the required tensile strain in the QW layer and (b) have a compatible band alignment with LH confinement. A candidate material system is Ge with GaAs/InGaAs barriers [28]. However, mixing group III-V and group IV elements can result in low quality interfaces, and is difficult to integrate with Si processing. Another group IV-only option is to grow a $Si_{1-x}Ge_x$ QW on a stack of multiple $Si_{1-y}Ge_y$ barriers with different compositions [29]. This approach is superior in terms of Si compatibility but implements the qubit in $Si_{1-y}Ge_y$, which could lead to smaller SOI, and smaller mobilities due to alloy scattering [30]. Finally, a LH ground state in Ge can be realized by introducing Sn into the barriers. Since the lattice constant of Sn is larger than that of Ge, sufficient Sn content and strain relaxation in the barriers will introduce a large amount of tensile strain in Ge, leading to LH confinement in Ge [31, 32]. One potential advantage of this material system is its direct bandgap across the QW and barrier stack, where directness in the barriers is provided by the incorporation of Sn and that in the well by large tensile strain (roughly +1.68% tensile strain or more, see Chapter 5).

In light of the previous discussion, it is of great interest to investigate the spin properties of LHs in group IV low-dimensional systems, which have been left aside in favor of HHs

in literature. Although they share the same total angular momentum $j = 3/2$, LH spins behave quite differently than HH spins as will be shown in this thesis. In addition, the novel $Ge_{1-x}Sn_x$-based system involves mixed type-I and type-II band alignments that are not well documented. Effective models that have been derived for HH spins must therefore be carefully revisited for LH systems, which is the central subject of this thesis.

1.3 Research objectives

To address the scientific questions raised in Section 1.2, this thesis is constructed around the following main objectives:

- Develop a strain resolved $k \cdot p$ theory framework to investigate light hole spin properties in group-IV semiconductor nanostructures;
- Benchmark the $k \cdot p$ theory, as well as the material parametrization of group-IV semiconductors;
- Elucidate the interplay of strain, strain relaxation, and material concentration on the nature of light hole confinement;
- Investigate the dynamics of light holes as well as their spin-orbit coupling properties in Ge low dimensional systems;
- Introduce a light hole qubit design and investigate its properties.

1.4 Thesis outline

The next Chapter of this dissertation is a review of the current knowledge on the physics of electron and holes in semiconductor low-dimensional systems. We emphasize the importance of SOC on the behavior of charge carriers, before discussing the implications of the hyperfine coupling on spin dynamics, as well as opportunities towards photon-to-spin hybrid devices brought by semiconductor nanostructures. The review also covers the progress that has been made so far regarding the development of spin qubit devices in group-IV semiconductor heterostructures. The chapter then concludes with a review of state-of-the-art modeling techniques of electron and holes in heterostructures using $k \cdot p$ theory. Chapter 3 is devoted to a thorough description of the $k \cdot p$ model that was developed to accurately describe LH spin dynamics in heterostructures. The amount of details included should be sufficient for anyone with reasonable background in solid-state physics to reproduce the results of the remaining chapters. Chapter 4 consists of the benchmark of the theoretical

framework applied to the experimental observation of vanishing Zeeman energies in Ge two-dimensional hole gases [33]. Chapter 5 introduces a group-IV platform based on $Ge_{1-x}Sn_x$ heterostructures that are promising candidates for realizing a LH ground state in tensile strained Ge [34]. Conditions on the materials, strain and sizes of the layers for the appearance of a LH ground state are laid out. This is followed by an exploration of the LH ground state properties for a wide range of heterostructure parameters, such as residual strain, Sn content in the barrier layers and QW thickness. Chapter 6 focuses on one particular point in the parameter space that was explored in Chapter 5 and describes the dynamics of LH qubits in $Ge_{1-x}Sn_x$/Ge/$Ge_{1-x}Sn_x$ gate defined quantum dots [24]. Finally, Chapter 7 introduces a tensile strained Ge Metal-Oxide-Semiconductor (MOS) QW. We show that this configuration can still host a LH ground state, but allows a much greater control on the SOC strength, with "cold" and "hot" spots appearing for certain QW geometries. This chapter also covers the effects of tilted magnetic fields and elongation of the quantum dot on the dynamics of LH spins. Following the conclusion in Chapter 8, a few appendices can be found, which offer complementary information on the theoretical framework of Chapter 3.

CHAPTER 2 LITERATURE REVIEW

2.1 Holes in group-IV semiconductors

2.1.1 Spin-orbit coupling-enabled phenomena

Spin-orbit coupling (SOC) is a relativistic effect induced by the perceived motion of the crystal ion lattice relative to a moving electron. The spin-orbit Hamiltonian for such an electron is derived from Dirac's equation, and reads [35]:

$$H_{\mathrm{SO}} = -\frac{\hbar}{4m_0^2c^2}\mathbf{p}\cdot\boldsymbol{\sigma}\times\mathbf{f}(\mathbf{r}), \tag{2.1}$$

where $\mathbf{f}(\mathbf{r}) = -[V(\mathbf{r}), \mathbf{p}]/(i\hbar)$ is the Lorentz force on the electron from the crystal's periodic potential $V(\mathbf{r})$. SOC is particularly stronger for p-like valence band holes compared to s-like conduction band electrons. In the former case, SOC lifts the degeneracy of the 3-fold degenerate $l = 1$ levels (6-fold including spin) into the 4-fold degenerate $j = 3/2$ group of HHs and LHs, and into the $j = 1/2$ group of SO holes. The energy difference between the $j = 3/2$ and the $j = 1/2$ groups is called the spin-orbit gap Δ_0. SOC has profound effects on the energy spectrum of holes in semiconductor heterostructures. For instance, by engineering the band offsets between adjacent materials and/or by applying a DC out-of-plane gate electric field, the inversion symmetry of the heterostructure may be broken, resulting in a $B = 0$ spin splitting called the Rashba effect [2]. For s-like conduction electrons, the Rashba effect is modelled to lowest order in momentum $\mathbf{k}$ by the Hamiltonian [36]

$$H_c^{\mathrm{R}} = \alpha\mathbf{k}\times\mathbf{F}\cdot\boldsymbol{\sigma} \tag{2.2a}$$

$$\rightarrow \alpha F_z \begin{bmatrix} 0 & k_- \\ k_+ & 0 \end{bmatrix}, \tag{2.2b}$$

where $\mathbf{F}$ is the external electric field, $\boldsymbol{\sigma}$ is the vector of Pauli matrices σ_i, $k_\pm = k_x \pm ik_y$, and where the second line corresponds to $\mathbf{F} = F_z\mathbf{e}_z$. It is evident from (2.2a) that the spin splitting is linear in the field F_z and linear in momentum k. It should be noted however that (2.2a) is even with time-reversal. In fact, one can show that the Rashba Hamiltonian (2.2a) does not break the Kramers degeneracy

$$E_+(\mathbf{k}_\parallel) = E_-(-\mathbf{k}_\parallel), \tag{2.3}$$

where $E_\pm$ are the eigenvalues of (2.2a) and $\mathbf{k}_\parallel = k_x\mathbf{e}_x + k_y\mathbf{e}_y$. A similar Hamiltonian can be derived for the $j = 3/2$ holes at the edge of the valence band [36]. This gives

$$H_v^{\mathrm{R}} = \alpha_1 \mathbf{k}\times\mathbf{F}\cdot\mathbf{J} + \alpha_2 \mathbf{k}\times\mathbf{F}\cdot\boldsymbol{\mathcal{J}} \tag{2.4a}$$

$$\to \alpha_1 F_z \begin{bmatrix} 0 & \sqrt{3}k_-/2 & 0 & 0 \\ & 0 & k_- & 0 \\ & & 0 & \sqrt{3}k_-/2 \\ & \dagger & & 0 \end{bmatrix} + \alpha_2 F_z \begin{bmatrix} 0 & 7\sqrt{3}k_-/8 & 0 & 3k_+/4 \\ & 0 & 5k_-/2 & 0 \\ & & 0 & 7\sqrt{3}k_-/8 \\ & \dagger & & 0 \end{bmatrix}, \tag{2.4b}$$

where $\mathbf{J}$ is the vector of (unit-less) spin 3/2 matrices ($[J_\alpha, J_\beta] = i\epsilon_{\alpha\beta\gamma}J_\gamma$), $\boldsymbol{\mathcal{J}} = \mathcal{J}_x\mathbf{e}_x + \mathcal{J}_y\mathbf{e}_y + \mathcal{J}_z\mathbf{e}_z$ is the vector of $\mathcal{J}_i \equiv J_i^3$ matrices, and α_2 is usually much smaller than α_1, since the former arises only from couplings with higher conduction bands. Ignoring for now the α_2 term, a comparison between the LH subspace in (2.4a) with (2.2a) indicates that the Rashba splitting for LHs is quite similar to that of electrons. Moreover, it is also clear that no linear-in-k spin splitting occurs for HHs, at least not in this simple 4-band model. Rashba spin splitting for HHs either require the α_2 parameter or arises from expanding invariants beyond linear-in-k terms. In fact, the next contributing terms for HHs are cubic in k, and come in two varieties, illustrated by the following Rashba Hamiltonian for HHs up to k^3 terms [1]:

$$H^{\mathrm{R}} = \left(i\beta_1 k_+ - i\beta_2 k_-^3 + i\beta_3 k_+ k_- k_+\right)\sigma_+ + \mathrm{H.c.}. \tag{2.5}$$

Here the β_i coefficients are the Rashba parameters, with $\beta_1 = 3\alpha_2 F_z/4$ being the linear term from (2.4a), and $\beta_{2,3}$ corresponding to the two aforementioned varieties of cubic-in-momentum Rashba SOI.

Rashba spin physics in solid state systems has been an active area of research in the last few decades. New phenomena have emerged from Rashba physics such as spin interferometers [37, 38], the spin Hall effect [39–41] and the quantum spin Hall effect [42, 43]. The cubic Rashba SOI in quasi 2D hole system was investigated in InGaAs [44] and GaAs [45] QW heterostructures. However, the presence of cubic-in-k Dresselhaus SOI arising from the bulk inversion asymmetry of III-V semiconductors makes it more challenging to differentiate it from Rashba SOI. In contrast, the simplicity of the band structure and lack of Dresselhaus SOI in group IV semiconductors such as Ge make them ideal environments to investigate

cubic-in-k Rashba SOI [46]. In qubit devices, the cubic Rashba interaction is an essential ingredient for electric dipole spin resonance (EDSR). The inherently large SOI of Ge has therefore made it a material of choice to implement electrically driven hole spin qubits [47]. It should be noted that, despite successful attempts to make EDSR-driven heavy hole spin qubits in Ge [48], the relevant term in (2.5) that contributes to driving, β_3, is much smaller than β_2 for heavy holes. It is still an open question whether EDSR has other contributions aside from the β_3 term in experiments. There have been suggestions that linear-in-k Rashba terms arising from inhomogeneous strain fields can increase Rabi-frequencies by one order of magnitude [49, 50].

Similarly to Rashba SOI, the crystal lattice also influences the g-factor of charge carriers. For an electron in free space submerged in a uniform and constant magnetic field $\mathbf{B}$, the g-factor is the proportionality factor between the strength of the field $B = \sqrt{\mathbf{B} \cdot \mathbf{B}}$ and the energy difference between its two spin eigenstates due to the Zeeman effect. This is described by a Hamiltonian similar to that of the Rashba effect (2.2a), but with $\mathbf{k}$ replaced by the mechanical wavenumber $\mathbf{K} = \mathbf{k} + e\mathbf{A}/\hbar$ where $\mathbf{A}$ is the vector potential and with the electric field $\mathbf{F}$ being replaced by $i\mathbf{K}$ [36]:

$$H_e^{\mathrm{Z}} = \frac{i\alpha_0 g_0}{2} \mathbf{K} \times \mathbf{K} \cdot \boldsymbol{\sigma} \tag{2.6a}$$

$$= \frac{1}{2} g_0 \mu_{\mathrm{B}} \mathbf{B} \cdot \boldsymbol{\sigma}, \tag{2.6b}$$

where $\alpha_0 = \hbar^2/(2m_0)$, $\mu_{\mathrm{B}} = e\hbar/(2m_0)$ is the Bohr magneton and where the $\mathbf{B}$ field arises from the non-commutativity of the $\mathbf{K}$'s: $\mathbf{K} \times \mathbf{K} = e\mathbf{B}/(i\hbar)$. Conduction band electrons in semiconductors have a similar Zeeman Hamiltonian but with g_0 being replaced by an effective g-factor, simply labeled g in this thesis, that is material-dependent. The same connection to Rashba SOI also exists for the 4-fold HH and LH subspace:

$$H_v^{\mathrm{Z}} = 2\kappa \mu_{\mathrm{B}} \mathbf{B} \cdot \mathbf{J} + 2q\mu_{\mathrm{B}} \mathbf{B} \cdot \boldsymbol{\mathcal{J}}. \tag{2.7}$$

Here, the κ parameter is the hole effective g-factor and q is the so-called cubic-in-J correction to the g-factor. As with g, both parameters are material dependent. In parallel with the α_2 parameter in (2.4a), q is likewise much smaller than κ [51]. It is straightforward to show that the Hamiltonian (2.7) gives anisotropic Zeeman splitting with respect to the field's orientation. For instance, the HH and LH g-factor for out-of-plane fields are $6\kappa + 27q/2$ and $2\kappa + q/2$ respectively, while for in-plane fields they are $3q$ and $4\kappa + 10q$ respectively. This

agrees with magneto-transport experiments realized in 2D HH gases in Ge [52]. In contrast, as illustrated by (2.6), the g-factor of conduction band electrons is independent of the field orientation [53].

In addition to being material-dependent, modifications to the g-factor can emerge from confinement effects, coupling to the SO band, as well as wavefunction spread into adjacent layers [33, 54, 55]. In nanowire devices, strong spin-orbit coupling, confinement and orbital effects from the applied magnetic field were shown to strongly renormalize the hole g-factor [56]. Site-dependent and anisotropic g-factors were also reported in Ge hut wire singlet-triplet qubit devices [57]. Moreover, hole density-dependent g-factors are indication of the non-parabolicity of the hole band structure [58]. Confinement effects and anisotropies of the conduction band electron g-tensor were also reported in Ge QWs [59]. Moreover, non-vanishing off-diagonal g-tensor components were reported in group III-V QW devices grown along low-symmetry crystallographic orientations [60]. Lastly, giant g-factors in large SOC systems offer ideal platforms for topological-qubit-based quantum computing [61]. It is an understatement to say that g-factor engineering plays a central role in the realization of qubit devices and spintronics in general.

2.1.2 Isotopic purification and hyperfine interaction

The spin of a charge carrier in a crystal (nano)structure interacts with the surrounding nuclear spins through hyperfine interaction. An electron spin interacts with a nearby nucleus through three mechanisms [62]: (a) the Fermi contact hyperfine interaction, (b) the (anisotropic) dipole-dipole interaction and (c) the coupling of the electron orbital angular momentum to the nuclear spin. For s-like particles such as conduction band electrons, the orbital angular momentum contribution can be neglected as a good approximation [63, 64], resulting in the isotropic Fermi contact interaction dominating. On the other hand, due to the p-symmetry of holes, the Fermi contact hyperfine interaction is weaker [20]. However, since holes have $l \neq 0$, the orbital angular momentum contribution term has a significant contribution to the total hyperfine coupling [65]. Hyperfine coupling parameters A calculated for electrons and HHs in Si with neighboring ^{29}Si isotopes illustrate the anisotropy of the hyperfine interaction for holes: $A = -2.4\,\mu$eV for electrons, and $A_\parallel = -2.5\,\mu$eV, $A_\perp = -0.01\,\mu$eV for HHs [65]. In particular, $A_\perp$ being very small indicates a mostly Ising-like interaction to the nuclear spin bath. A similar calculation for HHs in Ge is likely to give qualitatively similar results, thanks to the similar crystal structure. On the other hand, dynamics of LH spins show a qualitatively different behavior compared to HHs [20]. For instance, it was shown that LH spins aligned with the z axis and with a magnetic field $\mathbf{B} \parallel \mathbf{e}_z$ will decay and experience

oscillations over time, in contrast to HHs that remain in a steady state. Moreover, a HH-LH mixed spin hyperfine interaction is more isotropic than that of pure HH spins. The hyperfine interaction for holes in Si and Ge quantum dots was also shown to be sensitive to the device geometry and tunable with external electric fields [66].

Group IV semiconductors Si, Ge and Sn all have stable isotopes with zero and non-zero nuclear spins. Si has three stable isotopes: ^{28}Si and ^{30}Si with zero spin and ^{29}Si with spin 1/2 and natural abundance of 4.68%. Ge has five stable isotopes, four of which have zero nuclear spin: ^{70}Ge, ^{72}Ge, ^{74}Ge, ^{76}Ge, and only ^{73}Ge with nuclear spin 9/2 and natural abundance 7.73%. Sn has 10 stable isotopes, 3 of which have spin 1/2 nuclei and 7 without spin that amount to 83.4% of the natural abundance. As will be discussed below, Si-purified qubit devices have already been realized on multiple occasions. On the other hand, Ge-purified qubit devices are yet to be demonstrated, but are likely to occur in the near future, since purified ^{70}Ge QWs have already been realized [67].

2.1.3 Photon-to-spin interfaces

As quantum networks grow larger in size, transferring a qubit state to another qubit over large distances will become a necessity. Despite solid-state qubits being a good choice for quantum state storage, they are not ideal for long-range information transfer that would be required, for instance, in long-range entanglement or quantum key distribution. Converting the solid-state qubit to a more suitable implementation for long-range communication and vice-versa needs to be addressed.

One useful qubit implementation for long-range information transfer is the polarization degree of freedom of photons. The solid-state to-be-encoded qubit would act as a photodetector in the process of transferring the polarization state of the photon to that of the electron or hole. The mechanisms involved in this conversion depend on whether the solid-state qubit is encoded in the spin of an electron, of a HH or of a LH. Previous proposals have already investigated various options [26]. An important aspect is that the conversion from the photon to the spin involves both holes and electrons, and maximal coherence in the solid-state qubit should involve separable hole and electron spin components. For this, the two spin projections of the electron should be accessible from only one spin component of the hole, or vice-versa. To this end, the authors in Reference [26] suggested to leverage the p-like character and $m_j = 1/2$ characteristic of LHs, in addition to their large out-of-plane and in-plane g-tensor components. The main challenge is of course to engineer the required amount of tensile strain in the active layer to push LHs to the ground state, for which the authors in Reference [26] suggested combining Si with III-V semiconductors. Another recent work also suggested to

encode the qubit in the spin polarization of a HH subject to in-plane **B**-fields, leveraging their vanishingly small g-factor in such configuration [27].

2.2 Spin qubit devices in group-IV semiconductor heterostructures

2.2.1 Si/Si$_{1-x}$Ge$_x$ and Si-MOS spin-qubit devices

The first reported implementations of a Loss-DiVincenzo qubit [7] in group IV planar heterostructures were performed with electron spins in a Si/Si$_{1-x}$Ge$_x$ QW in 2009 [17] and in a Si-MOS device in 2010 [18]. In the former, a type-II QW band alignment confines electrons of the band minima located along Δ near the X point of the FBZ in the tensile strained Si layer. In these devices, epitaxial strain is an essential ingredient to partially lift the degeneracy of the 6 equivalent Δ valleys into a 4-fold group of higher energy and a 2-fold group of lower energy, hosting the qubit. However, the proximity of these 2 valleys brings complex intervalley spin dynamics [68], and introduces a decoherence channel for qubits [69–72]. Multiple approaches have been employed to increase the valley splitting energy, such as tuning the gate field potentials [73–75], introducing a Ge concentration peak at the interfaces [76] or within the Si well [77]. Another promising approach is to introduce an oscillating concentration of Ge inside the Si well [78]. On the other hand, small intrinsic SOC in Si combined with the absence of Dresselhaus SOI leads to longer coherence times compared to group III-V devices [17]. Suppressing hyperfine interactions by eliminating nuclear spin-full isotopes from the Si QW has also been realized for qubit devices [11, 70, 79–92] and for multi-qubit devices [93–95], enhancing coherence times.

In Si-MOS devices, Δ-valley electrons are confined by a triangular potential at the interface between Si and an oxide, usually SiO_2. Despite Dresselhaus SOI being absent in bulk Si, carriers confined near an interface are subject to a Dresselhaus term [96–98]. The sign of the Dresselhaus-like scale parameter changes with monoatomic shifts of the interface, while the usual Rashba SOI parameter remains unchanged [99]. Cooperation of the two SOI types can lead to valley-state dependent g-factors [100] as well as g-factor renormalization [98]. In addition, SOI-driven Stark shifts of the g-factor [19] contributes to dephasing, but can be mitigated by tilting the magnetic field towards a magic angle such that the Rashba and Dresselhaus SOI enter destructive interference [101]. Improvements to coherence times can also be realized by means of isotopic purification of Si, which has already been made in a number of experiments [19, 100–113], in some cases leading to very long spin lifetimes of $\sim 1\,\mathrm{s}$ [103, 109].

Despite the rich SOI effects, Si is still a semiconductor with weak SOI, with a spin-orbit

gap Δ_0 of only 44 meV. Consequently, driving the qubit usually requires oscillating magnetic fields generated from on-chip ESR microwave transmission lines [102]. In more recent devices, EDSR is enabled by applying gradient magnetic fields to boost the otherwise small SOI of Si [11, 87, 88] or even without micromagnets, relying solely on electric field gradients [114].

2.2.2 Ge/$Si_{1-x}Ge_x$ spin-qubit devices

$Si_{1-x}Ge_x$/Ge/$Si_{1-x}Ge_x$ QW heterostructures provide a type-I band alignment, thus confining electrons, HHs and LHs into the Ge layer. The epitaxial growth of Ge on lattice mismatched $Si_{1-x}Ge_x$ barriers leads to compressive strain in Ge, typically around -0.6% for $x = 0.8$ Ge content [22, 115], ensuring a HH ground state in Ge. Despite holes suffering from typically shorter coherence times compared to electron spin qubits in Si, hole qubits in Ge typically have shorter gate times [116]. Moreover, many complications of Si-based electron qubits including valley states are not an issue in hole systems. Ge is also a higher SOI semiconductor, with a split-off gap Δ_0 more than 6.5 times that of Si. The p-symmetry of the hole wavefunction provides additional leverage of SOI, thus enabling fast all-electrical control of the qubit without the need of additional ESR striplines [21]. Moreover, the very large mobility of holes in Ge [115] inherited from small effective masses alleviates size constraints of gate patterns, allowing larger quantum dot designs and therefore simplifying the fabrication process [48]. So far, significant progress has been made towards enhancing the qubit relaxation times [117], achieving single-hole occupation regimes [48], realizing multi-qubit arrays [21, 48, 118–124], quantum simulators [125] and quantum processors [12, 126]. The anisotropic nature of hole spins was also investigated in a two-qubit system [127], revealing that strong g-factor anisotropies make the qubit sensitive to electric field fluctuations, inducing charge-noise-mediated decoherence. Hyperfine coupling with nearby ^{73}Ge atoms was also found to be highly anisotropic and to be detrimental for the qubit coherence. Isotopically enriched ^{70}Ge quantum wells would mitigate this decoherence channel [67].

2.3 $k \cdot p$ modelling of energy bands in cubic semiconductors

$k \cdot p$ theory is a pseudo-empirical approach to evaluating the band structure of semiconductors. It is a Schrödinger-like eigenvalue problem based on the Bloch solutions of electrons in periodic potentials. One major advantage of $k \cdot p$ theory is its ability to produce very accurate band structures with only a small set of material parameters, while requiring few computational resources. Moreover, $k \cdot p$ theory can be adapted for heterostructures, where band-edge offsets between adjacent materials lead to discrete energy spectra. This theory is still widely used to this day in many areas of solid-state physics. In optoelectronics for in-

stance, it provides invaluable information on epitaxial strain and material composition effects on band edge energies, and therefore on absorption or on emission wavelengths [128, 129]. $k \cdot p$ theory can also provide information on discrete energy level spacings [130–132], non-parabolicity effects [133], symmetry breaking effects [134, 135], and more, all of which are relevant in many technological applications.

$k \cdot p$ theory was originally introduced in 1950 by W. Shockley as a means of evaluating energy surfaces in cubic semiconductors with as few material parameters as possible [136]. His work was driven by strong evidence of the non-parabolicity of hole and electron energy surfaces in Ge, revealed by magneto-transport experiments [137]. In the following years, J. M. Luttinger and W. Kohn pioneered the so-called theory of invariants to expand $k \cdot p$ theory where band minima are not necessarily at $\mathbf{k} = \mathbf{0}$, and to include effects from impurity states in cubic semiconductors [138, 139]. These works layed the groundwork for the now extensively used Luttinger-Kohn (LK) and Kane $k \cdot p$ Hamiltonians, where the latter incorporated the lowest conduction band to the theory to accurately describe the absorption spectra of small bandgap material InSb [140]. In the next decade, efforts were made in an attempt to expand $k \cdot p$ theory away from band minima to cover the whole first Brillouin zone (FBZ). This gave rise to the now extensively used 15-band (or 30-band including spin) $k \cdot p$ framework, which was first demonstrated in 1966 by M. Cardona *et al.* for the band structure of Si and Ge [141].

The first application of $k \cdot p$ theory for semiconductor heterostructures, where material parameters are position dependent, was performed in 1975 by G. Bastard *et al.* who pointed out its relevance in graded mixed semiconductors such as $Cd_xHg_{1-x}Te$ and $Zn_xCd_{1-x}S$ [142]. This variation of $k \cdot p$ theory is now referred as the envelope function approximation (EFA), and is applicable in systems where the band edge energies of the constituent semiconductors vary slowly on the length scale of the lattice constant. However, the space-dependence of material parameters implies non-commutativity with momentum operators, and therefore brings a problem of proper operator ordering. Following the works of G. Bastard, many attempts to rederive the $k \cdot p$ Hamiltonian from first principles were made. To this end, the works of M. G. Burt and B. A. Foreman [143–146] have provided the widely used Burt-Foreman operator ordering, which is also the one employed for the work described in this thesis.

A well-known problem in EFA $k \cdot p$ theory involving violently oscillating envelope functions and energy levels within the bandgap can appear if the lowest conduction bands are included in the theory, as in the Kane model. These unphysical "solutions", or spurious solutions, are a consequence of a loss of ellipticity of the coupled differential equations for certain sets of material parameters [147]. Furthermore, otherwise well-behaved sets of material parameters might lead to non-ellipticity following the removal of remote band contributions

when introducing more bands to the $k \cdot p$ matrix. In such cases, the solution proposed by B. A. Foreman is to adjust the parameter responsible for the coupling between the CB and the VB, the so-called Kane parameter P, such that the electron effective mass exactly vanishes without its remote band contributions [148]. His approach also specifies the proper operator ordering for the linear-in-momentum terms belonging to the subspace coupling the CB and VB. An artifact to this approach, already highlighted in Reference [148], is discontinuous CB envelope functions at abrupt interfaces. Spurious solutions encountered in the work presented in this thesis were completely removed following the approach in Reference [148], without additional tuning required. A first-principle derivation of the 14-band EFA $k \cdot p$ Hamiltonian was also provided by T. Eißfeller in [149, 150], where a symmetry-adapted finite-element scheme was introduced to alleviate spurious solution problems. Also incorporated were the cubic-in-J correction to the hole g-factor and an explicit derivation of the terms arising from external magnetic fields.

The books from L. C. Lew Yan Voon [151] and R. Winkler [35] are must-reads for anyone interested in $k \cdot p$ theory, its history and its applications in large spin-orbit coupling systems.

CHAPTER 3 THEORETICAL FRAMEWORK

This chapter is devoted to laying out the notation, the physical background, and the theoretical framework behind a large portion of the results presented in this thesis. Sections are mostly organised following a bottom-up approach, where more general concepts are discussed first, before delving into more specialized subjects. Plenty of detail is provided for anyone who wishes to refine their understanding of $k \cdot p$ theory, and the results derived from it. This also helps removing ambiguities such as operator orderings, material parameter rescaling, perturbation theory orders, and notably, basis phase factors. To make this Chapter as self-consistent as possible, every equation and result following Hamiltonian (3.64) has been rederived with proper operator orderings, giving rise to commutator and anti-commutator terms that have been overlooked in the past, and according to the basis employed by R. Winkler in Reference [35]. An attentive reader might notice small sign or phase differences in a few matrix elements compared to other works, but these are insignificant and do not change the predictions of the theory, as long as they are consistent with the basis being used.

Overall, this chapter provides an all-consistent framework derived from $k \cdot p$ theory to describe SOC effects in semiconductor heterostructures for the lowest conduction band electrons, LHs, HHs and SO holes. A notable result is that in quantum well heterostructures, charge carriers can be organised in two groups of quantum levels, referred here as "light" (η for short) and "heavy" (H). The latter corresponds simply to HHs, whereas the former is a superposed state of $m_j = \pm 1/2$ carriers, namely CB electrons, LHs and SO holes. Consequently, all equations pertaining to η levels are a generalization of those for pure electron, LH, and SO hole systems.

We also point out the following convention employed therein: energy points "upwards". A typical electron band minimum like $\smile$ is assigned a positive curvature (positive effective mass), whereas a typical hole band maximum like $\frown$ has negative curvature (negative effective mass). Also, the sign of diagonal g-tensor elements for electron *and* holes are such that g is positive if $E_+ - E_- > 0$, where $\pm$ is the projection of the particle's pseudo-spin along the z axis.

3.1 Electron in a periodic lattice: the $k \cdot p$ theory

3.1.1 General $k \cdot p$ formulation

Let an electron with charge $q = -e$ and free mass m_0 move in an infinite periodic ion lattice. The potential $V(\mathbf{r})$ felt by the electron from the surrounding positively charged nuclei is

$$V(\mathbf{r}) = -\frac{eQ}{4\pi\epsilon_0} \sum_{lmn} \sum_{s=1}^{2} \frac{1}{\|\mathbf{r} - \mathbf{c}_s - \mathbf{R}_{lmn}\|}, \tag{3.1}$$

where $\mathbf{c}_{1,2}$ are the position of the two atomic sites contained in the primitive cell specified by $\mathbf{R}_{lmn}$ and Q is their (positive) charge. Including spin-orbit coupling (but not strain for simplicity), the corresponding Hamiltonian is

$$H = \frac{p^2}{2m_0} + V(\mathbf{r}) - \frac{\hbar}{4m_0^2c^2}\mathbf{p} \cdot \boldsymbol{\sigma} \times \mathbf{f}(\mathbf{r}), \tag{3.2}$$

where $\mathbf{f}(\mathbf{r}) = -[V(\mathbf{r}), \mathbf{p}]/(i\hbar)$ is the force on the electron from the nuclei. The Schrödinger equation for the electron reads

$$H\,|\varphi\rangle = E\,|\varphi\rangle\,. \tag{3.3}$$

It is clear from (3.1) that H is invariant with respect to any translation by a lattice vector $\mathbf{R}_{lmn}$, since this corresponds only to a rearrangement of the terms in the sum (3.1). This suggests Bloch waves eigenstates

$$|\varphi\rangle \equiv |\varphi_{n\mathbf{k}}\rangle = e^{i\mathbf{k}\cdot\mathbf{r}}\,|n\mathbf{k}\rangle\,, \tag{3.4}$$

where the wavevector $\mathbf{k} \in$ FBZ and n is a band index. The functions $u_{n\mathbf{k}}(\mathbf{r}) \equiv \langle\mathbf{r}|n\mathbf{k}\rangle$ are periodic in $\mathbf{r}$: $u_{n\mathbf{k}}(\mathbf{r} + \mathbf{R}_{lmn}) = u_{n\mathbf{k}}(\mathbf{r})$. Inserting (3.4) into (3.3) and multiplying from the left on both sides by $e^{-i\mathbf{k}\cdot\mathbf{r}}$ gives a Schrödinger equation for the $|n\mathbf{k}\rangle$ functions only:

$$\tilde{H}(\mathbf{k})\,|n\mathbf{k}\rangle = E_n(\mathbf{k})\,|n\mathbf{k}\rangle\,, \tag{3.5}$$

where the $\mathbf{k}$-dependent Hamiltonian $\tilde{H}(\mathbf{k}) \equiv e^{-i\mathbf{k}\cdot\mathbf{r}}He^{i\mathbf{k}\cdot\mathbf{r}}$. From the canonical relations $[r_i, p_j] = i\hbar\delta_{i,j}$, one finds

$$e^{-i\mathbf{k}\cdot\mathbf{r}}p^2e^{i\mathbf{k}\cdot\mathbf{r}} = p^2 + 2\hbar\mathbf{k}\cdot\mathbf{p} + \hbar^2k^2, \tag{3.6a}$$

$$e^{-i\mathbf{k}\cdot\mathbf{r}}\mathbf{p}e^{i\mathbf{k}\cdot\mathbf{r}} = \mathbf{p} + \hbar\mathbf{k}. \tag{3.6b}$$

Defining

$$\boldsymbol{\pi} = \mathbf{p} - \frac{\hbar}{4m_0c^2}\boldsymbol{\sigma}\times\mathbf{f}(\mathbf{r}), \tag{3.7}$$

and using (3.6), the $\mathbf{k}$-dependent Hamiltonian $\tilde{H}(\mathbf{k})$ becomes

$$\tilde{H}(\mathbf{k}) = \frac{p^2}{2m_0} + V(\mathbf{r}) + \frac{\hbar}{m_0}\mathbf{k}\cdot\boldsymbol{\pi} + \frac{\hbar^2k^2}{2m_0} - \frac{\hbar}{4m_0^2c^2}\mathbf{p}\cdot\boldsymbol{\sigma}\times\mathbf{f}(\mathbf{r}). \tag{3.8}$$

A $k\cdot p$ matrix is constructed by projecting (3.8) onto an orthonormal basis. The eigenstates of Hamiltonian (3.8) evaluated at $\mathbf{k}=\mathbf{0}$ and without the spin-orbit interaction terms define such a basis:

$$\left[\frac{p^2}{2m_0} + V(\mathbf{r})\right]|\nu\sigma\rangle = \mathcal{E}_\nu\,|\nu\sigma\rangle\,, \tag{3.9}$$

where ν is a band index and σ is the spin index. In this basis, the matrix elements $\tilde{H}^{\nu'\sigma'}_{\nu\sigma}(\mathbf{k}) = \langle\nu\sigma|\tilde{H}(\mathbf{k})|\nu'\sigma'\rangle$ are

$$\tilde{H}^{\nu'\sigma'}_{\nu\sigma}(\mathbf{k}) = \left(\mathcal{E}_\nu + \frac{\hbar^2k^2}{2m_0}\right)\delta_{\nu,\nu'}\delta_{\sigma,\sigma'} + \frac{\hbar}{m_0}\mathbf{k}\cdot\mathbf{P}^{\nu'\sigma'}_{\nu\sigma} + \Delta^{\nu'\sigma'}_{\nu\sigma}, \tag{3.10}$$

where $\mathbf{P}^{\nu'\sigma'}_{\nu\sigma} = \langle\nu\sigma|\boldsymbol{\pi}|\nu'\sigma'\rangle \approx \langle\nu|\mathbf{p}|\nu'\rangle\,\delta_{\sigma,\sigma'}$ are momentum matrix elements and

$$\Delta^{\nu'\sigma'}_{\nu\sigma} = -\frac{\hbar}{4m_0^2c^2}\,\langle\nu\sigma|\mathbf{p}\cdot\boldsymbol{\sigma}\times\mathbf{f}(\mathbf{r})|\nu'\sigma'\rangle\,. \tag{3.11}$$

Finally, eigenstates $|n\mathbf{k}\rangle$ of $\tilde{H}(\mathbf{k})$ are obtained from an expansion in terms of the basis kets $|\nu\sigma\rangle$:

$$|n\mathbf{k}\rangle = \sum_{\nu\sigma} c^{(n)}_{\nu\sigma}(\mathbf{k})\,|\nu\sigma\rangle, \tag{3.12}$$

where the scalars $c^{(n)}_{\nu\sigma}(\mathbf{k}) = \langle\nu\sigma|n\mathbf{k}\rangle$ result from the diagonalization of (3.10):

$$\sum_{\nu'\sigma'} \tilde{H}^{\nu'\sigma'}_{\nu\sigma}(\mathbf{k}) c^{(n)}_{\nu'\sigma'}(\mathbf{k}) = E_n(\mathbf{k}) c^{(n)}_{\nu\sigma}(\mathbf{k}). \tag{3.13}$$

In principle, the infinite dimensional eigenvalue problem (3.13) solves the energy dispersion of the electron for all the bands n everywhere in the FBZ. However, in most situations one is only interested in a subset of bands that are close in energy to the bandgap of the material. The infinite dimensional problem (3.13) is therefore often turned into a finite dimensional problem by merely *truncating* the set $\{|\nu\sigma\rangle\}$ to include only the bands of interest, plus a few more below and above in energy to take in account inter-band couplings. An example of such truncation is the extensively used 30-band $k \cdot p$ framework, which, as its name suggests, includes in its basis a total of 15 ν-bands ($\times 2$ including spin σ) starting from the fundamental valence band level Γ_1^+ and up in energy. This set gives accurate energy dispersions for the bands below the bandgap and those above, but not too far from the bandgap. The energies $\mathcal{E}_\nu$, the momentum matrix elements $\mathbf{P}^{\nu'\sigma'}_{\nu\sigma}$ and the spin-orbit constants $\Delta^{\nu'\sigma'}_{\nu\sigma}$ are usually obtained from experiment, and/or by fitting the $k \cdot p$ dispersion with other theoretical models. Moreover, many elements in $\mathbf{P}^{\nu'\sigma'}_{\nu\sigma}$ and $\Delta^{\nu'\sigma'}_{\nu\sigma}$ vanish because of strict symmetry requirements, thus greatly reducing the number of free parameters. The theory of invariants is a powerful tool for determining which elements in $\mathbf{P}^{\nu'\sigma'}_{\nu\sigma}$ and $\Delta^{\nu'\sigma'}_{\nu\sigma}$ must vanish by symmetry. It is important to note that the basis $|\nu\sigma\rangle$ is derived from a spin-independent Hamiltonian, hence the functions $|\nu\rangle$ transform according to the irreps $\Gamma^{\pm}_{1,\ldots,5}$ of O_h. However, since $\tilde{H}(\mathbf{k})$ includes spin-orbit coupling, the levels $|n\mathbf{0}\rangle$ transform according to the $\Gamma^{\pm}_{6,7,8}$ irreps of the O_h double group.

The $E_n(\mathbf{k})$ relation along Δ up to X and along Λ up to L are shown for Si, Ge and Sn in Fig. 3.1. In all cases, the lowest band transforms according to $\Gamma_6^+ = \Gamma_1^+ \otimes \mathcal{D}_{1/2}^+$ as mentioned earlier. The energy difference between the split-off band (Γ_7^+) and the degenerate HH-LH bands (Γ_8^+) is smaller in Si ($\sim 0.044\,\text{eV}$) than in Ge ($\sim 0.290\,\text{eV}$). The lowest band above the bandgap in Si transforms according to Γ_6^-, in contrast to Ge where it transforms as Γ_7^-. According to the parameters given in [152], this ordering changes around $\text{Si}_{0.70}\text{Ge}_{0.30}$. The two pairs of 2-fold degenerate bands transforming according to $\Gamma_8^{\pm}$ are difficult to distinguish in Si at this energy scale. In Sn, the two lowest bands transform according to Γ_6^+ and Γ_7^+ like Si and Ge, but the Γ_7^- band is located below the Γ_8^+ band, making Sn a bandgap-free material. According to the parameters given in [153], the ordering between Γ_7^- and Γ_8^+ changes (or the bandgap closes) around $\text{Ge}_{0.70}\text{Sn}_{0.30}$. Table 3.1 gives a summary of the band symmetries and energies for Ge.

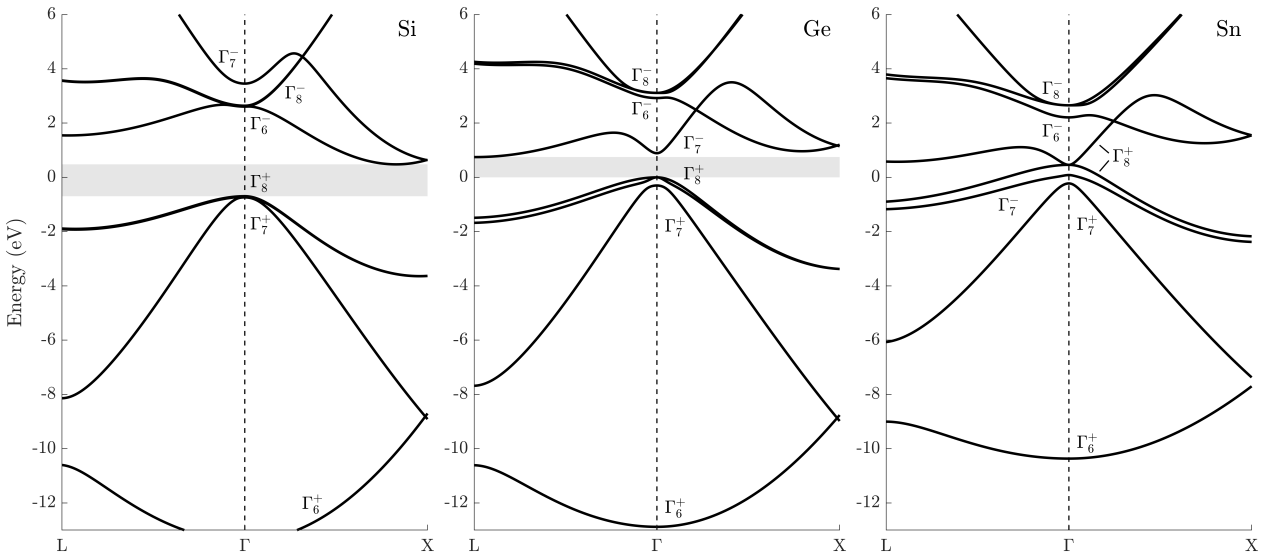

Figure 3.1 Bulk energy dispersion $E_n(\mathbf{k})$ of Si, Ge and Sn obtained from the 30-band $k \cdot p$ model (3.10). The $k \cdot p$ parameters for Si and Ge are taken from [152], while those for Sn are taken from [153]. The labels indicate according to which irrep of the O_h double group the bands transform at the Γ point. The zero-energy point is set at the top of the Γ_8^+ band in Ge, while the dispersions for Si and Sn are aligned with that of Ge according to the valence band offsets listed in Reference [154] and [155] respectively. The bandgap in Si and Ge is indicated by the shaded area.

3.1.2 Strain effects in $k \cdot p$ theory

A material's crystal structure undergoes small deformations when external stress is applied. Crystal deformations are quantified by the strain tensor ε_{ij} (in general position-dependent), and is connected to the external stress tensor σ_{ij} by a rank-four stiffness tensor C_{ijkl}:

$$\sigma_{ij} = \sum_{kl} C_{ijkl} \varepsilon_{kl}. \tag{3.14}$$

In particular, the component i of a lattice vector $\mathbf{R}'$ in the deformed crystal lattice is connected to the components of the unstrained lattice vector $\mathbf{R}$ by

$$R'_i = \sum_j \left(\delta_{ij} + \varepsilon_{ij}\right) R_j. \tag{3.15}$$

In heterostructures, stress may be generated by epitaxial growth on a lattice mismatched substrate. Non-zero strain tensor elements appear in the deposited material near the interface with the substrate to match the lattice constants of both materials. At a certain critical

Table 3.1 Band symmetries and energies without and with spin-orbit coupling (SOC). Bands are ordered as in Ge.

no SOC			**with SOC**	
Sym.	Energy		Sym.	Energy
Γ_4^-	$\mathcal{E}_{\Gamma_4^-}$	$\nearrow$	Γ_8^-	$E_{\Gamma_8^-} = \mathcal{E}_{\Gamma_4^-} + \Delta_0'/3$
		$\searrow$	Γ_6^-	$E_{\Gamma_6^-} = \mathcal{E}_{\Gamma_4^-} - 2\Delta_0'/3 = E_{\Gamma_8^+} + E'_{g\Gamma}$
Γ_2^-	$\mathcal{E}_{\Gamma_2^-}$	$\rightarrow$	Γ_7^-	$E_{\Gamma_7^-} = \mathcal{E}_{\Gamma_2^-} = E_{\Gamma_8^+} + E_{g\Gamma}$
		Bandgap		
Γ_5^+	$\mathcal{E}_{\Gamma_5^+}$	$\nearrow$	Γ_8^+	$E_{\Gamma_8^+} = \mathcal{E}_{\Gamma_5^+} + \Delta_0/3$
		$\searrow$	Γ_7^+	$E_{\Gamma_7^+} = \mathcal{E}_{\Gamma_5^+} - 2\Delta_0/3$
Γ_1^+	$\mathcal{E}_{\Gamma_1^+}$	$\rightarrow$	Γ_6^+	$E_{\Gamma_6^+} = \mathcal{E}_{\Gamma_1^+}$

thickness, the strain energy in the deposited material becomes too large, and dislocations start to appear as a means to relieve strain energy in a process called strain relaxation [156]. An [001]-oriented epitaxial growth of a material with diamond crystal structure results in a strain tensor whose elements are easily computed from the lattice constant mismatch. If a_0 is the lattice constant of the substrate "S" and a is that of the grown material "A", the strain tensor in material A has no shear components (off-diagonal terms):

$$\varepsilon = \begin{bmatrix} \varepsilon_{\parallel} & 0 & 0 \\ 0 & \varepsilon_{\parallel} & 0 \\ 0 & 0 & \varepsilon_{\perp} \end{bmatrix}, \tag{3.16}$$

with $\varepsilon_{\parallel} = (a - a_0)/a_0$, and $\varepsilon_{\perp} = -2\,(c_{12}/c_{11})\,\varepsilon_{\parallel}$, where c_{11} and c_{12} are material-specific elastic constants. The cases $\varepsilon_{\parallel} > 0$ and $\varepsilon_{\parallel} < 0$ are called tensile and compressive strain respectively. Strain effects are easily incorporated in the $k \cdot p$ framework through the so-called Bir-Pikus Hamiltonian [157].

The crystal deformation and symmetry reduction from strain has important effects on the energy band structure. The first notable effect is a modification of the direct bandgap energy $E_{g\Gamma}$ which increases with compressive strain and decreases with tensile strain. This has important consequences in optoelectronics, since an indirect bandgap material may become direct with tensile strain if the rate of change of $E_{g\Gamma}$ with $\varepsilon_{\parallel}$ is larger than that of the indirect transition. Material specific parameters that quantify the effects of strain on energy transitions are called deformation potentials. The second notable effect is the energy splitting between the heavy hole (HH) and the light hole (LH) bands that are otherwise degenerate at the Γ point. This arises from the symmetry reduction of the crystal to a subgroup of O_h. The

deformation potential b determines the band ordering at a given strain, and is negative for Si, Ge, Sn and for many group III-V semiconductors [158]. Therefore, tensile (compressive) strain pushes the LH (HH) band towards the bandgap. This plays a crucial role in hole engineering, since strain may change the type of holes in the ground state. The energy difference between LHs and HHs also changes many hole properties such as the g-factor and effective mass.

3.1.3 Finite-dimensional $k \cdot p$ Hamiltonians

The 30-band $k \cdot p$ Hamiltonian from the previous section is appropriate for calculating the energy dispersion of the bands near the bandgap in the whole FBZ. However, for most situations we only require a description of these bands for small $\mathbf{k}$ near the Γ point. In this case, it is more practical to write an effective Hamiltonian $H_{\mathcal{A}}$ only for the relevant set of bands $\mathcal{A}$, with other bands (the so-called remote bands) taken in account perturbatively. The dispersion from this effective Hamiltonian matches that of the 30-band $k \cdot p$ for small values of $\mathbf{k}$ before diverging at larger $\mathbf{k}$. Two methods are available to construct the effective Hamiltonian $H_{\mathcal{A}}$; the first being the theory of invariants, and the second being Löwdin's partitioning method.

Theory of invariants

The theory of invariants is a powerful tool for constructing Hamiltonians only from symmetry considerations. Despite being unable to predict how large a given Hamiltonian term is, it is still particularly useful for identifying *which* terms are allowed in the Hamiltonian. The approach consists of writting the effective Hamiltonian $H_{\mathcal{A}}(\mathcal{K})$ as a sum of $\mathcal{K}$-independent matrices $\mathcal{X}$ that transform according to specific irreps of the symmetry group of the Hamiltonian, multiplied by combinations of the components of $\mathcal{K}$ that transform according to those irreps [35]:

$$H_{\mathcal{A}} = \sum_{\kappa,\lambda,\mu} c_{\kappa,\lambda,\mu} \mathcal{I}_{\kappa,\lambda,\mu}, \tag{3.17}$$

where

$$\mathcal{I}_{\kappa,\lambda,\mu} = \sum_{l=1}^{d_\kappa} \mathcal{X}_l^{(\kappa,\lambda)} \mathcal{K}_l^{(\kappa,\mu)*} \tag{3.18}$$

are the so-called invariants. Here $\mathcal{K}$ is a general tensor operator that represents for instance

the wavevector $\mathbf{k}$, the magnetic field $\mathbf{B}$, the strain tensor ε_{ij} or an electric field $\mathbf{F}$. The κ index represents the irrep Γ_κ of dimension d_κ, λ (μ) represents different sets of matrices $\mathcal{X}$ (tensor operators $\mathcal{K}$) transforming according to the irrep κ. The l index labels the d_κ matrices (tensor operators) that transform within each other according to irrep Γ_κ. The constants $c_{\kappa,\lambda,\mu}$ are material dependent and can be extracted from experiment. For an effective matrix block $H_{\alpha\beta}$ where α and β indicates to which irrep the basis functions transform, the irreps Γ_κ are identified as those that are contained in the direct product $\Gamma_\alpha \otimes \Gamma_\beta^*$.

For instance, the Γ_κ irreps of a 3×3 effective Hamiltonian $H_{\Gamma_5^+,\Gamma_5^+}$ (ignoring spin, strain, magnetic or electric fields) for the three valence bands that transform according to Γ_5^+ are

$$\Gamma_5^+ \otimes \Gamma_5^{+*} = \Gamma_1^+ \oplus \Gamma_3^+ \oplus \Gamma_4^+ \oplus \Gamma_5^+ . \tag{3.19}$$

Nine linearly independent 3×3 matrices are obtained by forming linear combinations of the products $I_i I_j$, where the three matrices $I_{x,y,z}$ are the generators of rotations:

$$I_x = \begin{bmatrix} 0 & 0 & 0 \\ 0 & 0 & -i \\ 0 & i & 0 \end{bmatrix}, \qquad I_y = \begin{bmatrix} 0 & 0 & i \\ 0 & 0 & 0 \\ -i & 0 & 0 \end{bmatrix}, \qquad I_z = \begin{bmatrix} 0 & -i & 0 \\ i & 0 & 0 \\ 0 & 0 & 0 \end{bmatrix}. \tag{3.20}$$

For properly chosen combinations, these 9 matrices provide a basis that block diagonalizes $\Gamma_5^+ \otimes \Gamma_5^{+*}$ according to (3.19) (see Table 3.2). It is apparent from (3.19) that no odd powers of $\mathbf{k}$ are allowed in this Hamiltonian, since all irreps involved in (3.19) are even with respect to inversion (the + superscript). By forming products with the $\mathcal{X}$ and $\mathcal{K}$, one obtains the invariants that constitute the Hamiltonian $H_\mathcal{A}$. The most general spin-less Hamiltonian for the Γ_5^+ subspace up to k^2 is therefore

$$H_{\Gamma_5^+,\Gamma_5^+}(\mathbf{k}) = c_{1,1} + c_{1,2}(k_x^2 + k_y^2 + k_z^2) + c_3(I_x^2 k_x^2 + \text{c.p.}) + c_5(\{I_x, I_y\}k_x k_y + \text{c.p.}) \tag{3.21a}$$

$$= c_{1,1} + Mk^2 + \begin{bmatrix} (L-M)k_x^2 & Nk_x k_y & Nk_x k_z \\ Nk_y k_x & (L-M)k_y^2 & Nk_y k_z \\ Nk_z k_x & Nk_z k_y & (L-M)k_z^2 \end{bmatrix}. \tag{3.21b}$$

where L, M, and N are simply combinations of the c constants. In contrast, if the Γ_2^- conduction band is also included in the effective Hamiltonian, the 1×3 block that couples the valence band with the conduction band must be linear in $\mathbf{k}$, since $\Gamma_5^+ \otimes \Gamma_2^{-*} = \Gamma_4^-$ is

odd under inversion and corresponds to the symmetry of (k_x, k_y, k_z). The resulting block is simply

$$H_{\Gamma_2^-,\Gamma_5^+} = iP \begin{bmatrix} k_x & k_y & k_z \end{bmatrix}, \tag{3.22}$$

where the i factor is conventional. A similar procedure yields matrices for the block coupling the Γ_5^+ subspace with the Γ_4^- subspace ($H_{\Gamma_4^-,\Gamma_5^+}$, linear in $\mathbf{k}$) and the 6-fold $\mathcal{D}_{1/2}^+ \otimes \Gamma_5^+$ subspace (H_{SO}, independent of k):

$$H_{\Gamma_4^-,\Gamma_5^+} = Q \begin{bmatrix} 0 & k_z & k_y \\ k_z & 0 & k_x \\ k_y & k_x & 0 \end{bmatrix}, \tag{3.23}$$

$$H_{\mathrm{SO}} = \frac{\Delta_0}{3} \sum_j \sigma_j \otimes I_j. \tag{3.24}$$

Just as c, L, M, and N, the constants P, Q and Δ_0 are material parameters. P and Q are specific momentum matrix elements $\langle \nu | \mathbf{p} | \nu' \rangle$, whereas Δ_0 is a spin-orbit coupling constant [c.f. (3.11)].

Table 3.2 List of matrices $\mathcal{X}$ and wavevector operators $\mathbf{k}$ that transform according to (3.19) for $\mathbf{B} = \mathbf{0}$. $\{A, B\} = AB + BA$ is the anti-commutator.

Irrep	$\mathcal{X}$	$\mathcal{K}$
Γ_1^+	$2 = I_x^2 + I_y^2 + I_z^2$	$1,\ k_x^2 + k_y^2 + k_z^2$
Γ_3^+	$(I_x^2 - I_y^2,\ I_x^2 + I_y^2 - 2I_z^2)$	$(k_x^2 - k_y^2,\ k_x^2 + k_y^2 - 2k_z^2)$
Γ_4^+	(I_x, I_y, I_z)	None for $\mathbf{B} = \mathbf{0}$
Γ_5^+	$(\{I_x, I_y\}, \{I_y, I_z\}, \{I_z, I_x\})$	$(k_x k_y, k_y k_z, k_z k_x)$

Löwdin's partitioning method

The other approach to obtain $H_{\mathcal{A}}$ is based on perturbation theory, or the so-called Löwdin partitioning method (also called a Schrieffer-Wolff transformation). We start from a general multi-band Hamiltonian $H = H_0 + W$, where H_0 is a Hamiltonian with known eigenvalues E_i and associated eigenstates $|\varphi_i\rangle$ and W is a perturbation term with unknown eigenvalues and eigenstates. In the eigenbasis of H_0, the matrix for H consists of one diagonal term

$\mathbf{E}_0 = \mathrm{diag}\{E_1, E_2, \dots\}$ containing all the eigenvalues E_i of H_0, plus a matrix for W: (bold characters represent matrices)

$$\mathbf{H} = \mathbf{E}_0 + \mathbf{W}. \tag{3.25}$$

In basis $\{|\varphi_i\rangle\}$, the matrix elements of $\mathbf{E}_0$ and $\mathbf{W}$ are

$$\langle\varphi_i|H_0|\varphi_j\rangle = E_i\delta_{i,j} \tag{3.26}$$

$$\langle\varphi_i|W|\varphi_j\rangle = W_{i,j} = W^*_{j,i}. \tag{3.27}$$

The total Hilbert space $\mathcal{H}$ is then divided into one Hilbert space $\mathcal{H}_\mathcal{A}$ generated by the set of bands $\mathcal{A}$ for which we want an effective Hamiltonian. The orthogonal complement Hilbert space $\mathcal{H}_\mathcal{R}$ is generated by all the other bands $\mathcal{R}$, also called the *remote* bands. The idea is to find an unitary matrix $e^{\mathbf{S}}$ such that $\tilde{\mathbf{H}} = e^{\mathbf{S}}\mathbf{H}e^{-\mathbf{S}}$ is block-diagonal with respect to the subspaces $\mathcal{A}$ and $\mathcal{R}$, with the blocks coupling the $\mathcal{A}$ set with the $\mathcal{R}$ set equal to zero. The $\mathbf{S}$ matrix can be found iteratively, with each iteration corresponding to a degree of perturbation. Once the Hamiltonian is block diagonalized to the desired perturbation order, the block corresponding to the $\mathcal{A}$ set is the final effective Hamiltonian $H_\mathcal{A}$. The structure of this Hamiltonian should be identical to that obtained by means of the theory of invariants. Combining the two methods provides explicit expressions for the effective masses that appear in $H_\mathcal{A}$ in terms of the momentum matrix elements $\mathbf{P}^{\nu'\sigma'}_{\nu\sigma}$ and the energies $\mathcal{E}_\nu$ from (3.10). It should be noted that the perturbation is with respect to the wavenumber $\mathbf{k}$ and the magnetic field $\mathbf{B}$, which should remain small for $H_\mathcal{A}$ to be accurate. It is customary to build $H_\mathcal{A}$ up to 2^{nd} order in perturbation, resulting in a matrix depending at most quadratically in $\mathbf{k}$ or linearly in $\mathbf{B}$.

As an example, we consider an effective 6×6 Hamiltonian for the three valence bands Γ_5^+ that were discussed earlier in the context of the theory of invariants, and with spin-orbit effects included. The full Hamiltonian matrix $\mathbf{H}$ corresponds to (3.10), while the part with known eigenvalues and eigenvectors $\mathbf{E}_0$ is given by $\left[\mathcal{E}_{\Gamma_5^+} + \hbar^2k^2/(2m_0)\right]\mathbb{1}_{6\times6}$. The zero-th order approximation of H_6, noted $\mathbf{H}_6^{(0)}$, is obtained by neglecting entirely W. Its matrix elements within the subspace spanned by the $\mathcal{A}$ bands are simply those of $\mathbf{E}_0$:

$$\left(H_6^{(0)}\right)_{\alpha,\beta} = E_\alpha\delta_{\alpha,\beta} \tag{3.28a}$$

$$= \left(\mathcal{E}_{\Gamma_5^+} + \frac{\hbar^2 k^2}{2m_0}\right)\delta_{\alpha,\beta}, \tag{3.28b}$$

where α and β are indices labelling dimensions within the $\mathcal{A}$ subspace only. The first order contribution matrix elements $\left(H_6^{(1)}\right)_{\alpha,\beta}$ are simply the matrix elements of W in basis $\{|\varphi_i\rangle\}$ within the subspace spanned by the $\mathcal{A}$ bands:

$$\left(H_6^{(1)}\right)_{\alpha,\beta} = W_{\alpha,\beta} \tag{3.29a}$$

$$= \frac{\Delta_0}{3}\left(\sum_j \sigma_j \otimes I_j\right)_{\alpha,\beta}. \tag{3.29b}$$

Finally, the matrix elements for the second order contribution $\mathbf{H}_6^{(2)}$ are given by a sum that involve remote bands within the $\mathcal{R}$ set:

$$\left(H_6^{(2)}\right)_{\alpha,\beta} = \frac{1}{2}\sum_\mu W_{\alpha,\mu}W_{\mu,\beta}\left(\frac{1}{\Delta_{\alpha,\mu}} + \frac{1}{\Delta_{\beta,\mu}}\right), \tag{3.30}$$

where $\Delta_{i,j} = E_i - E_j$ and the μ index runs only within the $\mathcal{R}$ subspace. The sum in (3.30) is expanded according to the structure of the Hamiltonian blocks that couple the $\mathcal{A}$-set with the $\mathcal{R}$-set (c.f. (3.22)-(3.23)). The final effective Hamiltonian H_6 is obtained by summing all the perturbative contributions:

$$H_6 = H_6^{(0)} + H_6^{(1)} + H_6^{(2)}. \tag{3.31}$$

It is straightforward to verify that the structure of H_6 within a given spin subspace (neglecting spin-orbit coupling) is identical to (3.21b), with the added benefit of explicit perturbative expressions for the parameters L, M, and so on, in terms of the momentum matrix elements and the energies $\mathcal{E}_\nu$.

3.1.4 List of bulk parameters

The $k \cdot p$ framework described later in section 3.3 requires 20 material parameters. Those are the lattice constant a_0, the direct bandgap energy at the Γ point $E_{g\Gamma}$ (with spin-orbit interaction included, see Table 3.1), the valence band energy $\mathcal{E}_{\Gamma_5^+}$ (relative to vacuum; corresponds to $E_{v,\text{avg}}$ in Reference [154]), the spin-orbit gap Δ_0 between Γ_8^+ and Γ_7^+:

$$\Delta_0 = \frac{3i\hbar}{4m_0^2c^2}\langle X|[\mathbf{p}\times\mathbf{f}(\mathbf{r})]_y|Z\rangle\,, \tag{3.32}$$

the conduction band inverse effective mass $\gamma_c = m_0/m_{c\Gamma}$ and g-factor g, three Luttinger parameters γ_1, γ_2, and γ_3, the hole g-factor parameter κ, the cubic-in-J correction to the g-factor q, the material density ρ, the elastic constants c_{11}, c_{12}, and c_{44}, the hydrostatic deformation potential a_c and a_v for the Γ_7^- and Γ_8^+ band respectively, the b and d deformation potentials for Γ_8^+, and the Kane energy parameter $E_p = P^2/\alpha_0$, where $\alpha_0 = \hbar^2/(2m_0)$ and P is a momentum matrix element:

$$P = \frac{\hbar}{im_0}\langle S\,|\,p_x\,|\,X\rangle\,. \tag{3.33}$$

A list of all parameters appearing in the $k\cdot p$ framework for Si, Ge and Sn is presented in Table 3.3. Additionally, a few complementary parameters are required in order to calculate self consistently some of the parameters listed in Table 3.3, or to evaluate the bandgap directness. Those are presented in Table 3.4. The superscripts "X" and "L" in the deformation potentials Ξ correspond to the conduction band minima along the Δ and the Λ directions, respectively.

An "L" superscript on an effective mass or a g-factor parameter indicates that it contains all remote band contributions. The $k\cdot p$ framework of section 3.3 uses rescaled versions of the "L" parameters. This rescaling removes the remote band contributions that are included in the "L" parameters, which assume that the Γ_7^+, the Γ_8^+ and the Γ_7^- bands are treated perturbatively from each other. For an Hamiltonian that explicitly depends on $\{\Gamma_7^+, \Gamma_8^+, \Gamma_7^-\}$, the rescaling is:

$$\gamma_c = \gamma_c^{\mathrm{L}} - \frac{2E_p}{3E_g}\frac{3E_g/2+\Delta_0}{E_g+\Delta_0} \tag{3.34a}$$

$$g = g^{\mathrm{L}} + \frac{2E_p}{3E_g}\frac{\Delta_0}{E_g+\Delta_0} \tag{3.34b}$$

$$\gamma_1 = \gamma_1^{\mathrm{L}} - \frac{E_p}{3E_g} \tag{3.34c}$$

$$\gamma_2 = \gamma_2^{\mathrm{L}} - \frac{E_p}{6E_g} \tag{3.34d}$$

$$\gamma_3 = \gamma_3^{\mathrm{L}} - \frac{E_p}{6E_g} \tag{3.34e}$$

$$\kappa = \kappa^{\mathrm{L}} - \frac{E_p}{6E_g}, \tag{3.34f}$$

All material parameters of the $Si_{1-x}Ge_x$ and $Ge_{1-x}Sn_x$ alloys, except the effective masses and g-factors, were calculated in the full composition range by interpolating the parameters from the pure elements:

$$P(x) = (1-x)P^{\mathrm{A}} + xP^{\mathrm{B}} - x(1-x)b_P. \tag{3.35}$$

Here $0 \leq x \leq 1$ is the alloy fraction and b_P is a bowing constant for the parameter P, if necessary. Temperature-dependent quantities such as the lattice constant or bandgaps are evaluated by applying (3.35) on the temperature-dependent parameters of the pure elements. For instance if $P^{\mathrm{A,B}}(T)$ is temperature-dependent, $P(x,T)$ of the alloy is given by

$$P(x,T) = (1-x)P^{\mathrm{A}}(T) + xP^{\mathrm{B}}(T) - x(1-x)b_P. \tag{3.36}$$

In particular, the temperature dependence of the bandgaps of pure elements follows a Varshni relation:

$$E_g^{\mathrm{A}}(T) = E_g^{\mathrm{A}}(0) - \frac{\alpha^{\mathrm{A}}T^2}{\beta^{\mathrm{A}} + T}. \tag{3.37}$$

Effective masses and g-factors of $Si_{1-x}Ge_x$

The three Luttinger parameters $\gamma_{1,2,3}^{\mathrm{L}}$, the electron inverse mass γ_c^{L}, and the hole and electron g-factor parameters κ^{L} and g^{L} respectively were computed based on the approach employed in Reference [131, 134] and following the theory outlined in Reference [162]. The procedure starts by removing the contributions of the Γ_2^- and Γ_4^- bands from γ_i^{L} and κ^{L}:

$$\bar{\gamma}_1 = \gamma_1^{\mathrm{L}} + \frac{1}{3}\left(F + 2H_1\right), \tag{3.38a}$$

$$\bar{\gamma}_2 = \gamma_2^{\mathrm{L}} + \frac{1}{6}\left(F - H_1\right), \tag{3.38b}$$

$$\bar{\gamma}_3 = \gamma_3^{\mathrm{L}} + \frac{1}{6}\left(F + H_1\right), \tag{3.38c}$$

$$\bar{\kappa} = \kappa^{\mathrm{L}} + \frac{1}{6}\left(F - H_1\right), \tag{3.38d}$$

and interpolate the obtained rescaled parameters, as well as D (see Table 3.4), according to (3.35) without bowing. The constants $F = -E_p/E_{g\Gamma}$ and $H_1 = -E_p'/E_{g\Gamma}'$, where E_p and E_p' are calculated from the Luttinger parameters:

Table 3.3 Material parameters and bowings for the $k \cdot p$ Hamiltonian.

		Si	$Si_{1-x}Ge_x$	**Ge**	$Ge_{1-x}Sn_x$	**Sn**
Lattice constant						
a_0	[Å @ 0 K]	5.429815[a]	0.0246[h]	5.652357[a]	−0.083[j*]	6.480117[b]
Band energies						
$E_{g\Gamma}$	[eV @ 0 K]	4.185[b]		0.8981[b]	2.46[k*]	−0.413[b]
α_Γ	[10^{-4} eV/ K]	5.367[c]		6.842[i]		−7.94[k]
β_Γ	[K]	745.8[c]		398[i]		11[k]
Δ_0	[eV]	0.0441[b]		0.290[b]	−0.100[j]	0.770[g]
$\mathcal{E}_{\Gamma_5^+}$	[eV]	−0.68[d†]		0		0.69[l†]
Mechanical properties						
c_{11}	[GPa]	165.77[b]		124[b]		69.0[b]
c_{12}	[GPa]	63.93[b]		41.3[b]		29.3[b]
c_{44}	[GPa]	79.62[b]		68.3[b]		36.2[b]
ρ	[g/cm^3]	2.329[b]		5.3234[b]		7.285[b]
Deformation potentials[‡]						
$a_{c\Gamma}$	[eV]	1.98[d]		−8.24[d]		−6.00[m]
a_v	[eV]	2.46[d]		1.24[d]		1.58[n]
b	[eV]	−2.1[e]		−2.86[e]		−2.7[o]
d	[eV]	−4.85[e]		−5.28[e]		−4.1[b]
Effective mass and spin parameters						
$m_{c\Gamma}^{\mathrm{L}}$	[m_0]	0.234[§]	[¶]	0.0382[§]		−0.058[§]
g^{L}	.	1.963[§]	[¶]	−2.81[§]		84.9[§]
γ_1^{L}	.	4.285[f]	[¶]	13.38[f]	[#]	−14.97[g]
γ_2^{L}	.	0.339[f]	[¶]	4.24[f]	[#]	−10.61[g]
γ_3^{L}	.	1.446[f]	[¶]	5.69[f]	[#]	−8.52[g]
κ^{L}	.	−0.26[g]	[¶]	3.41[g]		−11.84[g]
q	.	0.01[f]		0.06[f]		0.30[g]

References: [a]: [159], [b]: [160], [c]: [131], [d]: [154], [e]: [161], [f]: [35], [g]: [162], [h]: [163], [i]: [164], [j]: [165], [k]: [166], [l]: [155], [m]: [167], [n]: [168], [o]: [169]

[*] See (3.36)

[†] Relative to Ge

[‡] The convention $a_{\mathrm{tot}} = a_c - a_v$ is used

[§] Calculated from Luttinger parameters of pure constituents [see (3.44)]

[¶] See (3.44)

[#] See (3.45)

$$E_p = E_{g\Gamma}\left(\frac{1}{3}\gamma_1^{\mathrm{L}} + \frac{4}{3}\gamma_2^{\mathrm{L}} + 2\gamma_3^{\mathrm{L}} + 2\kappa^{\mathrm{L}} + 4q + 1\right), \tag{3.39a}$$

$$E'_p = E'_{g\Gamma}\left(\frac{1}{2}\gamma_1^{\mathrm{L}} - \gamma_2^{\mathrm{L}} + \frac{3}{2}\gamma_3^{\mathrm{L}} - \frac{3}{2}\kappa^{\mathrm{L}} - \frac{117}{24}q\right). \tag{3.39b}$$

$E'_{g\Gamma}$, E_p and E'_p are interpolated according to

$$E'_{g\Gamma}(x) = E'^{\mathrm{Si}}_{g\Gamma}\left(\frac{a^{\mathrm{Si}}}{a(x)}\right)^{\epsilon}, \tag{3.40a}$$

$$E_p(x) = E_p^{\mathrm{Si}}\left[1 + \alpha\left(D(x) - D^{\mathrm{Si}}\right)\right]\left(\frac{a^{\mathrm{Si}}}{a(x)}\right)^2, \tag{3.40b}$$

$$E'_p(x) = E'^{\mathrm{Si}}_p\left[1 + \alpha'\left(D(x) - D^{\mathrm{Si}}\right)\right]\left(\frac{a^{\mathrm{Si}}}{a(x)}\right)^2. \tag{3.40c}$$

with ϵ, α and α' that are consistent with $E'_{g\Gamma}$, E_p and E'_p of Si and Ge. Next, $F(x)$, $H_1(x)$ and $y(x)$ are evaluated for arbitrary alloy concentration x:

$$F(x) = -\frac{E_p(x)}{E_{g\Gamma}(x)}, \tag{3.41}$$

$$H_1(x) = -\frac{E'_p(x)}{E'_{g\Gamma}(x)}, \tag{3.42}$$

$$y(x) = \frac{\Delta_0(x)}{E_{g\Gamma}(x) + \Delta_0(x)}, \tag{3.43}$$

from which the Luttinger parameters at arbitrary x are extracted:

$$\gamma_1^{\mathrm{L}}(x) = \bar{\gamma}_1^{\mathrm{L}}(x) - \frac{1}{3}\left(F(x) + 2H_1(x)\right), \tag{3.44a}$$

$$\gamma_2^{\mathrm{L}}(x) = \bar{\gamma}_2^{\mathrm{L}}(x) - \frac{1}{6}\left(F(x) - H_1(x)\right), \tag{3.44b}$$

$$\gamma_3^{\mathrm{L}}(x) = \bar{\gamma}_3^{\mathrm{L}}(x) - \frac{1}{6}\left(F(x) + H_1(x)\right), \tag{3.44c}$$

$$\kappa^{\mathrm{L}}(x) = \bar{\kappa}^{\mathrm{L}}(x) - \frac{1}{6}\left(F(x) - H_1(x)\right), \tag{3.44d}$$

$$\gamma_c^{\mathrm{L}}(x) = 1 - F(x)(1 - y(x)) + F', \tag{3.44e}$$

$$g^{\mathrm{L}}(x) = 2(1 + F(x)y(x)), \tag{3.44f}$$

where $F' \approx -2$.

Effective masses and g-factors of $\mathbf{Ge_{1-x}Sn_x}$

The electron effective mass $m_{c\Gamma}^{\mathrm{L}}$ and the electron g^{L} factor of Sn were calculated similarly to those of $Si_{1-x}Ge_x$, following the approach outlined in Reference [162] to ensure consistency with the bandgaps and energy couplings listed in Tables 3.3 and 3.4. The three Luttinger parameters $\gamma_{1,2,3}^{\mathrm{L}}$ were interpolated between pure Ge and $Ge_{0.80}Sn_{0.20}$ using the data from Reference [170], giving

$$\gamma_i^{\mathrm{L}}(x) = \gamma_i^{\mathrm{L,Ge}}\left(1 - \frac{x}{0.2}\right) + \gamma_i^{\mathrm{L,GeSn}}\left(\frac{x}{0.2}\right) - b_i\frac{x}{0.2}\left(1 - \frac{x}{0.2}\right), \tag{3.45}$$

with $\gamma_i^{\mathrm{L,Ge}}$ listed in table 3.3, and $\gamma_1^{\mathrm{L,GeSn}} = 29.2108$, $\gamma_2^{\mathrm{L,GeSn}} = 12.2413$, $\gamma_3^{\mathrm{L,GeSn}} = 13.7387$ and $b_1 = 20.3391$, $b_2 = 9.6609$, $b_3 = 9.8187$.

Table 3.4 Complementary material parameters and bowings.

		Si	$Si_{1-x}Ge_x$	**Ge**	$Ge_{1-x}Sn_x$	**Sn**
Band energies						
$E'_{g\Gamma}$	[eV @ 0 K]	3.400[a]	*	3.124[a]		2.400[h]
$E_{g\mathrm{L}}$	[eV @ 0 K]	2.010[b]		0.740[b]	1.23[g†]	0.100[i]
$E_{g\mathrm{X}}$	[eV @ 0 K]	1.155[b]	0.206[b]	0.931[b]		0.7352[i]
α_{L}	[10^{-4} eV/ K]	5.367[a]		4.561[c]		
α_{X}	[10^{-4} eV/ K]	7.021[c]		4.774[a]		
β_{L}	[K]	745.8[a]		210[c]		
β_{X}	[K]	1108[c]		235[a]		
Deformation potentials[‡]						
$a_{c\mathrm{L}}$	[eV]	−0.66[d]		−1.54[e]		−2.14[j]
$a_{c\mathrm{X}}$	[eV]	4.18[e]		2.55[d]		
Ξ_u^{L}	[eV]	16.14[d]		16.2[d]		
Ξ_u^{X}	[eV]	8.6[d]		9.42[d]		
Kane energy coupling parameters						
E_p	[eV]	22.148[§]	*	26.542[§]		23.812[§]
E'_p	[eV]	14.667[§]	*	17.424[§]		15.942[§]
Other						
D	.	1[f]		1.25[f]		1.475[f]

References: [a]: [131], [b]: [171], [c]: [164], [d]: [161], [e]: [154], [f]: [172], [g]: [173], [h]: [162], [i]: [165], [j]: [168],

* See (3.40)

† See (3.36)

‡ The convention $a_{\mathrm{tot}} = a_c - a_v$ is used

§ Calculated from Luttinger parameters [see (3.39)]

Spurious solutions

The Kane momentum matrix element P coupling the Γ_2^- band to the Γ_5^+ bands is known to sometimes cause spurious solutions, often appearing as levels within the bandgap or with violently oscillating envelopes [147–149]. The approach employed here to eliminate spurious solutions is described in Reference [148], and consists of rescaling P:

$$P^2 = 3\alpha_0\gamma_c^{\mathrm{L}}\left(\frac{2}{E_{g\Gamma}} + \frac{1}{E_{g\Gamma}+\Delta_0}\right)^{-1}. \tag{3.46}$$

The remote band contributions in the Luttinger parameters are then readjusted according to (3.34) with $E_p = P^2/\alpha_0$ and P defined as above.

3.2 $k \cdot p$ theory for heterostructures

In this section, the $k \cdot p$ formalism for bulk materials discussed so far is extended to the case of heterostructures consisting of semiconducting layers epitaxially deposited on top of each other. The growth direction is oriented towards the [001] crystal direction and taken parallel to the $+z$ axis.

3.2.1 The envelope function approximation

In semiconductor heterostructures, the energy dispersion dictating the motion of electrons changes with position $\mathbf{r}$, therefore invalidating the Bloch wave solution $|\varphi_{n\mathbf{k}}\rangle = e^{i\mathbf{k}\cdot\mathbf{r}}\,|n\mathbf{k}\rangle$. It was shown in Reference [174] that in heterostructures, it is sufficient to replace the plane wave part in $|\varphi_{n\mathbf{k}}\rangle$ by slowly varying envelope functions. For instance, with confinement along the z-axis (2 degrees of freedom in the x-y plane), the k_z component of $\mathbf{k}$ no longer commutes with the Hamiltonian resulting in envelope functions in the z-dimension. The Bloch wave expansion (3.4) of $|\varphi_{n\mathbf{k}}\rangle$ in terms of $|n\mathbf{k}\rangle$ becomes

$$|\varphi_{j\mathbf{k}_\parallel}\rangle = e^{ik_x x}e^{ik_y y}\,|j\mathbf{k}_\parallel\rangle\,, \tag{3.47}$$

where the band index n has been replaced by a *subband* index j, and where the $e^{ik_z z}$ plane wave is now part of $|j\mathbf{k}_\parallel\rangle$ in the form of an envelope function $\langle z|f^{\nu\sigma}_{j\mathbf{k}_\parallel}\rangle = f^{\nu\sigma}_{j\mathbf{k}_\parallel}(z)$:

$$|j\mathbf{k}_\parallel\rangle = \sum_{\nu\sigma}|\nu\sigma\rangle\,|f^{\nu\sigma}_{j\mathbf{k}_\parallel}\rangle, \tag{3.48}$$

with $\mathbf{k}_\parallel = k_x\mathbf{e}_x + k_y\mathbf{e}_y$. A subband $|\varphi_{j\mathbf{k}_\parallel}\rangle$ is subject to the orthonormality relation

$$\begin{aligned}
\left\langle \varphi_{j\mathbf{k}_\parallel} \,\middle|\, \varphi_{j'\mathbf{k}'_\parallel} \right\rangle &= \int \mathrm{d}^3 r \, \langle \varphi_{j\mathbf{k}_\parallel} | \mathbf{r} \rangle \langle \mathbf{r} | \varphi_{j'\mathbf{k}'_\parallel} \rangle \\
&= \int \mathrm{d}^3 r \left[e^{-ik_x x} e^{-ik_y y} \sum_{\nu\sigma} \langle \nu\sigma | \, f^{\nu\sigma}_{j\mathbf{k}_\parallel}(z)^* \right] \left[e^{ik'_x x} e^{ik'_y y} \sum_{\nu'\sigma'} |\nu'\sigma'\rangle \, f^{\nu'\sigma'}_{j'\mathbf{k}'_\parallel}(z) \right] \\
&= \int \mathrm{d}x \, e^{-ik_x x} e^{ik'_x x} \int \mathrm{d}y \, e^{-ik_y y} e^{ik'_y y} \sum_{\nu\sigma} \int \mathrm{d}z \, f^{\nu\sigma}_{j\mathbf{k}_\parallel}(z)^* f^{\nu\sigma}_{j'\mathbf{k}'_\parallel}(z) \\
&= \delta^2(\mathbf{k}_\parallel - \mathbf{k}'_\parallel) \sum_{\nu\sigma} \int \mathrm{d}z \, f^{\nu\sigma}_{j\mathbf{k}_\parallel}(z)^* f^{\nu\sigma}_{j'\mathbf{k}_\parallel}(z) \\
&= \delta^2(\mathbf{k}_\parallel - \mathbf{k}'_\parallel) \delta_{j,j'}.
\end{aligned} \tag{3.49}$$

In heterostructures, the wavevector components generally do not commute with material parameters since these are now $\mathbf{r}$-dependent. Consequently, in contrast to bulk where material parameters are simply constants, in heterostructures they are instead represented by operators. For example, if γ is a material parameter that changes with z (this could be an effective mass, a strain tensor component, an energy bandgap, ...), we have $[\gamma, k_z] \neq 0$. One can find a matrix for the operator γ by acting with it on position eigenstates $|z\rangle$:

$$\gamma \, |z\rangle = \gamma(z) \, |z\rangle \,, \tag{3.50}$$

where γ is the operator and $\gamma(z)$ is a function returning the value of γ at coordinate z. Material parameters γ are thus diagonal in $\{|z\rangle\}$: $\gamma_{z,z'} = \gamma(z)\delta(z - z')$. In contrast, the matrix for k_z in position basis is clearly not diagonal:

$$\langle z | \, k_z = -i \frac{\mathrm{d}}{\mathrm{d}z} \langle z | \,. \tag{3.51}$$

Special care must be attributed to the operator ordering between material parameters and k_z operators, as an improper ordering is known to result in inaccurate g-factors and unphysical (spurious) solutions [148, 150].

3.2.2 Numerical implementation

In quantum well heterostructures, any material parameter γ is a function of only the z-coordinate, with the growth direction taken as $+z$. Accordingly, the position representation of the Hamiltonian implies the substitution $k_z \to -i\frac{\mathrm{d}}{\mathrm{d}z}$, where the derivative is numerically implemented by means of finite differences. We describe in this section the numerical imple-

mentation of the operators appearing in the $k \cdot p$ Hamiltonian.

The heterostructure is partitioned into a one-dimensional mesh grid, with each point i corresponding to a specific z coordinate equal to z_i. Adjacent mesh points are all separated by the same distance $\delta z = z_{i+1} - z_i$. The mesh is generated by first specifying the $z = 0$ coordinate within the heterostructure. This point is also referred as the *mesh stem*, from which mesh points are appended in both directions a distance δz apart until the whole heterostructure is covered. This approach is beneficial in inversion symmetric systems, since a mesh stem placed on the point of symmetry guarantees a symmetric mesh for any chosen δz. If the heterostructure is of thickness L, and extends from $z = -L_-$ up to $z = L_+$ with $L = L_- + L_+$ and $L_\pm$ positive, the total number of mesh points is $N = \lfloor L_-/\delta z \rfloor + \lfloor L_+/\delta z \rfloor + 1$. The mesh grid indices are ordered such that $z_1 < z_2 < \cdots < z_N$ and $z_{i_0} = 0$, where i_0 is the index of the mesh stem. Figure 3.2 depicts a 7 layer heterostructure partitioned into 11 equally spaced mesh points.

A material parameter γ evaluated at a mesh point z_i located within a layer made of material MTR is simply given by the value of γ for the material MTR. However, if z_i is exactly on an interface, it is ambiguous to which layer it belongs to. In that case, we do one of the following:

- If z_i is to the left of the mesh stem ($z_i < z_{i_0}$), then γ_i corresponds to the value of γ for the material to the *right* of the interface;
- If z_i is to the right of the mesh stem ($z_i > z_{i_0}$), then γ_i corresponds to the value of γ for the material to the *left* of the interface;
- If the mesh stem is on an interface, then γ_i corresponds to the value of γ for the material to the *right* of the mesh stem, except if the mesh stem is exactly on the surface ($0 = z_{i_0} = L_+$, $L_- = L$).

In the finite difference scheme, all operators appearing in the $k \cdot p$ matrix are themselves matrices of dimension $N \times N$, where N is the number of mesh points. The corresponding matrices are implemented differently depending on how many k_z operators appear in a term. For the present $k \cdot p$ framework, only three types of terms are allowed at $\mathbf{k}_\parallel = \mathbf{0}$: (1) k_z-independent terms γ, (2) quadratic-in-k_z terms $k_z \gamma k_z$, and (3) linear-in-k_z terms $i\gamma k_z$ (and Hermitian conjugate thereof $(i\gamma k_z)^\dagger$).

The first are simply material parameter operators such as γ. As mentioned earlier, these operators are diagonal in position basis $\{|z\rangle\}$. When position space is partitioned into a

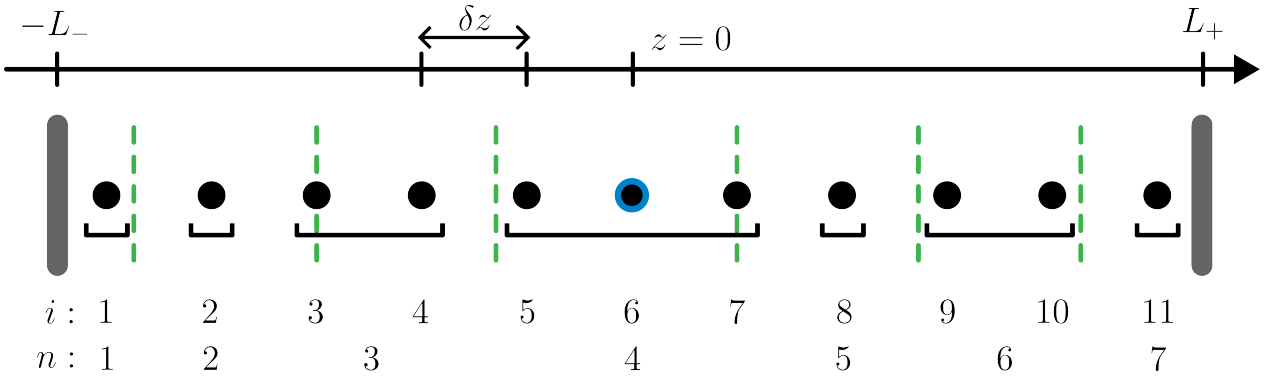

Figure 3.2 Sketch of a z-mesh. Dots are the mesh points with coordinates z_i. The dot with a blue circle is the mesh stem, with index $i_0 = 6$ and coordinate $z_{i_0} = 0$. The dashed green lines are interfaces, and the two thick gray lines are the edges of the simulation domain. There are 7 layers and 8 interfaces (including boundaries) in this mesh. The brackets indicate the set of mesh points belonging to a layer n.

discrete set of N mesh points $z \to z_i$, γ becomes a $N \times N$ diagonal matrix, with diagonal elements $\langle z_i|\gamma|z_i\rangle = \gamma(z_i) \equiv \gamma_i$:

$$\langle z_i|\,\gamma\,|z_j\rangle = \begin{bmatrix} \gamma_1 & 0 & \cdots & 0 \\ 0 & \gamma_2 & \cdots & 0 \\ \vdots & \vdots & \ddots & 0 \\ 0 & 0 & 0 & \gamma_N \end{bmatrix}. \tag{3.52}$$

Since all material parameters are real, material parameter operators are automatically Hermitian.

The second type of operators are those that involve two k_z operators, one on both sides of γ: $k_z\gamma k_z$. Operators as such are clearly non-diagonal. The action of $k_z\gamma k_z$ on an envelope function $|f\rangle$ gives the following in position basis $\langle z|$:

$$\langle z|\,k_z\gamma k_z\,|f\rangle = -\frac{\mathrm{d}}{\mathrm{d}z}\gamma(z)\frac{\mathrm{d}}{\mathrm{d}z}f(z) \tag{3.53a}$$

$$= -\gamma'(z)f'(z) - \gamma(z)f''(z). \tag{3.53b}$$

The finite difference stencil must be chosen such that (a) the matrix associated with $k_z\gamma k_z$ is Hermitian, and (b) upon application on an envelope point $f_i \equiv f(z_i)$, the finite differences should involve $\gamma_{i'}$ and $f_{i'}$ in equal proportions with respect to i. For example, if $k_z\gamma k_z f_i$

involves $f_{i+1}/2$, then it should also involve $f_{i-1}/2$. We point out that satisfying condition (b) does not automatically satisfy condition (a). The following finite difference stencil fulfils conditions (a) and (b):

$$\begin{aligned}\frac{\mathrm{d}}{\mathrm{d}z}\gamma(z)\frac{\mathrm{d}}{\mathrm{d}z}f(z) &\approx \frac{1}{\delta z}\frac{\mathrm{d}}{\mathrm{d}z}\gamma(z)(f_{i+1/2}-f_{i-1/2}) \\ &= \frac{1}{\delta z}\frac{\mathrm{d}}{\mathrm{d}z}\gamma(z)f_{i+1/2} - \frac{1}{\delta z}\frac{\mathrm{d}}{\mathrm{d}z}\gamma(z)f_{i-1/2} \\ &\approx \frac{1}{\delta z^2}(\gamma_{i+1/2}f_{i+1}-\gamma_{i-1/2}f_i) - \frac{1}{\delta z^2}(\gamma_{i+1/2}f_i-\gamma_{i-1/2}f_{i-1}) \\ &= \frac{1}{\delta z^2}\left[\gamma_{i+1/2}f_{i+1} - 2\bar{\gamma}_i f_i + \gamma_{i-1/2}f_{i-1}\right], \end{aligned} \tag{3.54}$$

where $\gamma_{i\pm1/2} = (\gamma_i + \gamma_{i\pm1})/2$ and $\bar{\gamma}_i = (\gamma_{i+1/2} + \gamma_{i-1/2})/2$. It is apparent from (3.54) that $k_z\gamma k_z$ is symmetric in i. The matrix for $k_z\gamma k_z$ is also tridiagonal and Hermitian:

$$\langle z_i|\, k_z\gamma k_z\, |z_j\rangle = -\frac{1}{\delta z^2}\begin{bmatrix} -2\bar{\gamma}_1 & \gamma_{1.5} & 0 & \cdots & 0 & 0 \\ \gamma_{1.5} & -2\bar{\gamma}_2 & \gamma_{2.5} & \cdots & 0 & 0 \\ 0 & \gamma_{2.5} & -2\bar{\gamma}_3 & \cdots & 0 & 0 \\ \vdots & \vdots & \vdots & \ddots & \vdots & \vdots \\ 0 & 0 & 0 & \cdots & -2\bar{\gamma}_{N-1} & \gamma_{N-1/2} \\ 0 & 0 & 0 & \cdots & \gamma_{N-1/2} & -2\bar{\gamma}_N \end{bmatrix}. \tag{3.55}$$

If $\gamma(z)$ is constant for all z, then (3.54) and (3.55) reduce to an ordinary centered 3-point 2$^{\text{nd}}$ order derivative.

The third type of operators is found in the coupling blocks between the Γ_5^+ and the Γ_2^- bands, which are of the form $i\gamma k_z$. Importantly, $i\gamma k_z$ is in general not Hermitian since $[\gamma, k_z] \neq 0$. We adopt the convention used in Reference [148], which is to write the Γ_2^--Γ_5^+ elements as $i\gamma k_z$, and the corresponding Hermitian conjugate Γ_5^+-Γ_2^- element as $(i\gamma k_z)^\dagger$, therefore ensuring hermiticity of the full Hamiltonian. The i factor is added so that $i\gamma k_z$ is real. In contrast with $k_z\gamma k_z$, one cannot use a centered finite difference stencil for $i\gamma k_z$, as it is known to lead to violently oscillating envelope functions [175]. Any de-centered stencil without gaps in i (e.g., if the stencil involves f_{i+1} and f_{i-2}, it should also involve f_i and f_{i-1}) gives well behaved solutions. Here we use the 4-point stencil $\{1/6, -1, \underline{1/2}, 1/3\}$:

$$\langle z_i|\, ik_z\, |z_j\rangle = \frac{1}{\delta z}\begin{bmatrix} 1/2 & 1/3 & 0 & 0 & \cdots & 0 \\ -1 & 1/2 & 1/3 & 0 & \cdots & 0 \\ 1/6 & -1 & 1/2 & 1/3 & \cdots & 0 \\ 0 & 1/6 & -1 & 1/2 & \cdots & 0 \\ \vdots & \vdots & \vdots & \vdots & \ddots & 0 \\ 0 & 0 & 0 & 1/6 & -1 & 1/2 \end{bmatrix}. \tag{3.56}$$

The matrix for $i\gamma k_z$ is obtained by simply multiplying the matrix for γ in (3.52) with that of ik_z (3.56).

Away from $\mathbf{k}_\parallel = \mathbf{0}$, two other types of operators appear in the $k \cdot p$ Hamiltonian. The first type corresponds to the commutator $[\gamma, k_z]$. Its application on $|f\rangle$ gives

$$\begin{aligned} \langle z|\, [\gamma, k_z]\, |f\rangle &= \langle z|\, \gamma k_z\, |f\rangle - \langle z|\, k_z \gamma\, |f\rangle \\ &= -i\gamma(z)\frac{\mathrm{d}}{\mathrm{d}z}f(z) + i\left[\frac{\mathrm{d}}{\mathrm{d}z}\gamma(z)\right] f(z) + i\gamma(z)\frac{\mathrm{d}}{\mathrm{d}z}f(z) \\ &= i\gamma'(z)f(z). \end{aligned} \tag{3.57}$$

Since $[\gamma, k_z]\, |f\rangle$ does not involve derivatives on $f(z)$, the matrix for $[\gamma, k_z]$ is diagonal in position space, and its elements are given by $i\gamma_i'$, where γ_i' is the derivative of γ evaluated at $z = z_i$. The derivatives γ_i' are obtained by applying a finite difference operator D_{ij} on γ_i, consisting of the 2-point centered stencil $\{-1/2, \underline{0}, 1/2\}$ for interior i and de-centered 3-point stencils $\{\underline{-3/2}, 2, -1/2\}$ and $\{1/2, -2, \underline{3/2}\}$ for $i = 1$ and $i = N$ respectively:

$$\gamma_i' = \sum_j D_{ij}\gamma_j \tag{3.58}$$

$$\Leftrightarrow \begin{bmatrix} \gamma_1' \\ \gamma_2' \\ \gamma_3' \\ \gamma_4' \\ \vdots \\ \gamma_N' \end{bmatrix} = \frac{1}{\delta z}\begin{bmatrix} -3/2 & 2 & -1/2 & 0 & \cdots & 0 \\ -1/2 & 0 & 1/2 & 0 & \cdots & 0 \\ 0 & -1/2 & 0 & 1/2 & \cdots & 0 \\ 0 & 0 & -1/2 & 0 & \cdots & 0 \\ \vdots & \vdots & \vdots & \vdots & \ddots & 0 \\ 0 & 0 & 0 & 1/2 & -2 & 3/2 \end{bmatrix}\begin{bmatrix} \gamma_1 \\ \gamma_2 \\ \gamma_3 \\ \gamma_4 \\ \vdots \\ \gamma_N \end{bmatrix}. \tag{3.59}$$

The matrix for γ' is the diagonal matrix of γ_i':

$$\langle z_i|\,\gamma'\,|z_j\rangle = \begin{bmatrix} \gamma'_1 & 0 & \cdots & 0 \\ 0 & \gamma'_2 & \cdots & 0 \\ \vdots & \vdots & \ddots & 0 \\ 0 & 0 & 0 & \gamma'_N \end{bmatrix}. \tag{3.60}$$

The second type of operators for $\mathbf{k}_\parallel \neq \mathbf{0}$ corresponds to anti-commutators $\{\gamma, k_z\}$. In contrast with $[\gamma, k_z]$, $\{\gamma, k_z\}$ is a non-diagonal matrix, since $\langle z|\,\{\gamma, k_z\}\,|f\rangle$ has terms proportional to $f'(z)$. In that situation, the matrix for $\{\gamma, k_z\} = \gamma k_z + k_z\gamma$ is simply the multiplication of the matrix for γ with a Hermitian matrix representing k_z, based on a 2-point centered stencil $\{-1/2, \underline{0}, 1/2\}$.

3.3 The 8-band $k \cdot p$ Hamiltonian

In this section we present the effective Hamiltonian for the Γ_7^+, Γ_8^+ and Γ_7^- bands. These 8 bands are the closest to the bandgap in Ge and $Ge_{1-x}Sn_x$ with $x < 0.30$. However, the closest band above the bandgap in $Si_{1-x}Ge_x$ is Γ_6^- for $x < 0.30$ but becomes Γ_7^- for $x > 0.30$. Treating Γ_6^- as a remote band is not an issue since only Ge-rich $Si_{1-x}Ge_x$ are considered in this thesis. In the remaining, we may refer to the Γ_7^+ band as the split-off (SO) band, Γ_8^+ as the heavy hole (HH) and light hole (LH) bands and Γ_7^- as the conduction band (CB). The implementation of the effective $k \cdot p$ matrix is based on the 8-band part of the 14-band model presented in References [149,150]. For the sake of transparency, the notation employed below makes abstraction of the numerical approach described in Section 3.2.2, unless mentioned otherwise.

3.3.1 General formulation

The basis used to write the Hamiltonian matrix is usually referred as the Cartesian basis. It consists of the single s-like ν band that transforms as Γ_2^-, denoted $|S\rangle$ and the three p-like ν-bands transforming as Γ_5^+, denoted $|X\rangle, |Y\rangle, |Z\rangle$, times the spin 1/2 degree of freedom:

$$\mathcal{B}_X = \{|S+\rangle, |S-\rangle, |X+\rangle, |Y+\rangle, |Z+\rangle, |X-\rangle, |Y-\rangle, |Z-\rangle\}. \tag{3.61}$$

The magnetic field $\mathbf{B}$ is described by a vector potential $\mathbf{A}$ which is kept arbitrary for the moment. A Peirels substitution on the wavevector components is required to properly take in account orbital effects from the $\mathbf{B}$-field:

$$\mathbf{K} = \mathbf{k} + \frac{e}{\hbar}\mathbf{A}. \tag{3.62}$$

This results in non-zero commutation relations between the components of $\mathbf{K}$:

$$\mathbf{K} \times \mathbf{K} = \frac{e}{i\hbar}\mathbf{B}. \tag{3.63}$$

The 8-band Hamiltonian H_8 is written as a sum of different contributions:

$$H_8 = H_k + H_{\mathrm{SO}} + H_\varepsilon + V. \tag{3.64}$$

The first term $H_k = H_k(\mathbf{K})$ includes the $\mathbf{K}$-dependent part of the energy dispersion as well as the Zeeman splitting from the commutation relations (3.63):

$$H_k = \begin{bmatrix} H_{cc}^k & \mathbb{1}_{2\times2} \otimes H_{cv}^k \\ \mathbb{1}_{2\times2} \otimes H_{cv}^{k\dagger} & \mathbb{1}_{2\times2} \otimes H_{vv}^k \end{bmatrix} + \begin{bmatrix} H_B & \mathbb{0} \\ \mathbb{0} & H_B \otimes \mathbb{1}_{3\times3} \end{bmatrix} + H_q \tag{3.65}$$

with

$$H_{cc}^k = \alpha_0 \sum_\alpha K_\alpha \gamma_c K_\alpha + \frac{i\alpha_0}{2} \sum_{\alpha\beta\gamma} \epsilon_{\alpha\beta\gamma} K_\alpha (g - g_0) K_\beta \sigma_\gamma, \tag{3.66}$$

$$(H_{vv}^k)_{i,j} = \begin{cases} \sum_\alpha K_\alpha M K_\alpha + K_i (L - M) K_i & i = j \\ K_i N_+ K_j + K_j N_- K_i & i \neq j \end{cases}, \tag{3.67}$$

$$H_{cv}^k = \begin{bmatrix} iPK_x & iPK_y & iPK_z \end{bmatrix}, \tag{3.68}$$

$$H_B = \frac{i\alpha_0 g_0}{2} \sum_{\alpha\beta\gamma} \epsilon_{\alpha\beta\gamma} K_\alpha K_\beta \sigma_\gamma, \tag{3.69}$$

$$H_q = U_{X\leftarrow J}^0 \begin{bmatrix} \mathbb{0}_{2\times2} & \mathbb{0} & \mathbb{0} \\ \mathbb{0} & -2i\alpha_0 \sum_{\alpha\beta\gamma} \epsilon_{\alpha\beta\gamma} K_\alpha q K_\beta J_\gamma^3 & \mathbb{0} \\ \mathbb{0} & \mathbb{0} & \mathbb{0}_{2\times2} \end{bmatrix} U_{X\leftarrow J}^{0\dagger}. \tag{3.70}$$

Here $\alpha_0 = \hbar^2/(2m_0)$, $g_0 \approx 2$ is the free electron g-factor, $\epsilon_{\alpha\beta\gamma}$ is the Levi-Civita tensor, K_α are the Cartesian components of the wavevector $\mathbf{K}$ (ordering of products $K_\alpha K_\beta$ is important due to (3.63)), σ_γ are the Pauli matrices ($[\sigma_\alpha, \sigma_\beta] = 2i\epsilon_{\alpha\beta\gamma}\sigma_\gamma$), J_γ are the (unit-less) spin-3/2 matrices ($[J_\alpha, J_\beta] = i\epsilon_{\alpha\beta\gamma}J_\gamma$) and (i, j) in (3.67) iterate through $\{x, y, z\}$. The unitary matrix $U_{X\leftarrow J}^0$ is described further below.

The four valence band effective mass parameters L, M and $N_\pm$ are linear combinations of the Luttinger parameters $\gamma_{1,2,3}$ and κ:

$$\begin{bmatrix}\gamma_1\\ \gamma_2\\ \gamma_3\\ \kappa\end{bmatrix} = -\frac{1}{6\alpha_0}\begin{bmatrix}2 & 4 & 0 & 0\\ 1 & -1 & 0 & 0\\ 0 & 0 & 1 & 1\\ 0 & 0 & 1 & -1\end{bmatrix}\begin{bmatrix}L\\ M\\ N_+ + \alpha_0\\ N_- - \alpha_0\end{bmatrix}. \tag{3.71}$$

The spin-orbit interaction term H_{SO} is non-diagonal in basis $\mathcal{B}_X$:

$$H_{\mathrm{SO}} = \mathbb{0}_{2\times2} \oplus \frac{\Delta_0}{3}\sum_\alpha \sigma_\alpha \otimes I_\alpha = \frac{\Delta_0}{3}\begin{bmatrix}0 & 0 & 0 & 0 & 0 & 0 & 0 & 0\\ 0 & 0 & 0 & 0 & 0 & 0 & 0 & 0\\ 0 & 0 & 0 & -i & 0 & 0 & 0 & 1\\ 0 & 0 & i & 0 & 0 & 0 & 0 & -i\\ 0 & 0 & 0 & 0 & 0 & -1 & i & 0\\ 0 & 0 & 0 & 0 & -1 & 0 & i & 0\\ 0 & 0 & 0 & 0 & -i & -i & 0 & 0\\ 0 & 0 & 1 & i & 0 & 0 & 0 & 0\end{bmatrix}, \tag{3.72}$$

with eigenvalues 0 ($\times2$), $-2\Delta_0/3$ ($\times2$), and $\Delta_0/3$ ($\times4$). The strain term H_ε is

$$H_\varepsilon = \begin{bmatrix}H_{cc}^\varepsilon & \mathbb{0}_{2\times6}\\ \mathbb{0}_{6\times2} & \mathbb{1}_{2\times2}\otimes H_{vv}^\varepsilon\end{bmatrix}, \tag{3.73}$$

with

$$H_{cc}^\varepsilon = \mathbb{1}_{2\times2} a_c \mathrm{Tr}\{\varepsilon\}, \tag{3.74}$$

$$(H_{vv}^\varepsilon)_{i,j} = \begin{cases} m\mathrm{Tr}\{\varepsilon\} + (l-m)\varepsilon_{ii} & i = j\\ n\varepsilon_{ij} & i \neq j\end{cases}, \tag{3.75}$$

with l, m and n being related to a_v, b and d by [157]:

$$\begin{bmatrix}a_v\\ b\\ d\end{bmatrix} = \frac{1}{3}\begin{bmatrix}1 & 2 & 0\\ 1 & -1 & 0\\ 0 & 0 & \sqrt{3}\end{bmatrix}\begin{bmatrix}l\\ m\\ n\end{bmatrix}. \tag{3.76}$$

Finally, the potential energy term V includes the band energy alignments $\mathcal{E}_{\Gamma_5^+}$ and $\mathcal{E}_{\Gamma_2^-} = \mathcal{E}_{\Gamma_5^+} + E_{g\Gamma} + \Delta_0/3$, out-of-plane electric fields $\mathbf{F} = F_z\mathbf{e}_z$ and in-plane confinement profiles:

$$V = \left(\mathbb{1}_{2\times2} \otimes \mathcal{E}_{\Gamma_2^-} \oplus \mathbb{1}_{6\times6} \otimes \mathcal{E}_{\Gamma_5^+}\right) + eF_z z + V_{\parallel}(x,y) \tag{3.77a}$$

$$= \begin{bmatrix} \mathbb{1}_{2\times2} \otimes \mathcal{E}_{\Gamma_2^-} & \mathbb{0}_{2\times6} \\ \mathbb{0}_{6\times2} & \mathbb{1}_{6\times6} \otimes \mathcal{E}_{\Gamma_5^+} \end{bmatrix} + eF_z z + V_{\parallel}(x,y). \tag{3.77b}$$

Note that the energy difference $\mathcal{E}_{\Gamma_2^-} - \mathcal{E}_{\Gamma_5^+}$ overestimates the bandgap $E_{g\Gamma}$ by $\Delta_0/3$. This is corrected in the final energy spectrum of H_8 by the 4 eigenvalues $\Delta_0/3$ and the 2 eigenvalues $-2\Delta_0/3$ within the valence band subspace of H_{SO}. If doping profiles are incorporated to the heterostructure, it might be relevant to also include with V the potential V_{ch} associated with the redistribution of charges across layers. The $k \cdot p$ envelope functions are then solved self-consistently with the Poisson equation. This is explained in Appendix B.

The 8-band Hamiltonian H_8 is also often written in a basis that diagonalizes the spin-orbit term H_{SO}, the so-called angular momentum basis $\mathcal{B}_J^0$. This basis is the set of joint eigenstates of J_z and J^2, where $\mathbf{J} = \mathbf{L} + \mathbf{S}$ is the total angular momentum of the electron/hole. The s-like electron in Γ_2^- corresponds to $l = 0$ and $s = 1/2$, which gives $j = 1/2$. The two basis states are therefore $\left|\frac{1}{2}, \pm\frac{1}{2}\right\rangle_c$, and provide a basis for Γ_7^-. The p-like holes in Γ_5^+ have $l = 1$ and $s = 1/2$ and are thus categorized in two groups, one with $j = 3/2$ and the other with $j = 1/2$. The four states within the first group provide a basis for Γ_8^+ and correspond to the HHs $\left|\frac{3}{2}, \pm\frac{3}{2}\right\rangle$ and the LHs $\left|\frac{3}{2}, \pm\frac{1}{2}\right\rangle$. The two states within the second group provide a basis for Γ_7^+ and correspond to the SO holes $\left|\frac{1}{2}, \pm\frac{1}{2}\right\rangle$. A somewhat conventional ordering is as follows [35]:

$$\mathcal{B}_J^0 = \left\{\left|\frac{1}{2},\frac{1}{2}\right\rangle_c, \left|\frac{1}{2},-\frac{1}{2}\right\rangle_c, \left|\frac{3}{2},\frac{3}{2}\right\rangle, \left|\frac{3}{2},\frac{1}{2}\right\rangle, \left|\frac{3}{2},-\frac{1}{2}\right\rangle, \left|\frac{3}{2},-\frac{3}{2}\right\rangle, \left|\frac{1}{2},\frac{1}{2}\right\rangle, \left|\frac{1}{2},-\frac{1}{2}\right\rangle\right\} \tag{3.78a}$$

$$= \{|\mathrm{CB}+\rangle, |\mathrm{CB}-\rangle, |\mathrm{HH}+\rangle, |\mathrm{LH}+\rangle, |\mathrm{LH}-\rangle, |\mathrm{HH}-\rangle, |\mathrm{SO}+\rangle, |\mathrm{SO}-\rangle\}. \tag{3.78b}$$

In terms of the Cartesian basis functions, the angular momentum basis functions are given by:

$$\left|\frac{1}{2},\frac{1}{2}\right\rangle_c = |S+\rangle \qquad \left|\frac{1}{2},-\frac{1}{2}\right\rangle_c = |S-\rangle \tag{3.79a}$$

$$\left|\frac{3}{2},\frac{3}{2}\right\rangle = -\frac{1}{\sqrt{2}}\left(|X+\rangle + i\,|Y+\rangle\right) \qquad \left|\frac{3}{2},-\frac{3}{2}\right\rangle = \frac{1}{\sqrt{2}}\left(|X-\rangle - i\,|Y-\rangle\right) \tag{3.79b}$$

$$\left|\frac{3}{2},\frac{1}{2}\right\rangle = \frac{1}{\sqrt{6}}\left(2\,|Z+\rangle - |X-\rangle - i\,|Y-\rangle\right) \qquad \left|\frac{3}{2},-\frac{1}{2}\right\rangle = \frac{1}{\sqrt{6}}\left(|X+\rangle - i\,|Y+\rangle + 2\,|Z-\rangle\right) \tag{3.79c}$$

$$\left|\frac{1}{2},\frac{1}{2}\right\rangle = -\frac{1}{\sqrt{3}}\left(|Z+\rangle + |X-\rangle + i\,|Y-\rangle\right) \qquad \left|\frac{1}{2},-\frac{1}{2}\right\rangle = -\frac{1}{\sqrt{3}}\left(|X+\rangle - i\,|Y+\rangle - |Z-\rangle\right) \tag{3.79d}$$

In matrix representation, this gives

$$U^0_{X\leftarrow J} = \begin{bmatrix} 1 & 0 & 0 & 0 & 0 & 0 & 0 & 0 \\ 0 & 1 & 0 & 0 & 0 & 0 & 0 & 0 \\ 0 & 0 & -s_2 & 0 & s_6 & 0 & 0 & -s_3 \\ 0 & 0 & -is_2 & 0 & -is_6 & 0 & 0 & is_3 \\ 0 & 0 & 0 & s_{23} & 0 & 0 & -s_3 & 0 \\ 0 & 0 & 0 & -s_6 & 0 & s_2 & -s_3 & 0 \\ 0 & 0 & 0 & -is_6 & 0 & -is_2 & -is_3 & 0 \\ 0 & 0 & 0 & 0 & s_{23} & 0 & 0 & s_3 \end{bmatrix}, \tag{3.80}$$

where $s_2 = 1/\sqrt{2}$, $s_3 = 1/\sqrt{3}$, $s_6 = 1/\sqrt{6}$, and $s_{23} = \sqrt{2/3}$. The Hamiltonian matrix in basis $\mathcal{B}^0_J$ is therefore $U^{0\dagger}_{X\leftarrow J} H_8 U^0_{X\leftarrow J}$.

Comparison with the 30-band $k\cdot p$ Hamiltonian

A comparison between the $E_n(\mathbf{k})$ relation given by the 30-band and that given by the 8-band Hamiltonian for bulk Ge with $\mathbf{B} = \mathbf{0}$ is shown in Fig. 3.3. The 8-band model reproduces the band energies and their curvature at the Γ point. However, as $\mathbf{k}$ increases, the fit becomes noticeably worse, especially for the Γ_7^- conduction band, which normally reaches an extremum away from $\mathbf{k} = \mathbf{0}$ before going down towards the band gap. This is of little importance in situations where one is interested only in the band structure for small $\mathbf{k}$. The Hamiltonian H_8 provides a good fit up to around 1/10 of the distance between the Γ point and the edges of the FBZ, which for Ge corresponds to $\|\mathbf{k}\| \lesssim 1\,\mathrm{nm}^{-1}$.

3.3.2 The quantum well Hamiltonian ($\mathbf{B} = \mathbf{0}$)

In this section we derive a Hamiltonian H_{QW} for the QW system starting from the Hamiltonian H_8 of the preceding section with $V_\parallel(x,y) = 0$ and $B = 0$. In principle, one could directly

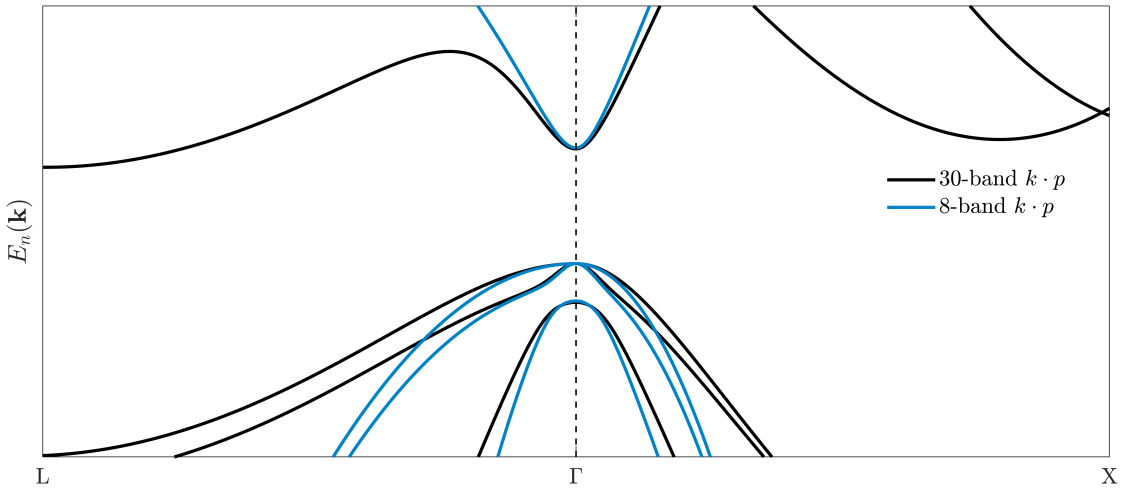

Figure 3.3 Comparison between the 30-band (black lines) and the 8-band (blue lines) $k \cdot p$ models for bulk Ge.

inject into H_{QW} the wavevector components k_x, k_y, and $k_z = -i\frac{\mathrm{d}}{\mathrm{d}z}$ and solve the eigenvalue problem for each k_x and k_y. However, this would be highly inefficient in practice as will be shown further below, since a fairly large matrix (typically $10^5 \times 10^5$ elements) would need to be diagonalized for each (k_x, k_y). In the following, we derive a basis in which the Hamiltonian matrix is much smaller, while keeping the same accuracy for sufficiently small $\mathbf{k}_\parallel$.

The Hamiltonian matrix H_{QW} depends on the three components of the wavevector $\mathbf{k}$. Out of these three components, only $k_{x,y}$ commute with H_{QW}, since k_z is associated with the derivative $-i\frac{\mathrm{d}}{\mathrm{d}z}$. H_{QW} is Hermitian for any $\mathbf{k}_\parallel$. Let H_0 be H_{QW} evaluated at $\mathbf{k}_\parallel = \mathbf{0}$, and let W be the remaining part of H_{QW}: $W = H_{\mathrm{QW}} - H_0$. If we define the basis $\mathcal{B}_J$ consisting of the following re-ordering of the angular-momentum basis $\mathcal{B}_J^0$:

$$\mathcal{B}_J = \left\{ \left|\frac{1}{2}, \frac{1}{2}\right\rangle_c, \left|\frac{3}{2}, \frac{1}{2}\right\rangle, \left|\frac{1}{2}, \frac{1}{2}\right\rangle, \left|\frac{3}{2}, \frac{3}{2}\right\rangle, \left|\frac{1}{2}, -\frac{1}{2}\right\rangle_c, \left|\frac{3}{2}, -\frac{1}{2}\right\rangle, \left|\frac{1}{2}, -\frac{1}{2}\right\rangle, \left|\frac{3}{2}, -\frac{3}{2}\right\rangle \right\}, \tag{3.81}$$

and associated unitary transformation $U_{X \leftarrow J}$:

$$U_{X\leftarrow J} = U^0_{X\leftarrow J}\begin{bmatrix} 1 & 0 & 0 & 0 & 0 & 0 & 0 & 0 \\ 0 & 0 & 0 & 0 & 1 & 0 & 0 & 0 \\ 0 & 0 & 0 & 1 & 0 & 0 & 0 & 0 \\ 0 & 1 & 0 & 0 & 0 & 0 & 0 & 0 \\ 0 & 0 & 0 & 0 & 0 & 1 & 0 & 0 \\ 0 & 0 & 0 & 0 & 0 & 0 & 0 & 1 \\ 0 & 0 & 1 & 0 & 0 & 0 & 0 & 0 \\ 0 & 0 & 0 & 0 & 0 & 0 & 1 & 0 \end{bmatrix}, \tag{3.82}$$

the matrix $U^\dagger_{X\leftarrow J} H_0 U_{X\leftarrow J}$ takes a block-diagonal shape:

$$U^\dagger_{X\leftarrow J} H_0 U_{X\leftarrow J} = \begin{bmatrix} H_+ & 0 \\ 0 & H_- \end{bmatrix}, \tag{3.83}$$

where

$$H_{\sigma=\pm} = H^k_\sigma + H^\varepsilon_\sigma + V^z, \tag{3.84a}$$

$$V^z = E_{\Gamma_8^+} + \begin{bmatrix} E_{g\Gamma} & 0 & 0 & 0 \\ & 0 & 0 & 0 \\ \dagger & & -\Delta_0 & 0 \\ & & & 0 \end{bmatrix} + eF_z z, \tag{3.84b}$$

$$H^k_\sigma = \alpha_0 \begin{bmatrix} k_z\gamma_c k_z & i\sqrt{2/3}c_p k_z & -i\sigma c_p k_z/\sqrt{3} & 0 \\ & -k_z\gamma_+ k_z & 2\sqrt{2}\sigma k_z\gamma_2 k_z & 0 \\ \dagger & & -k_z\gamma_1 k_z & 0 \\ & & & -k_z\gamma_- k_z \end{bmatrix}, \tag{3.84c}$$

$$H^\varepsilon_\sigma = \mathrm{Tr}\{\varepsilon\}\begin{bmatrix} a_c & 0 & 0 & 0 \\ & a_v & 0 & 0 \\ \dagger & & a_v & 0 \\ & & & a_v \end{bmatrix} + b\cdot\delta\varepsilon \begin{bmatrix} 0 & 0 & 0 & 0 \\ & -1 & \sqrt{2}\sigma & 0 \\ \dagger & & 0 & 0 \\ & & & 1 \end{bmatrix}. \tag{3.84d}$$

Here we defined $\gamma_\pm = \gamma_1 \pm 2\gamma_2$, $c_p = \sqrt{E_p/\alpha_0}$ and $\delta\varepsilon = \varepsilon_{xx} - \varepsilon_{zz}$. The parameter $\sigma = \pm 1$ is a pseudo-spin quantum number. It should be noted that since products like $\Delta_0 \cdot k_\alpha$, or $\varepsilon_{ij}k_\alpha$ do not appear in H_{QW}, W does not depend on Δ_0 nor on ε_{ij}. In other words, all information pertaining to strain or spin-orbit coupling is contained within H_0. It is apparent from (3.84)

that H_σ are themselves block-diagonal. The first 3×3 block corresponds to a CB-LH-SO superposition with pseudo-spin σ, whereas the 1×1 block corresponds to a pure HH with pseudo-spin σ. From this, eigenstates of H_0 are categorized into four kinds of levels: pure HH states (referred as H-states, one for each σ), and CB-LH-SO superposed states (referred as η-states, one for each σ). This can be written as follow:

$$|\mathrm{H}\sigma; l\rangle = \left|\frac{3}{2}, \frac{3\sigma}{2}\right\rangle |h_l\rangle\,, \tag{3.85a}$$

$$|\eta\sigma; j\rangle = \left|\frac{1}{2}, \frac{\sigma}{2}\right\rangle_c |c_j\rangle + \left|\frac{3}{2}, \frac{\sigma}{2}\right\rangle |\ell_j\rangle + \sigma \left|\frac{1}{2}, \frac{\sigma}{2}\right\rangle |s_j\rangle\,, \tag{3.85b}$$

where l is a subband index for H states and j is a subband index for η states. The second ket in each term are envelope functions. For example, $\langle z \,|\, \ell_j\rangle = f_j^\ell(z)$ is the envelope function in the LH part of the spinor for the j-th η level (evaluated at $\mathbf{k}_\parallel = \mathbf{0}$). H states are normalized such that

$$\langle \mathrm{H}\sigma; l \,|\, \mathrm{H}\sigma'; l'\rangle = \delta_{\sigma,\sigma'}\delta_{l,l'}, \tag{3.86}$$

where the orthogonality on σ is provided by the bulk Bloch states $\left|\frac{3}{2}, \frac{3\sigma}{2}\right\rangle$, and the orthogonality on l is provided by the envelope functions $|h_l\rangle$. Similarly, η states are normalized such that

$$\langle \eta\sigma; j \,|\, \eta\sigma'; j'\rangle = \delta_{\sigma,\sigma'}\left(\langle c_j \,|\, c_{j'}\rangle + \langle \ell_j \,|\, \ell_{j'}\rangle + \langle s_j \,|\, s_{j'}\rangle\right) = \delta_{\sigma,\sigma'}\delta_{j,j'}. \tag{3.87}$$

Here again, the bulk Bloch states $\left|\frac{3}{2}, \frac{\sigma}{2}\right\rangle$ and so on provide the orthogonality on σ, whereas the envelopes provide the orthogonality on j. Orthogonality from the envelopes is guaranteed by the hermiticity of H_0. It should be noted that a specific envelope function, say $|\ell_j\rangle$, is by itself not an eigenstate of any particular Hamiltonian. Instead, the three envelopes $|c_j\rangle$, $|\ell_j\rangle$, and $|s_j\rangle$ are *mutually* eigenstates of the 3×3 block in (3.84). The level ηj (shorthand for $|\eta\sigma; j\rangle$) may be referred as CB-like, LH-like or SO-like depending on the relative weights of its envelopes $|c_j\rangle$, $|\ell_j\rangle$, and $|s_j\rangle$. For instance, an η level such that $\langle \ell \,|\, \ell\rangle > \langle c \,|\, c\rangle$ and $\langle \ell \,|\, \ell\rangle > \langle s \,|\, s\rangle$ may be identified as LH-like. Note also that since H_σ is real, the envelope functions $f^h(z)$, $f^c(z)$, $f^\ell(z)$, and $f^s(z)$ are also real. The classification into η and H levels clearly indicates that from the point of view of 8-band $k \cdot p$ theory, the lowest conduction band electrons, LHs and SO holes are the *same* thing; they merely correspond to different relative weights of the three envelopes $|c\rangle$, $|\ell\rangle$ and $|s\rangle$. An equation for η levels is therefore

valid for all three particles and superpositions thereof.

For each eigenstate $|\tau\sigma; j\rangle$ (where $\tau = \{\eta, \mathrm{H}\}$ and j is a general subband index) corresponds an eigenenergy E_j^τ that is independent of σ. This is because H_+ and H_- in (3.84) are time-reversed versions of each other, and because no **B**-fields enter the Hamiltonian H_0. The set of eigenstates $\{|\tau\sigma, j\rangle\}$ provide an orthonormal basis $\mathcal{B}_0$ (also referred here as the *subband-edge basis*[1]) on which the full Hamiltonian H_{QW} can be projected onto. To generate a basis, one only needs to diagonalize H_+ for the $N_\perp$ levels closest to a given energy[2]. This results in a set of N_H H levels and N_η η levels of pseudo-spin $\sigma = +$ ($N_\perp = N_\mathrm{H} + H_\eta$). The eigenstates of H_- are then simply constructed as the time-reversed versions of eigenstates of H_+ [see (3.85)]. The basis $\mathcal{B}_0$ therefore consists of the $N_\perp$ calculated eigenstates of H_+ plus the $N_\perp$ constructed eigenstates of H_-, totaling $2N_\perp$ elements. The original dimension of H_{QW} imply that $N_\perp$ cannot exceed $4N$, with N being the number of mesh points along z. The elements in $\mathcal{B}_0$ are ordered as such:

$$\begin{aligned}\mathcal{B}_0 &= \{|\mathrm{H}+\rangle, |\eta+\rangle, |\eta-\rangle, |\mathrm{H}-\rangle\} \\ &\equiv \{|\mathrm{H}+;1\rangle, |\mathrm{H}+;2\rangle, \ldots, |\eta+;1\rangle, |\eta+;2\rangle, \ldots, \\ &\quad |\eta-;1\rangle, |\eta-;2\rangle, \ldots, |\mathrm{H}-;1\rangle, |\mathrm{H}-;2\rangle, \ldots\}.\end{aligned} \tag{3.88}$$

A Hamiltonian matrix for $H_{\mathrm{QW}} = H_0 + W$ with arbitrary $\mathbf{k}_\parallel$ may now be constructed by projecting H_{QW} onto $\mathcal{B}_0$. In this basis, H_0 is, by construction, the diagonal matrix $\mathbf{E}_0^{\mathrm{QW}}$ consisting of all the energies E_j^τ arranged according to (3.88) (bold is used for matrices written in basis $\mathcal{B}_0$). The matrix $\mathbf{W}$ is obtained by performing the following:

$$\mathbf{W} = U_{J\leftarrow 0}^\dagger U_{X\leftarrow J}^\dagger (H_{\mathrm{QW}} - H_0) U_{X\leftarrow J} U_{J\leftarrow 0}, \tag{3.89}$$

where the unitary $U_{J\leftarrow 0}$ is the matrix whose columns are the eigenstates of H_0 ordered according to (3.88), and where the rows are ordered according to (3.81):

$$U_{J\leftarrow 0} = \begin{bmatrix} |\mathrm{H}+\rangle & |\eta+\rangle & |\eta-\rangle & |\mathrm{H}-\rangle \end{bmatrix} \tag{3.90a}$$

[1] Subbands usually reach their global extremum at $\mathbf{k}_\parallel = \mathbf{0}$. That point is therefore located on the "edge" of that subband

[2] Here $\perp$ signifies "perpendicular-to-the-QW-plane"; the $N_\perp$ levels provide a basis for the one-dimensional QW problem, with confinement along the z axis

$$= \begin{bmatrix} 0 & 0 & & |c_1\rangle & |c_2\rangle & & 0 & 0 & & 0 & 0 & \\ 0 & 0 & & |\ell_1\rangle & |\ell_2\rangle & & 0 & 0 & & 0 & 0 & \\ 0 & 0 & & |s_1\rangle & |s_2\rangle & & 0 & 0 & & 0 & 0 & \\ |h_1\rangle & |h_2\rangle & \dots & 0 & 0 & \dots & 0 & 0 & \dots & 0 & 0 & \dots \\ 0 & 0 & & 0 & 0 & & |c_1\rangle & |c_2\rangle & & 0 & 0 & \\ 0 & 0 & & 0 & 0 & & |\ell_1\rangle & |\ell_2\rangle & & 0 & 0 & \\ 0 & 0 & & 0 & 0 & & -|s_1\rangle & -|s_2\rangle & & 0 & 0 & \\ 0 & 0 & & 0 & 0 & & 0 & 0 & & |h_1\rangle & |h_2\rangle & \end{bmatrix}. \tag{3.90b}$$

The complete Hamiltonian $\mathbf{H}_{\mathrm{QW}} = \mathbf{E}_0^{\mathrm{QW}} + \mathbf{W}$ is therefore:

$$\mathbf{H}_{\mathrm{QW}} = \mathbf{E}_0^{\mathrm{QW}} + \alpha_0 \left[\mathbf{M}_\gamma k_\parallel^2 + \left(i\mathbf{M}_1 k_- + \mathbf{M}_2 k_-^2 + \mathrm{H.c.} \right) \right], \tag{3.91}$$

where $k_\parallel^2 = k_x^2 + k_y^2$, $k_\pm = k_x \pm i k_y$ and

$$\mathbf{E}_0^{\mathrm{QW}} = \begin{bmatrix} \mathbf{E}^{\mathrm{H}} & 0 & 0 & 0 \\ & \mathbf{E}^{\eta} & 0 & 0 \\ \dagger & & \mathbf{E}^{\eta} & 0 \\ & & & \mathbf{E}^{\mathrm{H}} \end{bmatrix}, \qquad \mathbf{M}_\gamma = \begin{bmatrix} \mathbf{\Gamma}_\parallel^{\mathrm{H}} & 0 & 0 & 0 \\ & \mathbf{\Gamma}_\parallel^{\eta} & 0 & 0 \\ \dagger & & \mathbf{\Gamma}_\parallel^{\eta} & 0 \\ & & & \mathbf{\Gamma}_\parallel^{\mathrm{H}} \end{bmatrix}, \tag{3.92a}$$

$$\mathbf{M}_1 = \begin{bmatrix} 0 & \mathbf{T}^{\mathrm{x}} & 0 & 0 \\ 0 & 0 & \mathbf{T}^{\eta} & 0 \\ 0 & 0 & 0 & \mathbf{T}^{\mathrm{x}\dagger} \\ \mathbf{T}^{\mathrm{H}} & 0 & 0 & 0 \end{bmatrix}, \qquad \mathbf{M}_2 = \begin{bmatrix} 0 & 0 & \boldsymbol{\mu} & 0 \\ 0 & 0 & 0 & \boldsymbol{\mu}^\dagger \\ \boldsymbol{\delta}^\dagger & 0 & 0 & 0 \\ 0 & \boldsymbol{\delta} & 0 & 0 \end{bmatrix}. \tag{3.92b}$$

As mentioned earlier, the diagonal matrices $\mathbf{E}^\tau$ are the energies of each quantum well subband: $\mathbf{E}^\tau = \mathrm{diag}\{E_1^\tau, E_2^\tau, \dots\}$ ($\tau = \{\eta, \mathrm{H}\}$). The other matrices $\mathbf{\Gamma}_\parallel$, $\mathbf{T}$, $\boldsymbol{\mu}$, and $\boldsymbol{\delta}$ are:

$$\mathbf{\Gamma}_\parallel^{\eta} = \langle c \,|\, \gamma_c \,|\, c \rangle - \frac{1}{3} \langle + \,|\, \gamma_1 + \gamma_2 \,|\, + \rangle - \frac{2}{3} \langle - \,|\, \gamma_1 - 2\gamma_2 \,|\, - \rangle, \tag{3.93a}$$

$$\mathbf{\Gamma}_\parallel^{\mathrm{H}} = -\langle h \,|\, \gamma_1 + \gamma_2 \,|\, h \rangle, \tag{3.93b}$$

$$\mathbf{T}^{\mathrm{x}} = \frac{1}{\sqrt{2}} \langle h | \left[c_p \,|c\rangle - \sqrt{6} i \left(u_+ \,|-\rangle + \frac{7}{4} [q, k_z] \,|\ell\rangle \right) \right], \tag{3.93c}$$

$$\mathbf{T}^{\eta} = \frac{1}{\sqrt{6}}\left(\langle c\,|\,c_p\,|\,+\rangle + \langle +\,|\,c_p\,|\,c\rangle\right) \\ +i\left(\frac{1}{2}\langle c\,|\,[g,k_z]\,|\,c\rangle - \langle +\,|\,u_+\,|\,-\rangle + \langle -\,|\,u_-\,|\,+\rangle - 5\,\langle \ell\,|\,[q,k_z]\,|\,\ell\rangle\right), \tag{3.93d}$$

$$\mathbf{T}^{\mathrm{H}} = -\frac{3i}{2}\langle h\,|\,[q,k_z]\,|\,h\rangle\,, \tag{3.93e}$$

$$\boldsymbol{\mu} = \frac{\sqrt{3}}{2}\langle h\,|\,\gamma_2+\gamma_3\,|\,+\rangle\,, \tag{3.93f}$$

$$\boldsymbol{\delta} = \frac{\sqrt{3}}{2}\langle h\,|\,\gamma_2-\gamma_3\,|\,+\rangle\,, \tag{3.93g}$$

with $|\pm\rangle = |\ell\rangle \pm 2^{\pm 1/2}\,|s\rangle$, $u_\pm = \{\gamma_3, k_z\} \pm [\kappa, k_z]$, and $\{A,B\} = AB + BA$ being the anti-commutator. Subband indices in (3.93) are omitted for simplicity. For instance, the $(1,2)$ matrix element of $\mathbf{T}^{\mathrm{H}}$ would be $T^{\mathrm{H}}_{1,2} = -3i\,\langle h_1\,|\,[q,k_z]\,|\,h_2\rangle\,/2$. Bra-ket products involving a material parameter are integrals as such:

$$\langle c|\gamma_c|c\rangle = \int \mathrm{d}z\, f^c(z)^*\gamma_c(z)f^c(z), \tag{3.94}$$

which in the framework of finite differences described in Section 3.2.2 gives

$$\langle c|\gamma_c|c\rangle = \delta z \sum_{i=1}^{N} f_i^{c*}(\gamma_c)_i f_i^c, \tag{3.95}$$

where the sum is performed on the mesh points i and δz is the mesh spacing. The matrices $\mathbf{E}^\tau$, $\boldsymbol{\Gamma}^\tau_\parallel$, and $\mathbf{T}^\tau$ are all real and Hermitian ($\tau = \eta, \mathrm{H}$), while $\mathbf{T}^{\mathrm{x}}$, $\boldsymbol{\mu}$, and $\boldsymbol{\delta}$ are real, but not Hermitian.

Eigenvectors of (3.91) at finite $\mathbf{k}_\parallel$ have the following structure:

$$\left|\varphi(\mathbf{k}_\parallel)\right\rangle = \sum_{\tau,\sigma,j} c^j_{\tau\sigma}\,|\tau\sigma; j\rangle : \begin{bmatrix} \mathbf{c}_{\mathrm{H}+} \\ \mathbf{c}_{\eta+} \\ \mathbf{c}_{\eta-} \\ \mathbf{c}_{\mathrm{H}-} \end{bmatrix}, \tag{3.96}$$

where $\mathbf{c}_{\eta\sigma}$ ($\mathbf{c}_{\mathrm{H}\sigma}$) is a N_η-component (N_{H}-component) vector indicating the contribution of $|\eta\sigma; j\rangle$ ($|\mathrm{H}\sigma; l\rangle$) in $\left|\varphi(\mathbf{k}_\parallel)\right\rangle$. Useful information can be extracted from $\left|\varphi(\mathbf{k}_\parallel)\right\rangle$ such as envelope functions $\left\langle z\,\middle|\,\varphi(\mathbf{k}_\parallel)\right\rangle$:

$$\begin{aligned}\left\langle z \,\middle|\, \varphi(\mathbf{k}_\parallel)\right\rangle &= \langle z| \left(\sum_{\tau,\sigma,j} |\tau\sigma; j\rangle \langle \tau\sigma; j|\right) \left|\varphi(\mathbf{k}_\parallel)\right\rangle \\ &= \sum_{\tau,\sigma,j} \langle z|\tau\sigma; j\rangle \, c^j_{\tau\sigma}(\mathbf{k}_\parallel) \\ &= \sum_{\sigma,j} c^j_{\eta\sigma}(\mathbf{k}_\parallel) \left[\left|\frac{1}{2}, \frac{\sigma}{2}\right\rangle_c f^c_j(z) + \left|\frac{3}{2}, \frac{\sigma}{2}\right\rangle f^\ell_j(z) + \sigma \left|\frac{1}{2}, \frac{\sigma}{2}\right\rangle f^s_j(z)\right] \\ &+ \sum_{\sigma,l} c^l_{\mathrm{H}\sigma}(\mathbf{k}_\parallel) \left|\frac{3}{2}, \frac{3\sigma}{2}\right\rangle f^h_l(z),\end{aligned} \tag{3.97}$$

or the H contribution within $\left|\varphi(\mathbf{k}_\parallel)\right\rangle$ indicating the amount of η-H mixing ρ:

$$\begin{aligned}\rho &= \langle P_{\mathrm{H}}\rangle \\ &= \left\langle \varphi(\mathbf{k}_\parallel)\right| \left(\sum_{\sigma,l} |\mathrm{H}\sigma; l\rangle \langle \mathrm{H}\sigma; l|\right) \left|\varphi(\mathbf{k}_\parallel)\right\rangle \\ &= \mathbf{c}^\dagger_{\mathrm{H}+}\mathbf{c}_{\mathrm{H}+} + \mathbf{c}^\dagger_{\mathrm{H}-}\mathbf{c}_{\mathrm{H}-},\end{aligned} \tag{3.98}$$

where P_{H} is the projection operator associated with the H subspace.

Bulk band alignments

A bulk band alignment is a plot of the bulk band edges as a function of position, or growth direction z. These plots give important information on the confinement type of the heterostructure (see Figure 1.1), as well as valuable information on the strength of confinement a carrier is subject to. The band alignment for the CB, the LH, the HH and the SO hole bands at the Γ point are computed by finding the 4 eigenvalues of the 4×4 Hamiltonian[3] (3.84) with $k_z = 0$. For each coordinate z along the growth direction, material parameters in (3.84) are replaced by their value at coordinate z. In heterostructures where the alloy concentration changes with position, material parameters (including strain tensor elements) are evaluated at that position according to the alloy concentration at that point. The eigenvalues of Hamiltonian (3.84) with $k_z = 0$ precisely correspond to the results of the so-called model-solid theory [154].

[3]Here the Hamiltonian really *is* 4×4; i.e. there is no Hilbert space associated with the z degree of freedom, and all material parameters are scalars.

The band alignments of the conduction band minima along Δ and Λ are computed using the approach outlined in Reference [154]. The energy $E_{\rm V}$ of a valley V is given by

$$E_{\rm V} = \mathcal{E}_{\Gamma_5^+} + \frac{\Delta_0}{3} + E_{g{\rm V}} + {\rm Tr}\left\{\Xi_d^{\rm V} + \Xi_u^{\rm V}(\mathbf{n}:\mathbf{n})\cdot\varepsilon\right\}, \tag{3.99}$$

where ${\rm V} = \{{\rm L}, {\rm X}\}$, $\Xi_d^{\rm V} = a_{c{\rm V}} - \Xi_u^{\rm V}/3$ (see Table 3.4), "$\cdot$" is the usual matrix product, ":" is the dyadic product, and $\mathbf{n}$ is the unitary vector pointing towards the valley V. With isotropic bi-axial strain, the 4 Δ valleys lying in the QW plane are degenerate, and so are the 2 Δ valleys perpendicular to the QW plane. All 8 Λ valleys remain degenerate under these circumstances.

Accuracy of the projection onto $\mathcal{B}_0$

The accuracy of the envelopes and their associated energy obtained from the full diagonalization of $H_{\rm QW}$ depends only on the number of mesh points that discretize the heterostructure (see section 3.2.2 for more details on the numerical implementation). For N mesh points along the z-direction, the $k\cdot p$ matrix for $H_{\rm QW}$ is $8N\times 8N$ with $8N$ orthogonal eigenstates. If each of these $8N$ subbands were included in the basis $\mathcal{B}_0$ (corresponding to the limit $N_\perp = 4N$), the unitary transformation (3.89) would correspond to an *exact* change of basis from $H_{\rm QW}$ to $\mathbf{H}_{\rm QW}$, with both matrices sharing exactly the same eigenvalues. One advantage of projecting $H_{\rm QW}$ onto $\mathcal{B}_0$ is that only a subset of the $8N$ subbands are necessary in $\mathcal{B}_0$ to achieve good accuracy. If one is interested in a small set of subbands $\mathcal{A}$, only the subbands $\mathcal{A}$ plus a few more that are close in energy should be included in the basis $\mathcal{B}_0$. In most situations, the size of $\mathcal{B}_0$ can be taken much smaller than $8N$ ($2N_\perp \ll 8N$), which reduces significantly the size of the $k\cdot p$ matrix. Furthermore, levels corresponding to $\sigma = -$ can be constructed from the eigenstates of H_+, thus reducing the problem of diagonalizing a $8N\times 8N$ matrix to diagonalizing a $N_\perp \times N_\perp$ matrix. This procedure is in very close analogy with the strategy that was employed to reduce the infinite dimensional bulk dispersion problem (3.10) to the finite size matrix of 30-band $k\cdot p$, except now the dimension of the starting Hamiltonian is $8N$ instead of infinite.

To illustrate this, consider a ${\rm Si}_{1-x}{\rm Ge}_x/{\rm Ge}/{\rm Si}_{1-x}{\rm Ge}_x$ heterostructure with $x = 0.80$, where the thickness of the Ge layer is 16 nm and that of the ${\rm Si}_{1-x}{\rm Ge}_x$ barriers is 50 nm each, for a total thickness $L = 116$ nm. A typical mesh size $\delta z = 0.01$ nm gives a total of $N = 11601$ mesh points, $8N = 92808$ orthonormal eigenstates, and a 92808×92808 $H_{\rm QW}$ matrix. Figure 3.4a shows the energy dispersion $E(k_x)$ for the first H and the first η subband computed from the exact diagonalization of the $8N\times 8N$ Hamiltonian. Also shown are the dispersion obtained

from the Hamiltonian projected on basis $\mathcal{B}_0$ with various $N_\perp$. For smaller $N_\perp = 100$, the dispersion from $\mathbf{H}_{\mathrm{QW}}$ is more accurate over a larger range of k_x for H1 compared to $\eta 1$. This is attributed to $N_\perp$ not being large enough to include higher energy subbands that couple strongly with $\eta 1$. Increasing $N_\perp$ to 200 subbands improves the accuracy for both H1 and $\eta 1$. At $N_\perp = 400$, which is still much smaller than $4N = 46404$, the dispersion given by $\mathbf{H}_{\mathrm{QW}}$ is essentially the same as that given by H_{QW} for the whole range of validity of 8-band $k \cdot p$ theory ($k_x \lesssim 1\,\mathrm{nm}^{-1}$, see Fig. 3.3). A similar calculation is performed in Fig. 3.4b for an infinite Ge well with the same strain as in the system from Fig. 3.4a. In case (b), the energy dispersion given by $\mathbf{H}_{\mathrm{QW}}$ converges faster with $N_\perp$ compared to case (a), with $N_\perp = 50$ (mint line) being already very accurate. This is caused by the finite QW band offsets in case (a), leading to a large density of plane wave levels outside the QW and across the barriers. If an accurate dispersion requires a basis that spans an energy window ΔE, much fewer bands are required in $\mathcal{B}_0$ to span that energy range when the well has infinite band offsets, due to the discrete nature of the energy spectrum.

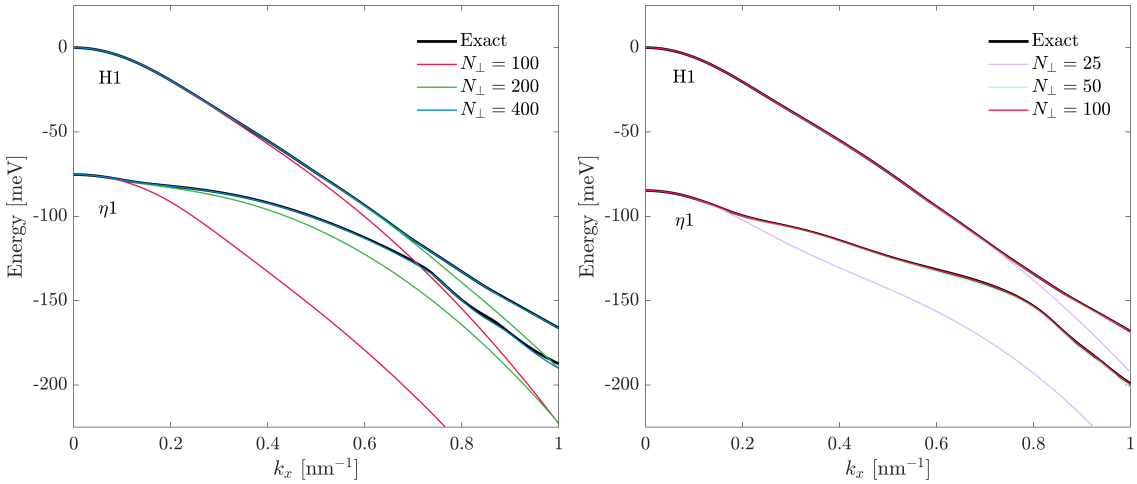

Figure 3.4 Energy dispersion $E(k_x)$ for H1 and $\eta 1$ calculated directly from H_{QW} (Exact) and by projecting H_{QW} onto $\mathcal{B}_0$ for various basis size $N_\perp$. Excited H and η levels are not shown for clarity. (a) Finite quantum well system: $\mathrm{Si}_{1-x}\mathrm{Ge}_x/\mathrm{Ge}/\mathrm{Si}_{1-x}\mathrm{Ge}_x$ with 16 nm Ge QW and 50 nm $\mathrm{Si}_{1-x}\mathrm{Ge}_x$ barriers with $x = 0.80$. (b) Infinite Ge QW of thickness 16 nm. In-plane strain in Ge is $\varepsilon_\parallel = -0.86\%$ in both systems.

For simple QW geometries, the eigenvalue problem (3.84) for the envelopes is accelerated by assuming a certain shape for the envelopes. For instance, in an infinite square well potential, the envelope for Hl must be either a cosine (for odd l) or a sine (for even l). Similarly, in the η subspace, even LH and SO envelopes (cosines) must come with odd CB envelopes (sines), because the coupling terms CB-LH and CB-SO are linear in k_z. In the general case, quantum wells have finite band offsets (such as in the $\mathrm{Si}_{1-x}\mathrm{Ge}_x/\mathrm{Ge}/\mathrm{Si}_{1-x}\mathrm{Ge}_x$

QW example), are subject to external electric fields $\mathbf{F} = F_z \mathbf{e}_z$, or could be in close proximity to another QW. For isolated bands such as H-levels, this is in principle still solvable by assuming some shape for the envelope wavefunctions. However, for η-levels, where CBs, LHs and SOs are superposed, such procedure becomes quickly impractical. This is worsened by position-dependent material parameters that lead to complex boundary conditions at interfaces between two materials. The eigenvalue problem (3.84) is therefore solved entirely numerically, without any assumptions on the shape of the envelopes. Advantages of this approach include the benefits from requiring only one implementation of the $k \cdot p$ solver that is applicable to any type of confinement. Another advantage is the ability to write closed formulas for hole parameters, such as (3.93) and more in the following, that are valid for *any* type of confinement. Once a formula for some parameter is written for an arbitrary envelope $f(z)$, it is straightforward to analytically evaluate a particular case where the shape of $f(z)$ is known by symmetry. Unless specified otherwise, hole parameters and matrix elements are applicable for any type of confinement in the z-axis and are not bound to any assumptions on the dependence of material parameters on z.

A disadvantage of the full numerical approach for solving (3.84) is obviously larger computation times. A remedy is the projection of H_{QW} onto the basis $\mathcal{B}_0$, where the same level of accuracy is obtained by the much smaller Hamiltonian $\mathbf{H}_{\mathrm{QW}}$. It should be noted that the $\mathbf{M}$ matrices and the energies $\mathbf{E}_0^{\mathrm{QW}}$ in $\mathbf{H}_{\mathrm{QW}}$ can be evaluated only once for a given heterostructure, thus making the computation for $\mathbf{k}_\parallel \neq \mathbf{0}$ even faster. For reference, generating the "Exact" curve for the infinite QW of Fig. 3.4b with 251 k_x points from 0 to $1\,\mathrm{nm}^{-1}$ took about one hour, while the $N_\perp = 100$ curve took about 5 seconds.

3.3.3 The quantum well Hamiltonian for B ∥ z ($A_z = 0$ gauge)

When the heterostructure is submerged in a magnetic field, the components of the wavevector must undergo a Peierls substitution to incorporate the orbital effects from the field [see (3.62)]. An appropriate gauge for a perpendicular field $\mathbf{B} = B\mathbf{e}_z$ is one that has no z component $\mathbf{e}_z \cdot \mathbf{A}(\mathbf{r}) = 0$ and no dependence on the z operator:

$$\mathbf{A}(\mathbf{r}) = B\left(-y \sin^2 \Lambda \mathbf{e}_x + x \cos^2 \Lambda \mathbf{e}_y\right), \tag{3.100}$$

where Λ is a free gauge parameter that has no effect on $\mathbf{B}$. Setting $\Lambda = \pi/4$, the components of the mechanical wavevector $\mathbf{K} = \mathbf{k} + e\mathbf{A}/\hbar$ are given by

$$K_x = k_x - \frac{y}{2l_B^2}, \tag{3.101a}$$

$$K_y = k_y + \frac{x}{2l_B^2}, \tag{3.101b}$$

$$K_z = k_z, \tag{3.101c}$$

with $l_B = \sqrt{\hbar/eB}$. In terms of the circular components $K_\pm = K_x \pm iK_y$, the wavevector satisfies the commutation relation

$$\frac{1}{l_B^2} = \frac{1}{2}[K_-, K_+]. \tag{3.102}$$

One can also write $K_\parallel^2 = K_x^2 + K_y^2$ in terms of the anti-commutator

$$K_\parallel^2 = \frac{1}{2}\{K_-, K_+\}. \tag{3.103}$$

A matrix Hamiltonian $\mathbf{H}_{\mathrm{QW}}$ for arbitrary $\mathbf{K}$ (and B) is constructed following the approach outlined in the previous subsection. When evaluated at $B = 0$ and $k_x = k_y = 0$, $H_{\mathrm{QW}}(\mathbf{K}) \to H_0$, where H_0 is the same as in (3.84). Projecting $H_{\mathrm{QW}}(\mathbf{K})$ onto the eigenbasis of H_0, while carefully preserving the ordering between the components of $\mathbf{K}$, we obtain the following matrix Hamiltonian:

$$\mathbf{H}_{\mathrm{QW}} = \mathbf{E}_0^{\mathrm{QW}} + \alpha_0 \mathbf{M}_\gamma K_\parallel^2 + \frac{\alpha_0}{2l_B^2}\mathbf{M}_g + \alpha_0 \left(i\mathbf{M}_1 K_- + \mathbf{M}_2 K_-^2 + \mathrm{H.c.} \right), \tag{3.104}$$

where $\mathbf{E}_0^{\mathrm{QW}}$, $\mathbf{M}_\gamma$, $\mathbf{M}_1$, and $\mathbf{M}_2$ are the same as in the $B = 0$ case (3.91) and

$$\mathbf{M}_g = \begin{bmatrix} \mathbf{G}_\perp^{\mathrm{H}} & 0 & 0 & 0 \\ & \mathbf{G}_\perp^{\eta} & 0 & 0 \\ \dagger & & -\mathbf{G}_\perp^{\eta} & 0 \\ & & & -\mathbf{G}_\perp^{\mathrm{H}} \end{bmatrix}, \tag{3.105}$$

with

$$\mathbf{G}_\perp^{\mathrm{H}} = -\left\langle h \right| 6\kappa + \frac{27q}{2} \left| h \right\rangle, \tag{3.106a}$$

$$\mathbf{G}_{\perp}^{\eta} = \langle c|g|c\rangle - 2\langle +|\kappa|+\rangle - \frac{1}{2}\langle \ell|q|\ell\rangle - \frac{4}{3}(\langle +|+\rangle - \langle -|-\rangle) \tag{3.106b}$$

being real and Hermitian matrices. We also note that $\alpha_0/l_B^2 = \mu_{\mathrm{B}}B$, where $\mu_{\mathrm{B}} = e\hbar/(2m_0)$ is the Bohr magneton. Hamiltonian (3.91) is recovered when setting $B = 0$ into (3.104), as expected.

Diagonalizing (3.104) for $B > 0$ is more challenging than in the $B = 0$ case, since neither k_x, k_y, K_x and K_y are good quantum numbers. The strategy is thus to write the in-plane components of $\mathbf{K}$ in terms of a new operator that commutes with $\mathbf{H}_{\mathrm{QW}}$ for all values of B. Under certain approximations, this new operator takes a very simple form, and the Hamiltonian is easily diagonalized.

The first approximation consists of neglecting the small cubic-in-J g-factor correction for H levels: $\mathbf{T}^{\mathrm{H}} = 0$. This is a very good approximation in Si, Ge and Sn since $\mathbf{T}^{\mathrm{H}}$ is directly proportional to the parameter q, which is very small compared to the hole g-factor parameter κ. In the second approximation, known as the *axial* approximation, the Hamiltonian terms that capture the cubic symmetry of the crystal are neglected, leading to isotropic energy dispersions in the QW plane. The axial approximation is excellent in Ge, since these cubic terms are proportional to $\gamma_2 - \gamma_3$, and in Ge, $\gamma_2 \approx \gamma_3$. In the Hamiltonian (3.104), the axial approximation simply consists of setting $\boldsymbol{\delta} = 0$ in the matrix $\mathbf{M}_2$. Setting $\mathbf{T}^{\mathrm{H}} = 0$ and $\boldsymbol{\delta} = 0$ in (3.104) gives:

$$\begin{aligned}\tilde{\mathbf{H}}_{\mathrm{QW}} = &\begin{bmatrix} \mathbf{E}^{\mathrm{H}} & & & \\ & \mathbf{E}^{\eta} & & \\ & & \mathbf{E}^{\eta} & \\ & & & \mathbf{E}^{\mathrm{H}} \end{bmatrix} + \frac{\alpha_0}{2l_B^2}\begin{bmatrix} \mathbf{G}_{\perp}^{\mathrm{H}} & & & \\ & \mathbf{G}_{\perp}^{\eta} & & \\ & & -\mathbf{G}_{\perp}^{\eta} & \\ & & & -\mathbf{G}_{\perp}^{\mathrm{H}} \end{bmatrix} \\ &+ \alpha_0 \begin{bmatrix} \boldsymbol{\Gamma}_{\parallel}^{\mathrm{H}} K_{\parallel}^2 & i\mathbf{T}^{\mathrm{x}} K_- & \boldsymbol{\mu} K_-^2 & \mathbf{0} \\ & \boldsymbol{\Gamma}_{\parallel}^{\eta} K_{\parallel}^2 & i\mathbf{T}^{\eta} K_- & \boldsymbol{\mu}^{\dagger} K_-^2 \\ \dagger & & \boldsymbol{\Gamma}_{\parallel}^{\eta} K_{\parallel}^2 & i\mathbf{T}^{\mathrm{x}\dagger} K_- \\ & & & \boldsymbol{\Gamma}_{\parallel}^{\mathrm{H}} K_{\parallel}^2 \end{bmatrix}.\end{aligned} \tag{3.107}$$

By defining the operator $a = il_B K_-/\sqrt{2}$, we get the following identities:

$$K_- = \frac{\sqrt{2}a}{il_B}, \qquad\qquad K_+ = -\frac{\sqrt{2}a^{\dagger}}{il_B}, \tag{3.108}$$

$$K_-^2 = -\frac{2a^2}{l_B^2}, \qquad K_+^2 = -\frac{2a^{\dagger 2}}{l_B^2}, \tag{3.109}$$

$$K_\parallel^2 = \frac{1}{l_B^2}\left(aa^\dagger + a^\dagger a\right) = \frac{1}{l_B^2}(2n+1), \tag{3.110}$$

$$\left[a, a^\dagger\right] = 1, \tag{3.111}$$

where $n = a^\dagger a$. The commutation relation (3.111) reveals that a is a harmonic oscillator-like ladder operator, and that its action on the eigenstates of n is as follow:

$$a^\dagger a\left|n\right\rangle = n\left|n\right\rangle, \quad a\left|n\right\rangle = \sqrt{n}\left|n-1\right\rangle, \quad a^\dagger\left|n\right\rangle = \sqrt{n+1}\left|n+1\right\rangle, \quad a\left|0\right\rangle = 0, \tag{3.112}$$

where the quantum number n is any integer ≥ 0. In terms of a, $\tilde{\mathbf{H}}_{\mathrm{QW}}$ becomes

$$\begin{aligned}\tilde{\mathbf{H}}_{\mathrm{QW}} = &\begin{bmatrix} \mathbf{E}_+^{\mathrm{H}}(B) & & & \\ & \mathbf{E}_+^{\eta}(B) & & \\ & & \mathbf{E}_-^{\eta}(B) & \\ & & & \mathbf{E}_-^{\mathrm{H}}(B) \end{bmatrix} \\ &+ \frac{\alpha_0}{l_B^2}\begin{bmatrix} 2\boldsymbol{\Gamma}_\parallel^{\mathrm{H}} a^\dagger a & \sqrt{2} l_B \mathbf{T}^{\mathrm{x}} a & -2\boldsymbol{\mu} a^2 & \mathbf{0} \\ & 2\boldsymbol{\Gamma}_\parallel^{\eta} a^\dagger a & \sqrt{2} l_B \mathbf{T}^{\eta} a & -2\boldsymbol{\mu}^\dagger a^2 \\ \dagger & & 2\boldsymbol{\Gamma}_\parallel^{\eta} a^\dagger a & \sqrt{2} l_B \mathbf{T}^{\mathrm{x}\dagger} a \\ & & & 2\boldsymbol{\Gamma}_\parallel^{\mathrm{H}} a^\dagger a \end{bmatrix},\end{aligned} \tag{3.113}$$

where $\mathbf{E}_\pm^\tau(B) = \mathbf{E}^\tau + \frac{\alpha_0}{l_B^2}\left(\boldsymbol{\Gamma}_\parallel^\tau \pm \mathbf{G}_\perp^\tau/2\right)$. The first term in $\tilde{\mathbf{H}}_{\mathrm{QW}}$ is diagonal in $\left|n\right\rangle$ since it contains no a operators. However, the second term involves various powers of a and $a^\dagger$ in a way that suggests an eigenspinor of the form [139]:

$$\left|\varphi\right\rangle = \begin{bmatrix} \mathbf{c}_{\mathrm{H}+}\left|m-1\right\rangle \\ \mathbf{c}_{\eta+}\left|m\right\rangle \\ \mathbf{c}_{\eta-}\left|m+1\right\rangle \\ \mathbf{c}_{\mathrm{H}-}\left|m+2\right\rangle \end{bmatrix}, \tag{3.114}$$

where $\mathbf{c}_{\tau\pm}$ are N_τ-component vectors ($N_{\mathrm{H}} + N_\eta = N_\perp$) and m is the Landau level index, whose value must be such that n remains ≥ 0. If $m = -2$, only the H$-$ subspace is allowed

in the Hamiltonian since $|m+2\rangle = |0\rangle$. In that case, the Hamiltonian collapses to

$$\tilde{\mathbf{H}}_{\mathrm{QW}}^{m=-2} = \mathbf{E}_{-}^{\mathrm{H}}(B) + \frac{2\alpha_0}{l_B^2}\boldsymbol{\Gamma}_{\parallel}^{\mathrm{H}} a^\dagger a \tag{3.115a}$$

$$= \mathbf{E}_{-}^{\mathrm{H}}(B). \tag{3.115b}$$

Note that $\mathbf{E}_{\pm}^{\tau}(B)$ is not necessarily diagonal with respect to $|\tau\sigma; j\rangle$, since $\boldsymbol{\Gamma}_{\parallel}^{\tau}$ and $\mathbf{G}_{\perp}^{\tau}$ generally have non-zero off-diagonal terms, especially if envelopes spread across multiple materials. If $m = -1$, only the H$-$ and the $\eta-$ subspaces are allowed. The Hamiltonian becomes:

$$\tilde{\mathbf{H}}_{\mathrm{QW}}^{m=-1} = \begin{bmatrix} \mathbf{E}_{-}^{\eta}(B) & \\ & \mathbf{E}_{-}^{\mathrm{H}}(B) \end{bmatrix} + \frac{\alpha_0}{l_B^2}\begin{bmatrix} 2\boldsymbol{\Gamma}_{\parallel}^{\eta} a^\dagger a & \sqrt{2} l_B \mathbf{T}^{\mathrm{x}\dagger} a \\ & 2\boldsymbol{\Gamma}_{\parallel}^{\mathrm{H}} a^\dagger a \end{bmatrix} \tag{3.116a}$$

$$= \begin{bmatrix} \mathbf{E}_{-}^{\eta}(B) & \\ & \mathbf{E}_{-}^{\mathrm{H}}(B) \end{bmatrix} + \frac{\alpha_0}{l_B^2}\begin{bmatrix} \mathbf{0} & \sqrt{2} l_B \mathbf{T}^{\mathrm{x}\dagger} \\ & 2\boldsymbol{\Gamma}_{\parallel}^{\mathrm{H}} \end{bmatrix}. \tag{3.116b}$$

Similarly, if $m = 0$, only the H$+$ subspace is forbidden in the Hamiltonian. Hence, $\tilde{\mathbf{H}}_{\mathrm{QW}}$ becomes:

$$\tilde{\mathbf{H}}_{\mathrm{QW}}^{m=0} = \begin{bmatrix} \mathbf{E}_{+}^{\eta}(B) & & \\ & \mathbf{E}_{-}^{\eta}(B) & \\ & & \mathbf{E}_{-}^{\mathrm{H}}(B) \end{bmatrix} + \frac{\alpha_0}{l_B^2}\begin{bmatrix} 2\boldsymbol{\Gamma}_{\parallel}^{\eta} a^\dagger a & \sqrt{2} l_B \mathbf{T}^{\eta} a & -2\boldsymbol{\mu}^\dagger a^2 \\ & 2\boldsymbol{\Gamma}_{\parallel}^{\eta} a^\dagger a & \sqrt{2} l_B \mathbf{T}^{\mathrm{x}\dagger} a \\ & & 2\boldsymbol{\Gamma}_{\parallel}^{\mathrm{H}} a^\dagger a \end{bmatrix} \tag{3.117a}$$

$$= \begin{bmatrix} \mathbf{E}_{+}^{\eta}(B) & & \\ & \mathbf{E}_{-}^{\eta}(B) & \\ & & \mathbf{E}_{-}^{\mathrm{H}}(B) \end{bmatrix} + \frac{\alpha_0}{l_B^2}\begin{bmatrix} \mathbf{0} & \sqrt{2} l_B \mathbf{T}^{\eta} & -2\sqrt{2}\boldsymbol{\mu}^\dagger \\ & 2\boldsymbol{\Gamma}_{\parallel}^{\eta} & 2 l_B \mathbf{T}^{\mathrm{x}\dagger} \\ & & 4\boldsymbol{\Gamma}_{\parallel}^{\mathrm{H}} \end{bmatrix}. \tag{3.117b}$$

Finally, for $m \geq 1$, all subspaces are allowed:

$$\tilde{\mathbf{H}}_{\mathrm{QW}}^{m\geq 1} = \begin{bmatrix} \mathbf{E}_{+}^{\mathrm{H}}(B) & & & \\ & \mathbf{E}_{+}^{\eta}(B) & & \\ & & \mathbf{E}_{-}^{\eta}(B) & \\ & & & \mathbf{E}_{-}^{\mathrm{H}}(B) \end{bmatrix} + \frac{\alpha_0}{l_B^2} \begin{bmatrix} 2\boldsymbol{\Gamma}_{\parallel}^{\mathrm{H}}(m-1) & \sqrt{2}l_B\mathbf{T}^{\mathrm{x}}\sqrt{m} & -2\boldsymbol{\mu}\sqrt{m(m+1)} & \mathbf{0} \\ & 2\boldsymbol{\Gamma}_{\parallel}^{\eta}m & \sqrt{2}l_B\mathbf{T}^{\eta}\sqrt{m+1} & -2\boldsymbol{\mu}^{\dagger}\sqrt{(m+1)(m+2)} \\ & & 2\boldsymbol{\Gamma}_{\parallel}^{\eta}(m+1) & \sqrt{2}l_B\mathbf{T}^{\mathrm{x}\dagger}\sqrt{m+2} \\ & & & 2\boldsymbol{\Gamma}_{\parallel}^{\mathrm{H}}(m+2) \end{bmatrix}. \tag{3.118}$$

The QW energy dispersion as a function of B is obtained by solving $\tilde{\mathbf{H}}_{\mathrm{QW}}^{m}$ for as many Landau levels $m \geq -2$ as required. The result is called a fan-diagram. A Zeeman spin-split pair corresponds to any pair of η or H levels that is degenerate at $B = 0$ and shares the same n quantum number at finite B. For instance, a spin-down $m = -2$ H level is the spin-split partner of the spin-up $m = 1$ H level. Similarly, a spin-down $m = -1$ η level is the spin-split partner of the spin-up $m = 0$ η level. We emphasize that m is a good quantum number only within the two aforementioned approximations (axial + no q). Otherwise, the corrections owing to the cubic symmetry of the crystal must be taken in account, which is described by the following Hamiltonian:

$$\mathbf{H}_{\square} = \frac{\alpha_0}{l_B^2} \begin{bmatrix} \mathbf{0} & \mathbf{0} & -2\boldsymbol{\delta}a^{\dagger 2} & \sqrt{2}l_B\mathbf{T}^{\mathrm{H}}a^{\dagger} \\ & \mathbf{0} & \mathbf{0} & -2\boldsymbol{\delta}^{\dagger}a^{\dagger 2} \\ \dagger & & \mathbf{0} & \mathbf{0} \\ & & & \mathbf{0} \end{bmatrix}. \tag{3.119}$$

3.3.4 The quantum well Hamiltonian for arbitrary B ($A_z = 0$ gauge)

In-plane components of the magnetic field can be taken in account by adding z-dependent terms in the in-plane components of the vector potential. If

$$\mathbf{B} = B\left(\sin\theta\cos\phi\mathbf{e}_x + \sin\theta\sin\phi\mathbf{e}_y + \cos\theta\mathbf{e}_z\right), \tag{3.120}$$

where θ and ϕ are the field's polar and azimuth angles respectively, then

$$\mathbf{A} = \mathbf{A}_\perp + \mathbf{A}_\parallel, \tag{3.121a}$$

$$\mathbf{A}_\perp = B\cos\theta\left(-y\sin^2\Lambda\mathbf{e}_x + x\cos^2\Lambda\mathbf{e}_y\right), \tag{3.121b}$$

$$\mathbf{A}_\parallel = zB\sin\theta\left(\sin\phi\mathbf{e}_x - \cos\phi\mathbf{e}_y\right). \tag{3.121c}$$

Here $\mathbf{A}_\perp$ and $\mathbf{A}_\parallel$ describe the out-of-plane and in-plane components of the magnetic field respectively. This choice of gauge is convenient since the z operator is easy to implement within the present theoretical framework (see Section 3.2.2). Every operator in the QW Hamiltonian that act on the z dimension, namely z and $K_z = k_z$, will be fully integrated following the projection onto the basis (3.88). It is thus natural to divide the mechanical wavevector $\mathbf{K}$ into one part that depends only on x and y (the same $\mathbf{K}$ as in the $\mathbf{B} \parallel z$ case but normalized by $\cos\theta$), and one other part containing the in-plane components of the field that are proportional to z. In other words, all operators acting on the z dimension will be pushed within the Hamiltonian matrices $\mathbf{M}_i$ and so on, such that the final Hamiltonian only depends on wavenumber components acting only in the QW plane degrees of freedom.

The mechanical wavevector $\mathbf{K} = \mathbf{k} + e\mathbf{A}/\hbar$ obeys the familiar commutation relations $\mathbf{K}\times\mathbf{K} = e\mathbf{B}/(i\hbar)$. Let's rewrite $\mathbf{K}$ in a way that brings forward the contributions from the out-of-plane and in-plane $\mathbf{B}$-field components:

$$\mathbf{K} = \tilde{\mathbf{K}} + \frac{e}{\hbar}\mathbf{A}_\parallel, \tag{3.122}$$

where

$$\tilde{\mathbf{K}} = \mathbf{k} + \frac{e}{\hbar}\mathbf{A}_\perp. \tag{3.123}$$

The wavenumber $\tilde{\mathbf{K}}$ only depends on the in-plane operators x, y, k_x and k_y, and has the following commutation relations:

$$\tilde{\mathbf{K}}\times\tilde{\mathbf{K}} = \frac{\cos\theta\mathbf{e}_z}{il_B^2}, \qquad \left[\tilde{K}_-, \tilde{K}_+\right] = \frac{2\cos\theta}{l_B^2}, \tag{3.124}$$

with circular components $\tilde{K}_\pm = \tilde{K}_x \pm i\tilde{K}_y$. The circular components $\tilde{K}_\pm$ and $K_\pm$ expand to:

$$\tilde{K}_\pm = k_\pm \pm \frac{i\zeta_\pm}{l_B^2}\cos\theta, \qquad\qquad K_\pm = \tilde{K}_\pm \mp \frac{ie^{\pm i\phi}}{l_B^2} z\sin\theta, \tag{3.125}$$

where $\zeta_\pm = (x \pm iy)/2$, and satisfy the commutation relations

$$[\zeta_\pm, k_\pm] = 0, \qquad\qquad [\zeta_\pm, k_\mp] = i. \tag{3.126}$$

As in the $B = 0$ and $\mathbf{B} \parallel z$ case, a Hamiltonian $\mathbf{H}_{\rm QW}$ for $B > 0$ is constructed by projecting $H_{\rm QW}$ onto the eigenbasis (3.88), while preserving the K-products ordering. The $\mathbf{K}$ wavenumbers are then expanded in terms of the $\tilde{\mathbf{K}}$'s, with the z contributions from the in-plane components of the field pushed into the matrices $\mathbf{M}_i$. The result is

$$\begin{aligned}\mathbf{H}_{\rm QW} = {} & \mathbf{E}_0 + \alpha_0 \mathbf{M}_\gamma \tilde{K}_\parallel^2 + \frac{\alpha_0\cos\theta}{l_B^2}\mathbf{M}_g + \alpha_0\left(i\mathbf{M}_1\tilde{K}_- + \mathbf{M}_2\tilde{K}_-^2 + \text{H.c.}\right) \\ & - \frac{\alpha_0\sin\theta}{l_B^2}\left(ie^{i\phi}\mathbf{M}'_\gamma\tilde{K}_- + e^{-i\phi}\mathbf{M}'_1 - 2ie^{-i\phi}\mathbf{M}'_2\tilde{K}_- + \text{H.c.}\right) \\ & + \frac{\alpha_0\sin^2\theta}{l_B^4}\left[\mathbf{M}''_\gamma - \left(e^{-2i\phi}\mathbf{M}''_2 + \text{H.c.}\right)\right],\end{aligned} \tag{3.127}$$

with $\tilde{K}_\parallel^2 = \left\{\tilde{K}_-, \tilde{K}_+\right\}/2$. Noting that $\tilde{K}_\pm \to K_\pm$ when $\theta \to 0$, equation (3.127) reduces to (3.104) when $\theta = 0$, as required. The primed matrices $\mathbf{M}_i$ have the same structure as their unprimed version (3.92):

$$\mathbf{M}'_\gamma = \begin{bmatrix} \boldsymbol{\Gamma}'^{\rm H}_\parallel & 0 & 0 & 0 \\ & \boldsymbol{\Gamma}'^{\eta}_\parallel & 0 & 0 \\ \dagger & & \boldsymbol{\Gamma}'^{\eta}_\parallel & 0 \\ & & & \boldsymbol{\Gamma}'^{\rm H}_\parallel \end{bmatrix}, \qquad \mathbf{M}''_\gamma = \begin{bmatrix} \boldsymbol{\Gamma}''^{\rm H}_\parallel & 0 & 0 & 0 \\ & \boldsymbol{\Gamma}''^{\eta}_\parallel & 0 & 0 \\ \dagger & & \boldsymbol{\Gamma}''^{\eta}_\parallel & 0 \\ & & & \boldsymbol{\Gamma}''^{\rm H}_\parallel \end{bmatrix}, \tag{3.128a}$$

$$\mathbf{M}'_1 = \begin{bmatrix} 0 & \mathbf{T}'^{\rm x} & 0 & 0 \\ 0 & 0 & \mathbf{T}'^{\eta} & 0 \\ 0 & 0 & 0 & \mathbf{T}'^{\rm x\dagger} \\ \mathbf{T}'^{\rm H} & 0 & 0 & 0 \end{bmatrix}, \tag{3.128b}$$

$$\mathbf{M}_2' = \begin{bmatrix} 0 & 0 & \boldsymbol{\mu}' & 0 \\ 0 & 0 & 0 & \boldsymbol{\mu}'^{\dagger} \\ \boldsymbol{\delta}'^{\dagger} & 0 & 0 & 0 \\ 0 & \boldsymbol{\delta}' & 0 & 0 \end{bmatrix}, \qquad \mathbf{M}_2'' = \begin{bmatrix} 0 & 0 & \boldsymbol{\mu}'' & 0 \\ 0 & 0 & 0 & \boldsymbol{\mu}''^{\dagger} \\ \boldsymbol{\delta}''^{\dagger} & 0 & 0 & 0 \\ 0 & \boldsymbol{\delta}'' & 0 & 0 \end{bmatrix}. \tag{3.128c}$$

Primed matrix elements are also based on the unprimed elements from (3.93), but with added powers of z depending on the number p of primes:

$$\boldsymbol{\Gamma}_{\parallel}^{p\eta} = \langle c| z^p \gamma_c |c\rangle - \frac{1}{3} \langle +| z^p (\gamma_1 + \gamma_2) |+\rangle - \frac{2}{3} \langle -| z^p (\gamma_1 - 2\gamma_2) |-\rangle , \tag{3.129a}$$

$$\boldsymbol{\Gamma}_{\parallel}^{p\mathrm{H}} = - \langle h| z^p (\gamma_1 + \gamma_2) |h\rangle , \tag{3.129b}$$

$$\mathbf{T}^{p\mathrm{x}} = \frac{1}{\sqrt{2}} \langle h| \left[z^p c_p |c\rangle - \sqrt{6} i \left(u_+^p |-\rangle + \frac{7}{4} [z^p q, k_z] |\ell\rangle - \frac{ipz^{p-1}}{\sqrt{2}} |s\rangle \right) \right], \tag{3.129c}$$

$$\begin{aligned} \mathbf{T}^{p\eta} = \frac{1}{\sqrt{6}} \left(\langle c| z^p c_p |+\rangle + \langle +| z^p c_p |c\rangle \right) \\ + i \left(\frac{1}{2} \langle c| [z^p g, k_z] |c\rangle - \langle +| u_+^p |-\rangle + \langle -| u_-^p |+\rangle - 5 \langle \ell| [z^p q, k_z] |\ell\rangle \right) \\ + \frac{p}{\sqrt{2}} \left(\langle s| z^{p-1} |-\rangle + \langle -| z^{p-1} |s\rangle \right), \end{aligned} \tag{3.129d}$$

$$\mathbf{T}^{p\mathrm{H}} = -\frac{3i}{2} \langle h| [z^p q, k_z] |h\rangle , \tag{3.129e}$$

$$\boldsymbol{\mu}^p = \frac{\sqrt{3}}{2} \langle h| z^p (\gamma_2 + \gamma_3) |+\rangle , \tag{3.129f}$$

$$\boldsymbol{\delta}^p = \frac{\sqrt{3}}{2} \langle h| z^p (\gamma_2 - \gamma_3) |+\rangle , \tag{3.129g}$$

where $u_\pm^p = \{z^p \gamma_3, k_z\} \pm [z^p \kappa, k_z]$. $p = 0$ corresponds to (3.93), and $p = 1, 2$ corresponds to one and two primes respectively. Similarly to (3.92), the matrices $\mathbf{M}_\gamma^p$, $\boldsymbol{\Gamma}_{\parallel}^{p\tau}$, and $\mathbf{T}^{p\tau}$ are real and Hermitian, while the matrices $\mathbf{M}_{1,2}^p$, $\mathbf{T}^{p\mathrm{x}}$, $\boldsymbol{\mu}^p$, and $\boldsymbol{\delta}^p$ are real but not Hermitian.

For purely in-plane magnetic fields, the wavevectors in Hamiltonian (3.127) reduce to scalars: $\tilde{K}_\pm \to k_\pm$. Since the latter do not contain any dependence on x or y, the Hamiltonian then commutes with $k_\pm$, which can be taken as quantum numbers. However, their physical significance must be taken with special care, since $k_\pm$ are gauge dependent. The corresponding gauge invariant quantities are the $K_\pm = k_\pm \mp \frac{ie^{\pm i\phi}}{l_B^2} z$ (no tilde on $K_\pm$), but these are not good quantum numbers because they contain a z operator. Taking the average value of $K_\pm$ and noting that $\langle k_\pm \rangle = k_\pm$ gives:

$$\langle K_\pm \rangle = k_\pm \mp \frac{ie^{\pm i\phi}}{l_B^2} \langle z \rangle \,. \tag{3.130}$$

Therefore, by carefully choosing the $z = 0$ coordinate such that $\langle z \rangle = 0$, one obtains $\langle K_\pm \rangle = k_\pm$, meaning that the quantum numbers $k_\pm$ that were once gauge dependent now correspond to the gauge invariant quantity $\langle K_\pm \rangle$. In inversion symmetric heterostructures such as quantum wells with identical barriers on both sides, this is achieved by placing the $z = 0$ coordinate in the center of the well. In heterostructures with additional in-plane confinement (quantum dots, quantum channels, etc ...), it is more convenient to put the in-plane contributions of the **B**-field into the z-component of **A**, thus eliminating any dependence on the z operator and removing any gauge invariance complications.

3.3.5 List of quantum well parameters

As discussed earlier, a general multi-band Hamiltonian can be simplified to describe only a subset of bands, with remote levels taken in account perturbatively. This was the main topic of the previous few sections, where the starting point was the bulk 30-band $k \cdot p$ model H_{30}, and the simplified, effective Hamiltonian was an 8-band matrix H_8 for the conduction, the heavy hole, the light hole and the split-off bands. Doing so introduced material-specific parameters in H_8 (see Section 3.1.4) such that the dispersion predicted by H_8 coincides with that of H_{30} close to the Γ point. In analogy with *bulk* band models, a similar procedure can be performed with *quantum well* multi-(sub)band Hamiltonians, where the starting multi-subband Hamiltonian is the $2N_\perp \times 2N_\perp$ matrix (3.91), (3.104) or (3.127). The simplified, effective Hamiltonian may describe any collection of subbands ηj and/or Hl, with all other subbands taken in account perturbatively. This Hamiltonian depends on a set of *quantum well* parameters that are specific to the material system, the heterostructure and the chosen set of subbands. The objective of this section is to evaluate quantum well parameters for single τj subband Hamiltonians. The corresponding effective matrices are 2×2 ($\sigma = \pm$) and are described by means of 4^{th} order perturbation theory. As in bulk band effective Hamiltonians, quantum well effective Hamiltonians are valid only for small $\mathbf{K}_\parallel$.

We take as the multi-subband Hamiltonian the matrix (3.104) for quantum wells in perpendicular fields. This matrix is written as a sum of one term with known eigenvalues (already diagonal) $\mathbf{E}_0$, and one term with unknown eigenvalues $\mathbf{W}$:

$$\mathbf{E}_0 = \begin{bmatrix} \mathbf{E}^{\mathrm{H}} & 0 & 0 & 0 \\ & \mathbf{E}^{\eta} & 0 & 0 \\ \dagger & & \mathbf{E}^{\eta} & 0 \\ & & & \mathbf{E}^{\mathrm{H}} \end{bmatrix}, \tag{3.131}$$

$$\mathbf{W} = \alpha_0 \mathbf{M}_\gamma K_\parallel^2 + \frac{\alpha_0}{2l_B^2}\mathbf{M}_g + \alpha_0 \left(i\mathbf{M}_1 K_- + \mathbf{M}_2 K_-^2 + \mathrm{H.c.} \right). \tag{3.132}$$

Notably, $\mathbf{W}$ vanishes if $\mathbf{K}_\parallel = \mathbf{0}$. An effective Hamiltonian $\mathbf{H}_{\text{eff}}$ is obtained by summing terms corresponding to different perturbation orders. Up to 4^{th} order:

$$\mathbf{H}_{\text{eff}} = \mathbf{H}^{(0)} + \mathbf{H}^{(1)} + \mathbf{H}^{(2)} + \mathbf{H}^{(3)} + \mathbf{H}^{(4)}. \tag{3.133}$$

Explicit expressions are found in Reference [35] for the p^{th} order correction $\mathbf{H}^{(p)}$ up to $p = 4$. These expressions undergo some simplifications in the special case where the levels of interest are fully degenerate, as is the case for $|\tau\pm; j\rangle$. In the following, we establish useful notation to make the perturbative equations more concise.

We first denote by $\mathcal{H}$ the whole Hilbert space generated by the $2N_\perp$-dimensional QW subband basis $\mathcal{B}_0$ [see (3.88)]. Every spin-degenerate pair $|\tau\pm; j\rangle$ generates a 2-dimensional Hilbert subspace of $\mathcal{H}$. We assume that there are no accidental degeneracies between a given ηj level and another Hl level. We adopt the following convention of indices:

- i, j: indices that run through the whole Hilbert space $\mathcal{H}$;
- α, β, γ, ϵ: indices that run within a degenerate subspace: for a given α, the indices β, γ and ϵ are restricted to the same degenerate subspace as α;
- λ, μ, ν: indices that run through the orthogonal complement Hilbert subspace of the degenerate subspace specified by the indices α, β, γ, ϵ.

Immediate corollaries are $E_\alpha = E_\beta = E_\gamma = E_\epsilon$ and $E_\alpha \neq E_\lambda$. We also define the quantities $\Delta_{i,j}$ and $I_{i,j}$:

$$\Delta_{i,j} = \begin{cases} E_i - E_j & \text{if } E_i \neq E_j \\ \infty & \text{otherwise} \end{cases}, \tag{3.134}$$

$$I_{i,j} = \begin{cases} 1 & \text{if } E_i = E_j \\ 0 & \text{otherwise} \end{cases}. \tag{3.135}$$

The $\mathbf{\Delta}$ matrix is defined as such since energy difference denominators are frequent in perturbation theory. Setting $\Delta_{i,j} = \infty$ if $E_i = E_j$ eliminates from a sum all the terms involving two elements from the same degenerate subspace. The $\mathbf{I}$ matrix can be thought of as a "selector" of degenerate subspaces, i.e., $I_{i,j} = 1$ if and only if i and j belong to the same degenerate subspace. We also define the dot- and the bar-matrix:

$$\dot{W}_{i,j} = \frac{W_{i,j}}{\Delta_{i,j}} \Leftrightarrow \dot{\mathbf{W}} = \mathbf{W} \oslash \mathbf{\Delta} \tag{3.136a}$$

$$\ddot{W}_{i,j} = \frac{W_{i,j}}{\Delta_{i,j}^2} \Leftrightarrow \ddot{\mathbf{W}} = \mathbf{W} \oslash \mathbf{\Delta}^2 \tag{3.136b}$$

$$\bar{W}_{i,j} = W_{i,j} I_{i,j} \Leftrightarrow \bar{\mathbf{W}} = \mathbf{W} \odot \mathbf{I}, \tag{3.136c}$$

where $\oslash$ is the element-wise matrix division and $\odot$ is the element-wise matrix multiplication, and $\mathbf{\Delta}^2 = \mathbf{\Delta} \odot \mathbf{\Delta}$. $\mathbf{\Delta}$ and $\mathbf{I}$ are such that the matrix elements of a dotted operator vanish within a degenerate subspace, while those of a bared operator are only non-zero within a degenerate subspace. This is useful in the numerical implementation of the following perturbative sums, as subspaces are automatically selected by either dividing by $\mathbf{\Delta}$ or by multiplying by $\mathbf{I}$. Lastly, we also define a left-to-right product rule for the matrices $\mathbf{W}$: products like $\dot{\mathbf{W}}\bar{\mathbf{W}}\ddot{\mathbf{W}}\bar{\mathbf{W}}$ for instance are evaluated by first replacing each dot- or bar-W by its definition (3.136), and then by performing the multiplications from left to right:

$$\dot{\mathbf{W}}\bar{\mathbf{W}}\ddot{\mathbf{W}}\bar{\mathbf{W}} \to \mathbf{W} \oslash \mathbf{\Delta}\mathbf{W} \odot \mathbf{I}\mathbf{W} \oslash \mathbf{\Delta}^2\mathbf{W} \odot \mathbf{I} \tag{3.137a}$$

$$\to \Big(\Big(\big(\big(\big(\big(\mathbf{W} \oslash \mathbf{\Delta}\big)\,\mathbf{W}\big) \odot \mathbf{I}\big)\,\mathbf{W}\big) \oslash \mathbf{\Delta}^2\Big)\,\mathbf{W}\Big) \odot \mathbf{I} \tag{3.137b}$$

$$\to \sum_{\lambda,\mu,\gamma} \frac{W_{\alpha,\lambda} W_{\lambda,\gamma} W_{\gamma,\mu} W_{\mu,\beta}}{\Delta_{\alpha,\lambda} \Delta_{\gamma,\mu}^2}. \tag{3.137c}$$

Common two-element products are:

$$\dot{\mathbf{W}}\bar{\mathbf{W}} = ((\mathbf{W} \oslash \mathbf{\Delta})\,\mathbf{W}) \odot \mathbf{I} = \sum_{\lambda} \frac{W_{\alpha,\lambda} W_{\lambda,\beta}}{\Delta_{\alpha,\lambda}}, \tag{3.138}$$

$$\ddot{\mathbf{W}}\bar{\mathbf{W}} = \left(\left(\mathbf{W} \oslash \mathbf{\Delta}^2\right)\mathbf{W}\right) \odot \mathbf{I} = \sum_{\lambda} \frac{W_{\alpha,\lambda} W_{\lambda,\beta}}{\Delta^2_{\alpha,\lambda}}, \tag{3.139}$$

$$\bar{\mathbf{W}}\bar{\mathbf{W}} = ((\mathbf{W} \odot \mathbf{I})\,\mathbf{W}) \odot \mathbf{I} = \sum_{\gamma} W_{\alpha,\gamma} W_{\gamma,\beta} \tag{3.140}$$

etc ...

while common three-element products are:

$$\dot{\mathbf{W}}\dot{\mathbf{W}}\bar{\mathbf{W}} = ((((\mathbf{W} \oslash \mathbf{\Delta})\,\mathbf{W}) \oslash \mathbf{\Delta})\,\mathbf{W}) \odot \mathbf{I} = \sum_{\lambda,\mu} \frac{W_{\alpha,\lambda} W_{\lambda,\mu} W_{\mu,\beta}}{\Delta_{\alpha,\lambda}\Delta_{\alpha,\mu}}, \tag{3.141}$$

$$\ddot{\mathbf{W}}\bar{\mathbf{W}}\bar{\mathbf{W}} = \left(\left(\left(\left(\mathbf{W} \oslash \mathbf{\Delta}^2\right)\mathbf{W}\right) \odot \mathbf{I}\right)\mathbf{W}\right) \odot \mathbf{I} = \sum_{\lambda,\gamma} \frac{W_{\alpha,\lambda} W_{\lambda,\gamma} W_{\gamma,\beta}}{\Delta^2_{\alpha,\lambda}}, \tag{3.142}$$

$$\bar{\mathbf{W}}\ddot{\mathbf{W}}\bar{\mathbf{W}} = \left(\left(((\mathbf{W} \odot \mathbf{I})\,\mathbf{W}) \oslash \mathbf{\Delta}^2\right)\mathbf{W}\right) \odot \mathbf{I} = \sum_{\lambda,\gamma} \frac{W_{\alpha,\gamma} W_{\gamma,\lambda} W_{\lambda,\beta}}{\Delta^2_{\gamma,\lambda}} \tag{3.143}$$

etc ...

In the perturbative expansion of $\mathbf{H}_{\text{eff}}$, every right-most term in a product ends with a bar-operator, since $\mathbf{H}_{\text{eff}}$ only describes pairs of degenerate levels.

This implementation of perturbative sums provides a powerful approach to evaluate the effective parameters of every degenerate pair $|\tau\pm; j\rangle$ *at once*. For example, if $N_\eta = 3$, $N_{\text{H}} = 2$ (so $\mathcal{H}$ is of dimension 10), the structure of any W-product ending in a bared operator (and therefore $\mathbf{H}_{\text{eff}}$) will look like the following:

$\mathbf{H}_{\text{eff}} =$ 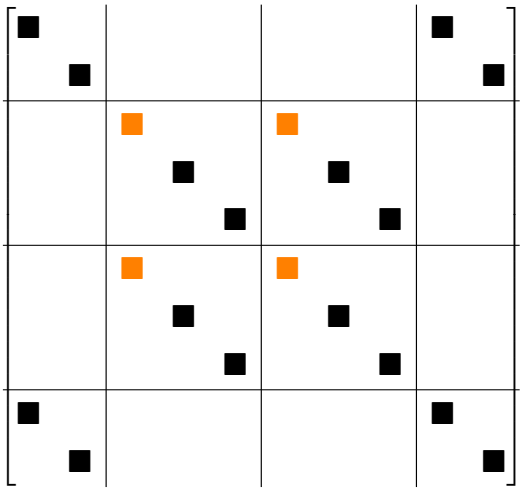 (3.144)

where ■ indicates a non-zero matrix element. If we are interested by the effective parameters of $\eta 1$, we only need to read in $\mathbf{H}_{\text{eff}}$ the relevant matrix elements for $|\eta\pm;1\rangle$ (marked in orange). The 0^{th} and the 1^{st} order corrections to the effective Hamiltonian are:

$$H^{(0)}_{\alpha,\beta} = E_\alpha \delta_{\alpha,\beta} \Leftrightarrow \mathbf{H}^{(0)} = \mathbf{E}_0, \tag{3.145}$$

$$H^{(1)}_{\alpha,\beta} = W_{\alpha,\beta} \Leftrightarrow \mathbf{H}^{(1)} = \bar{\mathbf{W}}. \tag{3.146}$$

The 2^{nd} order matrix elements are given by

$$H^{(2)}_{\alpha,\beta} = \sum_\lambda \frac{W_{\alpha,\lambda} W_{\lambda,\beta}}{\Delta_{\alpha,\lambda}} \tag{3.147}$$

$$\Leftrightarrow \mathbf{H}^{(2)} = \left(\left(\mathbf{W} \oslash \mathbf{\Delta}\right)\mathbf{W}\right) \odot \mathbf{I} = \dot{\mathbf{W}}\bar{\mathbf{W}}. \tag{3.148}$$

The 3^{rd} order correction is

$$H^{(3)}_{\alpha,\beta} = \sum_{\lambda,\mu} \frac{W_{\alpha,\lambda} W_{\lambda,\mu} W_{\mu,\beta}}{\Delta_{\alpha,\lambda}\Delta_{\alpha,\mu}} - \frac{1}{2}\sum_{\lambda,\gamma}\left[\frac{W_{\alpha,\lambda} W_{\lambda,\gamma} W_{\gamma,\beta}}{\Delta^2_{\alpha,\lambda}} + \frac{W_{\alpha,\gamma} W_{\gamma,\lambda} W_{\lambda,\beta}}{\Delta^2_{\gamma,\lambda}}\right] \tag{3.149}$$

$$\begin{aligned} \Leftrightarrow \mathbf{H}^{(3)} &= \dot{\mathbf{W}}\dot{\mathbf{W}}\bar{\mathbf{W}} - \frac{1}{2}\left(\ddot{\mathbf{W}}\bar{\mathbf{W}}\bar{\mathbf{W}} + \bar{\mathbf{W}}\ddot{\mathbf{W}}\bar{\mathbf{W}}\right) \\ &= \dot{\mathbf{W}}\dot{\mathbf{W}}\bar{\mathbf{W}} + [S]_3. \end{aligned} \tag{3.150}$$

Here $[S]_3$ refers to the permutations of dots and bars specific to 3^{rd} order perturbation.

Finally, the 4^{th} order correction is

$$\begin{aligned}
H^{(4)}_{\alpha,\beta} = &\sum_{\lambda,\mu,\nu} \frac{W_{\alpha,\lambda}W_{\lambda,\mu}W_{\mu,\nu}W_{\nu,\beta}}{\Delta_{\alpha,\lambda}\Delta_{\alpha,\mu}\Delta_{\alpha,\nu}} - \frac{1}{2}\sum_{\lambda,\mu,\gamma}\left[\frac{1}{\Delta^2_{\alpha,\lambda}\Delta_{\gamma,\mu}} + \frac{1}{\Delta_{\alpha,\lambda}\Delta^2_{\gamma,\mu}}\right] W_{\alpha,\lambda}W_{\lambda,\gamma}W_{\gamma,\mu}W_{\mu,\beta} \\
&- \frac{1}{2}\sum_{\lambda,\mu,\gamma}\left\{\left[\frac{1}{\Delta_{\alpha,\lambda}} + \frac{1}{\Delta_{\alpha,\mu}}\right]\frac{W_{\alpha,\lambda}W_{\lambda,\mu}W_{\mu,\gamma}W_{\gamma,\beta}}{\Delta_{\alpha,\lambda}\Delta_{\alpha,\mu}} + \left[\frac{1}{\Delta_{\gamma,\lambda}} + \frac{1}{\Delta_{\gamma,\mu}}\right]\frac{W_{\alpha,\gamma}W_{\gamma,\lambda}W_{\lambda,\mu}W_{\mu,\beta}}{\Delta_{\gamma,\lambda}\Delta_{\gamma,\mu}}\right\} \\
&+ \frac{1}{2}\sum_{\lambda,\gamma,\epsilon}\left[\frac{W_{\alpha,\lambda}W_{\lambda,\gamma}W_{\gamma,\epsilon}W_{\epsilon,\beta}}{\Delta^3_{\alpha,\lambda}} + \frac{W_{\alpha,\gamma}W_{\gamma,\epsilon}W_{\epsilon,\lambda}W_{\lambda,\beta}}{\Delta^3_{\epsilon,\lambda}}\right]
\end{aligned} \tag{3.151}$$

$$\begin{aligned}
\Leftrightarrow \mathbf{H}^{(4)} = &\dot{\mathbf{W}}\dot{\mathbf{W}}\dot{\mathbf{W}}\bar{\mathbf{W}} + \frac{1}{2}\left(\bar{\mathbf{W}}\bar{\mathbf{W}}\ddot{\mathbf{W}}\bar{\mathbf{W}} + \ddot{\mathbf{W}}\bar{\mathbf{W}}\bar{\mathbf{W}}\bar{\mathbf{W}}\right) \\
&- \frac{1}{2}\left(\bar{\mathbf{W}}\dot{\mathbf{W}}\ddot{\mathbf{W}}\bar{\mathbf{W}} + \dot{\mathbf{W}}\ddot{\mathbf{W}}\bar{\mathbf{W}}\bar{\mathbf{W}} + \ddot{\mathbf{W}}\bar{\mathbf{W}}\dot{\mathbf{W}}\bar{\mathbf{W}}\right) \\
&- \frac{1}{2}\left(\bar{\mathbf{W}}\ddot{\mathbf{W}}\dot{\mathbf{W}}\bar{\mathbf{W}} + \ddot{\mathbf{W}}\dot{\mathbf{W}}\bar{\mathbf{W}}\bar{\mathbf{W}} + \dot{\mathbf{W}}\bar{\mathbf{W}}\ddot{\mathbf{W}}\bar{\mathbf{W}}\right) \\
&= \dot{\mathbf{W}}\dot{\mathbf{W}}\dot{\mathbf{W}}\bar{\mathbf{W}} + [S]_4.
\end{aligned} \tag{3.152}$$

Once all the perturbation contributions have been summed, we collect and group terms with alike K-products while preserving the K-products ordering. We may change the ordering of a few products for convenience. For instance, we change the ordering of $K_-K_+K_+$ to the symmetrized form $K_+K_-K_+$ by making use of the commutation relation (3.102):

$$K_-K_+K_+ = (K_+K_- + [K_-, K_+])\,K_+ = K_+K_-K_+ + \frac{2}{l_B^2}K_+. \tag{3.153}$$

Similarly, we may use (3.103) to symmetrize products K_-K_+ as such:

$$K_-K_+ = \frac{1}{2}\{K_-, K_+\} + \frac{1}{2}[K_-, K_+] \tag{3.154a}$$

$$= K_\parallel^2 + \frac{1}{l_B^2}. \tag{3.154b}$$

The result is the following Hamiltonian:

$$\begin{aligned}\mathbf{H}_{\text{eff}} = \mathbf{E}_0 + \alpha_0 \left(\boldsymbol{\gamma} + \frac{\boldsymbol{\chi}_\perp}{2l_B^2}\right) K_\parallel^2 + \frac{\alpha_0}{2l_B^2}\mathbf{g}_\perp + \alpha_0 \boldsymbol{\zeta}_\gamma K_\parallel^4 + \frac{\alpha_0}{4l_B^4}\boldsymbol{\zeta}_\perp \\ + \left[i\boldsymbol{\beta}_1 K_- - i\boldsymbol{\beta}_2 K_+^3 + i\boldsymbol{\beta}_3 K_- K_+ K_- + \alpha_0 \boldsymbol{\zeta}_a K_-^4 - \frac{i\alpha_0}{l_B^2}\boldsymbol{\xi}_\perp K_- + \text{H.c.}\right].\end{aligned} \tag{3.155}$$

The effective parameter matrices represent:

- [0^{th}] E_0: $\mathbf{K}_\parallel = \mathbf{0}$ energy;
- [2^{nd}] γ: inverse effective mass, $\gamma = m_0/m^*$;
- [4^{th}] $\chi_\perp$: spin-dependent effective mass, for perpendicular fields;
- [2^{nd}] $g_\perp$: g-factor for perpendicular fields;
- [4^{th}] ζ_γ: $\mathbf{B}$-field independent non-parabolicity;
- [4^{th}] $\zeta_\perp$: perpendicular $\mathbf{B}$-field non linearity (quadratic in B term);
- [1^{st}] β_1: linear-in-K Rashba spin-orbit coupling;
- [3^{rd}] β_2: cubic-in-K Rashba spin-orbit coupling;
- [3^{rd}] β_3: cubic-in-K Rashba spin-orbit coupling;
- [4^{th}] ζ_a: anisotropy parameter;
- [3^{rd}] $\xi_\perp$: perpendicular $\mathbf{B}$-field correction to β_1 (vanishes for 2×2 Hamiltonians),

where the numbers in square brackets indicate the maximum perturbation order required to describe that parameter. As a general rule, this order cannot exceed the power of K associated with the parameter, since $\mathbf{W}$ is at least linear in K. For example, nothing new is learned from 3^{rd} order perturbation for γ, since γ is associated with $K_\parallel^2$. Each of these parameters are the prefactors that arise by collecting alike K-products in $\mathbf{H}_{\text{eff}}$. By increasing order of perturbation, we have:

$$\boldsymbol{\beta}_1 = \alpha_0 \bar{\mathbf{M}}_1, \tag{3.156a}$$

$$\boldsymbol{\gamma} = \bar{\mathbf{M}}_\gamma + \alpha_0 \left(\dot{\mathbf{M}}_1 \bar{\mathbf{M}}_1^\dagger + \dot{\mathbf{M}}_1^\dagger \bar{\mathbf{M}}_1 \right), \tag{3.156b}$$

$$\mathbf{g}_\perp = \bar{\mathbf{M}}_g + 2\alpha_0 \left(\dot{\mathbf{M}}_1 \bar{\mathbf{M}}_1^\dagger - \dot{\mathbf{M}}_1^\dagger \bar{\mathbf{M}}_1 \right), \tag{3.156c}$$

$$\boldsymbol{\beta}_2 = \alpha_0^2 \left(\dot{\mathbf{M}}_1^\dagger \bar{\mathbf{M}}_2^\dagger + \dot{\mathbf{M}}_2^\dagger \bar{\mathbf{M}}_1^\dagger \right) - \alpha_0^3 \left(\dot{\mathbf{M}}_1^\dagger \dot{\mathbf{M}}_1^\dagger \bar{\mathbf{M}}_1^\dagger + [S]_3 \right), \tag{3.156d}$$

$$\begin{aligned} \boldsymbol{\beta}_3 = {} & \alpha_0^2 \left(\dot{\mathbf{M}}_\gamma \bar{\mathbf{M}}_1 - \dot{\mathbf{M}}_1^\dagger \bar{\mathbf{M}}_2 + \dot{\mathbf{M}}_1 \bar{\mathbf{M}}_\gamma - \dot{\mathbf{M}}_2 \bar{\mathbf{M}}_1^\dagger \right) \\ & + \alpha_0^3 \left(\dot{\mathbf{M}}_1^\dagger \dot{\mathbf{M}}_1 \bar{\mathbf{M}}_1 + \dot{\mathbf{M}}_1 \dot{\mathbf{M}}_1^\dagger \bar{\mathbf{M}}_1 + \dot{\mathbf{M}}_1 \dot{\mathbf{M}}_1 \bar{\mathbf{M}}_1^\dagger + [S]_3 \right), \end{aligned} \tag{3.156e}$$

$$\begin{aligned} \boldsymbol{\chi}_\perp = {} & \alpha_0 \left(\dot{\mathbf{M}}_\gamma \bar{\mathbf{M}}_g + 8\dot{\mathbf{M}}_2 \bar{\mathbf{M}}_2^\dagger + \dot{\mathbf{M}}_g \bar{\mathbf{M}}_\gamma - 8\dot{\mathbf{M}}_2^\dagger \bar{\mathbf{M}}_2 \right) \\ & + \alpha_0^2 \left(6\dot{\mathbf{M}}_1 \dot{\mathbf{M}}_\gamma \bar{\mathbf{M}}_1^\dagger + 2\dot{\mathbf{M}}_\gamma \dot{\mathbf{M}}_1 \bar{\mathbf{M}}_1^\dagger - 2\dot{\mathbf{M}}_\gamma \dot{\mathbf{M}}_1^\dagger \bar{\mathbf{M}}_1 \right. \\ & - 6\dot{\mathbf{M}}_1^\dagger \dot{\mathbf{M}}_\gamma \bar{\mathbf{M}}_1 + 2\dot{\mathbf{M}}_1 \dot{\mathbf{M}}_1^\dagger \bar{\mathbf{M}}_\gamma - 2\dot{\mathbf{M}}_1^\dagger \dot{\mathbf{M}}_1 \bar{\mathbf{M}}_\gamma \\ & + \dot{\mathbf{M}}_1 \dot{\mathbf{M}}_g \bar{\mathbf{M}}_1^\dagger + \dot{\mathbf{M}}_g \dot{\mathbf{M}}_1 \bar{\mathbf{M}}_1^\dagger + \dot{\mathbf{M}}_g \dot{\mathbf{M}}_1^\dagger \bar{\mathbf{M}}_1 \\ & + \dot{\mathbf{M}}_1^\dagger \dot{\mathbf{M}}_g \bar{\mathbf{M}}_1 + \dot{\mathbf{M}}_1 \dot{\mathbf{M}}_1^\dagger \bar{\mathbf{M}}_g + \dot{\mathbf{M}}_1^\dagger \dot{\mathbf{M}}_1 \bar{\mathbf{M}}_g \\ & \left. - 8\dot{\mathbf{M}}_1 \dot{\mathbf{M}}_1 \bar{\mathbf{M}}_2^\dagger + 8\dot{\mathbf{M}}_2^\dagger \dot{\mathbf{M}}_1 \bar{\mathbf{M}}_1 - 8\dot{\mathbf{M}}_2 \dot{\mathbf{M}}_1^\dagger \bar{\mathbf{M}}_1^\dagger + 8\dot{\mathbf{M}}_1^\dagger \dot{\mathbf{M}}_1^\dagger \bar{\mathbf{M}}_2 + [S]_3 \right) \\ & + 4\alpha_0^3 \left(2\dot{\mathbf{M}}_1 \dot{\mathbf{M}}_1 \dot{\mathbf{M}}_1^\dagger \bar{\mathbf{M}}_1^\dagger + \dot{\mathbf{M}}_1 \dot{\mathbf{M}}_1^\dagger \dot{\mathbf{M}}_1 \bar{\mathbf{M}}_1^\dagger - 2\dot{\mathbf{M}}_1^\dagger \dot{\mathbf{M}}_1^\dagger \dot{\mathbf{M}}_1 \bar{\mathbf{M}}_1 - \dot{\mathbf{M}}_1^\dagger \dot{\mathbf{M}}_1 \dot{\mathbf{M}}_1^\dagger \bar{\mathbf{M}}_1 + [S]_4 \right), \end{aligned} \tag{3.156f}$$

$$\begin{aligned} \boldsymbol{\zeta}_\gamma = {} & \alpha_0 \left(\dot{\mathbf{M}}_\gamma \bar{\mathbf{M}}_\gamma + \dot{\mathbf{M}}_2 \bar{\mathbf{M}}_2^\dagger + \dot{\mathbf{M}}_2^\dagger \bar{\mathbf{M}}_2 \right) \\ & + \alpha_0^2 \left(\dot{\mathbf{M}}_1 \dot{\mathbf{M}}_\gamma \bar{\mathbf{M}}_1^\dagger + \dot{\mathbf{M}}_\gamma \dot{\mathbf{M}}_1 \bar{\mathbf{M}}_1^\dagger + \dot{\mathbf{M}}_\gamma \dot{\mathbf{M}}_1^\dagger \bar{\mathbf{M}}_1 \right. \\ & + \dot{\mathbf{M}}_1^\dagger \dot{\mathbf{M}}_\gamma \bar{\mathbf{M}}_1 + \dot{\mathbf{M}}_1 \dot{\mathbf{M}}_1^\dagger \bar{\mathbf{M}}_\gamma + \dot{\mathbf{M}}_1^\dagger \dot{\mathbf{M}}_1 \bar{\mathbf{M}}_\gamma \\ & - \dot{\mathbf{M}}_1 \dot{\mathbf{M}}_1 \bar{\mathbf{M}}_2^\dagger - \dot{\mathbf{M}}_1 \dot{\mathbf{M}}_2^\dagger \bar{\mathbf{M}}_1 - \dot{\mathbf{M}}_2^\dagger \dot{\mathbf{M}}_1 \bar{\mathbf{M}}_1 \\ & \left. - \dot{\mathbf{M}}_2 \dot{\mathbf{M}}_1^\dagger \bar{\mathbf{M}}_1^\dagger - \dot{\mathbf{M}}_1^\dagger \dot{\mathbf{M}}_2 \bar{\mathbf{M}}_1^\dagger - \dot{\mathbf{M}}_1^\dagger \dot{\mathbf{M}}_1^\dagger \bar{\mathbf{M}}_2 + [S]_3 \right) \\ & + \alpha_0^3 \left(\dot{\mathbf{M}}_1 \dot{\mathbf{M}}_1 \dot{\mathbf{M}}_1^\dagger \bar{\mathbf{M}}_1^\dagger + \dot{\mathbf{M}}_1^\dagger \dot{\mathbf{M}}_1^\dagger \dot{\mathbf{M}}_1 \bar{\mathbf{M}}_1 + \dot{\mathbf{M}}_1 \dot{\mathbf{M}}_1^\dagger \dot{\mathbf{M}}_1 \bar{\mathbf{M}}_1^\dagger \right. \\ & \left. + \dot{\mathbf{M}}_1^\dagger \dot{\mathbf{M}}_1 \dot{\mathbf{M}}_1^\dagger \bar{\mathbf{M}}_1 + \dot{\mathbf{M}}_1 \dot{\mathbf{M}}_1^\dagger \dot{\mathbf{M}}_1^\dagger \bar{\mathbf{M}}_1 + \dot{\mathbf{M}}_1^\dagger \dot{\mathbf{M}}_1 \dot{\mathbf{M}}_1 \bar{\mathbf{M}}_1^\dagger + [S]_4 \right), \end{aligned} \tag{3.156g}$$

$$\begin{aligned} \boldsymbol{\zeta}_\perp = {} & \alpha_0 \left(\dot{\mathbf{M}}_g \bar{\mathbf{M}}_g + 12\dot{\mathbf{M}}_2 \bar{\mathbf{M}}_2^\dagger + 12\dot{\mathbf{M}}_2^\dagger \bar{\mathbf{M}}_2 \right) \\ & + 4\alpha_0^2 \left(2\dot{\mathbf{M}}_1 \dot{\mathbf{M}}_\gamma \bar{\mathbf{M}}_1^\dagger + \frac{1}{2}\dot{\mathbf{M}}_1 \dot{\mathbf{M}}_g \bar{\mathbf{M}}_1^\dagger + 2\dot{\mathbf{M}}_1^\dagger \dot{\mathbf{M}}_\gamma \bar{\mathbf{M}}_1 - \frac{1}{2}\dot{\mathbf{M}}_1^\dagger \dot{\mathbf{M}}_g \bar{\mathbf{M}}_1 \right. \\ & + \frac{1}{2}\dot{\mathbf{M}}_g \dot{\mathbf{M}}_1 \bar{\mathbf{M}}_1^\dagger - \frac{1}{2}\dot{\mathbf{M}}_g \dot{\mathbf{M}}_1^\dagger \bar{\mathbf{M}}_1 + \frac{1}{2}\dot{\mathbf{M}}_1 \dot{\mathbf{M}}_1^\dagger \bar{\mathbf{M}}_g - \frac{1}{2}\dot{\mathbf{M}}_1^\dagger \dot{\mathbf{M}}_1 \bar{\mathbf{M}}_g \\ & - 3\,\dot{\mathbf{M}}_1 \dot{\mathbf{M}}_1 \bar{\mathbf{M}}_2^\dagger + \dot{\mathbf{M}}_1 \dot{\mathbf{M}}_2^\dagger \bar{\mathbf{M}}_1 - 3\dot{\mathbf{M}}_2^\dagger \dot{\mathbf{M}}_1 \bar{\mathbf{M}}_1 \\ & \left. - 3\,\dot{\mathbf{M}}_2 \dot{\mathbf{M}}_1^\dagger \bar{\mathbf{M}}_1^\dagger + \dot{\mathbf{M}}_1^\dagger \dot{\mathbf{M}}_2 \bar{\mathbf{M}}_1^\dagger - 3\dot{\mathbf{M}}_1^\dagger \dot{\mathbf{M}}_1^\dagger \bar{\mathbf{M}}_2 + [S]_3 \right) \\ & + 4\alpha_0^3 \left(3\dot{\mathbf{M}}_1 \dot{\mathbf{M}}_1 \dot{\mathbf{M}}_1^\dagger \bar{\mathbf{M}}_1^\dagger + \dot{\mathbf{M}}_1 \dot{\mathbf{M}}_1^\dagger \dot{\mathbf{M}}_1 \bar{\mathbf{M}}_1^\dagger - \dot{\mathbf{M}}_1 \dot{\mathbf{M}}_1^\dagger \dot{\mathbf{M}}_1^\dagger \bar{\mathbf{M}}_1 \right. \\ & \left. + 3\dot{\mathbf{M}}_1^\dagger \dot{\mathbf{M}}_1^\dagger \dot{\mathbf{M}}_1 \bar{\mathbf{M}}_1 + \dot{\mathbf{M}}_1^\dagger \dot{\mathbf{M}}_1 \dot{\mathbf{M}}_1^\dagger \bar{\mathbf{M}}_1 - \dot{\mathbf{M}}_1^\dagger \dot{\mathbf{M}}_1 \dot{\mathbf{M}}_1 \bar{\mathbf{M}}_1^\dagger + [S]_4 \right), \end{aligned} \tag{3.156h}$$

$$\begin{aligned}\boldsymbol{\zeta}_a = {} & \alpha_0 \dot{\mathbf{M}}_2 \bar{\mathbf{M}}_2 - \alpha_0^2 \left(\dot{\mathbf{M}}_1 \dot{\mathbf{M}}_1 \bar{\mathbf{M}}_2 + \dot{\mathbf{M}}_1 \dot{\mathbf{M}}_2 \bar{\mathbf{M}}_1 + \dot{\mathbf{M}}_2 \dot{\mathbf{M}}_1 \bar{\mathbf{M}}_1 + [S]_3 \right) \\ & + \alpha_0^3 \left(\dot{\mathbf{M}}_1 \dot{\mathbf{M}}_1 \dot{\mathbf{M}}_1 \bar{\mathbf{M}}_1 + [S]_4 \right).\end{aligned} \tag{3.156i}$$

With the effective parameters (3.156) written down, it is now possible to write effective 2×2 Hamiltonians for specific η levels and H levels by reading the matrix elements in (3.156) within the subspace corresponding to the subband of interest. For instance, the matrix $\boldsymbol{\beta}_1 = \alpha_0 \mathbf{M}_1 \odot \mathbf{I}$, where $\mathbf{M}_1$ consists of diagonal blocks shifted towards the right [see (3.93)]. The terms $\mathbf{T}^{\mathrm{x}}$ do not contribute to β_1 since they do not overlap with non-zero matrix elements of $\mathbf{I}$ [see (3.144)]. However, the terms $\mathbf{T}^{\eta}$ located in the σ_+ subspace of η levels ($\sigma_\pm = (\sigma_x \pm i\sigma_y)/2$) and the terms $\mathbf{T}^{\mathrm{H}}$ located in the σ_- subspace of H levels do contribute to $\mathbf{H}_{\text{eff}}$. The β_1 parameter for the ηj level and for the Hl level is therefore:

$$\beta_1^{\eta j} = \alpha_0 T^{\eta}_{j,j}, \tag{3.157a}$$

$$\beta_1^{\mathrm{H}l} = \alpha_0 T^{\mathrm{H}}_{l,l}. \tag{3.157b}$$

On the other hand, the g-factor $\mathbf{g}_\perp$ is a diagonal block matrix, since $\mathbf{M}_g$ is block diagonal and the products $\dot{\mathbf{M}}_1^\dagger \bar{\mathbf{M}}_1$ are as well. Additionally, the matrix element of $\mathbf{g}_\perp$ in the $\sigma_+\sigma_-$ subspace of either η or H has opposite sign with respect to that in the $\sigma_-\sigma_+$ subspace. The $g_\perp$ term in the final 2×2 effective Hamiltonian will therefore multiply a σ_z operator.

The final effective 2×2 Hamiltonian for η or H levels in a perpendicular-to-plane $\mathbf{B}$-field is

$$\begin{aligned}H^\tau_{\text{eff}} = {} & E^\tau + \alpha_0 \left(\gamma^\tau + \frac{\chi^\tau_\perp}{2l_B^2} \sigma_z \right) K_\parallel^2 + \frac{\alpha_0}{2l_B^2} g^\tau_\perp \sigma_z + \alpha_0 \zeta^\tau_\gamma K_\parallel^4 + \frac{\alpha_0}{4l_B^4} \zeta^\tau_\perp \\ & + \left[i\beta^\tau_1 K_- \sigma_\tau - i\beta^\tau_2 K_+^3 \sigma_\tau + i\beta^\tau_3 K_- K_+ K_- \sigma_\tau + \alpha_0 \zeta^\tau_a K_-^4 + \text{H.c.} \right],\end{aligned} \tag{3.158}$$

where in the σ operators, $\tau = \pm 1$ for η and H levels respectively. The three Rashba spin-orbit effects give rise to a spin-quantization whose amplitude is determined by β_i^τ times a power law in K and whose orientation is determined by the direction of in-plane motion ϕ and a winding number. Table 3.5 gives an overview of Rashba SOC for η and H levels. The spin orientation refers to the state of lowest energy (closer to the bandgap). It is important to note that if $B = 0$, Rashba SOC does not break time-reversal symmetry; the energy dispersion would still have a Kramers degeneracy $E_+(\mathbf{k}_\parallel) = E_-(-\mathbf{k}_\parallel)$.

Table 3.5 Rashba SOC in quantum wells. k and ϕ are defined by $k_+ = ke^{i\phi}$. $\beta_i^\tau > 0$.

Type	Amplitude	Winding #	Spin orientation	
			η	H
β_1^τ	$\sim k$	1	$\phi - \pi/2$	$\pi/2 - \phi$
β_2^τ	$\sim k^3$	3	$\pi/2 - 3\phi$	$3\phi - \pi/2$
β_3^τ	$\sim k^3$	1	$\phi - \pi/2$	$\pi/2 - \phi$

3.3.6 Key results and the particular case of the LK Hamiltonian

The parameters γ, $g_\perp$, and the Rashba $\beta_{1,2,3}$ parameters are arguably one of the most relevant when discussing the dynamics of charge carriers in quantum wells. It is instructive to investigate their behavior with respect to key characteristics of the heterostructure and the material system. This may also provide some physical intuition behind the set of equations (3.156), which might appear quite opaque at first glance. To facilitate the discussion, and unless specified otherwise, we work within the framework of the 4×4 Luttinger-Kohn Hamiltonian, where most expressions in (3.156) become quite simple. In addition, we assume infinite energy band offsets between the QW and the barrier materials. Within these approximations, the envelope functions corresponding to the conduction band $|c\rangle$ and the split-off hole band $|s\rangle$ exactly vanish. Moreover, boundary conditions imposed by the infinite band offsets fix the value of the envelopes to zero at the interfaces. Assuming that the QW is made of a single material, any material parameter γ within the well is constant with z, and therefore $[\gamma, k_z] = 0$.

Expanding the effective mass matrix $\boldsymbol{\gamma}$ gives:

$$\boldsymbol{\gamma} = \bar{\mathbf{M}}_\gamma + \alpha_0 \left(\dot{\mathbf{M}}_1 \bar{\mathbf{M}}_1^\dagger + \dot{\mathbf{M}}_1^\dagger \bar{\mathbf{M}}_1 \right) \tag{3.159a}$$

$$\begin{aligned} &= \begin{bmatrix} \bar{\boldsymbol{\Gamma}}_\parallel^{\mathrm{H}} & & & \\ & \bar{\boldsymbol{\Gamma}}_\parallel^{\eta} & & \\ & & \bar{\boldsymbol{\Gamma}}_\parallel^{\eta} & \\ & & & \bar{\boldsymbol{\Gamma}}_\parallel^{\mathrm{H}} \end{bmatrix} \\ &+ \alpha_0 \begin{bmatrix} \dot{\mathbf{T}}^{\mathrm{x}} \bar{\mathbf{T}}^{\mathrm{x}\dagger} & & & \\ & \dot{\mathbf{T}}^{\eta} \bar{\mathbf{T}}^{\eta} & & \\ & & \dot{\mathbf{T}}^{\mathrm{x}\dagger} \bar{\mathbf{T}}^{\mathrm{x}} & \\ & & & \dot{\mathbf{T}}^{\mathrm{H}} \bar{\mathbf{T}}^{\mathrm{H}} \end{bmatrix} + \alpha_0 \begin{bmatrix} \dot{\mathbf{T}}^{\mathrm{H}} \bar{\mathbf{T}}^{\mathrm{H}} & & & \\ & \dot{\mathbf{T}}^{\mathrm{x}\dagger} \bar{\mathbf{T}}^{\mathrm{x}} & & \\ & & \dot{\mathbf{T}}^{\eta} \bar{\mathbf{T}}^{\eta} & \\ & & & \dot{\mathbf{T}}^{\mathrm{x}} \bar{\mathbf{T}}^{\mathrm{x}\dagger} \end{bmatrix}. \end{aligned} \tag{3.159b}$$

Similarly, expanding the $\mathbf{g}_\perp$ matrix gives:

$$\boldsymbol{\gamma} = \bar{\mathbf{M}}_g + 2\alpha_0 \left(\dot{\mathbf{M}}_1 \bar{\mathbf{M}}_1^\dagger - \dot{\mathbf{M}}_1^\dagger \bar{\mathbf{M}}_1 \right) \tag{3.160a}$$

$$\begin{aligned} &= \begin{bmatrix} \bar{\mathbf{G}}_\perp^{\mathrm{H}} & & & \\ & \bar{\mathbf{G}}_\perp^{\eta} & & \\ & & -\bar{\mathbf{G}}_\perp^{\eta} & \\ & & & -\bar{\mathbf{G}}_\perp^{\mathrm{H}} \end{bmatrix} \\ &+ 2\alpha_0 \begin{bmatrix} \dot{\mathbf{T}}^{\mathrm{x}} \bar{\mathbf{T}}^{\mathrm{x}\dagger} & & & \\ & \dot{\mathbf{T}}^{\eta} \bar{\mathbf{T}}^{\eta} & & \\ & & \dot{\mathbf{T}}^{\mathrm{x}\dagger} \bar{\mathbf{T}}^{\mathrm{x}} & \\ & & & \dot{\mathbf{T}}^{\mathrm{H}} \bar{\mathbf{T}}^{\mathrm{H}} \end{bmatrix} - 2\alpha_0 \begin{bmatrix} \dot{\mathbf{T}}^{\mathrm{H}} \bar{\mathbf{T}}^{\mathrm{H}} & & & \\ & \dot{\mathbf{T}}^{\mathrm{x}\dagger} \bar{\mathbf{T}}^{\mathrm{x}} & & \\ & & \dot{\mathbf{T}}^{\eta} \bar{\mathbf{T}}^{\eta} & \\ & & & \dot{\mathbf{T}}^{\mathrm{x}} \bar{\mathbf{T}}^{\mathrm{x}\dagger} \end{bmatrix}. \end{aligned} \tag{3.160b}$$

From these expressions, the effective mass and the g-factor for the ηj level and Hl level respectively immediately follow:

$$\gamma^{\eta} = \Gamma^{\eta}_{\parallel;j,j} + \alpha_0 \left(\sum_l \frac{T^{\mathrm{x}*}_{l,j} T^{\mathrm{x}}_{l,j}}{E^{\eta}_j - E^{\mathrm{H}}_l} + \sum_{j' \neq j} \frac{T^{\eta}_{j,j'} T^{\eta}_{j',j}}{E^{\eta}_j - E^{\eta}_{j'}} \right), \tag{3.161}$$

$$\begin{aligned} \gamma^{\mathrm{H}} &= \Gamma^{\mathrm{H}}_{\parallel;l,l} + \alpha_0 \left(\sum_j \frac{T^{\mathrm{x}}_{l,j} T^{\mathrm{x}*}_{l,j}}{E^{\mathrm{H}}_l - E^{\eta}_j} + \sum_{l' \neq l} \frac{T^{\mathrm{H}}_{l,l'} T^{\mathrm{H}}_{l',l}}{E^{\mathrm{H}}_l - E^{\mathrm{H}}_{l'}} \right) \\ &\approx \Gamma^{\mathrm{H}}_{\parallel;l,l} + \alpha_0 \sum_j \frac{T^{\mathrm{x}}_{l,j} T^{\mathrm{x}*}_{l,j}}{E^{\mathrm{H}}_l - E^{\eta}_j}, \end{aligned} \tag{3.162}$$

and

$$g^{\eta}_\perp = G^{\eta}_{\perp;j,j} - 2\alpha_0 \left(\sum_l \frac{T^{\mathrm{x}*}_{l,j} T^{\mathrm{x}}_{l,j}}{E^{\eta}_j - E^{\mathrm{H}}_l} - \sum_{j' \neq j} \frac{T^{\eta}_{j,j'} T^{\eta}_{j',j}}{E^{\eta}_j - E^{\eta}_{j'}} \right), \tag{3.163}$$

$$\begin{aligned} g^{\mathrm{H}}_\perp &= G^{\mathrm{H}}_{\perp;l,l} + 2\alpha_0 \left(\sum_j \frac{T^{\mathrm{x}}_{l,j} T^{\mathrm{x}*}_{l,j}}{E^{\mathrm{H}}_l - E^{\eta}_j} - \sum_{l' \neq l} \frac{T^{\mathrm{H}}_{l,l'} T^{\mathrm{H}}_{l',l}}{E^{\mathrm{H}}_l - E^{\mathrm{H}}_{l'}} \right) \\ &\approx G^{\mathrm{H}}_{\perp;l,l} + 2\alpha_0 \sum_j \frac{T^{\mathrm{x}}_{l,j} T^{\mathrm{x}*}_{l,j}}{E^{\mathrm{H}}_l - E^{\eta}_j}. \end{aligned} \tag{3.164}$$

where in the second line of (3.162) and (3.164) the small cubic-in-J correction to the g-factor is neglected ($T^{\mathrm{H}} \to 0$). For H levels, subtracting half of (3.164) from (3.162) eliminates the sum on j. After inserting the definitions (3.93), the well-known formula that relates the effective mass and the g-factor [58] is recovered:

$$\frac{g^{\mathrm{H}}}{2} = \gamma_1 + \gamma_2 - 3\kappa + \gamma^{\mathrm{H}}. \tag{3.165}$$

Expanding (3.161)–(3.164) a bit more also reveals

$$\gamma^{\eta} = -(\gamma_1 - \gamma_2) + 12\alpha_0\gamma_3^2 \langle \ell_j | \, k_z \rho_j^{\eta} k_z \, | \ell_j \rangle \,, \tag{3.166}$$

$$\gamma^{\mathrm{H}} = -(\gamma_1 + \gamma_2) + 12\alpha_0\gamma_3^2 \langle h_l | \, k_z \rho_l^{\mathrm{H}} k_z \, | h_l \rangle \,, \tag{3.167}$$

$$g_{\perp}^{\eta} = -2\kappa - 24\alpha_0\gamma_3^2 \langle \ell_j | \, k_z \rho_j^{\eta} k_z \, | \ell_j \rangle \,, \tag{3.168}$$

$$g_{\perp}^{\mathrm{H}} = -6\kappa + 24\alpha_0\gamma_3^2 \langle h_l | \, k_z \rho_l^{\mathrm{H}} k_z \, | h_l \rangle \,, \tag{3.169}$$

where

$$\rho_j^{\eta} = \sum_l \frac{|h_l\rangle \langle h_l|}{E_j^{\eta} - E_l^{\mathrm{H}}}, \tag{3.170}$$

$$\rho_l^{\mathrm{H}} = \sum_j \frac{|\ell_j\rangle \langle \ell_j|}{E_l^{\mathrm{H}} - E_j^{\eta}}. \tag{3.171}$$

The well-known formulas for the masses and g-factors for η and H subbands are recovered if the ρ_j^{τ}-terms are neglected. However, the latter introduce important corrections to what would otherwise be merely *first order* approximations for the effective mass and g-factor. The second order corrections are inversely proportional to the energy difference, and directly proportional to the wavefunction overlap with neighboring levels. Note that the wavefunction overlap is stronger between levels of opposite parity, since $\mathbf{T}^{\mathrm{x}}$ and $\mathbf{T}^{\tau}$ involve k_z operators [see (3.93)]. As a general rule, the appearance of $\mathbf{M}_1$ inside a perturbative expansion indicates that opposite-parity η-η, η-H or H-H linear-in-K mixing has a contribution to the effective parameter, while the appearance of an $\mathbf{M}_2$ term indicates a contribution from same-parity quadratic-in-K mixing.

For the β_1^{η} parameter, a 4-band LK formula gives exactly $\beta_1^{\eta} = 0$ regardless of the QW

symmetry. A linear Rashba parameter only arises if envelopes are allowed to spread into barriers, owing to non-zero commutators $[\kappa, k_z]$ and $[q, k_z]$ in $\mathbf{T}$ matrices. Another way is to introduce the split-off band to the η spinor, in which case we get the following (assuming infinite band offsets):

$$\beta_1^{\eta} = -6\sqrt{2}\alpha_0\gamma_3\Im\left\{\langle \ell_j |\, k_z\, | s_j\rangle\right\}. \tag{3.172}$$

The bra-ket product $\langle \ell_j |\, k_z\, | s_j\rangle \neq 0$ only if

$$f^s(z) \neq C f^{\ell}(z), \tag{3.173}$$

where C is any scalar. In particular, the bra-ket is zero if $f^{\ell}(z)$ and $f^s(z)$ share the same parity. A necessary requirement for (3.173) is $\gamma_2 \neq 0$ [see (3.84)]. It should be noted that there is an implicit $1/\Delta_0$ dependence in (3.172) hidden within the $f^s(z)$ envelope function: for large Δ_0, the SO contribution in the LH-like η level becomes increasingly small. Recalling (3.87), the LH bra-ket $\langle \ell_j | \ell_j\rangle \to 1$, while $\langle s_j | s_j\rangle \sim 1/\Delta_0^2$, and therefore $\langle \ell_j | s_j\rangle \sim 1/\Delta_0$ (see Appendix A as well). On the other hand, in the case $\Delta_0 = 0$ (no SOC), (3.84) shares its eigenstates with those of L_z. Rewriting the $|j, m_j\rangle$ Bloch functions (3.79a) in terms of the orbital eigenstates $|l = 1, m_l\rangle \equiv |m_l\rangle$ of L_z:

$$|1\rangle = -\frac{1}{\sqrt{2}}\left(|X\rangle + i\,|Y\rangle\right), \tag{3.174a}$$

$$|0\rangle = |Z\rangle, \tag{3.174b}$$

$$|{-1}\rangle = \frac{1}{\sqrt{2}}\left(|X\rangle - i\,|Y\rangle\right), \tag{3.174c}$$

and inserting into (3.85) for η levels gives

$$|\eta{+}; j\rangle = \sqrt{\frac{2}{3}}\,|0, +\rangle\left(|\ell_j\rangle - |s_j\rangle/\sqrt{2}\right) + \frac{1}{\sqrt{3}}\,|1, -\rangle\left(|\ell_j\rangle + \sqrt{2}\,|s_j\rangle\right), \tag{3.175a}$$

$$|\eta{-}; j\rangle = \sqrt{\frac{2}{3}}\,|0, -\rangle\left(|\ell_j\rangle - |s_j\rangle/\sqrt{2}\right) + \frac{1}{\sqrt{3}}\,|{-1}, +\rangle\left(|\ell_j\rangle + \sqrt{2}\,|s_j\rangle\right). \tag{3.175b}$$

(3.175) diagonalizes (3.84) for any Δ_0 with properly chosen $|\ell_j\rangle$ and $|s_j\rangle$ and must also diagonalize L_z if $\Delta_0 = 0$. To fulfill the latter case, one of the two parentheses must vanish,

thereby forcing $|\ell_j\rangle = C\,|s_j\rangle$, which violates criterion (3.173) and implies $\beta_1^\eta = 0$. Note that β_1^η does not involve any levels other than ηj itself (the components $|\ell_j\rangle$ and $|s_j\rangle$ belong to the *same* ηj spinor of energy E_j^η).

Within the 4-band LK Hamiltonian, 1st and 3rd order perturbation terms do not contribute to any of the cubic Rashba parameters $\beta_{2,3}^\tau$. 2nd order terms give:

$$\beta_2^\eta = 3i\alpha_0^2\,(\gamma_2 - \gamma_3)\,\gamma_3\,\langle \ell_j|\left[k_z, \rho_j^\eta\right]|\ell_j\rangle\,, \tag{3.176}$$

$$\beta_2^{\mathrm{H}} = -3i\alpha_0^2\,(\gamma_2 + \gamma_3)\,\gamma_3\,\langle h_l|\left[k_z, \rho_l^{\mathrm{H}}\right]|h_l\rangle\,, \tag{3.177}$$

$$\beta_3^\eta = -3i\alpha_0^2\,(\gamma_2 + \gamma_3)\,\gamma_3\,\langle \ell_j|\left[k_z, \rho_j^\eta\right]|\ell_j\rangle\,, \tag{3.178}$$

$$\beta_3^{\mathrm{H}} = 3i\alpha_0^2\,(\gamma_2 - \gamma_3)\,\gamma_3\,\langle h_l|\left[k_z, \rho_l^{\mathrm{H}}\right]|h_l\rangle\,. \tag{3.179}$$

As expected for H subbands, β_2^{H} is proportional to $\gamma_2+\gamma_3$ while β_3^{H} is proportional to $\gamma_2-\gamma_3$. In the axial approximation, $\beta_3^{\mathrm{H}} = 0$, thus yielding isotropic dispersions. The reverse is true for η subbands; isotropic dispersions come from $\beta_2^\eta = 0$ in the axial approximation. On a related note, the anisotropy parameter ζ_a^τ is described exactly by 2nd order perturbation in the LK model. It vanishes for both η and H levels if $\gamma_2 = \gamma_3$:

$$\zeta_a^\eta = \frac{3\alpha_0}{4}\,\langle \ell_j|\,\gamma_2\rho_j^\eta\gamma_2 - \gamma_3\rho_j^\eta\gamma_3\,|\ell_j\rangle\,, \tag{3.180}$$

$$\zeta_a^{\mathrm{H}} = \frac{3\alpha_0}{4}\,\langle h_l|\,\gamma_2\rho_l^{\mathrm{H}}\gamma_2 - \gamma_3\rho_l^{\mathrm{H}}\gamma_3\,|h_l\rangle\,. \tag{3.181}$$

3.4 The 8-band $k\cdot p$ Hamiltonian with in-plane confinement ($A_z \neq 0$ gauge)

In the next few subsections, we introduce in-plane confinement through the potential function $V_\parallel(x,y)$. For simplicity, we assume that such confinement is provided by means of electrostatic potentials, where the field is generated by applying a DC voltage through an arrangement of electrostatic gates deposited at the surface of the heterostructure. We will consider the case of quantum channels (2D confinement, or 1 degree of freedom) and quantum dot systems (3D confinement, or no degrees of freedom). In all cases, we assume that material parameters are constant in the QW plane, and that the in-plane confinement profile is parabolic.

If in-plane confinement is absent, x and y operators in the vector potential must be avoided since they introduce unnecessary Hilbert spaces to a problem that should only involve the z-dimension. When in-plane confinement is present, in-plane Hilbert spaces must be introduced

in the framework. An ideal gauge therefore replaces all z-operator dependence with x and/or y operators, thus removing the complications of gauge invariance related with the average value $\langle z \rangle$. An arbitrarily oriented magnetic field $\mathbf{B}$ with magnitude B and orientation (θ, ϕ) is described by the following vector potential:

$$\mathbf{A} = B\cos\theta\left(-y\sin^2\Lambda\mathbf{e}_x + x\cos^2\Lambda\mathbf{e}_y\right) - Br_\phi\sin\theta\mathbf{e}_z, \tag{3.182}$$

where Λ is a gauge parameter that has no effects on $\mathbf{B}$ and $r_\phi = x\sin\phi - y\cos\phi$. Depending on the type of in-plane confinement, Λ may be chosen such that some operators disappear from the vector potential. Performing the Peierls substitution with (3.182), inserting into (3.64) and projecting onto the QW subband edge basis $\mathcal{B}_0$ gives

$$\begin{aligned}\mathbf{H} = \mathbf{E}_0^{\mathrm{QW}} &+ \alpha_0\left[\mathbf{M}_\gamma K_\parallel^2 + \frac{\cos\theta}{2l_B^2}\mathbf{M}_g + \frac{\sin\theta}{l_B^2}\left(\frac{\sin\theta}{l_B^2}\mathbf{N}_\gamma r_\phi^2 - \mathbf{N}'_\gamma r_\phi\right)\right] \\ &+ i\alpha_0\left[i\mathbf{M}_1 K_- + \mathbf{M}_2 K_-^2 + \frac{\sin\theta}{l_B^2}\left(\frac{e^{-i\phi}}{2}\mathbf{N}_g + i\mathbf{N}_1\left\{r_\phi, K_-\right\}\right) + \mathrm{H.c.}\right] - \alpha_0\left(\frac{x^2}{l_x^4} + \frac{y^2}{l_y^4}\right).\end{aligned} \tag{3.183}$$

Hamiltonian (3.183) reduces to (3.104) in the limit $l_{x,y} \to \infty$ and $\theta = 0$. The l_x and l_y parameters are characteristic lengths for the in-plane confinement. The additional terms r_ϕ and $\mathbf{N}$ matrices arise from the $A_z \neq 0$ component of the vector potential. In-plane components of $\mathbf{A}$ are still contained within the in-plane components of the mechanical wavevector $\mathbf{K}$. A minus sign is required in the potential energy for hole confinement. The $\mathbf{N}$ matrices are the following:

$$\mathbf{N}_\gamma = \begin{bmatrix} \boldsymbol{\Gamma}_\perp^{\mathrm{H}} & 0 & 0 & 0 \\ & \boldsymbol{\Gamma}_\perp^{\eta} & 0 & 0 \\ \dagger & & \boldsymbol{\Gamma}_\perp^{\eta} & 0 \\ & & & \boldsymbol{\Gamma}_\perp^{\mathrm{H}} \end{bmatrix}, \qquad \mathbf{N}'_\gamma = \begin{bmatrix} \boldsymbol{\Gamma}_\perp'^{\mathrm{H}} & 0 & 0 & 0 \\ & \boldsymbol{\Gamma}_\perp'^{\eta} & 0 & 0 \\ \dagger & & \boldsymbol{\Gamma}_\perp'^{\eta} & 0 \\ & & & \boldsymbol{\Gamma}_\perp'^{\mathrm{H}} \end{bmatrix}, \tag{3.184a}$$

$$\mathbf{N}_g = \begin{bmatrix} 0 & \mathbf{G}_\parallel^{\mathrm{x}} & 0 & 0 \\ 0 & 0 & \mathbf{G}_\parallel^{\eta} & 0 \\ 0 & 0 & 0 & \mathbf{G}_\parallel^{\mathrm{x}\dagger} \\ \mathbf{G}_\parallel^{\mathrm{H}} & 0 & 0 & 0 \end{bmatrix}, \qquad \mathbf{N}_1 = \begin{bmatrix} 0 & \mathbf{R}^{\mathrm{x}} & 0 & 0 \\ 0 & 0 & \mathbf{R}^{\eta} & 0 \\ 0 & 0 & 0 & \mathbf{R}^{\mathrm{x}\dagger} \\ 0 & 0 & 0 & 0 \end{bmatrix}, \tag{3.184b}$$

where

$$\mathbf{\Gamma}_{\perp}^{\eta} = \langle c|\gamma_c|c\rangle - \frac{1}{3}\langle +|\gamma_1 - 2\gamma_2|+\rangle - \frac{2}{3}\langle -|\gamma_1 + 4\gamma_2|-\rangle\,, \tag{3.185a}$$

$$\begin{aligned}\mathbf{\Gamma}_{\perp}^{\prime\eta} = \langle c|\{\gamma_c, k_z\}|c\rangle + i\sqrt{\frac{2}{3}}\left(\langle c|c_p|-\rangle - \langle -|c_p|c\rangle\right) \\ - \frac{1}{3}\langle +|\{\gamma_1 - 2\gamma_2, k_z\}|+\rangle - \frac{2}{3}\langle -|\{\gamma_1 + 4\gamma_2, k_z\}|-\rangle\,,\end{aligned} \tag{3.185b}$$

$$\mathbf{\Gamma}_{\perp}^{\mathrm{H}} = -\langle h|\gamma_1 - 2\gamma_2|h\rangle\,, \tag{3.185c}$$

$$\mathbf{\Gamma}_{\perp}^{\prime\mathrm{H}} = -\langle h|\{\gamma_1 - 2\gamma_2, k_z\}|h\rangle\,, \tag{3.185d}$$

$$\mathbf{G}_{\parallel}^{\mathrm{x}} = -2\sqrt{3}\langle h|\left(\kappa\,|-\rangle + \frac{7}{4}q\,|\ell\rangle - \frac{1}{\sqrt{2}}\,|s\rangle\right), \tag{3.185e}$$

$$\mathbf{G}_{\parallel}^{\eta} = \langle c|g|c\rangle - 2\langle +|\kappa|-\rangle - 2\langle -|\kappa|+\rangle - 10\langle \ell|q|\ell\rangle - \sqrt{2}\left(\langle -|s\rangle + \langle s|-\rangle\right), \tag{3.185f}$$

$$\mathbf{G}_{\parallel}^{\mathrm{H}} = -3\langle h|q|h\rangle\,, \tag{3.185g}$$

$$\mathbf{R}^{\mathrm{x}} = i\sqrt{3}\langle h|\gamma_3|-\rangle\,, \tag{3.185h}$$

$$\mathbf{R}^{\eta} = i\left(\langle +|\gamma_3|-\rangle - \langle -|\gamma_3|+\rangle\right). \tag{3.185i}$$

As in (3.93), the j and l indices are omitted for clarity.

3.4.1 The quantum channel Hamiltonian

A quantum channel is a device in which charge carriers are allowed to move freely only in one direction (say y). The two dimensions of confinement are provided by (a) the QW heterostructure and (b) by electrostatic gates with associated potential

$$V_{\parallel}(x) = -\frac{\alpha_0}{l_x^4}x^2. \tag{3.186}$$

l_x is a characteristic length to quantify the strength of in-plane confinement (as felt by an electron of mass m_0). This length is not necessarily the physical distance between the gates on the actual device. l_x is used instead as an abstraction of experimental details including the shape of the gates, the distance between the gates and the QW, and on the applied voltage. A full numerical 3D simulation could provide an estimation of l_x from a given gate pattern, but the approach here is to simply take l_x as a free parameter. By Laplace's equation, the DC field provided by the gate stack also includes an out-of-plane component, which is simply merged with the out-of-plane field parameter F_z. For simplicity, we also assume that the magnetic field has no x component, which would otherwise introduce an unwanted y operator into the z-component of $\mathbf{A}$. The y operator in the x-component of $\mathbf{A}$ is removed by

setting $\Lambda = 0$.

In analogy with the quantum well system, a subband edge basis $\mathcal{B}_0^{\mathrm{QC}}$ is constructed by diagonalizing the quantum channel Hamiltonian $\mathbf{H}_0^{\mathrm{QC}}$, which is given by (3.183) with $k_y = 0$ and $B = 0$:

$$\mathbf{H}_0^{\mathrm{QC}} = \mathbf{E}_0^{\mathrm{QW}} + \alpha_0 \left[\left(\mathbf{M}_\gamma + \mathbf{M}_2 + \mathbf{M}_2^\dagger \right) k_x^2 + i \left(\mathbf{M}_1 - \mathbf{M}_1^\dagger \right) k_x \right] - \frac{\alpha_0}{l_x^4} x^2. \tag{3.187}$$

Eigenstates of this Hamiltonian are denoted $|\varsigma; i, N\rangle$. Here, $\varsigma = \uparrow, \downarrow$ is a pseudo-spin quantum number for the channel subbands, i is an out-of-plane quantum number and N is an in-plane quantum number. The energy associated with $|\varsigma; i, N\rangle$ is denoted $E^c_{i,N}$, and is ς-independent. The kets $|\varsigma; i, N\rangle$ can be expanded as a linear combination of QW and in-plane basis states:

$$|\varsigma; i, N\rangle = \sum_{\tau,\sigma} \sum_{j,n} c_{\tau\sigma,j,n} \, |\tau\sigma; j\rangle \, |n\rangle \, : \, \begin{bmatrix} \mathbf{c}^\varsigma_{\mathrm{H}+} \\ \mathbf{c}^\varsigma_{\eta+} \\ \mathbf{c}^\varsigma_{\eta-} \\ \mathbf{c}^\varsigma_{\mathrm{H}-} \end{bmatrix}, \tag{3.188}$$

where $\mathbf{c}^\varsigma_{\tau\sigma}$ are $N_\tau N_x$-element vectors, with N_x the number of $|n\rangle$ levels in the in-plane basis. As with the quantum well case, it is possible to diagonalize $\mathbf{H}_0^{\mathrm{QC}}$ only for the $\varsigma = \uparrow$ subbands, with the degenerate time-reversed partners $\varsigma = \downarrow$ simply constructed from the $\varsigma = \uparrow$ levels. The strategy starts by first expanding the $\mathbf{M}$'s in $\mathbf{H}_0^{\mathrm{QC}}$ to get the following matrix:

$$\mathbf{H}_0^{\mathrm{QC}} = \mathbf{E}_0^{\mathrm{QW}} + \alpha_0 \begin{bmatrix} \mathbf{\Gamma}^{\mathrm{H}}_\parallel k_x^2 & i\mathbf{T}^{\mathrm{x}} k_x & \boldsymbol{\mu} k_x^2 & -i\mathbf{T}^{\mathrm{H}} k_x \\ -i\mathbf{T}^{\mathrm{x}\dagger} k_x & \mathbf{\Gamma}^{\eta}_\parallel k_x^2 & i\mathbf{T}^{\eta} k_x & \boldsymbol{\mu}^\dagger k_x^2 \\ \boldsymbol{\delta}^\dagger k_x^2 & -i\mathbf{T}^{\eta} k_x & \mathbf{\Gamma}^{\eta}_\parallel k_x^2 & i\mathbf{T}^{\mathrm{x}\dagger} k_x \\ i\mathbf{T}^{\mathrm{H}} k_x & \boldsymbol{\delta} k_x^2 & -i\mathbf{T}^{\mathrm{x}} k_x & \mathbf{\Gamma}^{\mathrm{H}}_\parallel k_x^2 \end{bmatrix} - \frac{\alpha_0}{l_x^4} x^2. \tag{3.189}$$

Since the confining potential $V_\parallel(x)$ is symmetric on the x axis, the wavefunctions $\langle \mathbf{r} | \varsigma; i, N \rangle$ must be either symmetric (S) or antisymmetric (A) with respect to the transformation $x \to -x$. Since even powers of x or k_x are symmetric, odd powers of x and k_x are antisymmetric, and from the structure of $\mathbf{H}_0^{\mathrm{QC}}$, the four $\tau\sigma$ subspaces of an eigenstate of $\mathbf{H}_0^{\mathrm{QC}}$ must have x-symmetry "SASA" or "ASAS". Noting that every element from the first group is in one-to-one correspondence (and degenerate) with an element from the second group, we can identify $\varsigma = \uparrow, \downarrow$ with "ASAS" and "SASA" respectively[4]. It is natural to introduce the ladder operator

[4]This is a convention; the opposite would work as well, but at the cost of g-factors with opposite sign compared to (3.163) and (3.164) in the limit $l_x \to \infty$.

$$a = \frac{1}{\sqrt{2}}\left(\frac{x}{l_x} + il_x k_x\right), \tag{3.190}$$

such that $\left[a, a^\dagger\right] = 1$ and $a^\dagger a\,|n\rangle = n\,|n\rangle$. Projecting the x and k_x operators in $\mathbf{H}_0^{\mathrm{QC}}$ onto the basis $|n\rangle$, and eliminating the subspaces that are incompatible with the "ASAS" symmetry (even n in H+ subspace, and so on) results in a $\varsigma =\uparrow$ Hamiltonian of dimension $N_\perp N_x \times N_\perp N_x$. The $N_\perp N_x$ other $\varsigma =\downarrow$ subbands are constructed from the $\varsigma =\uparrow$ eigenstates with

$$|\uparrow; i, N\rangle : \begin{bmatrix} \mathbf{c}_{\mathrm{H}+} \\ \mathbf{c}_{\eta+} \\ \mathbf{c}_{\eta-} \\ \mathbf{c}_{\mathrm{H}-} \end{bmatrix}, \qquad |\downarrow; i, N\rangle : \begin{bmatrix} \mathbf{c}_{\mathrm{H}-} \\ -\mathbf{c}_{\eta-} \\ \mathbf{c}_{\eta+} \\ -\mathbf{c}_{\mathrm{H}+} \end{bmatrix}. \tag{3.191}$$

The QC subband edge basis $\mathcal{B}_0^{\mathrm{QC}}$ is constructed by collecting $N_\parallel$ $\varsigma =\uparrow$ subbands and the corresponding $N_\parallel$ $\varsigma =\downarrow$ subbands close in energy to a set of QC subbands of interest. Similarly to the QW problem, the size of $\mathcal{B}_0^{\mathrm{QC}}$ is restricted to $2N_\perp N_x$, or $N_\parallel \leq N_\perp N_x$. The QC Hamiltonian away from $k_y = 0$ and $B = 0$ is obtained by projecting the remaining part of $\mathbf{H} - \mathbf{H}_0^{\mathrm{QC}}$ onto $\mathcal{B}_0^{\mathrm{QC}}$. The result is a $2N_\parallel \times 2N_\parallel$ matrix

$$\mathbf{H}^{\mathrm{QC}} = \mathbf{E}_0^{\mathrm{QC}} + \alpha_0\left(\mathbf{L}_1 k_y + \mathbf{L}_\gamma k_y^2 + \frac{1}{2l_B^2}\mathbf{L}_g + \frac{1}{2l_B^2}\mathbf{L}_3 k_y + \frac{1}{4l_B^4}\mathbf{L}_4\right), \tag{3.192}$$

where $\mathbf{E}_0^{\mathrm{QC}}$ is the diagonal matrix of energies $E_{i,N}^c$:

$$\mathbf{E}_0^{\mathrm{QC}} = \begin{bmatrix} \mathbf{E}^c & 0 \\ 0 & \mathbf{E}^c \end{bmatrix}, \tag{3.193}$$

and $\mathbf{E}^c = \mathrm{diag}\{E_{1,0}^c, E_{1,1}^c, \ldots, E_{2,0}^c, E_{2,1}^c, \ldots\}$. A few $\mathbf{L}$ matrices are further expanded:

$$\mathbf{L}_g = \mathbf{L}_{g\perp}\cos\theta + \mathbf{L}_{g\parallel}\sin\theta, \tag{3.194a}$$

$$\mathbf{L}_3 = \mathbf{L}_{3\perp}\cos\theta + \mathbf{L}_{3\parallel}\sin\theta, \tag{3.194b}$$

$$\mathbf{L}_4 = \mathbf{L}_{4\perp}\cos^2\theta + \mathbf{L}_{4\parallel}\sin^2\theta + \mathbf{L}_{4\times}\sin\theta\cos\theta. \tag{3.194c}$$

All $\mathbf{L}$ matrices have simple block structures inherited from the symmetry-based classification

of $\varsigma = \uparrow, \downarrow$:

$$\mathbf{L}_1 = \mathbf{T}^c\varsigma_1 = \langle \varsigma; i, N| \, \mathbf{m}_1 - 2\mathbf{m}_2 k_x \, |\varsigma'; i', N'\rangle \,, \tag{3.195a}$$

$$\mathbf{L}_\gamma = \mathbf{\Gamma}^c\varsigma_0 = \langle \varsigma; i, N| \, \mathbf{m}_0 \, |\varsigma'; i', N'\rangle \,, \tag{3.195b}$$

$$\mathbf{L}_{g\perp} = \mathbf{G}^c_\perp\varsigma_3 = \langle \varsigma; i, N| \, \mathbf{M}_g + 2\mathbf{m}_1 x - 2\mathbf{m}_2\{x, k_x\} \, |\varsigma'; i', N'\rangle \,, \tag{3.195c}$$

$$\mathbf{L}_{g\parallel} = \mathbf{G}^c_\parallel\varsigma_2 = \langle \varsigma; i, N| \, \mathbf{n}_g - 2\mathbf{N}'_\gamma x + 2\mathbf{n}'_1\{x, k_x\} \, |\varsigma'; i', N'\rangle \,, \tag{3.195d}$$

$$\mathbf{L}_{3\perp} = \mathbf{\Xi}_\perp\varsigma_2 = 4\,\langle \varsigma; i, N| \, \mathbf{m}_0 x \, |\varsigma'; i', N'\rangle \,, \tag{3.195e}$$

$$\mathbf{L}_{3\parallel} = \mathbf{\Xi}_\parallel\varsigma_3 = 4\,\langle \varsigma; i, N| \, \mathbf{n}_1 x \, |\varsigma'; i', N'\rangle \,, \tag{3.195f}$$

$$\mathbf{L}_{4\perp} = \mathbf{Z}_\perp\varsigma_0 = 4\,\langle \varsigma; i, N| \, \mathbf{m}_0 x^2 \, |\varsigma'; i', N'\rangle \,, \tag{3.195g}$$

$$\mathbf{L}_{4\parallel} = \mathbf{Z}_\parallel\varsigma_0 = 4\,\langle \varsigma; i, N| \, \mathbf{N}_\gamma x^2 \, |\varsigma'; i', N'\rangle \,, \tag{3.195h}$$

$$\mathbf{L}_{4\times} = \mathbf{Z}_\times\varsigma_1 = 8\,\langle \varsigma; i, N| \, \mathbf{n}_1 x^2 \, |\varsigma'; i', N'\rangle \,, \tag{3.195i}$$

with ς_0 the 2×2 identity matrix and $\varsigma_{1,2,3}$ the Pauli matrices. The $\mathbf{m}$ and $\mathbf{n}$ matrices are

$$\mathbf{m}_0 = \mathbf{M}_\gamma - \mathbf{M}_2 - \mathbf{M}_2^\dagger, \tag{3.196a}$$

$$\mathbf{m}_1 = \mathbf{M}_1 + \mathbf{M}_1^\dagger, \tag{3.196b}$$

$$\mathbf{m}_2 = i(\mathbf{M}_2 - \mathbf{M}_2^\dagger), \tag{3.196c}$$

$$\mathbf{n}_g = -i(\mathbf{N}_g - \mathbf{N}_g^\dagger), \tag{3.196d}$$

$$\mathbf{n}_1 = \mathbf{N}_1 + \mathbf{N}_1^\dagger, \tag{3.196e}$$

$$\mathbf{n}'_1 = i(\mathbf{N}_1 - \mathbf{N}_1^\dagger). \tag{3.196f}$$

3.4.2 List of quantum channel parameters

A 2×2 effective Hamiltonian for a given quantum channel subband $|\varsigma; i, N\rangle$ is derived from an approach similar to the one described in Sec 3.3.5. The part in (3.192) with known eigenvalues and eigenvectors is the $\mathbf{E}_0^{\mathrm{QC}}$ term, while the perturbation $\mathbf{W}$ is given by:

$$\mathbf{W} = \alpha_0 \left(\mathbf{L}_1 k_y + \mathbf{L}_\gamma k_y^2 + \frac{1}{2l_B^2}\mathbf{L}_g + \frac{1}{2l_B^2}\mathbf{L}_3 k_y + \frac{1}{4l_B^4}\mathbf{L}_4 \right). \tag{3.197}$$

Performing a 4^{th} order SWT gives the following Hamiltonian:

$$
\begin{aligned}
H^c_{\text{eff}} = E^c + \alpha_0 \left[\gamma^c + \frac{1}{2l_B^2}\left(\chi^c_\perp \cos\theta\varsigma_3 + \chi^c_\parallel \sin\theta\varsigma_2\right)\right] k_y^2 + \frac{\alpha_0}{2l_B^2}\left[g^c_\perp \cos\theta\varsigma_3 + g^c_\parallel \sin\theta\varsigma_2\right] \\
+ \alpha_0\zeta^c_\gamma k_y^4 + \frac{\alpha_0}{4l_B^4}\left[\zeta^c_\perp \cos^2\theta + \zeta^c_\parallel \sin^2\theta\right] + \left(\beta^c_1 + \beta^c_3 k_y^2\right) k_y\varsigma_1,
\end{aligned}
\tag{3.198}
$$

where the "c" superscript refers to QC subbands, and differentiates a parameter from its η and H QW counterpart. In increasing order of perturbation, the effective parameters are given by (in dot-bar notation):

$$\mathbf{g}^c_\perp = \bar{\mathbf{G}}^c_\perp, \tag{3.199a}$$

$$\mathbf{g}^c_\parallel = \bar{\mathbf{G}}^c_\parallel, \tag{3.199b}$$

$$\boldsymbol{\beta}^c_1 = \alpha_0 \bar{\mathbf{T}}^c, \tag{3.199c}$$

$$\boldsymbol{\gamma}^c = \bar{\boldsymbol{\Gamma}}^c + \alpha_0 \dot{\mathbf{T}}^c \bar{\mathbf{T}}^c, \tag{3.199d}$$

$$\boldsymbol{\zeta}^c_\perp = \bar{\mathbf{Z}}^c_\perp + \alpha_0 \dot{\mathbf{G}}^c_\perp \bar{\mathbf{G}}^c_\perp, \tag{3.199e}$$

$$\boldsymbol{\zeta}^c_\parallel = \bar{\mathbf{Z}}^c_\parallel + \alpha_0 \dot{\mathbf{G}}^c_\parallel \bar{\mathbf{G}}^c_\parallel, \tag{3.199f}$$

$$\boldsymbol{\beta}^c_3 = \alpha_0^2\left(\dot{\boldsymbol{\Gamma}}^c \bar{\mathbf{T}}^c + \dot{\mathbf{T}}^c \bar{\boldsymbol{\Gamma}}^c\right) + \alpha_0^3\left(\dot{\mathbf{T}}^c \dot{\mathbf{T}}^c \bar{\mathbf{T}}^c + [S]_3\right), \tag{3.199g}$$

$$\boldsymbol{\chi}^c_\perp = \alpha_0\left(\dot{\boldsymbol{\Gamma}}^c \bar{\mathbf{G}}^c_\perp + \dot{\mathbf{G}}^c_\perp \bar{\boldsymbol{\Gamma}}^c\right) + \alpha_0^2\left(\dot{\mathbf{T}}^c \dot{\mathbf{T}}^c \bar{\mathbf{G}}^c_\perp - \dot{\mathbf{T}}^c \dot{\mathbf{G}}^c_\perp \bar{\mathbf{T}}^c + \dot{\mathbf{G}}^c_\perp \dot{\mathbf{T}}^c \bar{\mathbf{T}}^c + [S]_3\right), \tag{3.199h}$$

$$\boldsymbol{\chi}^c_\parallel = \alpha_0\left(\dot{\boldsymbol{\Gamma}}^c \bar{\mathbf{G}}^c_\parallel + \dot{\mathbf{G}}^c_\parallel \bar{\boldsymbol{\Gamma}}^c\right) + \alpha_0^2\left(\dot{\mathbf{T}}^c \dot{\mathbf{T}}^c \bar{\mathbf{G}}^c_\parallel - \dot{\mathbf{T}}^c \dot{\mathbf{G}}^c_\parallel \bar{\mathbf{T}}^c + \dot{\mathbf{G}}^c_\parallel \dot{\mathbf{T}}^c \bar{\mathbf{T}}^c + [S]_3\right), \tag{3.199i}$$

$$\boldsymbol{\zeta}^c_\gamma = \alpha_0 \dot{\boldsymbol{\Gamma}}^c \bar{\boldsymbol{\Gamma}}^c + \alpha_0^2\left(\dot{\boldsymbol{\Gamma}}^c \dot{\mathbf{T}}^c \bar{\mathbf{T}}^c + \dot{\mathbf{T}}^c \dot{\boldsymbol{\Gamma}}^c \bar{\mathbf{T}}^c + \dot{\mathbf{T}}^c \dot{\mathbf{T}}^c \bar{\boldsymbol{\Gamma}}^c + [S]_3\right) + \alpha_0^3\left(\dot{\mathbf{T}}^c \dot{\mathbf{T}}^c \dot{\mathbf{T}}^c \bar{\mathbf{T}}^c + [S]_4\right), \tag{3.199j}$$

where the dot and bared matrices are defined in (3.195). In contrast to the QW system, here the two components of the g-tensor only require 1^{st} order perturbation.

3.4.3 The quantum dot Hamiltonian

A quantum dot is a device in which charge carriers are confined in all three spatial dimensions. The three dimensions of confinement are provided by (a) the QW heterostructure and (b) by electrostatic gates with associated potential

$$V_\parallel(x) = -\alpha_0\left(\frac{x^2}{l_x^4} + \frac{y^2}{l_y^4}\right). \tag{3.200}$$

l_x and l_y are characteristic lengths to quantify the strength of in-plane confinement (as felt

by an electron of mass m_0). Appearance of both x and y in the Hamiltonian allows magnetic fields with arbitrary orientation (θ, ϕ).

In analogy with the quantum well and the quantum channel systems, a subband edge basis $\mathcal{B}_0^{\mathrm{QD}}$ is constructed by diagonalizing the quantum dot Hamiltonian $\mathbf{H}_0^{\mathrm{QD}}$, which is given by (3.183) evaluated at $B = 0$:

$$\mathbf{H}_0^{\mathrm{QD}} = \mathbf{E}_0^{\mathrm{QW}} + \alpha_0 \left[\mathbf{M}_\gamma k_\parallel^2 + \left(i\mathbf{M}_1 k_- + \mathbf{M}_2 k_-^2 + \mathrm{H.c.}\right)\right] - \alpha_0 \left(\frac{x^2}{l_x^4} + \frac{y^2}{l_y^4}\right). \tag{3.201}$$

Eigenstates of this Hamiltonian are denoted $|\varsigma; i, N_1, N_2\rangle$. Here, $\varsigma = \uparrow, \downarrow$ is a pseudo-spin quantum number for the QD subbands, i is an out-of-plane quantum number and $N_{1,2}$ are in-plane quantum numbers. The energy associated with $|\varsigma; i, N_1, N_2\rangle$ is denoted E^d_{i,N_1,N_2}, and is ς-independent. The kets $|\varsigma; i, N_1, N_2\rangle$ can be expanded as a linear combination of QW and in-plane basis states:

$$|\varsigma; i, N_1, N_2\rangle = \sum_{\tau,\sigma} \sum_{j,n_1,n_2} c_{\tau\sigma,j,n_1,n_2} \, |\tau\sigma; j\rangle \, |n_1, n_2\rangle : \begin{bmatrix} \mathbf{c}^\varsigma_{\mathrm{H}+} \\ \mathbf{c}^\varsigma_{\eta+} \\ \mathbf{c}^\varsigma_{\eta-} \\ \mathbf{c}^\varsigma_{\mathrm{H}-} \end{bmatrix}, \tag{3.202}$$

where $\mathbf{c}^\varsigma_{\tau\sigma}$ are $N_\tau N_x N_y$-element vectors, with N_x the number of $|n_1\rangle$ levels and N_y the number of $|n_2\rangle$ levels in the in-plane basis. As with the quantum well and the quantum channel cases, it is possible to diagonalize $\mathbf{H}_0^{\mathrm{QD}}$ only for the $\varsigma = \uparrow$ subbands. The degenerate time-reversed partners $\varsigma = \downarrow$ are then simply constructed from the $\varsigma = \uparrow$ levels. The strategy used for the quantum channel can be recycled here, since $V_\parallel$ has inversion symmetry with respect to $x \to -x$ and $y \to -y$. In this case, the classification is performed according to the parity of $|n_1, n_2\rangle$. Assuming $n_{1,2} \geq 0$, $|n_1, n_2\rangle$ is even (odd) iff $n_1 + n_2$ is even (odd). Since even powers of $k_\pm$ preserve the parity of $|n_1, n_2\rangle$ and odd powers of $k_\pm$ do not, and from the structure of $\mathbf{H}_0^{\mathrm{QD}}$, eigenstates must be either "ASAS" or "SASA", as in the quantum channel case, with "ASAS" corresponding to $\varsigma = \uparrow$. We introduce the ladder operators

$$a_1 = \frac{1}{\sqrt{2}} \left(\frac{x}{l_x} + i l_x k_x\right), \qquad a_2 = \frac{1}{\sqrt{2}} \left(\frac{y}{l_y} + i l_y k_y\right), \tag{3.203}$$

such that $\left[a_i, a_j^\dagger\right] = \delta_{i,j}$ and $a_i^\dagger a_i \, |n_i\rangle = n_i \, |n_i\rangle$. Projecting x, y, k_x and k_y in $\mathbf{H}_0^{\mathrm{QC}}$ onto the basis $|n_1, n_2\rangle$, and eliminating the subspaces that are incompatible with the "ASAS"

symmetry (even $n_1 + n_2$ in H+ subspace, and so on) results in a $\varsigma = \uparrow$ Hamiltonian of dimension $N_\perp N_x N_y \times N_\perp N_x N_y$. The $N_\perp N_x N_y$ other $\varsigma = \downarrow$ subbands are constructed from the $\varsigma = \uparrow$ eigenstates as in the quantum channel system[5]:

$$|\uparrow; i, N_1, N_2\rangle : \begin{bmatrix} \mathbf{c}_{\mathrm{H}+} \\ \mathbf{c}_{\eta+} \\ \mathbf{c}_{\eta-} \\ \mathbf{c}_{\mathrm{H}-} \end{bmatrix}, \qquad |\downarrow; i, N_1, N_2\rangle : \begin{bmatrix} \mathbf{c}^*_{\mathrm{H}-} \\ -\mathbf{c}^*_{\eta-} \\ \mathbf{c}^*_{\eta+} \\ -\mathbf{c}^*_{\mathrm{H}+} \end{bmatrix}. \tag{3.204}$$

The QD subband edge basis $\mathcal{B}_0^{\mathrm{QD}}$ is constructed by collecting $N_\parallel$ $\varsigma = \uparrow$ subbands and the corresponding $N_\parallel$ $\varsigma = \downarrow$ subbands close in energy to a set of QD orbitals of interest. Similarly to the QC problem, the size of $\mathcal{B}_0^{\mathrm{QD}}$ is restricted to $2N_\perp N_x N_y$, or $N_\parallel \leq N_\perp N_x N_y$. The QD Hamiltonian for $B > 0$ is obtained by projecting the remaining part of $\mathbf{H} - \mathbf{H}_0^{\mathrm{QD}}$ onto $\mathcal{B}_0^{\mathrm{QD}}$. The result is a $2N_\parallel \times 2N_\parallel$ matrix

$$\begin{aligned} \mathbf{H}^{\mathrm{QD}} = \mathbf{E}_0^{\mathrm{QD}} + \frac{\alpha_0}{2l_B^2} \Bigg\{ & \cos\theta \mathbf{L}_{2\perp} + \frac{\cos^2\theta}{2l_B^2}\mathbf{L}_{4\perp} + \frac{\sin^2\theta}{2l_B^2}\mathbf{L}_{4\parallel} \\ & + \sin\theta \left[e^{-i\phi}\mathbf{L}_{2\parallel} + \frac{\sin\theta}{2l_B^2} e^{-2i\phi}\mathbf{L}'_{4\parallel} + \frac{\cos\theta}{2l_B^2} e^{-i\phi}\mathbf{L}_{4\times} + \mathrm{H.c.} \right] \Bigg\}, \end{aligned} \tag{3.205}$$

where $\mathbf{E}_0^{\mathrm{QD}}$ is the diagonal matrix of energies E^d_{i,N_1,N_2}:

$$\mathbf{E}_0^{\mathrm{QD}} = \begin{bmatrix} \mathbf{E}^d & 0 \\ 0 & \mathbf{E}^d \end{bmatrix}, \tag{3.206}$$

and $\mathbf{E}^d = \mathrm{diag}\{E^d_{1,0,0}, E^d_{1,0,1}, \ldots, E^d_{1,1,0}, E^d_{1,1,1}, \ldots, E^d_{2,0,0}, E^d_{2,0,1}, \ldots\}$. $\mathbf{L}$ matrices all have a 2×2 block structure inherited from the symmetry-based classification of $\varsigma = \uparrow, \downarrow$. If $\Lambda = \pi/4$, they are given by

$$\begin{aligned} \mathbf{L}_{2\perp} &= \mathbf{G}^d_\perp \varsigma_+\varsigma_- + \mathbf{G}^{d*}_\perp \varsigma_-\varsigma_+ \\ &= \langle \varsigma; i, N_1, N_2 | \, \mathbf{M}_g + [i\mathbf{M}_\gamma\{\zeta_+, k_-\} + 2\mathbf{M}_1\zeta_- - 4i\mathbf{M}_2\zeta_- k_- + \mathrm{H.c.}] \, |\varsigma'; i', N_1', N_2'\rangle \,, \end{aligned} \tag{3.207a}$$

[5]Complex conjugation is required for $\varsigma = \downarrow$ since for QDs, the $\mathbf{c}_{\tau\sigma}$ coefficients are in general complex. For QCs, the $\mathbf{c}_{\tau\sigma}$ coefficients are real.

$$\begin{aligned}\mathbf{L}_{2\|} &= \mathbf{G}^d_+\varsigma_+ + \mathbf{G}^d_-\varsigma_- \\ &= \langle \varsigma; i, N_1, N_2|\, \mathbf{N}_g - 2i\mathbf{N}'_\gamma\zeta_+ - 2\mathbf{N}_1\{\zeta_+, k_-\} + 4\mathbf{N}^\dagger_1\zeta_+k_+\, |\varsigma'; i', N'_1, N'_2\rangle\,,\end{aligned} \tag{3.207b}$$

$$\mathbf{L}_{4\perp} = \langle \varsigma; i, N_1, N_2|\, 4\mathbf{M}_\gamma\zeta_+\zeta_- - 4\left[\mathbf{M}_2\zeta^2_- + \text{H.c.}\right]|\varsigma'; i', N'_1, N'_2\rangle \tag{3.207c}$$

$$\mathbf{L}_{4\|} = \langle \varsigma; i, N_1, N_2|\, 8\mathbf{N}_\gamma\zeta_+\zeta_-\, |\varsigma'; i', N'_1, N'_2\rangle \tag{3.207d}$$

$$\mathbf{L}'_{4\|} = -4\,\langle \varsigma; i, N_1, N_2|\, \mathbf{N}_\gamma\zeta^2_+\, |\varsigma'; i', N'_1, N'_2\rangle \tag{3.207e}$$

$$\mathbf{L}_{4\times} = 8i\,\langle \varsigma; i, N_1, N_2|\, \mathbf{N}_1\zeta_+\zeta_- + \mathbf{N}^\dagger_1\zeta^2_+\, |\varsigma'; i', N'_1, N'_2\rangle \tag{3.207f}$$

with $\varsigma_\pm = (\varsigma_1 \pm i\varsigma_2)/2$ and $\zeta_\pm = (x \pm iy)/2$.

3.4.4 List of quantum dot parameters

A 2×2 effective Hamiltonian for a single quantum dot orbital $|\varsigma; i, N_1, N_2\rangle$ is obtained by performing a SWT on the $2N_\| \times 2N_\|$ QD Hamiltonian (3.205). The part with known eigenvalues is $\mathbf{E}^{\text{QD}}_0$, while the part with unknown eigenvalues is

$$\begin{aligned}\mathbf{W} = \frac{\alpha_0}{2l^2_B}\Bigg\{&\cos\theta\mathbf{L}_{2\perp} + \frac{\cos^2\theta}{2l^2_B}\mathbf{L}_{4\perp} + \frac{\sin^2\theta}{2l^2_B}\mathbf{L}_{4\|} \\ &+ \sin\theta\left[e^{-i\phi}\mathbf{L}_{2\|} + \frac{\sin\theta}{2l^2_B}e^{-2i\phi}\mathbf{L}'_{4\|} + \frac{\cos\theta}{2l^2_B}e^{-i\phi}\mathbf{L}_{4\times} + \text{H.c.}\right]\Bigg\}.\end{aligned} \tag{3.208}$$

A quick inspection of (3.208) reveals that the perturbation $\mathbf{W}$ is at least linear in B (or quadratic in K). Therefore, a quartic-in-K effective QD Hamiltonian only requires 2^{nd} order perturbation theory. In addition, the arguably most relevant parameters for QDs, the g-tensor components, all require only 1^{st} order perturbation. In this section we shall focus only on the g-tensor components.

A general Zeeman Hamiltonian for a 2-level system has the following structure:

$$H_Z = \frac{\alpha_0}{2l^2_B}\mathbf{n}\cdot\mathbf{g}\cdot\boldsymbol{\varsigma}, \tag{3.209}$$

where $\boldsymbol{\varsigma}$ is the vector of Pauli matrices, $\mathbf{g}$ is the 3×3 g-tensor, and $\mathbf{n}$ is the unit vector pointing along $\mathbf{B}$. In terms of (θ, ϕ) and the g-tensor components g^d_{ij}, $\mathbf{n}\cdot\mathbf{g}\cdot\boldsymbol{\varsigma}$ expands to

$$\mathbf{n}\cdot\mathbf{g}\cdot\boldsymbol{\varsigma} = \sum_{i=1}^{3}\left(g^d_{1i}\sin\theta\cos\phi + g^d_{2i}\sin\theta\sin\phi + g^d_{3i}\cos\theta\right)\varsigma_i. \tag{3.210}$$

Comparing this with the linear-in-B terms in $\bar{\mathbf{W}}$, namely $\bar{\mathbf{L}}_{2\perp}$ and $\bar{\mathbf{L}}_{2\parallel}$, we obtain the following g-tensor components for the QD orbital:

$$g^d_{11} = \frac{1}{2}\left(\bar{\mathbf{G}}^d_+ + \bar{\mathbf{G}}^{d*}_+ + \bar{\mathbf{G}}^d_- + \bar{\mathbf{G}}^{d*}_-\right), \tag{3.211a}$$

$$g^d_{12} = \frac{i}{2}\left(\bar{\mathbf{G}}^d_+ - \bar{\mathbf{G}}^{d*}_+ - \bar{\mathbf{G}}^d_- + \bar{\mathbf{G}}^{d*}_-\right), \tag{3.211b}$$

$$g^d_{21} = -\frac{i}{2}\left(\bar{\mathbf{G}}^d_+ - \bar{\mathbf{G}}^{d*}_+ + \bar{\mathbf{G}}^d_- - \bar{\mathbf{G}}^{d*}_-\right), \tag{3.211c}$$

$$g^d_{22} = \frac{1}{2}\left(\bar{\mathbf{G}}^d_+ + \bar{\mathbf{G}}^{d*}_+ - \bar{\mathbf{G}}^d_- - \bar{\mathbf{G}}^{d*}_-\right), \tag{3.211d}$$

$$g^d_{33} = \frac{1}{2}\left(\bar{\mathbf{G}}^d_\perp + \bar{\mathbf{G}}^{d*}_\perp\right), \tag{3.211e}$$

$$g^d_{31} = g^d_{32} = 0. \tag{3.211f}$$

3.5 $k \cdot p$ theory for hole-phonon coupling in quantum dots

A quantum dot prepared in a specific level can undergo phonon-mediated transitions through a electron-phonon coupling mechanism. For instance, a hole (or an electron) occupying the QD fundamental level can be promoted to an excited state by absorbing a phonon with frequency matching that of the transition. Similarly, a hole occupying an excited QD level can emit a phonon and fall into the QD ground state. A qubit defined by the 2-fold low energy spectrum of a QD is subject to relaxation through this phonon-mediated process, which we shall describe in this section.

From Fermi's golden rule, the transition rate from an initial QD level $|i\rangle$ to a final QD level $|f\rangle$ from a phonon-mediated interaction is

$$\Gamma = \frac{2\pi\mathcal{V}}{\hbar}\sum_\alpha \int \frac{\mathrm{d}^3 q}{(2\pi)^3}\,|\langle f|W_{\alpha\mathbf{q}}|i\rangle|^2\,\delta\left(\Delta e - \hbar\omega_{\alpha\mathbf{q}}\right), \tag{3.212}$$

where $\mathcal{V}$ is a volume, $\mathbf{q}$ is the phonon wavevector of amplitude q, $\alpha = \{\mathrm{L}, \mathrm{T1}, \mathrm{T2}\}$ is the phonon polarization index, $\omega_{\alpha\mathbf{q}}$ is the phonon frequency, Δe is the qubit Larmor frequency, and $W_{\alpha\mathbf{q}}$ is the electron-phonon interaction Hamiltonian. Assuming linear-in-q and isotropic phonon dispersions for all three branches, (3.212) simplifies into

$$\Gamma = \frac{\mathcal{V}}{(2\pi)^2}\frac{\omega^2}{\hbar^2}\sum_\alpha \frac{1}{v^3_\alpha}\int \sin\theta\,\mathrm{d}\theta\,\mathrm{d}\phi\,|\langle f|W_{\alpha\mathbf{q}}(\theta,\phi)|i\rangle|^2, \tag{3.213}$$

where v_α is the sound velocity in branch α. The integration (3.213) is performed with

the modulus of $\mathbf{q}$ fixed, such that the phonon energy matches that of the qubit transition: $q = q_\alpha = \omega/v_\alpha$, with $\omega = \Delta e/\hbar$.

In the phonon absorption process, the initial and final states are given respectively by

$$|i\rangle = |\mathbb{0}\rangle\,|\mathrm{TP}\rangle\,, \tag{3.214}$$

$$|f\rangle = \frac{1}{\sqrt{N_{\alpha\mathbf{q}}}}\,|\mathbb{1}\rangle\,b_{\alpha\mathbf{q}}\,|\mathrm{TP}\rangle\,, \tag{3.215}$$

while for phonon emission they are

$$|i\rangle = |\mathbb{1}\rangle\,|\mathrm{TP}\rangle\,, \tag{3.216}$$

$$|f\rangle = \frac{1}{\sqrt{N_{\alpha,-\mathbf{q}}+1}}\,|\mathbb{0}\rangle\,b^\dagger_{\alpha,-\mathbf{q}}\,|\mathrm{TP}\rangle\,. \tag{3.217}$$

Here $|\mathbb{0}\rangle$ and $|\mathbb{1}\rangle$ are the fundamental and first excited states of the quantum dot (separated in energy by Δe at some finite $\mathbf{B}$-field) and $|\mathrm{TP}\rangle$ is the thermal bath of phonons. It is an eigenstate of the phonon number operator $b^\dagger_{\alpha\mathbf{q}}b_{\alpha\mathbf{q}}$:

$$b^\dagger_{\alpha\mathbf{q}}b_{\alpha\mathbf{q}}\,|\mathrm{TP}\rangle = N_{\alpha\mathbf{q}}\,|\mathrm{TP}\rangle\,, \tag{3.218}$$

where $N_{\alpha\mathbf{q}} = \left(e^{\hbar\omega_{\alpha\mathbf{q}}/(k_\mathrm{B}T)}-1\right)^{-1}$ is the phonon occupation number. The total number of phonons N_ph that contribute to the transition rate Γ includes only those with $\omega_{\alpha\mathbf{q}} = \Delta e/\hbar$, so $N_\mathrm{ph} = \left(e^{\hbar\omega/(k_\mathrm{B}T)}-1\right)^{-1}$.

The interaction Hamiltonian $W_{\alpha\mathbf{q}}$ is the Bir-Pikus strain Hamiltonian (3.73), but with a strain tensor $\varepsilon_{\alpha\mathbf{q}}$ given by [176]:

$$\varepsilon_{\alpha\mathbf{q}} = iqA_{\alpha\mathbf{q}}\epsilon_{\alpha\mathbf{q}} \tag{3.219a}$$

$$= iq\sqrt{A_\alpha/q}e^{i\mathbf{q}\cdot\mathbf{r}}\left(b_{\alpha\mathbf{q}} + b^\dagger_{\alpha,-\mathbf{q}}\right)\epsilon_{\alpha\mathbf{q}} \tag{3.219b}$$

$$= i\sqrt{qA_\alpha}e^{i\mathbf{q}\cdot\mathbf{r}}\left(b_{\alpha\mathbf{q}} + b^\dagger_{\alpha,-\mathbf{q}}\right)\epsilon_{\alpha\mathbf{q}} \tag{3.219c}$$

$$= \varepsilon^\dagger_{\alpha,-\mathbf{q}}, \tag{3.219d}$$

where $A_{\alpha\mathbf{q}} = \sqrt{\hbar/(2\rho\mathcal{V}\omega_{\alpha\mathbf{q}})}e^{i\mathbf{q}\cdot\mathbf{r}}\left(b_{\alpha\mathbf{q}} + b^\dagger_{\alpha,-\mathbf{q}}\right)$ has units of length, and where $A_\alpha = \hbar/(2\rho\mathcal{V}v_\alpha)$ also has units of length. The 3×3 matrix $\epsilon_{\alpha\mathbf{q}}$ is

$$\epsilon_{\alpha\mathbf{q}} = \frac{1}{2}\begin{bmatrix} 2\hat{c}_x\hat{q}_x & \hat{c}_x\hat{q}_y + \hat{c}_y\hat{q}_x & \hat{c}_x\hat{q}_z + \hat{c}_z\hat{q}_x \\ \hat{c}_y\hat{q}_x + \hat{c}_x\hat{q}_y & 2\hat{c}_y\hat{q}_y & \hat{c}_y\hat{q}_z + \hat{c}_z\hat{q}_y \\ \hat{c}_z\hat{q}_x + \hat{c}_x\hat{q}_z & \hat{c}_z\hat{q}_y + \hat{c}_y\hat{q}_z & 2\hat{c}_z\hat{q}_z \end{bmatrix} = \begin{bmatrix} f_{xx} & f_{xy} & f_{zx} \\ f_{xy} & f_{yy} & f_{yz} \\ f_{zx} & f_{yz} & f_{zz} \end{bmatrix}, \tag{3.220}$$

where $f_{ij} = (\hat{c}_i\hat{q}_j + \hat{c}_j\hat{q}_i)/2$, $\hat{\mathbf{c}}$ is the phonon unit polarization vector, and $\hat{\mathbf{q}} = \mathbf{q}/q$. The z-dependent part $e^{iq_z z}$ of $e^{i\mathbf{q}\cdot\mathbf{r}}$ gets fully integrated during the basis change to the subband edge basis $\mathcal{B}_0$ [see (3.88)]. In addition, the modulus of $\mathbf{q}$ being fixed for each polarization, $W_{\alpha\mathbf{q}}$ can be written as

$$W_{\alpha\mathbf{q}} \to \mathbf{W}_{\alpha\mathbf{q}}(\theta,\phi) = i\sqrt{q}\left(b_{\alpha\mathbf{q}} + b^\dagger_{\alpha,-\mathbf{q}}\right)e^{ixq_\alpha\sin\theta\cos\phi}e^{iyq_\alpha\sin\theta\sin\phi}\mathbf{w}_\alpha(\theta,\phi), \tag{3.221}$$

where θ and ϕ are the polar and azimuthal phonon propagation angles respectively, and $\mathbf{w}_\alpha$ only depends on the $f_{ij}(\theta,\phi)$:

$$\begin{aligned}\mathbf{w}_\alpha(\theta,\phi) = {} & (f_{xx}+f_{yy}+f_{zz})\,\mathbf{C}_a + (f_{xx}+f_{yy}-2f_{zz})\,\mathbf{C}_b \\ & + (f_{xx}-f_{yy})\mathbf{C}_2 + \left[(f_{yz}+if_{zx})\,\mathbf{C}_1 + (if_{xy})\mathbf{C}_2' + \text{H.c.}\right],\end{aligned} \tag{3.222}$$

where the matrices $\mathbf{C}_i$ are

$$\mathbf{C}_a = \begin{bmatrix} \mathbf{a}^{\mathrm{H}} & 0 & 0 & 0 \\ 0 & \mathbf{a}^{\eta} & 0 & 0 \\ 0 & 0 & \mathbf{a}^{\eta} & 0 \\ 0 & 0 & 0 & \mathbf{a}^{\mathrm{H}} \end{bmatrix}, \qquad \mathbf{C}_b = \begin{bmatrix} \mathbf{b}^{\mathrm{H}} & 0 & 0 & 0 \\ 0 & \mathbf{b}^{\eta} & 0 & 0 \\ 0 & 0 & \mathbf{b}^{\eta} & 0 \\ 0 & 0 & 0 & \mathbf{b}^{\mathrm{H}} \end{bmatrix}, \tag{3.223a}$$

$$\mathbf{C}_1 = \begin{bmatrix} 0 & \mathbf{t}^{\mathrm{x}} & 0 & 0 \\ 0 & 0 & \mathbf{t}^{\eta} & 0 \\ 0 & 0 & 0 & \mathbf{t}^{\mathrm{x}\dagger} \\ 0 & 0 & 0 & 0 \end{bmatrix}, \qquad \mathbf{C}_2 = \begin{bmatrix} 0 & 0 & \boldsymbol{\beta} & 0 \\ 0 & 0 & 0 & \boldsymbol{\beta}^\dagger \\ \boldsymbol{\beta}^\dagger & 0 & 0 & 0 \\ 0 & \boldsymbol{\beta} & 0 & 0 \end{bmatrix}, \tag{3.223b}$$

$$\mathbf{C}_2' = \begin{bmatrix} 0 & 0 & \boldsymbol{\beta}' & 0 \\ 0 & 0 & 0 & \boldsymbol{\beta}'^\dagger \\ 0 & 0 & 0 & 0 \\ 0 & 0 & 0 & 0 \end{bmatrix}. \tag{3.223c}$$

The matrix elements in the $\mathbf{C}_i$'s are

$$\mathbf{a}^{\eta} = \langle c| a_c' |c\rangle + \frac{1}{3}\left(\langle +| a_v' |+\rangle + 2\langle -| a_v' |-\rangle\right) \tag{3.224a}$$

$$\mathbf{a}^{\mathrm{H}} = \langle h| a_v' |h\rangle \tag{3.224b}$$

$$\mathbf{b}^{\eta} = \frac{1}{6}\left(\langle +| b' |+\rangle - 4\langle -| b' |-\rangle\right) \tag{3.224c}$$

$$\mathbf{b}^{\mathrm{H}} = \frac{1}{2}\langle h| b' |h\rangle \tag{3.224d}$$

$$\mathbf{t}^{\mathrm{x}} = i\langle h| d' |-\rangle \tag{3.224e}$$

$$\mathbf{t}^{\eta} = \frac{i}{\sqrt{3}}\left(\langle +| d' |-\rangle - \langle -| d' |+\rangle\right) \tag{3.224f}$$

$$\boldsymbol{\beta} = -\frac{\sqrt{3}}{2}\langle h| b' |+\rangle \tag{3.224g}$$

$$\boldsymbol{\beta} = \langle h| d' |+\rangle, \tag{3.224h}$$

with the primed deformation potentials being $a_c' = \sqrt{A_\alpha} e^{izq_\alpha \cos\theta} a_c$ and so on. In the longitudinal polarization, $\hat{\mathbf{c}}$ is parallel to $\mathbf{q}$, which gives

$$f_{xx} + f_{yy} + f_{zz} = 1, \qquad f_{xx} + f_{yy} - 2f_{zz} = 1 - 3\cos^2\theta,$$
$$f_{xx} - f_{yy} = \sin^2\theta\cos 2\phi, \qquad f_{yz} + if_{zx} = \frac{i}{2}\sin 2\theta e^{-i\phi}, \quad f_{xy} = \frac{1}{2}\sin^2\theta\sin 2\phi.$$

The first transverse polarization corresponds to $\hat{\mathbf{c}}$ perpendicular to $\mathbf{q}$ and with $\hat{\mathbf{c}}$ such that the plane containing both vectors cuts through the QW plane at a 90° angle. The f-sums are

$$f_{xx} + f_{yy} + f_{zz} = 0, \qquad f_{xx} + f_{yy} - 2f_{zz} = \frac{3}{2}\sin 2\theta,$$
$$f_{xx} - f_{yy} = \frac{1}{2}\sin 2\theta\cos 2\phi, \qquad f_{yz} + if_{zx} = \frac{i}{2}\cos 2\theta e^{-i\phi}, \quad f_{xy} = \frac{1}{4}\sin 2\theta\sin 2\phi.$$

The second transverse polarization corresponds to $\hat{\mathbf{c}}$ perpendicular to $\mathbf{q}$ with $\hat{\mathbf{c}}$ lying in the QW plane. The f-sums are

$$f_{xx}+f_{yy}+f_{zz}=0, \qquad f_{xx}+f_{yy}-2f_{zz}=0,$$
$$f_{xx}-f_{yy}=-\sin\theta\sin 2\phi, \qquad f_{yz}+if_{zx}=\frac{1}{2}\cos\theta e^{-i\phi}, \quad f_{xy}=\frac{1}{2}\sin\theta\cos 2\phi.$$

Inserting $\mathbf{W}_{\alpha\mathbf{q}}$ into (3.213), evaluating the rate Γ for emission and absorption processes and taking the sum of both gives the final formula for the phonon-mediated relaxation rate:

$$\Gamma=\frac{\mathcal{V}}{(2\pi)^2}\frac{\omega^3}{\hbar^2}\coth\left(\frac{\hbar\omega}{2k_{\mathrm{B}}T}\right)\sum_{\alpha}\frac{1}{v_\alpha^4}\int\sin\theta\,\mathrm{d}\theta\,\mathrm{d}\phi\left|\langle\mathbb{0}|\,e^{iq_\alpha\sin\theta(x\cos\phi+y\sin\phi)}\mathbf{w}_\alpha(\theta,\phi)\,|\mathbb{1}\rangle\right|^2. \tag{3.225}$$

CHAPTER 4 VANISHING ZEEMAN ENERGY IN A TWO DIMENSIONAL HOLE GAS

4.1 Abstract

A clear signature of Zeeman split states crossing is observed in Landau fan-diagram of strained germanium two-dimensional hole gas. The underlying mechanisms are discussed based on a perturbative model yielding a closed formula for the critical magnetic fields. These fields depend strongly on the energy difference between the top-most and the neighboring valence bands and are sensitive to the quantum well thickness, strain, and spin-orbit-interaction. The latter is a necessary feature for the crossing to occur. This framework enables a straightforward quantification of the hole-state parameters from simple measurements, thus paving the way for its use in design and modelling of hole-based quantum devices.

4.2 Introduction

The inherently large and tunable spin-orbit interaction (SOI) energies of holes and their reduced hyperfine coupling with nuclear spins are behind the surging interest in hole spin qubits with fast all-electrical control [47, 48, 177–179]. Holes can also host superconducting pairing correlations, a key ingredient for the emergence of Majorana zero modes [180–184] for topological quantum computing. Because of its attractive properties [22,52,117,126,185–193], strained Ge low-dimensional system has been proposed as an effective building block to develop these emerging quantum devices. Interestingly, the simplicity of this system makes it a textbook model to uncover and elucidate subtle hole spin-related phenomena leading, for instance, to the recent observation of pure cubic Rashba spin-orbit coupling [46].

Measuring Zeeman splitting (ZS) of hole states under an external magnetic field has been central in probing hole spin properties, as it is directly related to the hole g-factor, which is itself strongly influenced by the underlying SOI, strain, symmetry, and confinement [35, 194]. In III-V semiconductors [194–207], hole spin splitting depends nonlinearly on the out-of-plane magnetic field strength B, causing Landau level crossings/anti-crossings [197, 208]. and Zeeman crossings/anti-crossings [22, 115, 134]. The nonlinearity is usually modeled by a quadratic-in-field contribution to ZS [194], which owes its existence to valence band mixing. Depending on the sign of the splitting, Zeeman energy can even vanish at some finite critical field, B_c. Theoretical studies attribute these nonlinearities to the mixing of heavy-hole (HH) and light-hole (LH) bands at finite energy [195]. Alongside with valence band mixing, Rashba

and Dresselhaus spin-orbit coupling were also shown to influence the crossing field, due to the lattice inversion asymmetry and the confining potential.

Detailed mechanisms of ZS of hole states are yet to be unravelled and understood and furthermore, ZS treatments for zinc-blende or diamond crystals that explicitly consider strain and SOI strength remain conspicuously missing in literature. Note that in early calculations [134] of Landau levels in Ge/SiGe quantum well (QW) to interpret cyclotron resonance experiments in Reference [209], the crossing of spin split states within the first HH subband was present and the corresponding field position was found to be sensitive to the strength of spin-orbit coupling. In that work, the authors insisted on the importance of including explicitly the split-off hole band, which was required to achieve a good agreement with experiments. Crucially, studies that included both strain and SOI were diagonalizing numerically the full $k \cdot p$ matrix [134, 198]. However, this mathematical rigor comes at the expense of identifying the physics governing the non-linearities in ZS.

To overcome these limitations and elucidate the underlying mechanisms of ZS, herein we uncover the clear signature of ZS crossings in a Ge high-mobility two-dimensional hole gas (2DHG). We also derive a theoretical framework describing the crossing of Zeeman split states that includes explicitly the SOI strength and strain. A closed formula for the crossing fields is obtained and validated by experiment. In addition to establishing the key parameters in Zeeman crossings, this analysis also provides a toolkit for a direct quantification from simple magnetotransport measurements of important physical quantities including HH out-of-plane g-factor, HH-LH splitting, and cubic Rashba spin-orbit coefficient.

4.3 Experimental details

The investigated 2DHG consists of a Ge/SiGe heterostructure including a strain-relaxed $Si_{0.2}Ge_{0.8}$ buffer setting the overall lattice parameter, a compressively-strained Ge QW, and a $Si_{0.2}Ge_{0.8}$ barrier separating the QW from a sacrificial Si cap layer. The growth was carried out in an Epsilon 2000 (ASMI) reduced pressure chemical vapor deposition reactor on a 100 mm n-type Si(001) substrate. The growth sequence starts with the deposition of a $Si_{0.2}Ge_{0.8}$ virtual substrate. This virtual substrate is obtained by growing a 1.6 µm strain-relaxed Ge buffer layer, a 1.6 µm reverse-graded $Si_{1-x}Ge_x$ layer with final Ge composition $x = 0.8$, and a 500 nm strain-relaxed $Si_{0.2}Ge_{0.8}$ buffer layer. A 16 nm compressively-strained Ge quantum well is then grown on top of the $Si_{0.2}Ge_{0.8}$ virtual substrate, followed by a strain-relaxed 17 nm-thick $Si_{0.2}Ge_{0.8}$ barrier. An in-plane compressive strain $\varepsilon_{\parallel} = -0.63\%$ is found in the QW via X-ray diffraction measurements [22]. A thin (< 2 nm) sacrificial Si cap completes the heterostructure. This cap is readily oxidized upon exposure to the cleanroom

environment after unloading the Ge/SiGe heterostructure from the growth reactor.

Hall-bar field effect transistors (H-FETs) are fabricated and operated with a negatively biased gate to accumulate a 2D hole gas into the QW and tune the carrier density. Fig. 1a shows an optical micrograph of the H-FET and a cross-section schematic of the active layers and the gate stack. A 170 nm deep trench mesa is dry-etched around the Hall-bar shaped H-FET in order to isolate the bonding pads from the device. The sample is dipped in HF to remove the native oxide prior to a 60 nm Pt layer deposition via e-beam evaporation. Ohmic contacts are obtained by diffusion of Pt into the quantum well occurring during the atomic layer deposition of a 30 nm Al_2O_3 dielectric layer at a temperature of 300 °C. Finally, a 10/200 nm-thick Ti/Au gate layer is deposited. An optimized $Si_{0.2}Ge_{0.8}$ barrier thickness of 17 nm was chosen, which is thin enough to allow for a large saturation carrier density [22] (up to 7.5×10^{11} cm^{-2}), while providing sufficient separation to reduce scattering of carriers in the QW from remote impurities [115], leading to large hole maximum mobility (2.6×10^5 cm^{-2}). Large density range and high mobility are key ingredients to observe Landau level fan-diagrams in magnetotransport with the clarity required to reveal subtle spin-related features.

In the magnetotransport studies, the longitudinal and transversal (ρ_{xx} and ρ_{xy}) component of the 2DHG resistivity tensor were measured via a standard four-probe low-frequency lock-in technique. The measurements are recorded at a temperature of $T = 260$ mK, measured at the cold finger of a ^{3}He dilution refrigerator. A source-drain voltage bias $V_{sd} = 0.1$ mV is applied at a frequency of 7.7 Hz. The magnetoresistance characterization of the device is performed by sweeping the voltage gate V_g and stepping B with a resolution of 15 mV and 25 mT, respectively. The energy E is obtained using the relation $E = p\pi\hbar^2/m^*$, where we obtain the carrier density p by Hall effect measurements at low B and we use the effective mass m^* measured as a function of density in similar heterostructures [115]. The ρ_{xx} vs. energy profiles in the upper panels of Figs. 3(a)-3(d) have been smoothed for clarity by using a Matlab routine based on Savitzky-Golay filtering method.

4.4 Magnetotransport studies of strained Ge 2DHG

The fan-diagram in Fig. 1b shows the normalized magnetoresistance oscillation amplitude $\Delta\rho_{xx}/\rho_0 = (\rho_{xx} - \rho_0)/\rho_0$ as a function of energy and out-of-plane external magnetic field B aligned along the growth direction $\hat{\mathbf{z}}$ and perpendicular to the 2DHG plane, where ρ_0 is the ρ_{xx} value at $B = 0$. The Zeeman split energy gap, corresponding to odd integer filling factors ν, deviates from its linear dependence on B, vanishes when the magnetic field reaches a critical value B_c, and then reopens at higher B values. We clearly observe the associated crossing

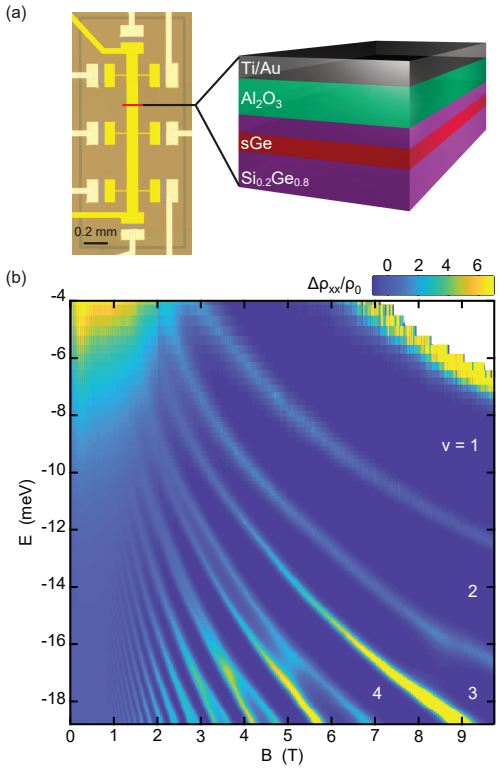

Figure 4.1 (a) Optical micrograph of a Hall-bar shaped Ge/SiGe heterostructure field effect transistor and cross section of the gate stack and active regions of the strained Ge/SiGe heterostructure below the red cut. The strained Ge (sGe) quantum well is 16 nm thick and the $Si_{0.2}Ge_{0.8}$ barrier on top is 17 nm thick. (b) Landau level fan-diagram reporting the magnetoresistance $\Delta\rho_{xx}/\rho_0 = (\rho_{xx} - \rho_0)/\rho_0$ as a function of out-of-plane magnetic field B and energy E. Labels of filling factors $\nu = 1 - 4$ are shown.

of Zeeman split states for odd integers $\nu = 3, 5, 7$, and 9. Partial signatures of Zeeman crossings occurring at similar magnetic fields were observed in earlier studies [22, 115], albeit the fan-diagram measurements were limited in density range [22] or affected by thermal broadening [115]. These observations point to an underlying mechanism that is independent of the QW position with respect to the surface gate.

4.5 Theoretical framework for hole dispersion in strained Ge 2DHG

To identify the mechanisms behind the non-linearities in ZS and the parameters affecting the crossing field, we employ the $k \cdot p$ framework derived in Section 3.3.3 for QWs in perpendicular magnetic fields. We further assume an abrupt and infinite band offset between the QW of width l_z and its barriers, no out-of-plane DC electric fields F_z, and no contributions from the conduction bands, thereby assuming only the effects of the 6-band subspace spanned by

HHs, LHs and split-off (SO) holes. The η spinor consequently only includes a LH envelope and a SO hole envelope:

$$|\eta\sigma; j\rangle = \left|\frac{3}{2}, \frac{\sigma}{2}\right\rangle |\ell_j\rangle + \sigma \left|\frac{1}{2}, \frac{\sigma}{2}\right\rangle |s_j\rangle \,, \tag{4.1}$$

where $|\ell_j\rangle = d_{\ell,j} |\varphi_j\rangle$, $|s_j\rangle = d_{s,j} |\varphi_j\rangle$, $\langle z|\varphi_j\rangle = \sqrt{\frac{2}{l_z}} \sin\left(\frac{j\pi z}{l_z}\right)$ and $d_{\ell,j}^2 + d_{s,j}^2 = 1$. Epitaxial strain is assumed to be bi-axial, and is accounted for by means of the Bir-Pikus Hamiltonian.

The starting point Hamiltonian is (3.113), with the integer m labeling the Landau levels. At $B = 0$, the energy spectrum of the Hamiltonian is easily solvable within the approximations mentionned earlier. For H-levels, we have (see Appendix A)

$$E_l^{\mathrm{H}} = -\alpha_0(\gamma_1 - 2\gamma_2) \left(\frac{l\pi}{l_z}\right)^2 + a_v \mathrm{Tr}\{\varepsilon\} + b \cdot \delta\varepsilon, \tag{4.2}$$

where $\delta\varepsilon = \varepsilon_{xx} - \varepsilon_{zz}$. For η-levels, we have

$$E_j^{\eta} = \mathfrak{E}_j + \mathfrak{e}_j - \frac{\Delta_0}{2} \pm \sqrt{(\mathfrak{e}_j + \Delta_0/2)^2 + 8\mathfrak{e}_j^2}, \tag{4.3}$$

where the "+" solution is for the LH-like level and the "−" solution is for the SO-like level, and

$$\mathfrak{E}_j = -\alpha_0\gamma_1 \left(\frac{j\pi}{l_z}\right)^2 + a_v \mathrm{Tr}\{\varepsilon\}, \tag{4.4}$$

$$\mathfrak{e}_j = -\alpha_0\gamma_2 \left(\frac{j\pi}{l_z}\right)^2 - \frac{b}{2}\delta\varepsilon. \tag{4.5}$$

A 2^{nd} order Schrieffer-Wolff transformation is performed on (3.113), leading to an effective Hamiltonian for spin-split Landau H-levels. The resulting effective 2×2 Hamiltonian does not couple spin-up ($\sigma = +$) and spin-down ($\sigma = -$) H-levels, as a consequence of spatial inversion symmetry of the QW. The energy dispersion as a function of B is thus simply the diagonal entries of the effective matrix. Shifting the Landau level index from $m \geq -2$ to $m \geq 1$ for the spin-down component (such that the filling factor $\nu = 2m - 1$), we obtain

$$E^{(2)}_{+,l,m}(B) = E^{\mathrm{H}}_l + 3m(m+1)\,(\kappa - F_l)\,\frac{\mu_{\mathrm{B}}B^2}{B^*_l} - \left[(2m-1)\,(\gamma_1+\gamma_2) + 3\kappa - 6mF_l\right]\mu_{\mathrm{B}}B, \tag{4.6a}$$

$$E^{(2)}_{-,l,m}(B) = E^{\mathrm{H}}_l + 3(m-2)(m-1)\,(\kappa - F_l)\,\frac{\mu_{\mathrm{B}}B^2}{B^*_l} - \left[(2m-1)\,(\gamma_1+\gamma_2) - 3\kappa - 6(m-1)F_l\right]\mu_{\mathrm{B}}B, \tag{4.6b}$$

with (using dot-bar notation)

$$B^*_l = \frac{3(\kappa - F_l)}{4\mu_{\mathrm{B}}\dot{\boldsymbol{\mu}}\bar{\boldsymbol{\mu}}^\dagger} = \frac{\kappa - F_l}{\mu_{\mathrm{B}}\,(\gamma_2+\gamma_3)^2}\left[\sum_j^* \frac{\left(d_{\ell,j} + \sqrt{2}d_{s,j}\right)^2}{E^{\mathrm{H}}_l - E^{\eta}_j}\right]^{-1} \tag{4.7a}$$

$$\approx \frac{\kappa - F_l}{\mu_{\mathrm{B}}\,(\gamma_2+\gamma_3)^2}\left(E^{\mathrm{HH}}_l - E^{\mathrm{LH}}_j\right) \tag{4.7b}$$

where the star on the sum indicates that j iterates on the only two η levels with the same number of nodes as the H level (one LH-like and one SO-like), and

$$F_l = \frac{\alpha_0}{3}\dot{\mathbf{T}}^{\mathrm{x}}\bar{\mathbf{T}}^{\mathrm{x}\dagger}. \tag{4.8}$$

The characteristic field B^*_l controls the crossing positions and is filling factor-independent, while F_l indicates the coupling strength between the H subband and neighboring η levels. The obtained Zeeman splitting energy $E_{\mathrm{Z}} \equiv E^{(2)}_{-,m}(B) - E^{(2)}_{+,m}(B)$ of the m-th spin-split Landau pair is (dropping the l subscript for simplicity):

$$E_{\mathrm{Z}} = 6(\kappa - F)\mu_{\mathrm{B}}B\left[1 - (2m-1)\left(\frac{B}{B^*}\right)\right]. \tag{4.9}$$

Solving for $E_{\mathrm{Z}} = 0$ results in a second order approximation for the filling factor-dependent crossing field B_c :

$$B^{(2)}_c(m) = \frac{B^*}{2m-1}. \tag{4.10}$$

The energy difference between the H subband edge and the crossings can also be found from the second order equations. When $m \to \infty$ (or $\nu \to \infty$) this energy difference becomes independent of m :

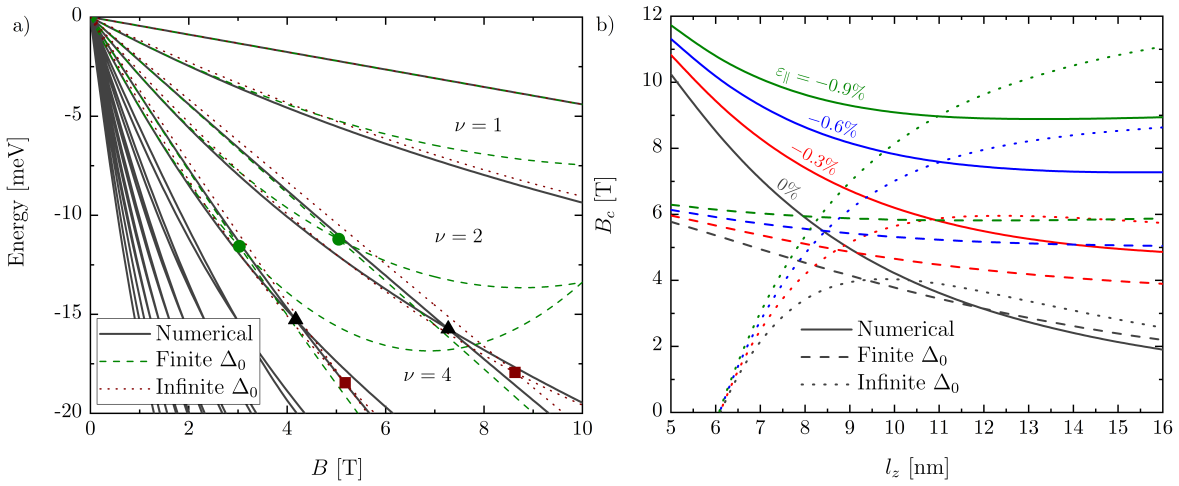

Figure 4.2 (a) Fan-diagram of the ground H level in a 16 nm Ge well subject to 0.6% compressive strain. Solid curves are the dispersion obtained from the numerical solution of (3.113), while the dashed curves are obtained from the second order dispersion assuming finite or infinite SOI respectively. Symbols indicate the Zeeman crossings. Filling factors ν are also indicated. (b) $\nu = 3$ crossing field as a function of the well thickness at various strain values obtained from the numerical solution of (3.113) (solid curves) and through Eq. (4.10) assuming finite or infinite SOI (dashed curves).

$$\Delta E = \left[\gamma_1 + \gamma_2 - \frac{3}{4}(\kappa + 3F)\right] \mu_{\mathrm{B}} B^*. \tag{4.11}$$

Equation (4.9) also yields the H-level weak-field g-factor :

$$g^{\mathrm{H}} = 6(\kappa - F). \tag{4.12}$$

The approximation (4.7b) holds only when SOI is large enough such that the SO band can be neglected from the $k \cdot p$ framework. An explicit criterion for this is derived from (4.3):

$$\Delta_0 \gg \alpha_0 \gamma_2 \left(\frac{\pi}{l_z}\right)^2 + \frac{b}{2}\delta\varepsilon. \tag{4.13}$$

In addition to the perturbation scheme, (3.113) is also numerically diagonalized to validate the accuracy of the perturbative model for various QW widths l_z and strain $\varepsilon_{\|}$. Since Ge has a rather high spin-orbit energy (see Table 3.3) it is worthwhile to look also at the behavior of the model with the assumption $\Delta_0 \to \infty$. We also focus on relaxed or compressively strained wells, which always result in a H-like valence band edge. The calculated fan-diagram of the ground H subband is displayed in Fig. 4.2a for a 16 nm-thick well with $\varepsilon_{\|} = -0.6\%$, similar

to the system analyzed in Fig. 4.1. Assuming finite Δ_0, the model reproduces the numerical fan-diagram up to $\sim 2\,\mathrm{T}$, which implies that $6(\kappa - F)$ is a very accurate approximation for the H g-factor at low fields. As the magnetic field increases, quadratic terms in B become more important and the dispersions eventually cross. The dispersion of a state with spin-up projection in a given spin-split Landau pair always has a bigger curvature than the spin-down one, which can be straightforwardly inferred from the coefficients $m(m+1)$ and $(m-2)(m-1)$ in (4.6). For that reason, a Zeeman crossing cannot occur, at least to second order, if the spin-up component lies closer to the bandgap than the spin-down one. Crossing fields are indicated in Fig. 4.2a for filling factors $\nu = 3$ and $\nu = 5$. The numerical solution of (3.113) gives a crossing field $B_c = 7.27\,\mathrm{T}$ for $\nu = 3$, whereas the second order formula (Eq. (4.10)) gives $B_c^{(2)} = 5.04\,\mathrm{T}$. Here the second order approximation underestimates B_c as it diverges from the numerical dispersion before the crossing. When assuming $\Delta_0 \to \infty$, however, the dispersion diverges less dramatically than its finite SOI counterpart and instead overestimates the crossing field. Assuming an infinite SOI for this particular system turns out to be a good approximation, because the right-hand side of (4.13) equals 21.2 meV, which is much smaller than spin-orbit gap in Ge.

Fig. 4.2b depicts the behavior of the crossing field as a function of the well thickness and strain, with and without the assumption of an infinite SOI. The crossing field B_c is well approximated by $B_c^{(2)}$ for a well thickness $> 10\,\mathrm{nm}$ with reduced strain levels, as in our experiments. For narrower and highly strained wells, third or higher perturbative terms become more important. These could be included in the model, but at the cost of extremely cumbersome equations, even with infinite SOI. On the other hand, for $\Delta_0 \to \infty$, $B_c^{(2)}$ misses completely the increase of the crossing field for thin wells, which highlights the explicit role of the SOI strength. This is consistent with criterion (4.13) : thin wells increase the right-hand side in (4.13) as $1/l_z^2$, thus requiring Δ_0 to be even larger for this criterion to be satisfied.

4.6 Discussion

From the present model, we see that Zeeman crossings still occur under the assumption of an infinite QW (no barrier effects), an infinite bandgap (6-band $k \cdot p$), and even an infinite spin-orbit gap (4-band $k \cdot p$ for HH and LH). Consequently, LH-HH mixing plays a crucial role in the crossing of spin-split states. Our assumptions also imply that structure inversion asymmetry (SIA) has no role in the observed crossing in ZS energy. SIA is indeed suppressed in infinite wells without external electric fields. Thus, Rashba SOI does not have a dominant effect on the value of B_c. The role of SOI and strain is, however, more evident in Eqs. (4.10) and (4.7). SOI and strain affect $B_c^{(2)}$ mostly through the energy splitting $E^{\mathrm{H}} - E^{\eta}$ and the

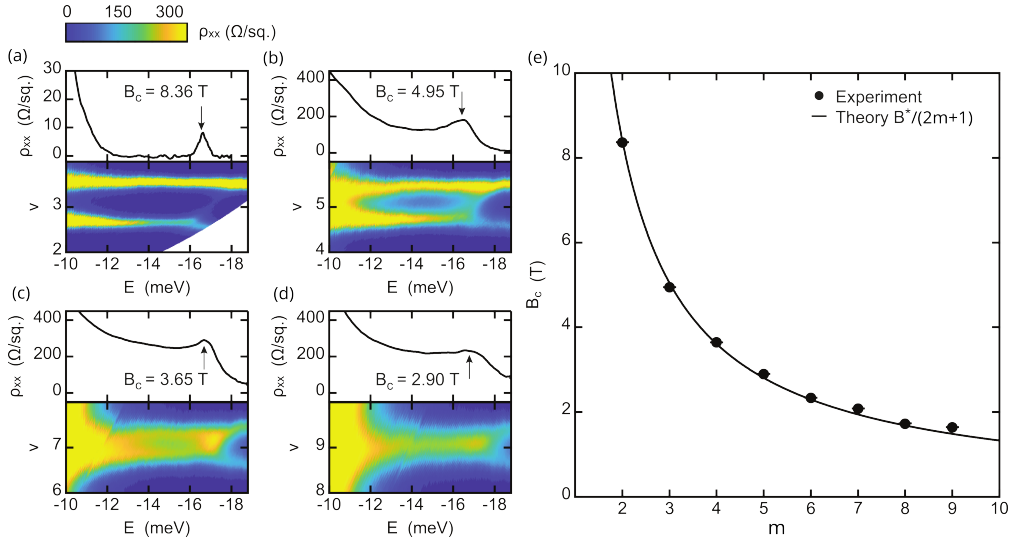

Figure 4.3 **Experiment vs. Theory.** (a)-(d) ρ_{xx} as a function of filing factor ν and energy E around the crossings of Zeeman split states. The upper parts of each panel shows a cross-section at odd filling factors $\nu = 3, 5, 7, 9$. (e) Experimental crossing fields (dots) for $\nu = 3, 5, 7, 9, 11, 13, 15, 17$ fitted using Eq. (4.10) (solid line). The fitting parameter $B^* = 25.258\,\mathrm{T}$.

parameter F. Compressive strain typically increases $E^{\mathrm{H}} - E^{\eta}$, which explains the increase of B_c at higher compressive strain. SOI also increases $E^{\mathrm{H}} - E^{\eta}$, mainly through the spin-orbit energy Δ_0 for SO-like η levels or through the out-of-plane effective mass for LH-like η levels. At $\Delta_0 = 0$ and any strain, the H subbands share the same spectrum as the "$-$" solution of η levels [see (4.3)]. Eq. (4.7) then gives $B^* = 0$ hence no Zeeman crossing occurs. SOI lifts this degeneracy between H and η levels, and thus allows the existence of Zeeman crossings.

The experimental observation of Zeeman crossings are further highlighted by plotting portions of the fan-diagram from Fig. 4.1b as a function of energy and filling factor (Fig. 4.3a-d). The upper part of each panel shows the ρ_{xx} as a function of the energy E at odd-integer values of filling factors from $\nu = 3$ to 9. Fingerprints of Zeeman crossing are observed for filing factors up to $\nu = 17$. In addition to describing the crossings in Zeeman split states, the theoretical framework described above also allows a straightforward evaluation of several parameters. First, we fit the crossing fields extracted from Fig. 4.3a-d ($\nu = 3, 5, ..., 17$) with Eq. (4.10) using B^* as the sole fitting parameter. This yields $B^* = 25.258\,\mathrm{T}$ and the crossing fields obtained from Eq. (4.10) match the experimental values with a relative error $< 4\%$ for $\nu = 3, 5, 7, 9, 11$ and $< 10\%$ for $\nu = 13, 15, 17$ (Fig. 4.3e). Zeeman crossings also approach a fixed energy value as ν increases, as demonstrated in Eq. (4.11). From Fig. 4.1(b), we have $\Delta E \approx 17\,\mathrm{meV}$. Knowing B^* and ΔE gives the value of F, leading to the effective mass and

weak-field g-factor. A rearrangement of Eq. (4.11) gives

$$F = \frac{4}{9}\left(\gamma_1 + \gamma_2 - \frac{\Delta E}{\mu_{\mathrm{B}} B^*}\right) - \frac{\kappa}{3} \approx 1.52. \tag{4.14}$$

From Eqs. (4.12) and (4.14), we extract $g^{\mathrm{H}} = 11.35$, which is close to 12.9 obtained by solving (3.113) numerically. An expression for the subband-edge H in-plane effective mass m^{H} involving the parameter F can also be derived by inserting Eq. (5) from Reference [58] into Eq. (4.12): $m^{\mathrm{H}}/m_0 = (\gamma_1 + \gamma_2 - 3F)^{-1} \approx 0.077$. This value is also close to those reported in the literature at similar hole density [115, 210]. A close relation exists between the crossing fields, the g-factor and the H-η splitting (Eqs. (4.7) and (4.7b)). Knowing two of these quantities is enough to obtain the third. For the system described in Fig. 4.1, the criterion (4.13) is also satisfied (LH-like η become pure LHs), thus the HH-LH splitting is found directly from Eq. (4.7b) :

$$E^{\mathrm{HH}} - E^{\mathrm{LH}} = \frac{6\left(\gamma_2 + \gamma_3\right)^2 \mu_{\mathrm{B}} B^*}{g^{\mathrm{H}}} \approx 76.0\,\mathrm{meV}. \tag{4.15}$$

A numerical solution of (3.113) yields a HH-LH splitting of 62.8 meV. This value does not change significantly when an effective out-of-plane electric field is introduced in (3.113). This is expected from square QWs whose HH-LH splitting is dominated by strain and quantum confinement [46]. For that reason, we assume that the HH-LH splitting does not change with hole concentration, or applied gate voltages. From the HH-LH splitting energy (Eq. (4.15)), one can finally estimate the cubic Rashba coefficient α_3 :

$$\alpha_3 = \frac{e\alpha_0^2\gamma_3}{12\left(\gamma_2 + \gamma_3\right)^3}\left(\frac{g^{\mathrm{H}}}{\mu_{\mathrm{B}} B^*}\right)^2 \approx 4.25 \times 10^5\, e\,\text{Å}^4, \tag{4.16}$$

where e is the elementary charge. α_3 appears in the cubic Rashba SOI Hamiltonian of HH states [46]: $H_3 = \beta_3 i(k_-^3\sigma_+ - k_+^3\sigma_-)$, where $k_\pm = k_x \pm ik_y$ and $\sigma_\pm = (\sigma_x \pm i\sigma_y)/2$ with $\sigma_{x,y}$ the Pauli spin matrices, and $\beta_3 = \alpha_3 F_z$, with $F_z = ep/\epsilon$ the effective out-of-plane electric field in the accumulation mode 2DHG [35], p the hole density and ϵ the Ge dielectric constant. The obtained α_3 is almost twice as large as the one obtained for Ge QW in Reference [46], which had a bigger HH-LH splitting of 110 meV. As mentioned above, we expect α_3 to be independent of the gate voltage or hole concentration, since it depends mostly on the HH-LH splitting. The Zeeman crossings appear at a density $p \sim 6.1 \times 10^{11}\,\mathrm{cm}^{-2}$, corresponding to $F_z \approx 6.8 \times 10^{-4}\,\mathrm{V\,Å}^{-1}$ (by taking $\epsilon = 16.2\epsilon_0$ for Ge), which yields $\beta_3 \approx 290\,\mathrm{eV\,Å}^3$. Note that α_3 or β_3 are hitherto hard to measure in these high

mobility systems with established methodologies : weak anti-localization measurements are impractical due to the small characteristic transport field B_L associated with μm-scale mean free paths [211, 212]; Shubnikov-de Haas oscillations lack sufficient spectral resolution before onset of ZS to resolve the beatings associated with spin-split subbands [190].

4.7 Conclusion

In summary, Zeeman energy crossing of H-levels is observed in a Ge 2DHG under out-of-plane magnetic fields and discussed within a perturbative model describing the hole dispersion. Only second order perturbation in the magnetic field is necessary to describe the crossing in which SOI emerges as an essential feature. However, our analysis indicates that SIA has no effective role. Additionally, this analysis also provides a straightforward framework to evaluate several physical parameters defining the hole states from simple magnetotransport measurements. Crucially, the detailed knowledge of parameters such as the effective g-factor, the in-plane effective mass, and the cubic Rashba coefficient of the underlying material platform will provide the necessary input to further advance design and modelling of hole spin qubits and other hole-based quantum devices.

CHAPTER 5 LIGHT HOLE SPIN CONFINED IN GERMANIUM

5.1 Abstract

The selective confinement of light holes (LHs) in tensile strained germanium (Ge) quantum well is studied by mapping the electronic structure of $Ge_{1-x}Sn_x$/Ge/$Ge_{1-x}Sn_x$ heterostructures as a function of Sn content, residual strain, and Ge well thickness. It is shown that above 12 at.% Sn and below 0.4% residual compressive strain in the barriers, the tensile strain in Ge becomes sufficiently large to yield a valence band edge with LH-like character, thus forming a quasi two-dimensional LH gas in Ge. The LH ground state has a larger in-plane effective mass than that of heavy hole (HH) in $Si_{1-y}Ge_y$/Ge/$Si_{1-y}Ge_y$ quantum wells. Moreover, LHs in optimal $Ge_{1-x}Sn_x$/Ge/$Ge_{1-x}Sn_x$ heterostructures are found to exhibit a strong g-tensor anisotropy, with the in-plane component one order of magnitude larger than that of HHs in typical planar systems. Two of three structure-inversion-asymmetry Rashba parameters, both of which are critical in electric-dipole-spin-resonance (EDSR) experiments, are effectively ten times the size of the cubic Rashba parameter in HH quantum wells. In the regime of LH selective confinement, every layer of the heterostructure is of direct bandgap which can be relevant for efficient optical photon-spin qubit interfaces. This work discusses the broad landscape of the characteristics of LH spin confined in Ge to guide the design and implementation of LH spin-based devices.

5.2 Introduction

Hole spins in group-IV planar gated quantum dots are promising candidates for robust and scalable qubits [12, 48, 117, 123, 126, 213, 214]. Developing these qubits has been so far exclusively based on heavy-hole (HH) states as the materials currently used are restricted to compressively strained germanium (Ge) heterostructures. Interestingly, the advent of germanium/germanium-tin (Ge/$Ge_{1-x}Sn_x$) material system provides an additional degree of freedom to tailor the valence band character in tensile strained Ge thus paving the way to implement silicon-compatible platforms for light-hole (LH) spin qubits [24, 31]. These LH qubits share many of the advantages benefiting the HH ones but also bring about other attractive characteristics pertaining to LHs and Ge/$Ge_{1-x}Sn_x$ heterostructures. These include a strong Rashba-type spin-orbit interaction (SOI) [24] and an efficient coupling with proximity induced superconductivity [25] in addition to the bandgap directness [215] relevant to coupling with optical photons. These characteristics can expand the functionalities of

hole spin qubits by facilitating the implementation of hybrid superconductor-semiconductor devices and photon-spin interfaces.

Although $Ge_{1-x}Sn_x$ semiconductors have been the subject of extensive studies in recent years, research in this area has mainly been focused on integrated photonics and optoelectronics leveraging $Ge_{1-x}Sn_x$ strain- and composition-dependent bandgap [215] leaving practically unexplored their spin properties [24, 216–218]. As a matter of fact, studies on hole spin in $Ge/Ge_{1-x}Sn_x$ are still conspicuously missing in the literature. Herein, this work addresses the dynamics of LH spin confined in $Ge_{1-x}Sn_x/Ge/Ge_{1-x}Sn_x$ heterostructures and elucidates the key parameters affecting its behavior as a function of strain, well thickness, Sn content, and magnetic field orientation. First, the paper describes and discusses the electronic structure of tensile strained Ge on $Ge_{1-x}Sn_x$. Second, the parameters defining the band alignment of the $Ge_{1-x}Sn_x/Ge/Ge_{1-x}Sn_x$ quantum well are introduced and the criteria for LH confinement in Ge are established. The third section outlines the Hamiltonian of the in-plane motion of LHs for out-of-plane and in-plane magnetic fields yielding LH parameters such as the effective mass, the g-tensor, and the Rashba-SOI parameters. LH-HH mixing within the LH ground state is investigated in the fourth section. It is important to note that the focus here is on LH properties in the planar system without the effects of electrostatic in-plane confinement introduced in quantum dot systems [24].

5.3 Light-Hole quantum well in $Ge_{1-x}Sn_x/Ge/Ge_{1-x}Sn_x$

5.3.1 $Ge_{1-x}Sn_x/Ge/Ge_{1-x}Sn_x$ heterostructure

Before delving into the details of the electronic structure of $Ge/Ge_{1-x}Sn_x$, it is instructive to examine the strain-related behavior of bulk Ge. Fig. 5.1a outlines the effect of tensile strain on the band structure of bulk Ge calculated by 8-band (full lines) and 4-band (dashed lines) $k \cdot p$ theory. Here, the calculations assume a bi-isotropic biaxial strain in the (001)-plane without any shear deformations, which is expected for an ideal [001]-oriented epitaxial growth [31,154]. Under these conditions, the 4-fold degeneracy of the VB edge at the Γ point is lifted yielding two spin-degenerate LH and HH bands. In the case of tensile strain, the VB edge is LH-like, while in the broadly studied compressively strained Ge the VB edge is of HH type. As discussed below, there is a threshold of tensile strain beyond which it becomes possible to control and selectively manipulate spin 1/2 LHs instead of spin 3/2 HHs.

The proposed heterostructure consists of a $Ge_{1-x}Sn_x/Ge/Ge_{1-x}Sn_x$ quantum well grown on silicon [31], as illustrated in Fig. 5.1b. Thick $Ge_{1-x}Sn_x$ buffer layers with an increasing Sn content from the Ge virtual substrate (VS) up to the bottom $Ge_{1-x}Sn_x$ barrier prevents the

propagation of defects and dislocations near the Ge quantum well [31]. The lattice mismatch between $Ge_{1-x}Sn_x$ and Ge (with Sn contents above $\sim$10 at. %) is leveraged to achieve high tensile strain in the coherently grown Ge quantum well. A top $Ge_{1-x}Sn_x$ barrier is then grown on the tensile strained Ge layer. As shown below, careful engineering of the lattice strain and Sn content leads to a direct bandgap Ge LH quantum well.

5.3.2 Band alignment and LH confinement

The energy band alignment of the $Ge_{1-x}Sn_x$/Ge/$Ge_{1-x}Sn_x$ heterostructure is computed within the assumption that the in-plane lattice constant $a_\parallel$ is the same in each layer, which is consistent with a pseudomorphic epitaxial growth. The in-plane components ε_{xx} and ε_{yy} of the strain tensor in a material i are given by $\varepsilon_{xx} = \varepsilon_{yy} = a_\parallel/a_0^i - 1$, where a_0^i is the lattice constant of the fully relaxed material i. The out-of-plane strain component ε_{zz} then follows immediately from the relation $\varepsilon_{zz} = -2(c_{12}/c_{11})\varepsilon_{xx}$, where c_{11} and c_{12} are the material elastic constants and $\varepsilon_{kl} = 0$ if $k \neq l$ [154]. Three parameters determine completely the band alignment of the $Ge_{1-x}Sn_x$/Ge/$Ge_{1-x}Sn_x$ heterostructure: the Sn content x, the in-plane strain $\varepsilon_{\mathrm{BR}}$ in the barriers, and the in-plane strain in the Ge well ε_{W}. Since the latter can be counted for from the condition that $a_\parallel$ is constant along the growth direction z, only the barrier composition and strain (x, $\varepsilon_{\mathrm{BR}}$) are required to evaluate the band alignment.

A typical band alignment is displayed in Fig. 5.1c for $x = 0.13$ and $\varepsilon_{\mathrm{BR}} = -0.125\%$. In this instance, HHs and electrons are pushed away from Ge and form a continuum of states in the $Ge_{0.87}Sn_{0.13}$ barriers. Meanwhile, LHs are selectively confined in Ge thereby forming a LH quantum well. Here the combination of large strain in Ge ($\varepsilon_{\mathrm{W}} = 1.95\%$) with small $\varepsilon_{\mathrm{BR}}$ pushes the LH ground state ($\eta 1$) above the HH continuum, leading to the possibility, at very low hole density, to populate only $\eta 1$ and thus to create a pure quasi two-dimensional η gas in Ge. Such system is achievable only in a specific region of the parameter space (x, $\varepsilon_{\mathrm{BR}}$), depending on four energy offsets (see Fig. 5.1c) :

$$\Delta E_1 = \max(\mathrm{LH}) - \max(\mathrm{HH}), \tag{5.1}$$

$$\Delta E_2 = E_1^\eta - \max(\mathrm{HH}), \tag{5.2}$$

$$\Delta E_3 = E_1^\eta - \min(\mathrm{LH}), \tag{5.3}$$

$$\begin{aligned} \mathrm{LBO} &= \max(\mathrm{LH}) - \min(\mathrm{LH}) \\ &= \Delta E_1 - \Delta E_2 + \Delta E_3. \end{aligned} \tag{5.4}$$

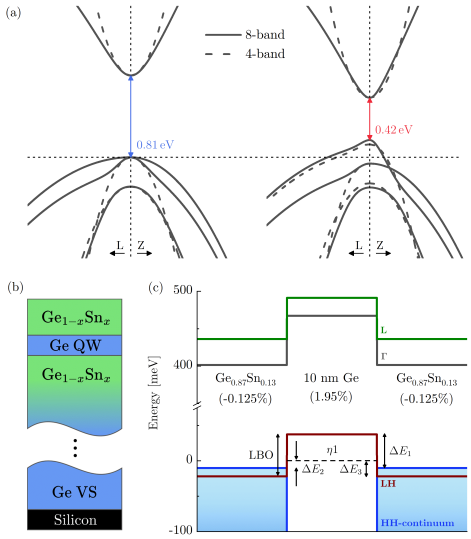

Figure 5.1 (a) Bulk dispersion near the Γ point ($\|\mathbf{k}\| \leq 2.5\,\mathrm{nm}^{-1}$ in both directions) of relaxed Ge (left) and tensile strained Ge (right) computed by the 8-band (full lines) and the 4-band (dashed lines) $k \cdot p$ frameworks. The non-zero components of the strain tensor are $\varepsilon_{xx} = \varepsilon_{yy} = 2\%$ and $\varepsilon_{zz} = -2(c_{12}/c_{11})\varepsilon_{xx} \approx -1.3\%$. The conduction band was obtained from an effective mass approximation in the 4-band computations. (b) Schematic illustration of the proposed $\mathrm{Ge}_{1-x}\mathrm{Sn}_x/\mathrm{Ge}/\mathrm{Ge}_{1-x}\mathrm{Sn}_x$ heterostructure. (c) Band alignment profile of a $\mathrm{Ge}_{1-x}\mathrm{Sn}_x/\mathrm{Ge}/\mathrm{Ge}_{1-x}\mathrm{Sn}_x$ quantum well for selected barrier parameters. In this case, $\Delta E_{1,2,3}$ and LBO are positive. ε_{xx} in each layer is written in parenthesis.

Here, max(LH) and min(LH) are the energies at the bottom and top of the LH quantum well, respectively, and max(HH) is the energy at the edge of the HH continuum. The zero energy point is placed on the ground η subband, i.e. $E_1^{\eta} = 0$. Band offsets ΔE_1 and LBO (LH band offset) do not depend on the well thickness w.

Fig. 5.2a presents a two-dimensional map of band offsets LBO and ΔE_1 with x and $\varepsilon_{\mathrm{BR}}$ as independent parameters. The corresponding strain in the Ge well ε_{W} is also shown (black dotted lines) only for the tensile strain regime ($\varepsilon_{\mathrm{W}} > 0$). The Ge indirect-to-direct transition occurs at $\varepsilon_{\mathrm{W}} = 1.68\%$ (solid black line) according to the parametrization of Table 3.3. Similarly, the $\mathrm{Ge}_{1-x}\mathrm{Sn}_x$ barriers exhibit bandgap directness above the dashed-dot blue line. Constant LBO are indicated by the solid red curves, where LBO = 0 corresponds to a completely flat LH profile along the growth direction. Finally, dashed red curves indicate constant ΔE_1, where $\Delta E_1 = 0$ corresponds to the LH band edge in Ge sitting at the same energy as the HH band edge in the barriers. As discussed below, a large and positive ΔE_1 allows η1 to emerge from the continuum for sufficiently thick quantum wells.

LHs are confined in Ge if and only if LBO > 0. However, depending on ΔE_1 and the well

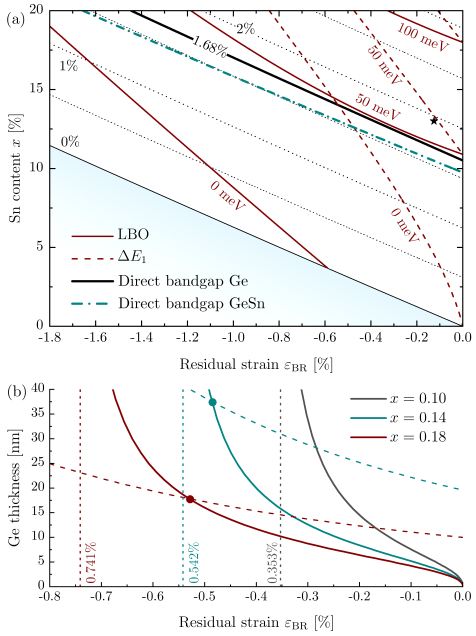

Figure 5.2 (a) Two-dimensional contour map of band offsets ΔE_1 and LBO, strain in Ge and bandgap directness as a function of x and $\varepsilon_{\mathrm{BR}}$ at $T = 300\,\mathrm{K}$. Contour lines for LBO and ΔE_1 are given at 0, 50 and 100 meV. The star indicates the system from Fig. 5.1c. (b) Minimal well thickness w_0 (solid lines) required for a LH-like valence band edge as a function of $\varepsilon_{\mathrm{BR}}$ at fixed Sn content in the barriers. Dashed lines are the Ge critical growth thickness h_c estimated from the People and Bean relation. Solid circles indicate where $w_0 = h_c$ for a given x. For $x = 0.10$, $h_c \approx 46\,\mathrm{nm}$ at $\varepsilon_{\mathrm{BR}} = 0$.

thickness w, these confined LHs could be situated within the HH continuum (negative ΔE_2). In the region $\Delta E_1 \leq 0$, LHs can never emerge from the continuum since the bottom of the LH well is below the HH band edge. However, if $\Delta E_1 > 0$, there is a minimal QW thickness w_0 for which $\eta 1$ emerges from the continuum. This lower bound depends on both Sn content and lattice strain (i.e., x and $\varepsilon_{\mathrm{BR}}$) in the barriers and is plotted in Fig. 5.2b (solid lines). At $w = w_0$, the energy required for $\eta 1$ to escape the well is exactly LBO $- \Delta E_1$, i.e. the strain-induced HH-LH splitting in the barriers. $w_0 \to \infty$ on the $\Delta E_1 = 0$ curve, while $w_0 = 0$ if the barriers are fully relaxed. In addition to the lower bound $w_0 < w$, the maximum strain energy that the Ge QW can accommodate also introduces an upper bound on w. This upper bound is given by the Ge critical growth thickness h_c, beyond which misfit dislocations start to appear at the interfaces and tensile strain in Ge is strongly suppressed. The dashed lines in Fig. 5.2b show an estimation of h_c based on the People and Bean formula [219, 220]. Here this model is applied for the critical thickness of a Ge layer with equilibrium lattice constant $a_0^{\mathrm{Ge}} \equiv a_0(0)$ pseudomorphically grown on $\mathrm{Ge}_{1-x}\mathrm{Sn}_x$ with lattice constant $a_0(x)\,(1 + \varepsilon_{\mathrm{BR}})$.

5.4 Light-Hole spin properties

5.4.1 Effective masses and spin parameters

In this section, the ground state subband effective mass, the out-of-plane and in-plane g factors, and the Rashba parameters are computed as a function of Sn content in the $Ge_{1-x}Sn_x$ barriers (x) and well thickness w. These parameters give important information on how LHs move in the plane and how they respond to magnetic fields. Despite being intrinsic to a given subband (here the focus is given to the lowest subband $\eta 1$), there is generally a significant influence from neighboring levels through inter-subband couplings. Moreover, the wavefunction spread across interfaces can also influence subband parameters. In heterostructures such as $Ge/Si_{1-y}Ge_y$ quantum wells, where both types of holes are confined into the same layer and the band offsets are large, inter-subband coupling is significant to an energy scale comprising only a few tens of subbands due to quantization effects. For instance, it is often a reasonable approximation to include the coupling to only one or two η subbands for a H ground state [189], or around 50 η subbands when band offsets are taken into account [54]. In $Ge/Ge_{1-x}Sn_x$ quantum wells, inter-subband couplings must include $\sim 10^2$ subbands due to the neighboring continuum. Moreover, small LBOs leading to a sizable spread of $\eta 1$ into the barriers require an accurate description of the subband envelopes. The approach described in Section 3.3.2 provides an efficient framework to solve problems as such, since it is applicable to any type of confinement. Due to the neighboring continuum of levels, the subband-edge basis $\mathcal{B}_0$ contains $2N_\perp = 400$ elements closest to $\eta 1$, which is large enough that all effective parameters converge for $\eta 1$. Our implementation of $k \cdot p$ theory and how strain is incorporated into the model is described in Chapter 3.

Here we recall that η levels such as $\eta 1$ always consists of a superposition of spin 1/2 CB electron, LH, and split-off (SO) hole envelopes. At $\mathbf{k}_\parallel = 0$, this is written as

$$|\eta\sigma\rangle = \left|\frac{1}{2}, \frac{\sigma}{2}\right\rangle_c |c\rangle + \left|\frac{3}{2}, \frac{\sigma}{2}\right\rangle |\ell\rangle + \sigma \left|\frac{1}{2}, \frac{\sigma}{2}\right\rangle |s\rangle \,, \tag{5.5}$$

where $\sigma = \pm 1$ is the pseudo-spin quantum number and $\langle z \,|\, c, \ell, s\rangle = f^{c,\ell,s}(z)$ are the CB, LH, and SO envelope functions, respectively. The additional contribution from H levels away from $\mathbf{k}_\parallel = 0$ is investigated in the next section. For reference, the SO contribution $\langle s \,|\, s\rangle$ in $\eta 1$ is typically smaller than 10% for the range of barrier and well parameters considered here, but it plays an important role in the effective mass calculations, as discussed below. The CB contribution $\langle c \,|\, c\rangle$ in $\eta 1$ is around 5%, where the envelopes $f^c(z)$ are anti-symmetric with respect to the center of the well and have their maximal amplitude near the interfaces.

We also recall that for an out-of-plane magnetic field $\mathbf{B} = B\mathbf{e}_z$, the in-plane motion of $|\eta\sigma\rangle$ up to K^3 is described by an effective two-dimensional Hamiltonian (see chapter 3)

$$\begin{aligned} H_{\text{eff}}^{\perp} &= \alpha_0\gamma K_{\parallel}^2 + \frac{\alpha_0}{\lambda^2}\frac{g_{\perp}}{2}\sigma_z \\ &\quad + i\beta_1\left(K_-\sigma_+ - \text{H.c.}\right) - i\beta_2\left(K_+^3\sigma_+ - \text{H.c.}\right) \\ &\quad + i\beta_3\left(K_-K_+K_-\sigma_+ - \text{H.c.}\right). \end{aligned} \tag{5.6}$$

The three Rashba parameters $\beta_{1,2,3}$ arise from space inversion asymmetry. When a small DC electric field $\mathbf{F} = F_z\mathbf{e}_z$ is applied to an otherwise symmetric well, all β_i parameters behave linearly with F_z and involve only odd powers of the field:

$$\beta_i = \alpha_i F_z + O\left(F_z^3\right), \tag{5.7}$$

where $i = 1, 2, 3$. For an in-plane magnetic field $\mathbf{B} = B(\mathbf{e}_x\cos\phi + \mathbf{e}_y\sin\phi)$ with vector potential $\mathbf{A} = B(\mathbf{e}_x\sin\phi - \mathbf{e}_y\cos\phi)z$, the in-plane motion is instead described by

$$\begin{aligned} H_{\text{eff}}^{\parallel} &= \alpha_0\gamma k_{\parallel}^2 + \frac{\alpha_0}{\lambda^2}\frac{g_{\parallel}}{2}\left(e^{-i\phi}\sigma_+ + \text{H.c.}\right) \\ &\quad + i\beta_1\left(k_-\sigma_+ - \text{H.c.}\right) - i\beta_2\left(k_+^3\sigma_+ - \text{H.c.}\right) \\ &\quad + i\beta_3\left(k_-k_+k_-\sigma_+ - \text{H.c.}\right). \end{aligned} \tag{5.8}$$

The in-plane g factor is given by

$$\begin{aligned} \frac{g_{\parallel}}{2} &= \Im\left\{\langle c\,|\,zgk_z\,|\,c\rangle - 2\left\langle +\,\middle|\,u_+'\,\middle|\,-\right\rangle\right\} \\ &\quad - \sqrt{2}\Re\left\{\frac{1}{\sqrt{3}\alpha_0}\langle c\,|\,zP\,|\,+\rangle + \langle -\,|\,s\rangle\right\}, \end{aligned} \tag{5.9}$$

where

$$|\pm\rangle = |\ell\rangle \pm 2^{\pm 1/2}\,|s\rangle\,, \tag{5.10}$$

$$u_{\pm}' = \{z\gamma_3, k_z\} \pm [z\kappa, k_z], \tag{5.11}$$

In (5.9), the $z = 0$ coordinate is chosen such that (see Section 3.3.4)

$$\langle z \rangle = \sum_{\tau=\{c,\ell,s\}} \langle \tau \,|\, z \,|\, \tau \rangle = 0. \tag{5.12}$$

This ensures, when setting $k_x = k_y = 0$, that $g_\parallel$ is gauge independent and corresponds to that at the subband edge. Equation (5.9) reduces to the well known $|g_\parallel| = 4\kappa$ in the special case of 4-band Luttinger Hamiltonian with LBO $\to \infty$. The in-plane effective mass γ, the g-factor components and the three Rashba parameters α_i are plotted as a function of x and w in Fig. 5.3 panel (a), (b)-(c) and (d)-(f) respectively. A negative g means that the spin-down level ($\sigma = -1$) is closer to the bandgap than the spin-up level.

5.4.2 η-H mixing

In the vicinity of $\mathbf{k}_\parallel = 0$, η levels acquire a small H component in addition to the three terms in (5.5), resulting in a η-H mixed state $|\psi, \mathbf{k}_\parallel\rangle$. For η1, this is written as (up to a normalization constant and to first order in k) :

$$|\psi, \mathbf{k}_\parallel\rangle = |\eta\sigma\rangle - i\sigma\alpha_0 k_{-\sigma} \left|\frac{3}{2}, \frac{3\sigma}{2}\right\rangle \sum_l \frac{T_l^{\mathrm{x}} \,|h_l\rangle}{E_1^\eta - E_l^{\mathrm{H}}} + \ldots, \tag{5.13}$$

where the coefficients T_l^{x} are given in (3.93) (with j indices dropped). To first order in k, mixing is stronger between η and H subbands with opposite parity (from k_z terms in T_l^{x}) and with the same spin component sign, i.e. $|\eta\sigma\rangle$ couples with $\left|\frac{3}{2}, \frac{3\sigma}{2}\right\rangle$. The H contribution ρ in the mixed subband $\left|\psi, \mathbf{k}_\parallel\right\rangle$ is given by the sum of the absolute square of each coefficient in front of H terms. By symmetry, only even powers of k must appear in ρ :

$$\rho = a k_\parallel^2 + O(k^4), \tag{5.14}$$

where a can be found from (5.13) :

$$a = \alpha_0^2 \sum_l \frac{|T_l^{\mathrm{x}}|^2}{\left(E_1^\eta - E_l^{\mathrm{H}}\right)^2}. \tag{5.15}$$

The expression $\rho \approx a k_\parallel^2$ is valid for small $\mathbf{k}_\parallel$ such that $\rho \ll 1$. In general, ρ lies in the interval $[0, 1]$ with $\rho = 0$ ($\rho = 1$) corresponding to a pure η (H) subband.

ρ as a function of k_x is displayed in Fig. 5.4a for $w = 6\,\mathrm{nm}$ and $w = 10\,\mathrm{nm}$ at $x = 0.13$. When k_x is small, the parabolic term in (5.14) fits well the numerically computed ρ. Mixing

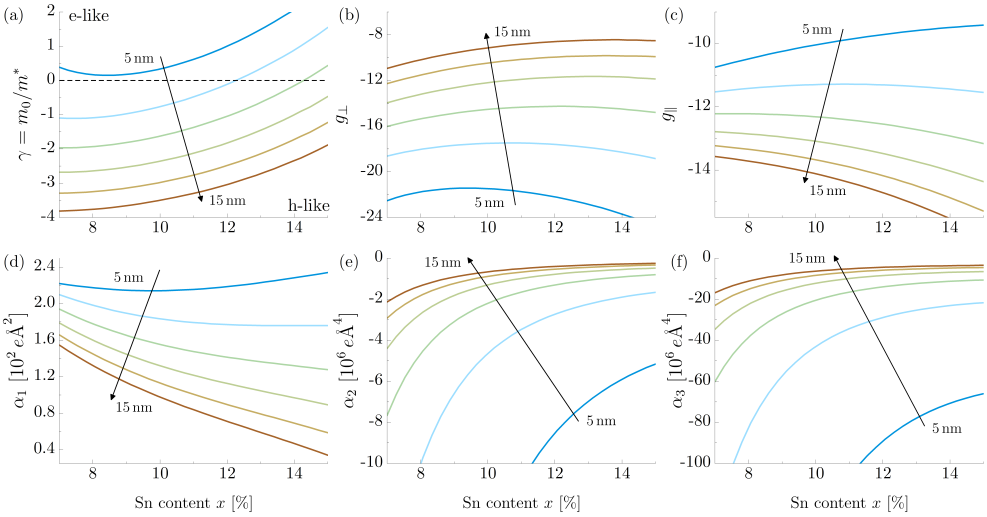

Figure 5.3 η1 subband parameters as a function of the well thickness and x for fully relaxed $Ge_{1-x}Sn_x$ barriers ($\varepsilon_{BR} = 0$). (a) Inverse effective mass γ. (b) out-of-plane g factor. (c) in-plane g factor. (d)-(e)-(f) α_1, α_2, α_3 Rashba parameters respectively. The calculations were carried out for a well thickness in the 5-15 nm range with 2 nm steps. The data displayed here are for thicknesses separated by a 2 nm-step.

decreases with increasing energy splitting between η1 and the H-level continuum, as indicated by smaller ρ at the larger well thickness $w = 10$ nm. This remains true for different Sn compositions, as illustrated in Fig. 5.4b where a is plotted as a function of w and x for $\varepsilon_{BR} = 0$.

5.5 Discussion

The results above demonstrate that the lattice mismatch between $Ge_{1-x}Sn_x$ alloys and Ge provides an additional degree of freedom to engineer the tensile strain required to confine LHs in Ge. According to Fig. 5.2a, the region of interest, as defined by the parameters (x, ε_{BR}), lies in the range where x is above 0.12 and the compressive strain in the barriers ε_{BR} is below -0.4% (i.e., $|\varepsilon_{BR}| \lesssim 0.4\%$). In this range, all band offsets ΔE_i are positive and the Ge layer is of direct bandgap. $Ge_{1-x}Sn_x$ layers at Sn content in the proposed range have already been demonstrated experimentally [215]. However, the addition of a highly tensile strained Ge layer on top of strain-relaxed $Ge_{1-x}Sn_x$ is still under development. For instance, the authors in Reference [31] reported a 1.65% tensile strained Ge quantum well on partially relaxed $Ge_{0.854}Sn_{0.146}$ barriers with a residual strain to $\varepsilon_{BR} \approx -0.54\%$. This system would be located near the crossing between the 0 meV ΔE_1 line and the 50 meV LBO line in Fig. 5.2a, very close to the optimal region of interest mentioned earlier. Strain relaxation in the barriers is

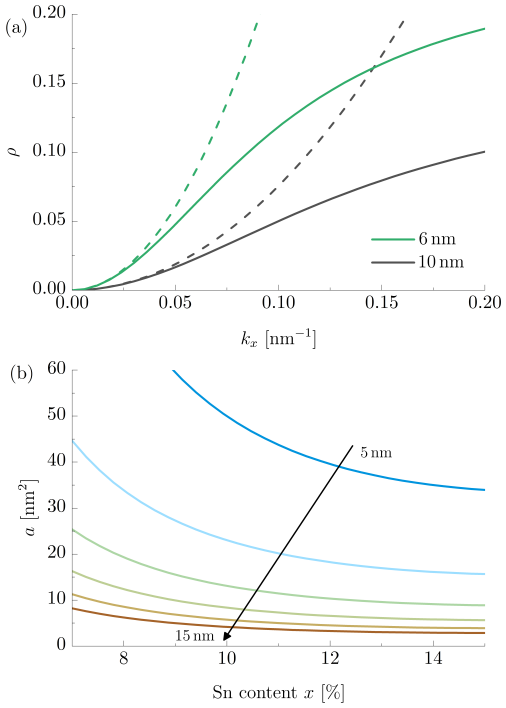

Figure 5.4 (a) HH contribution ρ as a function of the wavevector k_x for a quantum well thickness $w = 6\,\text{nm}$ and $w = 10\,\text{nm}$. Dashed lines correspond to the quadratic approximation $\rho \approx ak_{\parallel}^2$. (b) Coefficient a as a function of w and x. The data displayed here are for thicknesses separated by a 2 nm-step.

necessary to enhance confinement in Ge, while relaxing the criterion of minimal well thickness w_0 required for a LH-like valence band edge ($\Delta E_2 > 0$). The ideal amount of strain relaxation for a given barrier Sn content can be estimated from Fig. 5.2b. For example, a barrier with $x = 0.14$ does not allow a LH-like valence band edge for $|\varepsilon_{\text{BR}}| > 0.542\%$ compressive strain. The additional requirement $w_0 < h_c$, where h_c is the critical thickness of Ge, further reduces the range of $|\varepsilon_{\text{BR}}|$ to around $< 0.5\%$ compressive strain. Reducing the amount of Sn in the barriers relaxes the limit imposed by the critical thickness h_c, but at the cost of a smaller LBO. In contrast, increasing x to 0.18 for instance slightly increases the range for $|\varepsilon_{\text{BR}}|$ to around $< 0.525\%$, increases significantly the LBO and ΔE_1 (Fig. 5.2a) but at the expense of a smaller h_c and a narrower window $w_0 < w < h_c$, but still in the range typically achievable in epitaxial growth experiments.

The in-plane effective mass γ (Fig. 5.3a) shows a strong dependence on both x and w, with small γ expected from the general rule that η levels are heavier in the plane than H levels. There is also an interesting feature where the dispersion changes from a hole-like ($\gamma < 0$) to an electron-like ($\gamma > 0$) curvature at $\mathbf{k}_{\parallel} = 0$. In the hole-like regime, the valence band

edge is formed by a single valley located at $\mathbf{k}_\parallel = 0$. In contrast, in the electron-like regime, the valence band edge consists of 4 valleys, each located a distance k_0^* from $\mathbf{k}_\parallel = 0$ along the four equivalent $\langle 110 \rangle$ crystallographic directions in the QW plane. For instance, for a 5 nm well at $x = 0.13$ and $\varepsilon_{\mathrm{BR}} = 0$ the valley minima are located at $k_0^* \approx 0.0813\,\mathrm{nm}^{-1}$ away from $\mathbf{k}_\parallel = 0$. For larger wavevectors, the dispersion goes away from the bandgap as required, owing to k^4-terms or higher that are not taken in account by the effective Hamiltonians (5.6) and (5.8). According to Fig. 5.3a, electron-like subbands occur for small w and large x. This effect takes place for two reasons. The first is when the η subband anti-crosses a neighboring H subband such that the curvature is inverted at $\mathbf{k}_\parallel = 0$. This is typical in systems where the ground state is H-like and the first η subband is allowed to mix strongly with the first excited H subband [133], or when the η subband is close to a H-level continuum (e.g. when w is small). When a η level is far from neighboring H levels (e.g. when tensile strain is large), mixing decreases, as illustrated in Fig. 5.4b, and becomes too weak to invert the curvature. The second reason for a curvature change is related to the anti-crossing between the LH and the SO bands in the bulk dispersion of Ge for $k_z > 0$ (Fig. 5.1a). This anti-crossing results in a curvature sign change of the LH band at some point k_z^*, such that the bulk energy dispersion $E(k_x, k_y; k_z)$ has a hole-like (electron-like) curvature when k_z is fixed to a value smaller (larger) than k_z^* and $k_{x,y}$ are close to zero. For a quantum well along the z direction, the reciprocal-space envelope functions $\tilde{f}(k_z)$ become wider for thinner wells and thus get a larger contribution from the electron-like regions in k-space, resulting in a dispersion with inverted curvature at $\mathbf{k}_\parallel = 0$.

A major difference with η subbands is the large $g_\parallel$ compared to heavy hole systems [57, 117, 126, 178, 190]. A comparison between $g_\parallel$ and $g_\perp$ reveals an anisotropy for well thicknesses away from ∼10 nm. Both components have a stronger dependence on w than on x but have opposite behavior with w due to how they couple with neighboring subbands. For the out-of-plane component, $g_\perp \sim 2\kappa$ for large w because the coupling with neighboring levels becomes weaker as $\eta 1$ gets further from the continuum. In contrast, the in-plane g-factor does not depend on couplings with neighboring H levels (c.f. (5.9)) and is instead more influenced by the spatial distribution of the envelopes across the layers. Thus, for large (small) w, $g_\parallel \sim 4\kappa$ with κ being that of Ge ($\mathrm{Ge}_{1-x}\mathrm{Sn}_x$).

Another peculiar feature associated with η subbands is the absence of direct connection between γ and $g_\perp$ in contrast with heavy holes (see Eq. (5) in Reference [58] for instance). Perturbation theory gives the following for γ and $g_\perp$ (see Section 3.3.5):

$$\gamma = \Gamma^{\eta} + C + D, \tag{5.16a}$$

$$\frac{g_{\perp}}{2} = \frac{G^{\eta}}{2} - C + D, \tag{5.16b}$$

where Γ^{η}, G^{η} are given in (3.93) and (3.106a), while C and D are described in chapter 3.3.5. For H levels, a similar expansion gives:

$$\gamma^{\mathrm{H}} = \Gamma^{\mathrm{H}} + C', \tag{5.17a}$$

$$\frac{g_{\perp}^{\mathrm{H}}}{2} = \frac{G^{\mathrm{H}}}{2} + C'. \tag{5.17b}$$

In the latter case, one can combine the equations for γ^{H} and $g_{\perp}^{\mathrm{H}}$ to eliminate the C' term, resulting in the expression (3.165) involving only the mass and the g-factor [58,221]. However, the result is different for η subbands due to the additional D term in (5.16). The latter is also related to the non-zero β_1 coefficient of η subbands [24].

Rashba parameters follow the general behavior $\alpha_i \to 0$ as w increases. This is caused by a reduced sensitivity of the wavefunction to electric fields when the level does not spread as extensively into the barriers. Although the QW is characterized by relatively small LBOs ($\lesssim 100\,\mathrm{meV}$) and small out-of-plane effective masses, the device operation can comfortably sustain realistic DC electric fields along the growth direction regardless of the well thickness and LBO without inducing any envelope leak into the barriers. In devices where space inversion symmetry needs to be broken, such as in electric dipole spin resonance (EDSR) experiments, this should not be an issue as the relevant Rashba parameter α_3 for EDSR, (which is proportional to $\gamma_2 + \gamma_3$) is one order of magnitude larger than the α_2 Rashba parameter (proportional to $\gamma_2 - \gamma_3$), thus requiring smaller out-of-plane fields [24].

5.6 Conclusion

This work demonstrates how $Ge_{1-x}Sn_x/Ge/Ge_{1-x}Sn_x$ heterostructures can be tailored to achieve a selective confinement of LHs in Ge while pushing HHs in to the $Ge_{1-x}Sn_x$ barriers. For a sufficiently large Sn content ($x > 0.12$), small residual compressive strain in the barriers ($|\varepsilon_{\mathrm{BR}}| < 0.4\%$) and a well thickness $w > w_0$, the η ground state emerges from within the H-level continuum, thus yielding a pure η-like valence band edge ($\Delta E_2 > 0$). This regime also corresponds to a direct bandgap in both the well and its barriers, owing to the large

tensile strain in the Ge well and the high Sn content in the barriers. Satisfying the condition of $\Delta E_2 > 0$ imposes a threshold for residual strain in the barriers beyond which a LH-like VB edge becomes virtually impossible.

The in-plane effective mass, the out-of-plane and in-plane g-factor, and the Rashba parameters $\alpha_{1,2,3}$ were computed by explicitly taking in account the spread of the η-spinor envelopes into the barriers and the coupling with the neighboring H-level continuum. Small inverse effective masses γ are obtained. A peculiar sign change in γ appearing for small well thicknesses ($w \lesssim 7\,\mathrm{nm}$) is observed and attributed to the proximity of the η to the H continuum (larger η-H mixing) and the contribution of the split-off band in the η spinor. An increasingly strong anisotropy in the g-factor components is also observed for well thicknesses away from $\sim$10 nm. Most notably, the in-plane component of the g-tensor is significantly larger than what is expected in heavy hole systems. A non-zero linear Rashba parameter α_1 was obtained, as anticipated for η systems, with an α_3 coefficient one order of magnitude larger than α_2.

CHAPTER 6 LIGHT HOLE GATE-DEFINED SPIN-ORBIT QUBIT

6.1 Abstract

The selective confinement of LHs is demonstrated by introducing a low-dimensional system consisting of highly tensile-strained Ge quantum well enabling the design of an ultrafast gate-defined spin qubit under electric dipole spin resonance. The qubit size-dependent g-factor and dipole moment are mapped, and the parameters inducing their modulation are discussed. It is found that the LH qubit dipole moment is 2 to 3 orders of magnitude higher than that of the canonical heavy-hole qubit. This behavior originates from the significant spin splitting resulting from the combined action of large cubic and linear Rashba spin-orbit interactions that are peculiar to LHs. The qubit relaxation rate is also affected by the strong spin-orbit interaction and follows typically a B^7 behavior. The proposed all-group IV, direct bandgap LH qubit provides an effective platform for a scalable qubit-optical photon interface sought-after for long-range entanglement distribution and quantum networks.

6.2 Introduction

Gated quantum dots (QDs) exploiting the strong spin-orbit interaction (SOI) of holes and their quiet quantum environment provide practical building blocks for quantum processors [12,48,57,117,126,178,222–226]. However, due to the restricted choice of low-dimensional systems (e.g., Ge/SiGe), current hole spin qubits are based predominately on heavy-hole (HH) spins [47]. Notwithstanding this progress, the ability to utilize light-hole (LH) spins would enable additional degrees of freedom to engineer qubits with extended functionalities. Indeed, LHs allow simple schemes for a direct mapping of superposition from a flying qubit to a stationary spin qubit [26] as well as a better resilience against charge noise [227] and an enhanced proximity-induced superconductivity transfer [25]. Additionally, LHs are also known to have strong SOI yielding fast Rabi oscillations [227]. Nevertheless, the development of LH qubits has been hampered by the lack of proper material systems. Here, we address this limitation and introduce a new low-dimensional system to control LH states.

The selective confinement of LHs in Ge quantum well (QW) requires sufficiently high tensile strain, which can be achieved using the emerging germanium-tin ($Ge_{1-x}Sn_x$) alloys [31, 34]. $Ge/Ge_{1-x}Sn_x$ hole spin devices combine all advantages that are inherent to group IV semiconductors [82, 109]. Besides the weaker hyperfine interaction with the surrounding nuclear spin bath resulting from the p-symmetry of the hole wavefunction [20, 65, 228], the strong

SOI in the valence band of Ge and Sn would enable all-electrical driving of the qubit without the need for an external RF transmission line and create rich spin-related phenomena unique to holes [33, 46]. Moreover, the $Ge_{1-x}Sn_x$ alloy spans a wide range of lattice parameters [160, 165, 215], which is useful to control the hole spin properties through the epitaxial strain directly on silicon wafers [31, 229, 230].

6.3 Results and discussion

Fig. 6.1 illustrates the gate-defined LH QD. Note that the lattice mismatch between Ge and $Ge_{1-x}Sn_x$ induces a significant tensile strain in the Ge layer, which lifts the HH-LH degeneracy yielding a LH-like valence band edge (Fig 6.1b). The $Ge_{1-x}Sn_x$/Ge/$Ge_{1-x}Sn_x$ heterostructure confines LHs in the Ge layer for x typically higher than 0.11, while the HHs are pulled into the $Ge_{1-x}Sn_x$ barriers [31]. A set of electrostatic gates on top of the heterostructure helps confine the LH in the plane by applying a DC voltage. Note that Ge becomes a direct bandgap semiconductor at a tensile strain higher than 1.68% [34]. The EDSR is performed by applying a microwave voltage. A feature that is sometimes neglected [188, 189, 210] but needs to be accounted for in this system is the spread of the LH wavefunction into the barriers. Because the HHs are located in the barriers, LH-HH mixing wavefunction overlap only occurs outside the QW. Assuming a hard wall potential at the interface is therefore equivalent to neglecting entirely the LH-HH mixing. Moreover, the LH subband dispersion non-parabolicity must also be considered. The theoretical framework outlined in Chapter 3.3.5 for the in-plane motion of LHs explicitly takes into account these peculiar features.

Starting from Hamiltonian $\mathbf{H}_{\mathrm{QW}}$ [c.f. (3.104)] describing the motion of electron and holes in a QW with a perpendicular $\mathbf{B}$-field, an Hamiltonian H_{eff} for the in-plane motion of the ground η level up to K^4 with the usual assumptions of bi-axial epitaxial strain and [001]-oriented substrates is given by (3.158), which we explicitly rewrite here for $\tau = \eta$:

$$\begin{aligned} H_{\mathrm{eff}} = E^{\eta} + \alpha_0 \left(\gamma + \frac{\chi_\perp}{2l_B^2}\sigma_z\right) K_\parallel^2 + \frac{\alpha_0}{2l_B^2} g_\perp \sigma_z + \alpha_0 \zeta_\gamma K_\parallel^4 + \frac{\alpha_0}{4l_B^4}\zeta_\perp \\ + \left[i\beta_1 K_- \sigma_+ - i\beta_2 K_+^3 \sigma_+ + i\beta_3 K_- K_+ K_- \sigma_+ + \alpha_0 \zeta_a K_-^4 + \mathrm{H.c.}\right]. \end{aligned} \tag{6.1}$$

The approach described in 3.3.5 to obtain (6.1) is similar to that employed by References [188, 189, 210] for instance. However, we emphasize here that the spread of the wavefunction into the barriers and the effects of the DC field $\mathbf{F} = F_z \mathbf{e}_z$ are implicitly taken into account from the shape of the envelopes. The effective parameters in (6.1) are also calculated from

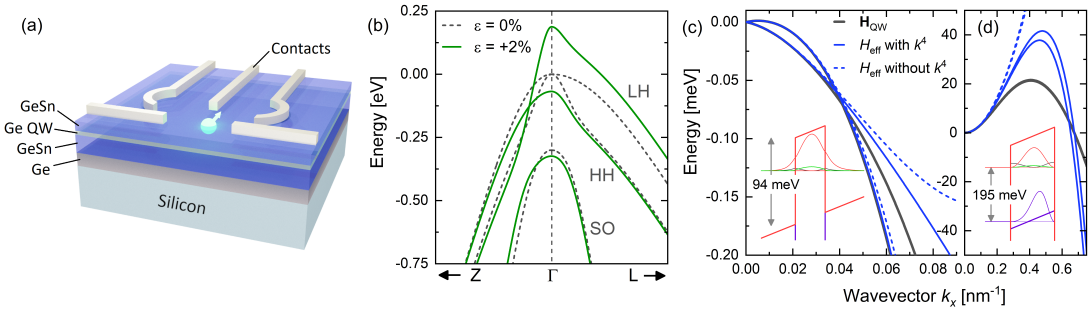

Figure 6.1 (a) Schematic of a gate-defined Ge/$Ge_{1-x}Sn_x$ LH qubit. (b) Band structure of the valence band in bulk Ge without strain (dashed lines) and with 2% tensile strain (solid lines). $k \cdot p$ parameters taken from Reference [152]. (c)-(d) Ground LH subband dispersion from the numerical diagonalization of $\mathbf{H}_{\mathrm{QW}}$ (black solid lines) and from H_{eff} with (without) k^4 terms in solid (dashed) blue. (c) : Ge/$Ge_{1-x}Sn_x$ LH QW with $F_z = 1\,\mathrm{V/\mu m}$. (d) : Infinite Ge LH QW with $F_z = 5\,\mathrm{V/\mu m}$. Energy scale is in meV in both panels. Insets show the envelope probability density of the lowest subband (ground HH subband is also shown in (d)). The larger component of the wavefunction is the LH part of the spinor (red). The smaller component with one lobe corresponds to the SO part (green) and the component with two small lobes at the Ge interfaces corresponds to the CB part (black). The tensile strain in Ge is 2.38% in both cases corresponding to $x = 0.15$.

a large subband edge basis due to the large number of H levels in the barriers. Fig. 6.1 shows the dispersion of the ground η subband for two different QWs. Fig.6.1(c) displays the case of a 13 nm Ge QW with relaxed $Ge_{0.85}Sn_{0.15}$ barriers. Close to $k_{\|} = 0$, H_{eff} fits exactly $\mathbf{H}_{\mathrm{QW}}$ because the effective parameters in (6.1) are given exactly by 4th order perturbation theory. H_{eff} diverges from $\mathbf{H}_{\mathrm{QW}}$ further away from $k_{\|} = 0$ because k^5-terms or higher become important. This behavior is exacerbated for a QW with infinite band offsets (Fig.6.1(d)). In both cases, H_{eff} diverges faster when k^4 terms are neglected.

The calculations also predict an effective mass for the ground LH subband of the opposite sign (clearly visible in Fig 6.1d, see also Chapter 5) for certain QW parameters. Such behavior was also observed for different material systems [133, 231, 232]. This effect becomes more prominent as the QW thickness decreases. The typical hole-like dispersion is recovered above a critical thickness, corresponding to 11 nm for the Ge/GeSn QW system in Fig. 6.1c. To simplify the LH qubit calculations, the thickness is fixed at 13 nm.

The QD Hamiltonian includes the isotropic and parabolic confinement from the top gates, which can be added directly to H_{eff} as a good approximation if the QD size is not too small: $H_{\mathrm{QD}} = H_{\mathrm{eff}} + m^*\omega_0^2\left(x^2+y^2\right)/2$, where $m^* = m_0/\gamma$ is the in-plane effective mass. H_{QD} is diagonalized by first writing $H_{\mathrm{QD}} = H_0 + H'$, where H_0 consists of the first two terms in (6.1) plus the parabolic confinement :

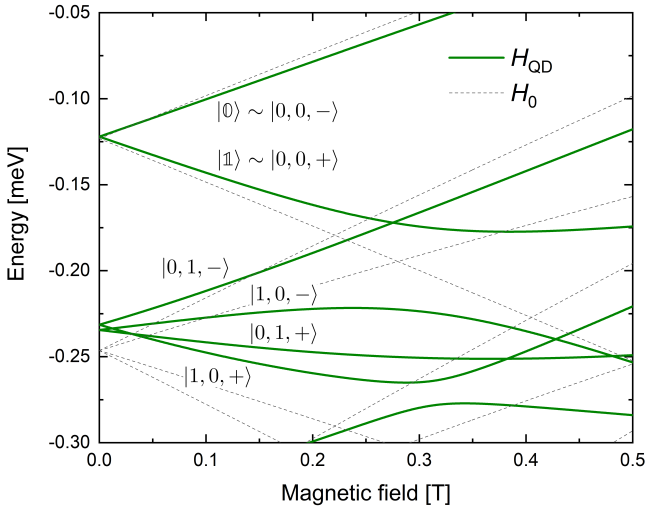

Figure 6.2 LH QD orbital energies as a function of B. The QD size l_0 at $B = 0$ is kept constant at 25 nm. Black dotted lines represent the eigenvalues of H_0, while the solid green lines are those of H_{QD}. The qubit levels $|\mathbb{0}\rangle$ and $|\mathbb{1}\rangle$ and excited orbitals are displayed with their main contributions from the eigenstates $|n_1, n_2, \sigma\rangle$ for $B = 0.1$ T. The QW parameters are the same as in Fig. 6.1c.

$$H_0 = \alpha_0 \gamma K_{\parallel}^2 + \frac{1}{2} m^* \omega_0^2 \left(x^2 + y^2\right) + \frac{\alpha_0}{l_B^2} \frac{g_\perp}{2} \sigma_z. \tag{6.2}$$

$$= \hbar\omega_l \left(a_1^\dagger a_1 + a_2^\dagger a_2 + 1\right) + \frac{\hbar\omega_c}{2} \left(a_1^\dagger a_1 - a_2^\dagger a_2\right) + \frac{\alpha_0}{l_B^2} \frac{g_\perp}{2} \sigma_z, \tag{6.3}$$

where

$$a_1 = \frac{x - iy}{2l} + \frac{ilk_-}{2}, \qquad a_2 = \frac{x + iy}{2l} + \frac{ilk_+}{2} \tag{6.4}$$

are ladder operators, $k_\pm = k_x \pm ik_y$, $\omega_c = eB/m^*$, $\omega_l^2 = \omega_0^2 + \omega_c^2/4$ and $l = \sqrt{\hbar/(m^*\omega_l)}$ is the effective quantum dot confinement length. The eigenstates of H_0, the so-called Fock-Darwin orbitals $|n_1, n_2, \sigma\rangle$ with $n_{1,2} = 0, 1, \ldots$ and $\sigma = \pm 1$, provide an orthonormal basis on which H_{QD} is projected (see Section 6.5). The eigenvalues of the resulting matrix for H_{QD} in the Fock-Darwin basis are then solved numerically. The two lowest energy orbitals $|\mathbb{0}\rangle$ and $|\mathbb{1}\rangle$ corresponding to energies $E_{\mathbb{0}}$ and $E_{\mathbb{1}}$ define the qubit. These are mostly composed of the Fock-Darwin orbitals $|0, 0, -\rangle$ and $|0, 0, +\rangle$ respectively, plus higher-energy orbitals :

$$|\mathbb{0}\rangle = |0,0\rangle\,|-\rangle + \left(c^{(\mathbb{0})}_{0,1}\,|0,1\rangle + c^{(\mathbb{0})}_{3,0}\,|3,0\rangle + c^{(\mathbb{0})}_{1,2}\,|1,2\rangle\right)|+\rangle \tag{6.5a}$$

$$|\mathbb{1}\rangle = |0,0\rangle\,|+\rangle + \left(c^{(\mathbb{1})}_{1,0}\,|1,0\rangle + c^{(\mathbb{1})}_{0,3}\,|0,3\rangle + c^{(\mathbb{1})}_{2,1}\,|2,1\rangle\right)|-\rangle\,. \tag{6.5b}$$

The coefficients $c^{(\mathbb{0},\mathbb{1})}_{n_1,n_2}$ were extracted from the numerical diagonalization of H_{QD} to avoid artifacts near crossings between Fock-Darwin orbitals. They can be evaluated with perturbation theory away from these crossings. For a driving field $\tilde{\mathbf{F}}(t) = \mathbf{e}_x F_{\mathrm{ac}} \cos(\omega t)$, where $\hbar\omega = |E_{\mathbb{0}} - E_{\mathbb{1}}|$ is the qubit energy, the Rabi frequency Ω is given in terms of the qubit dipole moment $d = e\,\langle \mathbb{0}\,|\,x\,|\,\mathbb{1}\rangle$ by $\Omega = F_{\mathrm{ac}}|d|/\hbar$.

Fig. 6.2 shows the QD orbital energies as a function of the out-of-plane magnetic field for a QD size $l_0 = \sqrt{\hbar/m^*\omega_0} = 25\,\mathrm{nm}$ and the same QW parameters as in Fig. 6.1a. The qubit undergoes a transition from a spin qubit to a charge qubit at the crossing between $|\mathbb{1}\rangle$ and the mostly $|0,1,-\rangle$ orbital near $B = 0.275\,\mathrm{T}$. The two levels cross because $|0,1,-\rangle$ is not present in the expansion of $|\mathbb{1}\rangle$.

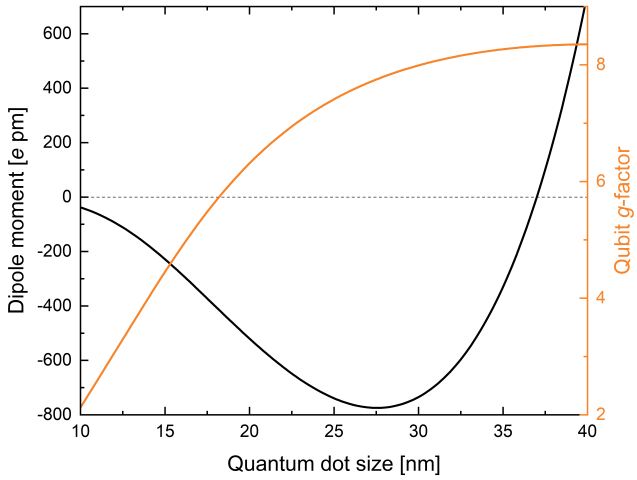

Figure 6.3 LH qubit dipole moment (left) and absolute value of the g-factor (right) as a function of the QD size l_0. The magnetic field is fixed at 0.05 T. The QW parameters are the same as in Fig. 6.1c.

The qubit dipole moment d and the qubit g-factor $|g_{\mathrm{QD}}|$ are plotted in Fig. 6.3 as a function of the QD size l_0 and $B = 0.05\,\mathrm{T}$. The g-factor has a strong dependence on l_0 for small QD sizes, and approaches asymptotically the QW value $g_\perp = 8.69$ at large l_0. The large $g_\perp$ value originates from the first order approximation $g_\perp \approx 2\kappa$ for a LH spin in a perpendicular magnetic field with $\kappa = 3.41$ in Ge (see Table 3.3). Deviations from 2κ come from the spread of the wavefunction and 2$^{\mathrm{nd}}$ order corrections [233]. The dipole moment d takes very

large values for two main reasons. First, the coefficient β_3 that contributes to EDSR by introducing a $|1,0,-\rangle$ contribution into $|\mathbb{1}\rangle$ depends on the sum $(\gamma_2+\gamma_3)$ for η levels whereas for H levels it depends on the difference $(\gamma_2-\gamma_3)$. In Ge, $\gamma_2 \approx \gamma_3$ [131] and therefore β_3 is much larger for η subbands. Secondly, the latter are subject to a linear Rashba spin splitting proportional to β_1. This additional term contributes to a large d similarly to β_3 by increasing the contribution of $|1,0,-\rangle$ into $|\mathbb{1}\rangle$. At $l_0 \approx 27.5\,\mathrm{nm}$, $|d|$ reaches a maximum as a result of the combined effects of β_1 and β_3, which gives a dipole moment that is 2 to 3 orders of magnitude larger than that of HHs in a compressively strained Ge [210, 234]. For instance, an in-plane driving field as small as $F_{\mathrm{ac}} = 1\,\mathrm{mV/\mu m}$ gives a Rabi frequency $\Omega \approx 1.2\,\mathrm{GHz}$.

There is, however, a range of QD sizes where the dipole moment is very small (Fig. 6.3). This happens because both β_1 and β_3 contribute to d. When B is small such that $|\mathbb{1}\rangle$ is far from the excited orbitals, the dipole moment is given by

$$|d| \approx \frac{em^{*2}l^2|g_\perp|\mu_{\mathrm{B}}B}{\hbar^4}\left|l^2\beta_1+2\beta_3\right|. \tag{6.6}$$

Therefore, when $\beta_1\beta_3<0$, d can vanish at specific values of l_0 and B. For the QW parameters in Fig. 6.1a, $\beta_1 = 0.42\,\mathrm{meV\,nm}$ and $\beta_3 = -290\,\mathrm{meV\,nm^3}$ which causes the dipole moment to vanish at $B = 0.05\,\mathrm{T}$ and $l_0 \approx 37\,\mathrm{nm}$. For $l_0 > 37\,\mathrm{nm}$ d increases again, but at the cost of a smaller orbital energy spacing.

An important feature of LH qubits is that EDSR is driven by both η-H and η-η mixing. This is because there is an allowed 1st order coupling between η subbands $\langle \eta+; j \,|\, \mathbf{H}_{\mathrm{QW}} \,|\, \eta-; j'\rangle = i\alpha_0 T^{\eta}_{j,j'}K_-$ that is essentially non-existent for HHs [see (3.93)]. The η-H mixing part contributes mainly to the β_3 parameter through a term proportional to $(\gamma_2+\gamma_3)$, while η-η mixing contributes to both β_3 and β_1. Notably, these two types of mixing are of equal importance given that β_1 and β_3 can interfere to suppress the dipole moment [c.f. (6.6)].

The relaxation time $T_1 = 1/\Gamma$ of the LH qubit was also evaluated for the system in Fig. 6.1a. The coupling of the hole to acoustic phonons was considered. The total relaxation rate $\Gamma = \Gamma_{\mathrm{em}} + \Gamma_{\mathrm{abs}}$, where Γ_{em} (Γ_{abs}) is the rate associated with the emission (absorption) of one phonon. Each of these rates is calculated by Fermi's golden rule [c.f. (3.212)]:

$$\Gamma = \frac{2\pi\mathcal{V}}{\hbar}\sum_{\alpha}\int \frac{\mathrm{d}^3q}{(2\pi)^3}\left|\langle f|W_{\alpha\mathbf{q}}|i\rangle\right|^2\delta\left(\hbar\omega-\hbar\omega_{\alpha\mathbf{q}}\right), \tag{6.7}$$

where the operator $W_{\alpha\mathbf{q}}$ is derived from the hole-phonon Hamiltonian in a procedure similar to that in References [176, 189, 235, 236]. Importantly, the matrix element $\langle f \,|\, W_{\alpha\mathbf{q}} \,|\, i\rangle$ takes into account the relaxation rate associated with all three spin-orbit parameters β_1, β_2, and

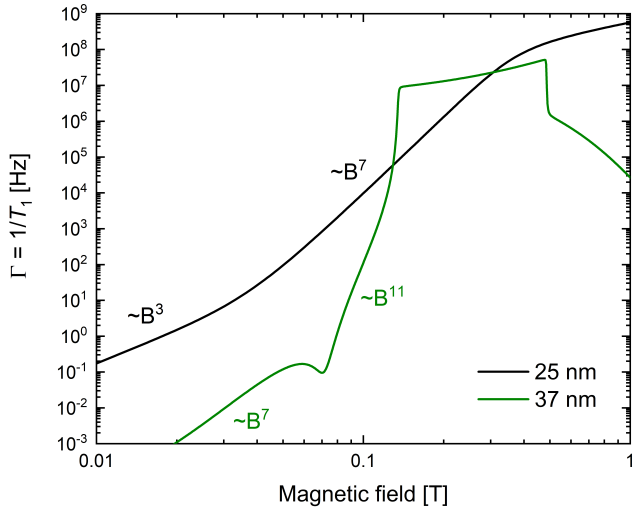

Figure 6.4 Relaxation rate $\Gamma = 1/T_1$ as a function of the magnetic field. The QW parameters are the same as in Fig. 6.1c.

β_3.

Fig. 6.4 shows the computed Γ as a function of B for the Ge/GeSn QW system in Fig. 6.1a at $l_0 = 25\,\text{nm}$. A relaxation time $T_1 = 100\,\mu\text{s}$ was extracted at $B = 0.1\,\text{T}$. Moreover, Γ follows a B^7 behavior when $B \gg \sqrt{12}k_\text{B}T/(g_\text{QD}\mu_\text{B})$ and a B^6 behavior when $B \ll \sqrt{12}k_\text{B}T/(g_\text{QD}\mu_\text{B})$. This higher relaxation rate for LHs compared to HHs [47, 189] is due to the larger spin-orbit coupling parameters $\beta_{1,2,3}$. The B^7 behavior at low temperature is associated to the spin-orbit term $|l^2\beta_1 + 2\beta_3|$ that was encountered in eq. (6.6) and from the sum $c^{(\mathbb{0})}_{0,1} + c^{(\mathbb{1})}_{1,0} \sim B$.

Similar calculations were also performed at a QD size $l_0 = 37.9\,\text{nm}$ for which the dipole moment vanishes at $B = 0.05\,\text{T}$ (Fig. 6.4). In this case, two different regimes were observed: for $B \ll 0.05\,\text{T}$ the relaxation rate exhibits a B^7 behavior, but at $B \gg 0.05\,\text{T}$ it evolves as $\sim B^{11}$. This is because the term associated with $|l^2\beta_1 + 2\beta_3|$ vanishes and the dominating terms in Γ are those associated with β_2, β_3 alone and the superposition coefficients $c^{(\mathbb{0},\mathbb{1})}_{n_1,n_2}$ with $n_1 + n_2 = 3$. At $B = 0.1\,\text{T}$, $T_1 = 8\,\text{ms}$, which is consistent with a much smaller dipole moment at this QD size. The abrupt change in behavior around $B = 0.14\,\text{T}$ is due to a very small anti-crossing between $|\mathbb{1}\rangle$ and the mostly $|1, 0, -\rangle$ orbital, while at $B = 0.5\,\text{T}$ it is caused by a small anti-crossing between the mostly $|1, 0, -\rangle$ and the mostly $|0, 3, -\rangle$ orbital.

6.4 Conclusion

This work unravels the spin properties of a light-hole gated quantum dot in tensile strained Ge under EDSR. A detailed framework is described taking into account the spread of the

envelopes in the barriers surrounding the quantum well and the effects of the dispersion non-parabolicity. It was found that light-holes have a dipole moment d significantly larger than that of the heavy-holes due to a larger cubic Rashba parameter (β_3) and the existence of a non-zero linear Rashba parameter (β_1). Interestingly, β_1 and β_3 can interfere destructively and cause the dipole moment to vanish at a specific quantum dot size. The relaxation rate Γ of a light hole qubit follows a B^7 behavior, except when $d \approx 0$ where Γ follows a B^{11} behavior. This direct bandgap Ge/GeSn device structure provides additional degrees of freedom to implement silicon-compatible and scalable quantum processors leveraging the advantages of light-hole spin properties in addition to their efficient coupling with optical photons and their ability to transfer superconductivity.

6.5 Solution of time-independent quantum dot Hamiltonian

In this section we diagonalize the time-independent quantum dot Hamiltonian H_{QD}. We divide this task in two parts: first we diagonalize H_0, that is, H_{QD} without the spin-orbit coupling term H'. Then we take in account H' by using the solutions from the H_0 part.

The Hamiltonian of the quantum dot without spin-orbit coupling is given by (6.2):

$$H_0 = \alpha_0 \gamma K_{\parallel}^2 + \frac{1}{2} m^* \omega_0^2 \left(x^2 + y^2\right) + \frac{\alpha_0}{l_B^2} \frac{g_\perp}{2} \sigma_z. \tag{6.8}$$

This Hamiltonian can be diagonalized analytically by defining the following ladder operators :

$$a_1 = \frac{x - iy}{2l} + \frac{ilk_-}{2}, \qquad a_2 = \frac{x + iy}{2l} + \frac{ilk_+}{2}, \tag{6.9}$$

where $k_\pm = k_x \pm ik_y$, $l = \sqrt{\hbar/(m^*\omega_l)}$ is the effective quantum dot size, $\omega_l^2 = \omega_0^2 + \omega_c^2/4$ and $\omega_c = eB/m^*$ is the cyclotron frequency. It is useful to define the dot size at zero magnetic field $l_0 = \sqrt{\hbar/(m^*\omega_0)}$, which is related to l by

$$\frac{1}{l^4} = \frac{1}{l_0^4} + \frac{1}{4l_B^4}. \tag{6.10}$$

The ladder operators a_1 and a_2 follow the usual commutation relations for bosons : $[a_i, a_j] = [a_i^\dagger, a_j^\dagger] = 0$ and $[a_i, a_j^\dagger] = \delta_{i,j}$. They also act upon the eigenstates $|n_1\rangle$ and $|n_2\rangle$ of the number operators $n_1 = a_1^\dagger a_1$ and $n_2 = a_2^\dagger a_2$ in the usual way : $a_1 |n_1\rangle = \sqrt{n_1}\,|n_1 - 1\rangle$, $a_1^\dagger |n_1\rangle = \sqrt{n_1 + 1}\,|n_1 + 1\rangle$, $n_1 |n_1\rangle = n_1 |n_1\rangle$ and similarly for a_2. In terms of a_1 and a_2, H_0

becomes

$$H_0 = \hbar\omega_l \left(a_1^\dagger a_1 + a_2^\dagger a_2 + 1\right) + \frac{\hbar\omega_c}{2}\left(a_1^\dagger a_1 - a_2^\dagger a_2\right) + \frac{\alpha_0}{l_B^2}\frac{g_\perp}{2}\sigma_z, \tag{6.11}$$

which directly leads to its eigenvalues

$$E_{n_1,n_2,\sigma} = \hbar\omega_l \left(n_1 + n_2 + 1\right) + \frac{\hbar\omega_c}{2}\left(n_1 - n_2\right) + \frac{\alpha_0}{l_B^2}\frac{g_\perp}{2}\sigma \tag{6.12}$$

and corresponding eigenstates $|n_1, n_2, \sigma\rangle$ with $n_{1,2} = \{0, 1, 2, \dots\}$ and $\sigma = \pm 1$.

The set of eigenstates of H_0 defines an orthonormal basis on which we can project H'. The spin-orbit term H' depends on products and powers of the $K_\pm$ operators [(6.1) in main text]. The matrix expression for H' in the $\{|n_1, n_2, \sigma\rangle\}$ basis can be found from the expression of $K_\pm$ in terms of a_1 and a_2 :

$$K_- = -i\kappa_+ a_1 + i\kappa_- a_2^\dagger, \tag{6.13}$$

$$K_\parallel^2 = \frac{1}{2}\{K_-, K_+\}, \tag{6.14}$$

where $\kappa_\pm = 1/l \pm l/(2l_B^2)$. We cannot however perform the projection on every basis states $|n_1, n_2, \sigma\rangle$ because H_{eff} diverges from the exact dispersion $\mathbf{H}_{\text{QW}}$ at some point. Thus, the projection is done only on the finite subset $n_1 + n_2 \leq 4$. The size of this truncated basis subset is chosen large enough to include the orbitals from the $n_1 + n_2 = 1$ and $n_1 + n_2 = 3$ groups that have a significant contribution in $|\mathbb{0}\rangle$ and $|\mathbb{1}\rangle$ [210, 237], but small enough that the expectation value

$$\sqrt{\left\langle K_\parallel^2 \right\rangle} = \sqrt{(n_1 + 1/2)\kappa_+^2 + (n_2 + 1/2)\kappa_-^2} \tag{6.15}$$

is smaller than the point in k-space where $H_{\text{eff}}(\mathbf{K}_\parallel)$ diverges from $\mathbf{H}_{\text{QW}}$ too significantly.

The qubit levels $|\mathbb{0}\rangle$ and $|\mathbb{1}\rangle$ can be expanded in terms of the Fock-Darwin orbitals $|n_1, n_2, \sigma\rangle$ using perturbation theory :

$$|\mathbb{0}\rangle = |0,0,-\rangle - \frac{\kappa_-\beta'}{E_{0,0,-}-E_{0,1,+}}|0,1,+\rangle - \frac{\sqrt{6}\kappa_+^3\beta_2}{E_{0,0,-}-E_{3,0,+}}|3,0,+\rangle + \frac{\sqrt{2}\kappa_-^2\kappa_+\beta_3}{E_{0,0,-}-E_{1,2,+}}|1,2,+\rangle \tag{6.16}$$

$$|\mathbb{1}\rangle = |0,0,+\rangle + \frac{\kappa_+\beta'}{E_{0,0,+}-E_{1,0,-}}|1,0,-\rangle + \frac{\sqrt{6}\kappa_-^3\beta_2}{E_{0,0,+}-E_{0,3,-}}|0,3,-\rangle - \frac{\sqrt{2}\kappa_+^2\kappa_-\beta_3}{E_{0,0,+}-E_{2,1,-}}|2,1,-\rangle\,, \tag{6.17}$$

where $\beta' = \beta_1 + (\kappa_+^2+\kappa_-^2)\beta_3$. These expressions are valid only far away from any crossing between Fock-Darwin states that would make a denominator vanish.

6.6 Light hole-phonon interaction

We estimate the relaxation time T_1 of the qubit by evaluating the rate of the single phonon-mediated qubit transitions. Assuming an isotropic phonon dispersion, $\Gamma = 1/T_1$ is given by (3.225).

We write the hole-phonon Hamiltonian $W_{\alpha\mathbf{q}} = \mathcal{Q}w_\alpha$ in the QW subband edge basis $\mathcal{B}_0$ along with $\mathbf{H}_{\rm QW}$ before performing a 2nd order SWT on $\mathbf{H} = \mathbf{E}_0^{\rm QW} + \mathbf{W} + \mathcal{Q}\mathbf{w}_\alpha$ to find an effective Hamiltonian for the LH-phonon interaction in the qubit subspace. We keep only terms that are linear in $b_{\alpha\mathbf{q}}$. With $\mathcal{Q}$ given by

$$\mathcal{Q} = i\sqrt{q_\alpha}\left(b_{\alpha\mathbf{q}} + b_{\alpha,-\mathbf{q}}^\dagger\right)e^{ixq_\alpha\sin\theta\cos\phi}e^{iyq_\alpha\sin\theta\sin\phi}, \tag{6.18}$$

the effective LH-phonon interaction is

$$W_{\alpha\mathbf{q}}^{\rm eff} = i\sqrt{q_\alpha}\left(b_{\alpha\mathbf{q}} + b_{\alpha,-\mathbf{q}}^\dagger\right)\left(W_{11}\sigma_+\sigma_- + W_{22}\sigma_-\sigma_+ + W_{12}\sigma_+ + W_{21}\sigma_-\right). \tag{6.19}$$

The expressions for W_{ij} are quite lengthy, so here we give as an example the result of the product $\langle\mathbb{1}\,|\,W_{11}\sigma_+\sigma_-\,|\,\mathbb{0}\rangle$:

$$\begin{aligned}\langle\mathbb{1}\,|\,W_{11}\sigma_+\sigma_-\,|\,\mathbb{0}\rangle \approx{}& \left[(f_{xx}+f_{yy})\left(\mathbf{a}^\eta+\mathbf{b}^\eta\right)+f_{zz}\left(\mathbf{a}^\eta-2\mathbf{b}^\eta\right)\right]c_{0,0}^{\mathbb{1}*}\left(c_{0,1}^{\mathbb{0}}e_{02}+c_{1,2}^{\mathbb{0}}e_{05}+c_{3,0}^{\mathbb{0}}e_{03}\right)\\ &-\alpha_0\kappa_-\left(f_{yz}-if_{zx}\right)c_{0,0}^{\mathbb{1}*}c_{0,1}^{\mathbb{0}}e_{00}\left(\dot{\mathbf{t}}^\eta\bar{\mathbf{T}}^\eta+\dot{\mathbf{T}}^{\mathrm{x}\dagger}\bar{\mathbf{t}}^{\mathrm{x}}\right).\end{aligned} \tag{6.20}$$

We make the assumption $e^{iqz\cos\theta} \approx 1$ in the 2nd order terms $\dot{\mathbf{t}}^{\eta}\bar{\mathbf{T}}^{\eta}$ and alike.

The braket products involving $e^{i\mathbf{q}_{\parallel}\cdot\mathbf{r}_{\parallel}}$, where $\mathbf{r}_{\parallel} = x\mathbf{e}_x + y\mathbf{e}_y$, are calculated analytically from the expressions of $|n_1, n_2\rangle$ in position space :

$$\phi_{0,0}(x,y) = \frac{1}{\sqrt{\pi}l}\exp\left[-\frac{x^2+y^2}{2l^2}\right] \tag{6.21}$$

$$\phi_{1,0}(x,y) = \phi^*_{0,1}(x,y) = \frac{x+iy}{l}\phi_{0,0}(x,y) \tag{6.22}$$

$$\phi_{3,0}(x,y) = \phi^*_{0,3}(x,y) = \frac{(x+iy)^3}{\sqrt{6}l^3}\phi_{0,0}(x,y) \tag{6.23}$$

$$\phi_{2,1}(x,y) = \phi^*_{1,2}(x,y) = \frac{x+iy}{\sqrt{2}l}\left(\frac{x^2+y^2}{l^2} - 2\right)\phi_{0,0}(x,y). \tag{6.24}$$

If we define $|0\rangle \equiv |0,0\rangle$, $|1\rangle \equiv |1,0\rangle$, $|2\rangle \equiv |0,1\rangle$, $|3\rangle \equiv |3,0\rangle$, $|4\rangle \equiv |2,1\rangle$, $|5\rangle \equiv |1,2\rangle$ and $|6\rangle \equiv |0,3\rangle$ with $e_{ab} \equiv \left\langle a \left| e^{i\mathbf{q}_{\parallel}\cdot\mathbf{r}_{\parallel}} \right| b \right\rangle$ we have :

$$e_{01} = \frac{it}{2}e^{i\phi}e_{00}, \qquad e_{02} = e^*_{01}(-q),$$

$$e_{03} = -\frac{it^3}{8\sqrt{6}}e^{3i\phi}e_{00}, \qquad e_{04} = -\frac{it^3}{8\sqrt{2}}e^{i\phi}e_{00},$$

$$e_{05} = e^*_{04}(-q), \qquad e_{06} = e^*_{03}(-q),$$

$$e_{12} = -\frac{t^2}{4}e^{-2i\phi}e_{00}, \qquad e_{13} = -\frac{3t^2}{4\sqrt{6}}\left(1 - \frac{t^2}{12}\right)e^{2i\phi}e_{00},$$

$$e_{15} = -\frac{t^2}{4\sqrt{2}}\left(1 - \frac{t^2}{4}\right)e^{-2i\phi}e_{00}, \qquad e_{24} = e^*_{15},$$

$$e_{26} = e^*_{13}, \qquad e_{34} = -\frac{\sqrt{3}t^2}{4}\left[1 - \frac{t^2}{4}\left(1 - \frac{t^2}{24}\right)\right]e^{-2i\phi}e_{00},$$

$$e_{36} = -\frac{t^2}{384}e^{-6i\phi}e_{00}, \qquad e_{45} = -\frac{t^2}{2}\left(1 - \frac{t^2}{8}\right)^2 e^{-2i\phi}e_{00},$$

$$e_{56} = e_{34},$$

where $t = ql\sin\theta$ and $e_{00} = e^{-t^2/4}$.

CHAPTER 7 TUNABLE SPIN-ORBIT COUPLING IN LIGHT HOLE GE QUANTUM CHANNELS

7.1 Introduction

SOI is a key ingredient in spin-based qubit devices with all-electrical driving. Planar systems with large intrinsic SOI leverage the Rashba effect to enable EDSR manipulation of the qubit, which does not require any oscillating magnetic fields. The strength of the Rashba SOI is strongly dependent on the confinement profile and on the type of carriers populating the ground state. For instance, the EDSR-compatible Rashba SOI term for HHs is typically 10 times smaller than the one associated with LHs (see Chapters 3, 5 and 6). One approach to increase SOI is to introduce an additional dimension of strong confinement, as in a nanowire geometry. In that case, the 2-dimensional confinement (in the x-z plane for instance) introduces a LH-HH mixing that persists even at $k_y = 0$ [238]. This gives rise to the so-called *direct* Rashba SOI (DRSOI) [180]. This type of SOI enables EDSR, but is also strongly tunable with perpendicular electric fields [180, 239]. Moreover, sweet spots in which the SOI is turned off for specific DC gate field amplitudes have been reported [240], and would essentially act like a switch to change the qubit in an operational state or in an idle state.

Besides nanowires, 2-dimensional confinement is also possible in planar heterostructures with gate-defined quantum channels (QC). These systems combine the scalability benefits from planar systems with the large DRSOI of nanowires. Notably, they have attracted attention lately as a potential candidate to host Majorana zero-modes [241]. In this Chapter, LH (or η) spin dynamics in tensile strained Ge QCs are investigated. Moreover, additional weaker confinements along the y direction, resulting in an elongated QD system, are also investigated. To circumvent the limitations on the DC gate field amplitude F_z due to the small LH band offsets (see Chapter 5), the top $Ge_{1-x}Sn_x$ barrier is replaced by a large band offset material (e.g. an oxide) that essentially acts like a hard wall for η and H levels.

This Chapter is organized as follows: the first section introduces the planar system, without in-plane confinement. Ground state properties such as η-H energy splitting, g-factors and Rashba parameters are calculated, revealing vanishing linear-in-k Rashba SOI for specific non-zero field amplitudes. Then, ground state properties of the QC system are computed and compared with those previously calculated for the planar system. Finally, Rabi frequencies in elongated QDs for various magnetic field configurations are computed for different dot sizes and DC gate fields, revealing hot and cold spots that strongly correlate with the linear-in-k

Rashba SOI of the planar system.

7.2 Results and discussion

A $Ge_{1-x}Sn_x$/Ge/barrier heterostructure provides the out-of-plane confinement for the holes (see Fig. 7.1a). The Ge QW is coherently deposited on a mostly strained-relaxed [001]-oriented $Ge_{1-x}Sn_x$ barrier, with the z axis taken parallel to the growth direction. Lattice mismatch between Ge and relaxed $Ge_{1-x}Sn_x$ is leveraged to generate a significant epitaxial biaxial strain in the Ge QW, which lifts the degeneracy between the LH and HH bands at the Γ point. The ensuing strain tensor is diagonal, with its components in Ge given by $\varepsilon_{xx} = \varepsilon_{yy} \equiv \varepsilon_{\parallel} = a_x/a_0 - 1$ and $\varepsilon_{zz} = -2\varepsilon_{\parallel}c_{12}/c_{11}$, where a_x is the lattice constant of $Ge_{1-x}Sn_x$ and c_{11}, c_{12} are elastic constants for Ge. a_x being larger than a_0, the LH band is pushed upwards closer to the bandgap, resulting in a LH-like valence band edge in Ge. The top barrier is taken as a thin, large band offset material allowing holes to remain inside the well even at reasonably large electric fields, without much leaking. This material could be a very thin Si capping (a few ångströms), an oxide, or a combination thereof.

Spatial confinement also breaks LH-HH degeneracy, but usually favors HHs to the ground state due to their larger effective mass along the growth direction. Large tensile strain is therefore required to invert the band ordering and to push LHs towards the valence band edge. The precise requirements for a LH-like Ge QW on $Ge_{1-x}Sn_x$ are non-trivial (see Chapter 5). One important aspect is that while LHs are confined in Ge, HHs are instead pushed away from Ge and form a continuum of levels in $Ge_{1-x}Sn_x$. The calculated confinement energy profile of the device in Fig. 7.1a is shown in Fig. 7.1b. The calculation takes in account the energy band offsets between bulk Ge and bulk $Ge_{1-x}Sn_x$ with strain effects included. An out-of-plane static electric field $\mathbf{F} = F_z\mathbf{e}_z$ tilts all the bands such that holes are pushed towards the surface. The inverted band alignment of the HH band creates an additional triangular well at the interface between $Ge_{1-x}Sn_x$ and Ge. Depending on the well thickness l_z and electric field strength F_z, the HH ground state may be located either at the interface (as in Fig. 7.1b) or at the surface. In any case, wavefunction overlap and/or wavefunction spread across the $Ge_{1-x}Sn_x$/Ge interface enables LH-HH mixing between the ground η subband and the closest H subband.

In Fig. 7.1c is shown the η1-H1 energy splitting as a function of l_z and F_z. Three regions are identified as follows: the first corresponds to the region in parameter space where the ground state is of H type, and is located at small l_z to the left of the bold dark line labelled "0 meV". Indeed, as l_z decreases, tensile strain is unable to compensate the increasingly strong confinement from the well, which eventually pushes the first H level to the ground

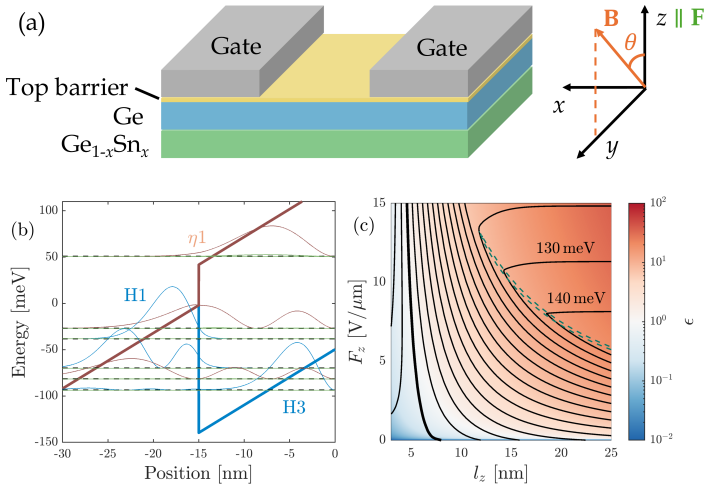

Figure 7.1 (a) Schematic of the device with Cartesian axes and fields. (b) Energy confinement profile along the growth direction. Sn content in the relaxed barrier is $x = 10\%$, the Ge well thickness is $l_z = 15\,\text{nm}$, and the static electric field strength $F_z = 6\,\text{V}/\mu\text{m}$. η and H level indices are indicated. Blue envelopes correspond to the HH part of the hole spinor, while red and green envelopes correspond to the LH and the SO part of the spinor, respectively. (c) η1-H1 energy splitting as a function of l_z and F_z for Sn content $x = 16\%$ (contour lines). The thicker black line indicates 0 meV splitting. The color scale indicates the triangular parameter ϵ. The first and second H levels are 2 meV apart on the dashed green line.

state. The second region corresponds to a ground level of η type, with the H1 level located at the $\text{Ge}_{1-x}\text{Sn}_x$/Ge interface (as in Fig. 7.1b). This region is situated directly to the right of the 0 meV line, where contour lines are closely spaced within each other. The last region indicates a ground state of η type, but with the ground H level located in Ge (see H3 in Fig. 7.1b). It is clearly identified by the horizontal contour lines with greater spacing between each other. The transition regime between regions 2 and 3 is marked by the dashed green line, which indicates where the energy difference between H1 and H2 is 2 meV. The size of this transition regime depends on the amount of hybridization of H levels located on either side of the triangular barrier at the $\text{Ge}_{1-x}\text{Sn}_x$/Ge interface. Large (low) strain increases (decreases) this barrier height, making the transition between regions 2 and 3 sharper (broader).

The color map in Fig. 7.1c indicates how much "triangular" the confinement is for the ground η level. It is defined by the ration $\epsilon = l_z^2/l_F^2$, where l_F is a characteristic electric length $l_F^3 = \alpha_0\,|\gamma_\perp^\eta|\,/(eF_z)$, with $\alpha_0 = \hbar^2/(2m_0)$ and $\gamma_\perp^\eta$ being the out-of-plane mass of η1. $\epsilon \gg 1$ indicates a mostly triangular confinement, while $\epsilon \ll 1$ indicates a mostly square confinement. Interestingly, the 0 meV η1-H1 energy splitting line follows roughly the region where confinement is neither square nor triangular ($\epsilon \sim 1$).

For static out-of-plane magnetic fields $\mathbf{B} = B\mathbf{e}_z$, the η-like QW ground state is described by

an effective 2-dimensional Hamiltonian [see (3.158)]

$$\begin{aligned} H_{\text{eff}}^{\eta} = E_1^{\eta} + \alpha_0 \left(\gamma_{\parallel}^{\eta} + \frac{\chi_{\perp}^{\eta}}{2l_B^2}\sigma_z\right) K_{\parallel}^2 + \frac{\alpha_0}{2l_B^2} g_{\perp}^{\eta} \\ + \left[\left(i\beta_1^{\eta} K_- - i\beta_2^{\eta} K_+^3 + i\beta_3^{\eta} K_- K_+ K_-\right)\sigma_+ + \text{H.c.}\right], \end{aligned} \tag{7.1}$$

where $\mathbf{K} = \mathbf{k} + e\mathbf{A}/\hbar$ is the mechanical wavenumber with $\mathbf{A}$ the vector potential, $K_{\pm} = K_x \pm iK_y$, $K_{\parallel}^2 = \{K_-, K_+\}/2$, $1/l_B^2 = [K_-, K_+]/2 = eB/\hbar$, and $\sigma_{\pm} = (\sigma_x \pm i\sigma_y)/2$. The effective parameters are the following: $\gamma_{\parallel}^{\eta}$ is the in-plane effective mass, $g_{\perp}^{\eta}$ is the out-of-plane g-tensor component, $\chi_{\perp}^{\eta}$ is a spin-dependent effective mass, and β_i^{η} with $i = 1, 2, 3$ are three kinds of Rashba spin-orbit coupling parameters. The "p" superscript indicates the planar geometry, without in-plane confinement. Perturbation theory up to a given order provides exact formulas for these parameters [24, 34], with $\beta_{2,3}^{\eta}$ requiring 3$^{\text{rd}}$ order perturbation, $g_{\perp}^{\eta}$ requiring 2$^{\text{nd}}$ order and β_1^{η} requiring only 1$^{\text{st}}$ order. Contour lines of $g_{\perp}^{\eta}$, and β_1^{η} are shown in Fig. 7.2 as a function of l_z and F_z with Sn content $x = 16\%$. $g_{\perp}^{\eta}$ diverges near 0 meV η1-H1 splitting (dashed line) because of vanishing energy denominators in the perturbative expansions. $g_{\perp}^{\eta}$ and β_1^{η} are well behaved at larger thicknesses l_z, and also become l_z-independent as $\epsilon \gg 1$, corresponding to a mostly triangular confinement profile. At a QW thickness $l_z = 15$ nm, the out-of-plane g-factor ~ -3 for the whole range of static electric fields. Most importantly, these maps reveal that β_1^{η} vanishes at a non-zero F_z due to the asymmetric confinement profile even at $F_z = 0$. The same is also true for the two other cubic Rashba parameters (supp file). Notably, the 0-value contour line coincides in parameter space for every Rashba parameter, suggesting a tunable SOC through the gate electric field $\mathbf{F}$. For instance, the system could be tuned into a high SOC regime for spin manipulation, and then brought back into low SOC regime for spin state storage.

The SOC tunability with respect to electric fields is investigated further for a QC geometry with the channel running along the y-direction, by writing a 2×2 effective Hamiltonian for the QC ground state $|\varsigma; i, N\rangle$ [see (3.198)]:

$$\begin{aligned} H_{\text{eff}}^{c} = E_{1,0}^{c} + \alpha_0 \left[\gamma^c + \frac{1}{2l_B^2}\left(\chi_{\perp}^{c}\cos\theta_{\varsigma 3} + \chi_{\parallel}^{c}\sin\theta_{\varsigma 2}\right)\right] k_y^2 \\ + \frac{\alpha_0}{2l_B^2}\left(g_{\perp}^{c}\cos\theta_{\varsigma 3} + g_{\parallel}^{c}\sin\theta_{\varsigma 2}\right) + \left(\beta_1^c + \beta_3^c k_y^2\right) k_y \varsigma_1, \end{aligned} \tag{7.2}$$

where ς is a pseudo-spin quantum number for the QC, $i \geq 1$ is a z-subband index and $N \geq 0$

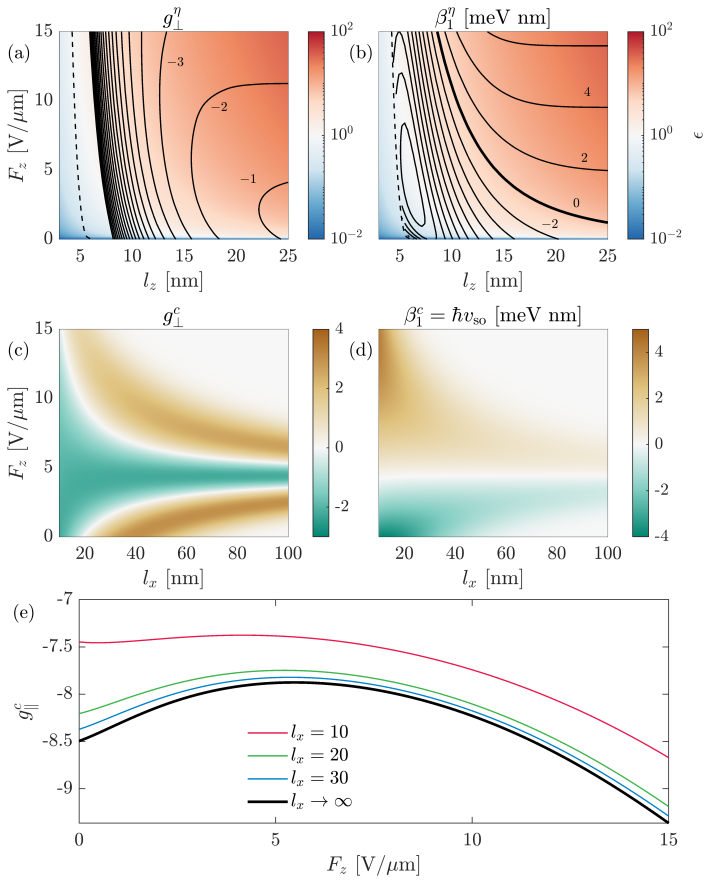

Figure 7.2 (a)-(b) Color map of ϵ and contour lines of $g_\perp^\eta$, and β_1^η parameters for $\eta 1$ as a function of l_z and F_z with $x = 0.16$. $\eta 1$ is the ground state to the right of the dashed line. Some contour lines are not shown near the dashed line for better visuals. The thick black line indicates $\beta_1^\eta = 0$. (c)-(d) Color map of $g_\perp^c$ and β_1^c for the ground QC level as a function of F_z and l_x. (e) Plot of $g_\parallel^c$ as a function of F_z and selected l_x. The thick black line corresponds to the QW limit.

is an in-plane subband index. Parameters in (7.2) are named similarly to those in (7.1), with a "c" superscript indicating the QC geometry. Hamiltonian (7.2) is written within the gauge $\mathbf{A} = Bx\,(\cos\theta \mathbf{e}_y - \sin\theta \mathbf{e}_z)$, such that the field $\mathbf{B}$ lies within the y-z plane with polar angle θ. The $\beta_1^c = \hbar v_{so}$ Rashba parameter is directly proportional to the so-called spin-orbit velocity v_{so} [226]. The QC channel in-plane confinement potential $V_\parallel$ is taken as $V_\parallel = -\alpha_0 x^2/l_x^4$, with the characteristic length l_x being relative to a carrier sharing the same mass as the bare electron mass m_0.

QC effective parameters $g_{\perp,\parallel}^c$ and β_1^c are evaluated similarly to those in (7.1) through perturbation theory. An exact description for these three parameters only requires 1st order SWT. $g_{\perp,\parallel}^c$ and β_1^c are displayed in Fig. 7.2(c)–(e) for various l_x and F_z with Sn content $x = 16\%$ and

well thickness $l_z = 15\,\text{nm}$, which is below the critical thickness for $x = 13\%$ in the $\text{Ge}_{1-x}\text{Sn}_x$ barrier (see Chapter 5). Panels (c) and (d) reveal that the out-of-plane g-factor is very close to the g-factor of the QW system near $4.4\,\text{V}/\mu\text{m}$, which coincides with $\beta_1^c = 0$. It can be shown that if $\beta_1^\eta l_x/\alpha_0 \ll 1$, the g-factor in the channel is well approximated by

$$g_\perp^c \approx g_\perp^\eta + \frac{1}{\sqrt{-\gamma_\parallel^\eta}}\left(\frac{\beta_1^\eta l_x}{\alpha_0}\right)^2. \tag{7.3}$$

Tuning the electric field F_z away from $\beta_1^\eta = 0$ eventually changes the sign of $g_\perp^c$ due to the positive parabolic-in-β_1^η correction term in (7.3) (brown regions in Fig. 7.2c). Another noticeable feature is both $g_\perp^c$ and β_1^c tend to zero for wide quantum channels, that is if l_x is such that:

$$l_x \gg \frac{1}{\sqrt{2}}\frac{\alpha_0 g_\perp^\eta}{\left(-\gamma^\eta\right)^{1/4}\beta_1^\eta}. \tag{7.4}$$

This regime corresponds to the linear Rashba term in (7.1) dominating the terms responsible for channel confinement. We point out that this peculiarity would not occur if $\beta_1^\eta \equiv 0$ for η levels. In that case, $g_\perp^c$ would unsurprisingly tend to the QW value $g_\perp^\eta$ as $l_x \to \infty$ for all F_z. This is in sharp contrast to the present case, where $\beta_1^\eta \neq 0$ everywhere except near $F_z \approx 4.4\,\text{V}/\mu\text{m}$. Note that $g_\perp^c \not\to g_\perp^\eta$ as $l_x \to \infty$ is not an inconsistency of the theory, since the energy dispersion $E(B)$ of the QC system for large l_x exactly coincides with the computed fan-diagram of the QW system, without in-plane confinement. On another note, the in-plane g-factor component shows little dependence on F_z for all l_x that were considered. $|g_\parallel^c|$ also decreases with decreasing l_x, in accordance with an enhancement of η-H mixing.

To evaluate the Rabi frequency of the η ground state associated with an electrical driving $\tilde{\mathbf{F}} = F_{\text{ac}}\mathbf{e}_y \cos\omega t$, where $\hbar\omega$ is the two-level system energy, we introduce a weak confinement along the y direction of characteristic length $l_y > l_x$, effectively turning the QC to an alongated quantum dot (QD). The Rabi frequency Ω is evaluated by computing the bra-ket product

$$\Omega = \frac{eF_{\text{ac}}}{\hbar}\left\langle \mathbb{0}\right| y \left|\mathbb{1}\right\rangle, \tag{7.5}$$

where $|\mathbb{0}\rangle$ and $|\mathbb{1}\rangle$ are the two-level system states defined by the two lowest energy levels obtained from (3.205). We introduce the magnetic field frequency $\omega_B \equiv \mu_{\text{B}} B_0/\hbar$, where B_0 is the magnitude of the applied $\mathbf{B}$-field that defines the two-level system, which is fixed to $B_0 = 0.05\,\text{T}$. Fig. 7.3a shows the computed Rabi frequency Ω in normalized units as a function of $l_y > l_x = 35\,\text{nm}$ and F_z with a perpendicular-to-plane $\mathbf{B}$-field configuration. The

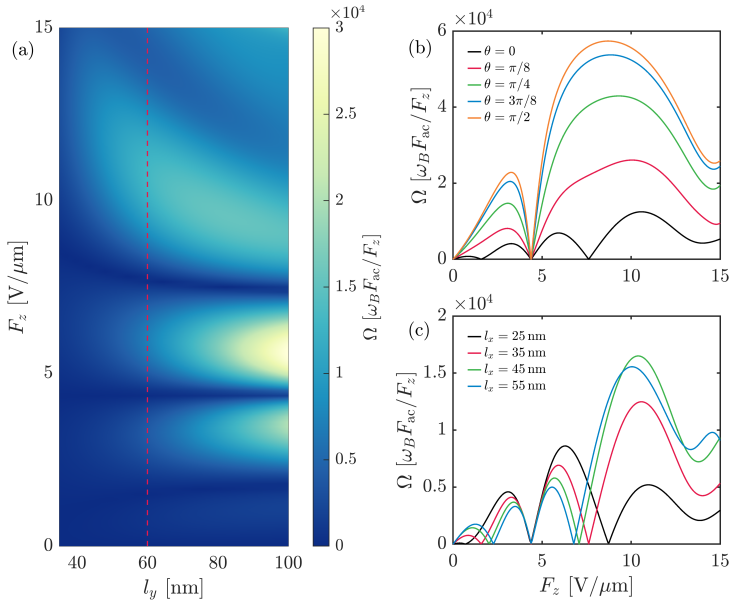

Figure 7.3 (a) Rabi frequency Ω as a function of F_z and l_y, with $l_x = 35\,\text{nm}$ and $\theta = 0$. (b) Rabi frequency along the dashed line in panel (a) for various θ, with $l_x = 35\,\text{nm}$, $l_y = 60\,\text{nm}$ and $\phi = \pi/2$. (c) Rabi frequency $\Omega(F_z)$ for selected l_x, with $l_y = 60\,\text{nm}$ and $\theta = 0$.

line at $4.4\,\text{V}/\mu\text{m}$ corresponding to $\beta_1^c = 0$ is clearly visible in Ω. We may refer to this line as the β-line. Moreover, two additional lines near $F_z \approx 2\,\text{V}/\mu\text{m}$ and $F_z \approx 7.5\,\text{V}/\mu\text{m}$ where $\Omega = 0$ are visible, and correspond to $g_\perp^c = 0$. We will refer to these lines as the g-lines. Fig 7.3b plots Ω along the dashed red line in panel (a) for various **B**-field polar angles θ. Ω increases as the field is tilted in the QW plane, in accordance with $g_\parallel^c > g_\perp^c$. Moreover, the two g-lines disapear as soon as **B** has an in-plane component, since the effective g factor g_θ^c in the tilted configuration is

$$|g_\theta^c| = \sqrt{\left(g_\perp^c \cos\theta\right)^2 + \left(g_\parallel^c \sin\theta\right)^2}, \tag{7.6}$$

and $g_\parallel^c$ never vanishes (see Fig. 7.2e). In contrast, the β-line remains unperturbed for all θ. A similar plot of Ω along the dashed red line is shown in panel (c) for $\theta = 0$ and for selected values of l_x. Here again, the β-line remains untouched for all l_x considered, whereas the two g-lines slighly shift towards the β-line with increasing l_x, in accordance with the $g_\perp^c = 0$ behavior observed in Fig. 7.2c. The stability of the β-line with respect to l_x, l_y and θ is attributed to the inheritance of β_1^c from the QW Rashba parameter β_1^η. In contrast, the g-lines are caused by $g_\perp^c = 0$, which does not inherit from the QW system, but rather from a combined effect involving β_1^η [see (7.3)].

7.3 Conclusion

This work investigated the LH (or η) spin dynamics in $Ge_{1-x}Sn_x$/Ge-MOS quantum channels and elongated quantum dots. The QW system exhibits an η ground state if the Ge well is thicker than ≈ 5–10 nm depending on the magnitude of the out-of-plane DC gate electric field and on the barrier Sn content x. The η-H splitting energy for η ground states consists of two regimes, depending on which layer hosts the lowest H level. The out-of-plane g-factor, in-plane g-factor, and linear Rashba parameter β_1 of η1 were investigated in the QW system, as well as in the QC system, revealing large in-plane g-factors, as well as non-vanishing linear Rashba parameters. Notably, the linear Rashba parameter β_1^η vanishes at finite values of the DC gate electric field, suggesting a strong electrical tunability of SOC strength. QC parameters $g_\perp^c$ and β_1^c surprisingly tend to zero for wide QC widths, except when $\beta_1^\eta = 0$ in the QW system, where they tend to the QW values. In elongated QDs, Rabi frequencies Ω of electrically driven η-like ground states inherit the peculiar behavior of β_1^c and $g_\perp^c$, which manifests through one β-line and two g-lines of vanishing Rabi frequencies. The β-line is especially stable towards variations in the magnetic field angle and QD dimensions.

7.4 Consistency of the theory for wide channels

The behavior of $g_\perp^c$ and β_1^c is inconsistent with the principle that the quantum well values should be recovered as $l_x \to \infty$. Indeed, Fig. 7.2a and 7.2c show that $g_\perp^c \to g_\perp^\eta$ only if $\beta_1^\eta = 0$. In this section, we show that the theory employed for the quantum channel *is* in fact coherent, despite what Fig. 7.2 might lead to believe.

Here we demonstrate that the energy dispersion of the channel orbitals versus B converge to the fan-diagram of the QW system as $l_x \to \infty$. We select the following heterostructure parameters: $l_z = 15\,\text{nm}$, $x = 16\%$, and $F_z = 6\,\text{V}/\mu\text{m}$, such that $\beta_1^\eta \neq 0$. The fan-diagram of the QW system η ground state is computed with (3.113) and is shown in Fig. 7.4 (bottom right). In contrast to H levels, where the fan-diagram opens up linearly with B, an η fan-diagram opens like a sideways parabola near $B = 0$ if $\beta_1^\eta \neq 0$.

This fan-diagram is shown alongside the dispersions obtained from (3.192) for finite l_x in Fig. 7.4. As l_x increases, the energy gap between adjacent QC orbitals decreases as expected. Coupling between orbitals cause the g-factor of the lowest QC orbital to become very small (this is noticeable in Fig. 7.4). For very large l_x, orbitals gather closely near $B = 0$, but remain well separated at larger fields, with some levels spectacularly changing order and reorganising such that the fan-diagram of the last panel is roughly recovered. The energy level structure computed from (3.192) does not show all spin-split pairs like the fan-diagram

from (3.113) does. This is merely an artifact of the eigenvalue sorting method. In the former, all levels closest to a given energy guess are shown, whereas in the former, all Landau levels closest to an energy guess are shown.

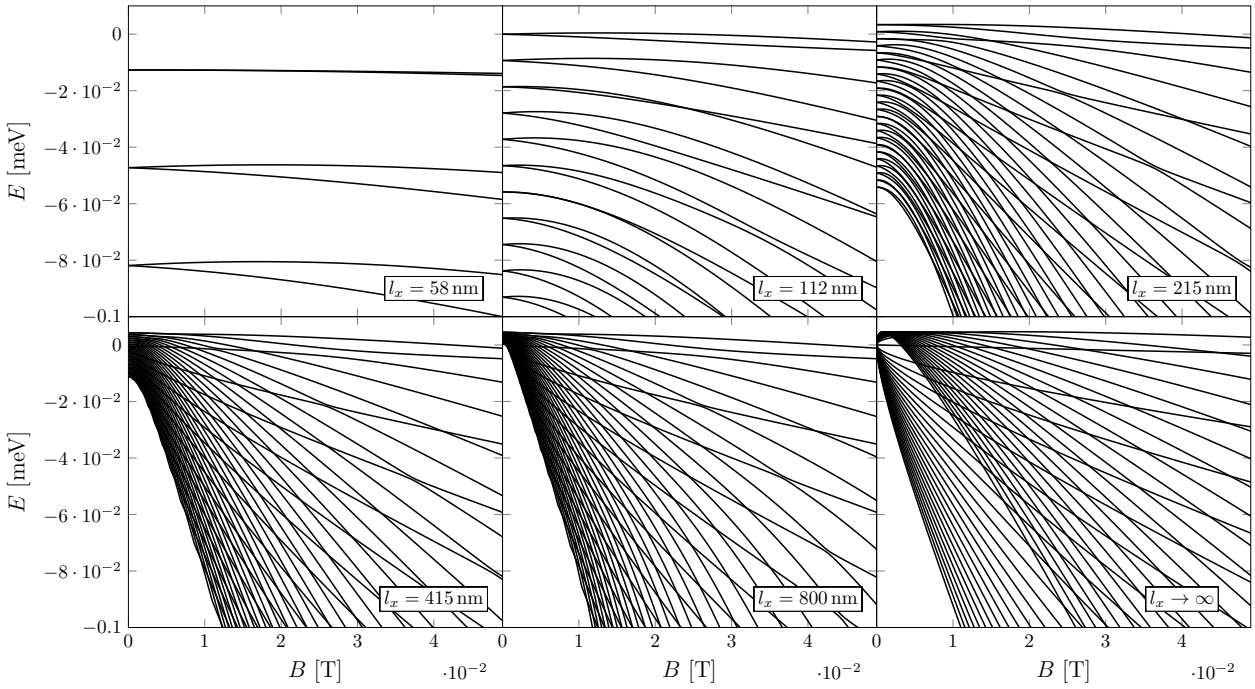

Figure 7.4 Quantum channel energy dispersion as a function of the out-of-plane magnetic field up to 0.05 T for increasing widths l_x. The bottom right panel labelled $l_x \to \infty$ is the fan-diagram of the QW system computed with (3.113). All other panels are computed from (3.192) with $k_y = 0$. QW parameters in all cases are $l_z = 15\,\mathrm{nm}$, $x = 16\%$ and $F_z = 6\,\mathrm{V/\mu m}$ ($\beta_1^{\eta} \approx 1.21\,\mathrm{meV\,nm}$). The zero of energy is placed on the QW $\eta 1$ subband ($E_1^{\eta} = 0$).

CHAPTER 8 CONCLUSIONS AND PERSPECTIVES

A summary of the work performed in this project is given in this chapter. It is followed by a few remarks on the limitations of the research, and includes a list of physical aspects that were overlooked in the theoretical modelling. Considering this, future improvements are discussed in the last subsection of this Chapter.

8.1 Summary of key contributions

This dissertation gave an in-depth description of the theoretical modelling that was performed to quantitatively describe the behavior of LH spins in semiconductor heterostructures and nanostructures. Strain-resolved $k \cdot p$ theory adapted for heterostructures was a central part in the theoretical framework used throughout this work. Important effects such as wavefunction leaking into barriers and coupling with higher energy bands required an explicit re-derivation of many LH properties predicted by $k \cdot p$ theory. The theoretical framework and material parametrization was then successfully benchmarked against experimental observation of vanishing Zeeman energies in planar hole devices, simultaneously enabling a tool for estimating relevant SOC-related quantities pertaining to planar systems. Next, the theory was employed to determine the conditions of LH confinement in tensile strained $Ge_{1-x}Sn_x/Ge/Ge_{1-x}Sn_x$ QW heterostructures. In systems where confinement is present, LH properties such as effective masses, g-tensor components, SOC parameters and η-H mixing were investigated. The theoretical framework was also employed to give predictions on the dynamics of a LH qubit device in tensile strained Ge quantum dots. Finally, the behavior of LH spins was investigated for various in-plane confinement configurations, such as quantum channels and elongated quantum dots, with MOS-like heterostructures. Estimations of Rabi frequencies indicate that LH-like semiconductor spin-qubits are promising candidates for scalable quantum computing, since their inherently favorable SOC characteristics can be leveraged to implement fast and efficient all-electrical manipulation schemes.

8.2 Limitations

The theoretical framework described in Chapter 3 is well adapted for envelope problems, where spread across multiple materials is non-negligible. In fact, the theory is applicable to *any* type of confinement profile along the growth direction (infinite, square, triangular, broaden interfaces, and combinations thereof). However, some important limitations are

inherent to the model.

The first notable approximation that was made is to neglect any shear strain components that might appear after the deposition of electrostatic gates on top of the heterostructure. In addition, theoretical calculations [49, 50], as well as strong experimental evidence in Si-MOS devices [242] suggest that these shear components may play a crucial role in HH spin qubit dynamics. Complex gate pattern geometries are also expected to give confining potentials that are not necessarily separable, as it was assumed in Section 3.4. This may give rise to non-zero g_{xz} and g_{yz} g-tensor components, which are identically equal to zero here. It is an open question whether shear strain components and non-separable confining potentials have a significant impact on η-like spin qubits.

This work also did not include the influence on Rabi frequencies from crystal defects like charge traps and interface roughness. These are known to have an influence on electron and HH spin qubits, with charge traps having a bigger influence compared to interface roughness. It was estimated that Rabi frequencies can drop by up to one order of magnitude for large charge trap densities [243]. On the same note, symmetry effects at the $\mathrm{Ge/Ge_{1-x}Sn_x}$ interfaces were neglected here. There is evidence that such symmetry breaking gives rise to Dresselhaus-type linear-in-momentum, and even small linear Rashba SOI contributions to the HH effective Hamiltonian [50]. Bulk inversion symmetry breaking in $\mathrm{Ge_{1-x}Sn_x}$ may introduce Dresselhaus-type SOI as well, however this has been conspeciously missing in the literature. Regarding the material parametrization of $\mathrm{Ge_{1-x}Sn_x}$, there are still many parameters that are yet to be measured and are therefore only linearly interpolated from those of pure Ge and pure Sn. These include the g-factor parameters κ and q, which could have a significant effect on Rabi frequencies.

8.3 Future Research

Considering the aforementioned main results and limitations of this work, we propose a few next steps to further refine the understanding of LH spin dynamics. First, studying the effects of shear strain and in-plane position-dependent strain tensor elements on LH qubits should improve the predictions made throughout this work. As a first step, specific gate patterns, associated currents, voltages and layer thicknesses should provide the necessary ingredients to evaluate the strain tensor $\varepsilon(\mathbf{r})$. It could also provide an estimation for the confining potential $V(\mathbf{r})$ (which may not be separable). Depending on $\varepsilon(\mathbf{r})$ and $V(\mathbf{r})$, a few approximations may allow one to keep the one-dimensional heterostructure discretization approach to improve computation times. Otherwise, solving the $k\cdot p$ Hamiltonian with in-plane position-dependent ε and V is likely to require a full 3D discretization of the simulation domain. To this end, we

suggest following the approaches in References [150, 175, 244]. Another next step would be to investigate interface and charge trap effects on LH qubit Rabi frequencies. Charge traps could dominate for LHs just as they do for HHs, but the different symmetry of LH states could lead to more interesting behavior. Additionally, oxides on Ge behave quite differently than those on Si, so further research on dangling bonds in Ge and how they interact with holes are probably necessary. This would also be a great opportunity to investigate their role on the relaxation and dephasing times of a LH qubit.

Another improvement to band structure calculations would be to include doping and charge redistribution effects to the confining potential V. This would give a more accurate description of band alignments in $Ge_{1-x}Sn_x$/Ge/$Ge_{1-x}Sn_x$ heterostructures. It would also guide doping experiments to optimize the population of LH levels within the tensile strained QW, and possibly reduce charge noise. Including doping effects to $k \cdot p$ theory requires a self-consistent solution with Poisson's equation. Details are provided in Appendix B.

Finally, it would be of great interest to develop a scheme in which the LH ground state is leveraged to transfer the polarization state of a photon to that of the LH spin. There have been many propositions [26, 27] suggesting that large in-plane g-factors are desirable in such conversion schemes. However, the resulting state configuration in the QD device would also involve electron spins, which are not confined within the same layer as LHs in $Ge_{1-x}Sn_x$-based heterostructures. Multi-QW $Ge_{1-x}Sn_x$ devices where LH and electron envelopes overlap across a given interface might lead to a solution, but further research is necessary.

REFERENCES

[1] E. Marcellina, A. R. Hamilton, R. Winkler, and D. Culcer, "Spin-orbit interactions in inversion-asymmetric two-dimensional hole systems: A variational analysis," *Phys. Rev. B*, vol. 95, p. 075305, Feb 2017. [Online]. Available: https://link.aps.org/doi/10.1103/PhysRevB.95.075305

[2] G. Bihlmayer, O. Rader, and R. Winkler, "Focus on the Rashba effect," *New Journal of Physics*, vol. 17, no. 5, p. 050202, may 2015. [Online]. Available: https://dx.doi.org/10.1088/1367-2630/17/5/050202

[3] P. Yu and M. Cardona, *Fundamentals of Semiconductors: Physics and Materials Properties*, ser. Graduate Texts in Physics. Springer Berlin Heidelberg, 2010. [Online]. Available: https://books.google.ca/books?id=5aBuKYBT_hsC

[4] G. Koster, *Properties of the Thirty-two Point Groups*, ser. M.I.T. Press research monographs. M.I.T. Press, 1963. [Online]. Available: https://books.google.ca/books?id=XTVRAAAAMAAJ

[5] P. Shor, "Algorithms for quantum computation: discrete logarithms and factoring," in *Proceedings 35th Annual Symposium on Foundations of Computer Science*, 1994, pp. 124–134.

[6] L. K. Grover, "A Fast Quantum Mechanical Algorithm for Database Search," in *Proceedings of the Twenty-Eighth Annual ACM Symposium on Theory of Computing*, ser. STOC '96. New York, NY, USA: Association for Computing Machinery, 1996, p. 212–219. [Online]. Available: https://doi.org/10.1145/237814.237866

[7] D. Loss and D. P. DiVincenzo, "Quantum computation with quantum dots," *Phys. Rev. A*, vol. 57, pp. 120–126, Jan 1998. [Online]. Available: https://link.aps.org/doi/10.1103/PhysRevA.57.120

[8] National Academies of Sciences, Engineering, and Medicine, *Quantum Computing: Progress and Prospects*. Washington, DC: The National Academies Press, 2019. [Online]. Available: https://www.nap.edu/catalog/25196/quantum-computing-progress-and-prospects

[9] R. Brunner, Y.-S. Shin, T. Obata, M. Pioro-Ladrière, T. Kubo, K. Yoshida, T. Taniyama, Y. Tokura, and S. Tarucha, "Two-Qubit Gate of Combined

Single-Spin Rotation and Interdot Spin Exchange in a Double Quantum Dot," *Phys. Rev. Lett.*, vol. 107, p. 146801, Sep 2011. [Online]. Available: https://link.aps.org/doi/10.1103/PhysRevLett.107.146801

[10] K. Takeda, A. Noiri, T. Nakajima, T. Kobayashi, and S. Tarucha, "Quantum error correction with silicon spin qubits," *Nature*, vol. 608, no. 7924, pp. 682–686, Aug 2022. [Online]. Available: https://doi.org/10.1038/s41586-022-04986-6

[11] A. R. Mills, C. R. Guinn, M. J. Gullans, A. J. Sigillito, M. M. Feldman, E. Nielsen, and J. R. Petta, "Two-qubit silicon quantum processor with operation fidelity exceeding 99%," *Science Advances*, vol. 8, no. 14, p. eabn5130, 2022. [Online]. Available: https://www.science.org/doi/abs/10.1126/sciadv.abn5130

[12] N. W. Hendrickx, W. I. L. Lawrie, M. Russ, F. van Riggelen, S. L. de Snoo, R. N. Schouten, A. Sammak, G. Scappucci, and M. Veldhorst, "A four-qubit germanium quantum processor," *Nature*, vol. 591, no. 7851, pp. 580–585, Mar 2021. [Online]. Available: https://doi.org/10.1038/s41586-021-03332-6

[13] R. Hanson, L. P. Kouwenhoven, J. R. Petta, S. Tarucha, and L. M. K. Vandersypen, "Spins in few-electron quantum dots," *Rev. Mod. Phys.*, vol. 79, pp. 1217–1265, Oct 2007. [Online]. Available: https://link.aps.org/doi/10.1103/RevModPhys.79.1217

[14] J. Medford, J. Beil, J. M. Taylor, S. D. Bartlett, A. C. Doherty, E. I. Rashba, D. P. DiVincenzo, H. Lu, A. C. Gossard, and C. M. Marcus, "Self-consistent measurement and state tomography of an exchange-only spin qubit," *Nature Nanotechnology*, vol. 8, no. 9, pp. 654–659, Sep 2013. [Online]. Available: https://doi.org/10.1038/nnano.2013.168

[15] G. Cao, H.-O. Li, T. Tu, L. Wang, C. Zhou, M. Xiao, G.-C. Guo, H.-W. Jiang, and G.-P. Guo, "Ultrafast universal quantum control of a quantum-dot charge qubit using Landau–Zener–Stückelberg interference," *Nature Communications*, vol. 4, no. 1, p. 1401, Jan 2013. [Online]. Available: https://doi.org/10.1038/ncomms2412

[16] G. de Lange, Z. H. Wang, D. Ristè, V. V. Dobrovitski, and R. Hanson, "Universal Dynamical Decoupling of a Single Solid-State Spin from a Spin Bath," *Science*, vol. 330, no. 6000, pp. 60–63, 2010. [Online]. Available: https://www.science.org/doi/abs/10.1126/science.1192739

[17] R. R. Hayes, A. A. Kiselev, M. G. Borselli, S. S. Bui, E. T. Croke III, P. W. Deelman, B. M. Maune, I. Milosavljevic, J.-S. Moon, R. S. Ross *et al.*, "Lifetime measurements (T1) of electron spins in Si/SiGe quantum dots," *arXiv preprint arXiv:0908.0173*, 2009.

[18] M. Xiao, M. G. House, and H. W. Jiang, "Measurement of the Spin Relaxation Time of Single Electrons in a Silicon Metal-Oxide-Semiconductor-Based Quantum Dot," *Phys. Rev. Lett.*, vol. 104, p. 096801, Mar 2010. [Online]. Available: https://link.aps.org/doi/10.1103/PhysRevLett.104.096801

[19] M. Veldhorst, J. C. C. Hwang, C. H. Yang, A. W. Leenstra, B. de Ronde, J. P. Dehollain, J. T. Muhonen, F. E. Hudson, K. M. Itoh, A. Morello, and A. S. Dzurak, "An addressable quantum dot qubit with fault-tolerant control-fidelity," *Nature Nanotechnology*, vol. 9, no. 12, pp. 981–985, Dec 2014. [Online]. Available: https://doi.org/10.1038/nnano.2014.216

[20] C. Testelin, F. Bernardot, B. Eble, and M. Chamarro, "Hole–spin dephasing time associated with hyperfine interaction in quantum dots," *Phys. Rev. B*, vol. 79, p. 195440, May 2009. [Online]. Available: https://link.aps.org/doi/10.1103/PhysRevB.79.195440

[21] W. J. Hardy, C. T. Harris, Y.-H. Su, Y. Chuang, J. Moussa, L. N. Maurer, J.-Y. Li, T.-M. Lu, and D. R. Luhman, "Single and double hole quantum dots in strained Ge/SiGe quantum wells," *Nanotechnology*, vol. 30, no. 21, p. 215202, mar 2019. [Online]. Available: https://dx.doi.org/10.1088/1361-6528/ab061e

[22] A. Sammak, D. Sabbagh, N. W. Hendrickx, M. Lodari, B. Paquelet Wuetz, A. Tosato, L. Yeoh, M. Bollani, M. Virgilio, M. A. Schubert, P. Zaumseil, G. Capellini, M. Veldhorst, and G. Scappucci, "Shallow and Undoped Germanium Quantum Wells: A Playground for Spin and Hybrid Quantum Technology," *Advanced Functional Materials*, vol. 29, no. 14, p. 1807613, 2019. [Online]. Available: https://onlinelibrary.wiley.com/doi/abs/10.1002/adfm.201807613

[23] A. Dobbie, M. Myronov, R. J. H. Morris, A. H. A. Hassan, M. J. Prest, V. A. Shah, E. H. C. Parker, T. E. Whall, and D. R. Leadley, "Ultra-high hole mobility exceeding one million in a strained germanium quantum well," *Applied Physics Letters*, vol. 101, no. 17, p. 172108, 2012. [Online]. Available: https://doi.org/10.1063/1.4763476

[24] P. Del Vecchio and O. Moutanabbir, "Light-hole gate-defined spin-orbit qubit," *Phys. Rev. B*, vol. 107, p. L161406, Apr 2023. [Online]. Available: https://link.aps.org/doi/10.1103/PhysRevB.107.L161406

[25] A. G. Moghaddam, T. Kernreiter, M. Governale, and U. Zülicke, "Exporting superconductivity across the gap: Proximity effect for semiconductor valence-band states due to contact with a simple-metal superconductor," *Phys. Rev. B*, vol. 89, p.

184507, May 2014. [Online]. Available: https://link.aps.org/doi/10.1103/PhysRevB.89.184507

[26] R. Vrijen and E. Yablonovitch, "A spin-coherent semiconductor photo-detector for quantum communication," *Physica E: Low-dimensional Systems and Nanostructures*, vol. 10, no. 4, pp. 569–575, 2001. [Online]. Available: https://www.sciencedirect.com/science/article/pii/S1386947700002964

[27] L. Gaudreau, A. Bogan, M. Korkusinski, S. Studenikin, D. G. Austing, and A. S. Sachrajda, "Entanglement distribution schemes employing coherent photon-to-spin conversion in semiconductor quantum dot circuits," *Semiconductor Science and Technology*, vol. 32, no. 9, p. 093001, aug 2017. [Online]. Available: https://dx.doi.org/10.1088/1361-6641/aa788d

[28] D. Saladukha, M. B. Clavel, F. Murphy-Armando, G. Greene-Diniz, M. Grüning, M. K. Hudait, and T. J. Ochalski, "Direct and indirect band gaps in Ge under biaxial tensile strain investigated by photoluminescence and photoreflectance studies," *Phys. Rev. B*, vol. 97, p. 195304, May 2018. [Online]. Available: https://link.aps.org/doi/10.1103/PhysRevB.97.195304

[29] P. Rauter, G. Mussler, D. Grützmacher, and T. Fromherz, "Tensile strained SiGe quantum well infrared photodetectors based on a light-hole ground state," *Applied Physics Letters*, vol. 98, no. 21, p. 211106, 2011. [Online]. Available: https://doi.org/10.1063/1.3593134

[30] S. R. Mehrotra, A. Paul, and G. Klimeck, "Atomistic approach to alloy scattering in $Si_{1-x}Ge_x$," *Applied Physics Letters*, vol. 98, no. 17, p. 173503, 04 2011. [Online]. Available: https://doi.org/10.1063/1.3583983

[31] S. Assali, A. Attiaoui, P. Del Vecchio, S. Mukherjee, J. Nicolas, and O. Moutanabbir, "A Light-Hole Germanium Quantum Well on Silicon," *Advanced Materials*, vol. 34, no. 27, p. 2201192, jun 2022. [Online]. Available: https://doi.org/10.1002%2Fadma.202201192

[32] O. Moutanabbir, S. Assali, A. Attiaoui, and P. Del Vecchio, "Quantum heterostructures, related devices and methods for manufacturing the same," *International Patent*, no. WO2020243831A1, 2020.

[33] P. Del Vecchio, M. Lodari, A. Sammak, G. Scappucci, and O. Moutanabbir, "Vanishing Zeeman energy in a two-dimensional hole gas," *Phys. Rev. B*, vol. 102, p. 115304, Sep 2020. [Online]. Available: https://link.aps.org/doi/10.1103/PhysRevB.102.115304

[34] P. Del Vecchio and O. Moutanabbir, "Light-hole spin confined in germanium," *Phys. Rev. B*, vol. 110, p. 045409, Jul 2024. [Online]. Available: https://link.aps.org/doi/10.1103/PhysRevB.110.045409

[35] R. Winkler, *Spin-orbit Coupling Effects in Two-Dimensional Electron and Hole Systems*. Springer, 2003, vol. 191.

[36] ——, "Rashba spin splitting in two-dimensional electron and hole systems," *Phys. Rev. B*, vol. 62, pp. 4245–4248, Aug 2000. [Online]. Available: https://link.aps.org/doi/10.1103/PhysRevB.62.4245

[37] T. Koga, J. Nitta, and M. van Veenhuizen, "Ballistic spin interferometer using the Rashba effect," *Phys. Rev. B*, vol. 70, p. 161302, Oct 2004. [Online]. Available: https://link.aps.org/doi/10.1103/PhysRevB.70.161302

[38] T. Koga, Y. Sekine, and J. Nitta, "Experimental realization of a ballistic spin interferometer based on the Rashba effect using a nanolithographically defined square loop array," *Phys. Rev. B*, vol. 74, p. 041302, Jul 2006. [Online]. Available: https://link.aps.org/doi/10.1103/PhysRevB.74.041302

[39] J. E. Hirsch, "Spin Hall Effect," *Phys. Rev. Lett.*, vol. 83, pp. 1834–1837, Aug 1999. [Online]. Available: https://link.aps.org/doi/10.1103/PhysRevLett.83.1834

[40] S. Murakami, N. Nagaosa, and S.-C. Zhang, "Dissipationless Quantum Spin Current at Room Temperature," *Science*, vol. 301, no. 5638, pp. 1348–1351, 2003. [Online]. Available: https://www.science.org/doi/abs/10.1126/science.1087128

[41] Y. K. Kato, R. C. Myers, A. C. Gossard, and D. D. Awschalom, "Observation of the Spin Hall Effect in Semiconductors," *Science*, vol. 306, no. 5703, pp. 1910–1913, 2004. [Online]. Available: https://www.science.org/doi/abs/10.1126/science.1105514

[42] C. L. Kane and E. J. Mele, "Z_2 Topological Order and the Quantum Spin Hall Effect," *Phys. Rev. Lett.*, vol. 95, p. 146802, Sep 2005. [Online]. Available: https://link.aps.org/doi/10.1103/PhysRevLett.95.146802

[43] B. A. Bernevig and S.-C. Zhang, "Quantum spin hall effect," *Phys. Rev. Lett.*, vol. 96, p. 106802, Mar 2006. [Online]. Available: https://link.aps.org/doi/10.1103/PhysRevLett.96.106802

[44] G. M. Minkov, A. A. Sherstobitov, A. V. Germanenko, O. E. Rut, V. A. Larionova, and B. N. Zvonkov, "Antilocalization and spin-orbit coupling in the

hole gas in strained GaAs/$In_xGa_{1-x}As$/GaAs quantum well heterostructures," *Phys. Rev. B*, vol. 71, p. 165312, Apr 2005. [Online]. Available: https://link.aps.org/doi/10.1103/PhysRevB.71.165312

[45] R. Winkler, H. Noh, E. Tutuc, and M. Shayegan, "Anomalous Rashba spin splitting in two-dimensional hole systems," *Phys. Rev. B*, vol. 65, p. 155303, Mar 2002. [Online]. Available: https://link.aps.org/doi/10.1103/PhysRevB.65.155303

[46] R. Moriya, K. Sawano, Y. Hoshi, S. Masubuchi, Y. Shiraki, A. Wild, C. Neumann, G. Abstreiter, D. Bougeard, T. Koga, and T. Machida, "Cubic Rashba Spin-Orbit Interaction of a Two-Dimensional Hole Gas in a Strained-Ge/SiGe Quantum Well," *Phys. Rev. Lett.*, vol. 113, p. 086601, Aug 2014. [Online]. Available: https://link.aps.org/doi/10.1103/PhysRevLett.113.086601

[47] G. Scappucci, C. Kloeffel, F. A. Zwanenburg, D. Loss, M. Myronov, J.-J. Zhang, S. De Franceschi, G. Katsaros, and M. Veldhorst, "The germanium quantum information route," *Nature Reviews Materials*, Dec 2020. [Online]. Available: https://doi.org/10.1038/s41578-020-00262-z

[48] N. W. Hendrickx, W. I. L. Lawrie, L. Petit, A. Sammak, G. Scappucci, and M. Veldhorst, "A single-hole spin qubit," *Nature Communications*, vol. 11, no. 1, p. 3478, Jul 2020. [Online]. Available: https://doi.org/10.1038/s41467-020-17211-7

[49] J. C. Abadillo-Uriel, E. A. Rodríguez-Mena, B. Martinez, and Y.-M. Niquet, "Hole-Spin Driving by Strain-Induced Spin-Orbit Interactions," *Phys. Rev. Lett.*, vol. 131, p. 097002, Sep 2023. [Online]. Available: https://link.aps.org/doi/10.1103/PhysRevLett.131.097002

[50] E. A. Rodríguez-Mena, J. C. Abadillo-Uriel, G. Veste, B. Martinez, J. Li, B. Sklénard, and Y.-M. Niquet, "Linear-in-momentum spin orbit interactions in planar Ge/GeSi heterostructures and spin qubits," *Phys. Rev. B*, vol. 108, p. 205416, Nov 2023. [Online]. Available: https://link.aps.org/doi/10.1103/PhysRevB.108.205416

[51] J. C. Hensel and K. Suzuki, "Anisotropy of the g Factor of the Free Hole in Ge and Conduction-Band Spin-Orbit Splitting," *Phys. Rev. Lett.*, vol. 22, pp. 838–840, Apr 1969. [Online]. Available: https://link.aps.org/doi/10.1103/PhysRevLett.22.838

[52] R. Mizokuchi, R. Maurand, F. Vigneau, M. Myronov, and S. De Franceschi, "Ballistic One-Dimensional Holes with Strong g-Factor Anisotropy in Germanium," *Nano*

Letters, vol. 18, no. 8, pp. 4861–4865, 2018, pMID: 29995419. [Online]. Available: https://doi.org/10.1021/acs.nanolett.8b01457

[53] F. F. Fang and P. J. Stiles, "Effects of a Tilted Magnetic Field on a Two-Dimensional Electron Gas," *Phys. Rev.*, vol. 174, pp. 823–828, Oct 1968. [Online]. Available: https://link.aps.org/doi/10.1103/PhysRev.174.823

[54] C.-A. Wang, H. E. Ercan, M. F. Gyure, G. Scappucci, M. Veldhorst, and M. Rimbach-Russ, "Modeling of planar germanium hole qubits in electric and magnetic fields," *npj Quantum Information*, vol. 10, no. 1, p. 102, Oct 2024. [Online]. Available: https://doi.org/10.1038/s41534-024-00897-8

[55] M. A. Semina, A. A. Golovatenko, and A. V. Rodina, "Influence of the spin-orbit split-off valence band on the hole g factor in semiconductor nanocrystals," *Phys. Rev. B*, vol. 104, p. 205423, Nov 2021. [Online]. Available: https://link.aps.org/doi/10.1103/PhysRevB.104.205423

[56] F. N. M. Froning, M. J. Rančić, B. Hetényi, S. Bosco, M. K. Rehmann, A. Li, E. P. A. M. Bakkers, F. A. Zwanenburg, D. Loss, D. M. Zumbühl, and F. R. Braakman, "Strong spin-orbit interaction and g-factor renormalization of hole spins in Ge/Si nanowire quantum dots," *Phys. Rev. Res.*, vol. 3, p. 013081, Jan 2021. [Online]. Available: https://link.aps.org/doi/10.1103/PhysRevResearch.3.013081

[57] D. Jirovec, P. M. Mutter, A. Hofmann, A. Crippa, M. Rychetsky, D. L. Craig, J. Kukucka, F. Martins, A. Ballabio, N. Ares, D. Chrastina, G. Isella, G. Burkard, and G. Katsaros, "Dynamics of Hole Singlet-Triplet Qubits with Large g-Factor Differences," *Phys. Rev. Lett.*, vol. 128, p. 126803, Mar 2022. [Online]. Available: https://link.aps.org/doi/10.1103/PhysRevLett.128.126803

[58] I. L. Drichko, A. A. Dmitriev, V. A. Malysh, I. Y. Smirnov, H. von Känel, M. Kummer, D. Chrastina, and G. Isella, "Effective g factor of 2D holes in strained Ge quantum wells," *Journal of Applied Physics*, vol. 123, no. 16, p. 165703, 2018. [Online]. Available: https://doi.org/10.1063/1.5025413

[59] A. Giorgioni, S. Paleari, S. Cecchi, E. Vitiello, E. Grilli, G. Isella, W. Jantsch, M. Fanciulli, and F. Pezzoli, "Strong confinement-induced engineering of the g factor and lifetime of conduction electron spins in Ge quantum wells," *Nature Communications*, vol. 7, no. 1, p. 13886, Dec 2016. [Online]. Available: https://doi.org/10.1038/ncomms13886

[60] C. Gradl, R. Winkler, M. Kempf, J. Holler, D. Schuh, D. Bougeard, A. Hernández-Mínguez, K. Biermann, P. V. Santos, C. Schüller, and T. Korn, "Asymmetric g Tensor in Low-Symmetry Two-Dimensional Hole Systems," *Phys. Rev. X*, vol. 8, p. 021068, Jun 2018. [Online]. Available: https://link.aps.org/doi/10.1103/PhysRevX.8.021068

[61] Y. Jiang, M. Ermolaev, G. Kipshidze, S. Moon, M. Ozerov, D. Smirnov, Z. Jiang, and S. Suchalkin, "Giant g-factors and fully spin-polarized states in metamorphic short-period InAsSb/InSb superlattices," *Nature Communications*, vol. 13, no. 1, p. 5960, Oct 2022. [Online]. Available: https://doi.org/10.1038/s41467-022-33560-x

[62] J. Fischer, W. A. Coish, D. V. Bulaev, and D. Loss, "Spin decoherence of a heavy hole coupled to nuclear spins in a quantum dot," *Phys. Rev. B*, vol. 78, p. 155329, Oct 2008. [Online]. Available: https://link.aps.org/doi/10.1103/PhysRevB.78.155329

[63] C. G. Van de Walle and P. E. Blöchl, "First-principles calculations of hyperfine parameters," *Phys. Rev. B*, vol. 47, pp. 4244–4255, Feb 1993. [Online]. Available: https://link.aps.org/doi/10.1103/PhysRevB.47.4244

[64] L. V. C. Assali, H. M. Petrilli, R. B. Capaz, B. Koiller, X. Hu, and S. Das Sarma, "Hyperfine interactions in silicon quantum dots," *Phys. Rev. B*, vol. 83, p. 165301, Apr 2011. [Online]. Available: https://link.aps.org/doi/10.1103/PhysRevB.83.165301

[65] P. Philippopoulos, S. Chesi, and W. A. Coish, "First-principles hyperfine tensors for electrons and holes in GaAs and silicon," *Phys. Rev. B*, vol. 101, p. 115302, Mar 2020. [Online]. Available: https://link.aps.org/doi/10.1103/PhysRevB.101.115302

[66] S. Bosco and D. Loss, "Fully Tunable Hyperfine Interactions of Hole Spin Qubits in Si and Ge Quantum Dots," *Phys. Rev. Lett.*, vol. 127, p. 190501, Nov 2021. [Online]. Available: https://link.aps.org/doi/10.1103/PhysRevLett.127.190501

[67] O. Moutanabbir, S. Assali, A. Attiaoui, G. Daligou, P. Daoust, P. D. Vecchio, S. Koelling, L. Luo, and N. Rotaru, "Nuclear Spin-Depleted, Isotopically Enriched ^{70}Ge/^{28}Si^{70}Ge Quantum Wells," *Advanced Materials*, vol. 36, no. 8, p. 2305703, 2024. [Online]. Available: https://onlinelibrary.wiley.com/doi/abs/10.1002/adma.202305703

[68] Y. Hada and M. Eto, "Electronic states in silicon quantum dots: Multivalley artificial atoms," *Phys. Rev. B*, vol. 68, p. 155322, Oct 2003. [Online]. Available: https://link.aps.org/doi/10.1103/PhysRevB.68.155322

[69] M. Friesen, S. Chutia, C. Tahan, and S. N. Coppersmith, "Valley splitting theory of SiGe/Si/SiGe quantum wells," *Phys. Rev. B*, vol. 75, p. 115318, Mar 2007. [Online]. Available: https://link.aps.org/doi/10.1103/PhysRevB.75.115318

[70] J. Yoneda, K. Takeda, T. Otsuka, T. Nakajima, M. R. Delbecq, G. Allison, T. Honda, T. Kodera, S. Oda, Y. Hoshi, N. Usami, K. M. Itoh, and S. Tarucha, "A quantum-dot spin qubit with coherence limited by charge noise and fidelity higher than 99.9%," *Nature Nanotechnology*, vol. 13, no. 2, pp. 102–106, Feb 2018. [Online]. Available: https://doi.org/10.1038/s41565-017-0014-x

[71] D. M. Zajac, A. J. Sigillito, M. Russ, F. Borjans, J. M. Taylor, G. Burkard, and J. R. Petta, "Resonantly driven CNOT gate for electron spins," *Science*, vol. 359, no. 6374, pp. 439–442, 2018. [Online]. Available: https://www.science.org/doi/abs/10.1126/science.aao5965

[72] T. F. Watson, S. G. J. Philips, E. Kawakami, D. R. Ward, P. Scarlino, M. Veldhorst, D. E. Savage, M. G. Lagally, M. Friesen, S. N. Coppersmith, M. A. Eriksson, and L. M. K. Vandersypen, "A programmable two-qubit quantum processor in silicon," *Nature*, vol. 555, no. 7698, pp. 633–637, Mar 2018. [Online]. Available: https://doi.org/10.1038/nature25766

[73] T. B. Boykin, G. Klimeck, M. A. Eriksson, M. Friesen, S. N. Coppersmith, P. von Allmen, F. Oyafuso, and S. Lee, "Valley splitting in strained silicon quantum wells," *Applied Physics Letters*, vol. 84, no. 1, pp. 115–117, 01 2004. [Online]. Available: https://doi.org/10.1063/1.1637718

[74] A. Jones, E. Pritchett, E. Chen, T. Keating, R. Andrews, J. Blumoff, L. De Lorenzo, K. Eng, S. Ha, A. Kiselev, S. Meenehan, S. Merkel, J. Wright, L. Edge, R. Ross, M. Rakher, M. Borselli, and A. Hunter, "Spin-Blockade Spectroscopy of Si/Si-Ge Quantum Dots," *Phys. Rev. Appl.*, vol. 12, p. 014026, Jul 2019. [Online]. Available: https://link.aps.org/doi/10.1103/PhysRevApplied.12.014026

[75] A. Hosseinkhani and G. Burkard, "Electromagnetic control of valley splitting in ideal and disordered Si quantum dots," *Phys. Rev. Res.*, vol. 2, p. 043180, Nov 2020. [Online]. Available: https://link.aps.org/doi/10.1103/PhysRevResearch.2.043180

[76] S. F. Neyens, R. H. Foote, B. Thorgrimsson, T. J. Knapp, T. McJunkin, L. M. K. Vandersypen, P. Amin, N. K. Thomas, J. S. Clarke, D. E. Savage, M. G. Lagally, M. Friesen, S. N. Coppersmith, and M. A. Eriksson, "The critical role of substrate

disorder in valley splitting in Si quantum wells," *Applied Physics Letters*, vol. 112, no. 24, p. 243107, 06 2018. [Online]. Available: https://doi.org/10.1063/1.5033447

[77] T. McJunkin, E. R. MacQuarrie, L. Tom, S. F. Neyens, J. P. Dodson, B. Thorgrimsson, J. Corrigan, H. E. Ercan, D. E. Savage, M. G. Lagally, R. Joynt, S. N. Coppersmith, M. Friesen, and M. A. Eriksson, "Valley splittings in Si/SiGe quantum dots with a germanium spike in the silicon well," *Phys. Rev. B*, vol. 104, p. 085406, Aug 2021. [Online]. Available: https://link.aps.org/doi/10.1103/PhysRevB.104.085406

[78] B. McJunkin, Thomasand Harpt, Y. Feng, M. P. Losert, R. Rahman, J. P. Dodson, M. A. Wolfe, D. E. Savage, M. G. Lagally, S. N. Coppersmith, M. Friesen, R. Joynt, and M. A. Eriksson, "SiGe quantum wells with oscillating Ge concentrations for quantum dot qubits," *Nature Communications*, vol. 13, no. 1, p. 7777, Dec 2022. [Online]. Available: https://doi.org/10.1038/s41467-022-35510-z

[79] A. Sigillito, J. Loy, D. Zajac, M. Gullans, L. Edge, and J. Petta, "Site-Selective Quantum Control in an Isotopically Enriched $^{28}Si/Si_{0.7}Ge_{0.3}$ Quadruple Quantum Dot," *Phys. Rev. Appl.*, vol. 11, p. 061006, Jun 2019. [Online]. Available: https://link.aps.org/doi/10.1103/PhysRevApplied.11.061006

[80] A. J. Sigillito, M. J. Gullans, L. F. Edge, M. Borselli, and J. R. Petta, "Coherent transfer of quantum information in a silicon double quantum dot using resonant SWAP gates," *npj Quantum Information*, vol. 5, no. 1, p. 110, Nov 2019. [Online]. Available: https://doi.org/10.1038/s41534-019-0225-0

[81] T. Struck, A. Hollmann, F. Schauer, O. Fedorets, A. Schmidbauer, K. Sawano, H. Riemann, N. V. Abrosimov, Ł. Cywiński, D. Bougeard, and L. R. Schreiber, "Low-frequency spin qubit energy splitting noise in highly purified $^{28}Si/SiGe$," *npj Quantum Information*, vol. 6, no. 1, p. 40, May 2020. [Online]. Available: https://doi.org/10.1038/s41534-020-0276-2

[82] A. Hollmann, T. Struck, V. Langrock, A. Schmidbauer, F. Schauer, T. Leonhardt, K. Sawano, H. Riemann, N. V. Abrosimov, D. Bougeard, and L. R. Schreiber, "Large, Tunable Valley Splitting and Single-Spin Relaxation Mechanisms in a Si/Si_xGe_{1-x} Quantum Dot," *Phys. Rev. Applied*, vol. 13, p. 034068, Mar 2020. [Online]. Available: https://link.aps.org/doi/10.1103/PhysRevApplied.13.034068

[83] J. Kerckhoff, B. Sun, B. Fong, C. Jones, A. Kiselev, D. Barnes, R. Noah, E. Acuna, M. Akmal, S. Ha, J. Wright, B. Thomas, C. Jackson, L. Edge, K. Eng, R. Ross, and T. Ladd, "Magnetic Gradient Fluctuations from Quadrupolar ^{73}Ge in Si/SiGe

Exchange-Only Qubits," *PRX Quantum*, vol. 2, p. 010347, Mar 2021. [Online]. Available: https://link.aps.org/doi/10.1103/PRXQuantum.2.010347

[84] A. Mills, C. Guinn, M. Feldman, A. Sigillito, M. Gullans, M. Rakher, J. Kerckhoff, C. Jackson, and J. Petta, "High-Fidelity State Preparation, Quantum Control, and Readout of an Isotopically Enriched Silicon Spin Qubit," *Phys. Rev. Appl.*, vol. 18, p. 064028, Dec 2022. [Online]. Available: https://link.aps.org/doi/10.1103/PhysRevApplied.18.064028

[85] P. Harvey-Collard, J. Dijkema, G. Zheng, A. Sammak, G. Scappucci, and L. M. K. Vandersypen, "Coherent Spin-Spin Coupling Mediated by Virtual Microwave Photons," *Phys. Rev. X*, vol. 12, p. 021026, May 2022. [Online]. Available: https://link.aps.org/doi/10.1103/PhysRevX.12.021026

[86] A. Noiri, K. Takeda, T. Nakajima, T. Kobayashi, A. Sammak, G. Scappucci, and S. Tarucha, "A shuttling-based two-qubit logic gate for linking distant silicon quantum processors," *Nature Communications*, vol. 13, no. 1, p. 5740, Sep 2022. [Online]. Available: https://doi.org/10.1038/s41467-022-33453-z

[87] ——, "Fast universal quantum gate above the fault-tolerance threshold in silicon," *Nature*, vol. 601, no. 7893, pp. 338–342, Jan 2022. [Online]. Available: https://doi.org/10.1038/s41586-021-04182-y

[88] X. Xue, M. Russ, N. Samkharadze, B. Undseth, A. Sammak, G. Scappucci, and L. M. K. Vandersypen, "Quantum logic with spin qubits crossing the surface code threshold," *Nature*, vol. 601, no. 7893, pp. 343–347, Jan 2022. [Online]. Available: https://doi.org/10.1038/s41586-021-04273-w

[89] S. G. J. Philips, M. T. Mądzik, S. V. Amitonov, S. L. de Snoo, M. Russ, N. Kalhor, C. Volk, W. I. L. Lawrie, D. Brousse, L. Tryputen, B. P. Wuetz, A. Sammak, M. Veldhorst, G. Scappucci, and L. M. K. Vandersypen, "Universal control of a six-qubit quantum processor in silicon," *Nature*, vol. 609, no. 7929, pp. 919–924, Sep 2022. [Online]. Available: https://doi.org/10.1038/s41586-022-05117-x

[90] L. Petit, M. Russ, G. H. G. J. Eenink, W. I. L. Lawrie, J. S. Clarke, L. M. K. Vandersypen, and M. Veldhorst, "Design and integration of single-qubit rotations and two-qubit gates in silicon above one Kelvin," *Communications Materials*, vol. 3, no. 1, p. 82, Nov 2022. [Online]. Available: https://doi.org/10.1038/s43246-022-00304-9

[91] B. Undseth, O. Pietx-Casas, E. Raymenants, M. Mehmandoost, M. T. Mądzik, S. G. J. Philips, S. L. de Snoo, D. J. Michalak, S. V. Amitonov, L. Tryputen, B. P. Wuetz, V. Fezzi, D. D. Esposti, A. Sammak, G. Scappucci, and L. M. K. Vandersypen, "Hotter is Easier: Unexpected Temperature Dependence of Spin Qubit Frequencies," *Phys. Rev. X*, vol. 13, p. 041015, Oct 2023. [Online]. Available: https://link.aps.org/doi/10.1103/PhysRevX.13.041015

[92] J. Dijkema, X. Xue, P. Harvey-Collard, M. Rimbach-Russ, S. L. de Snoo, G. Zheng, A. Sammak, G. Scappucci, and L. M. Vandersypen, "Two-qubit logic between distant spins in silicon," *arXiv preprint arXiv:2310.16805*, 2023.

[93] A. Zwerver, S. Amitonov, S. de Snoo, M. Mądzik, M. Rimbach-Russ, A. Sammak, G. Scappucci, and L. Vandersypen, "Shuttling an Electron Spin through a Silicon Quantum Dot Array," *PRX Quantum*, vol. 4, p. 030303, Jul 2023. [Online]. Available: https://link.aps.org/doi/10.1103/PRXQuantum.4.030303

[94] F. K. Unseld, M. Meyer, M. T. Mądzik, F. Borsoi, S. L. de Snoo, S. V. Amitonov, A. Sammak, G. Scappucci, M. Veldhorst, and L. M. K. Vandersypen, "A 2D quantum dot array in planar ^{28}Si/SiGe," *Applied Physics Letters*, vol. 123, no. 8, p. 084002, 08 2023. [Online]. Available: https://doi.org/10.1063/5.0160847

[95] M. Meyer, C. Déprez, I. N. Meijer, F. K. Unseld, S. Karwal, A. Sammak, G. Scappucci, L. M. K. Vandersypen, and M. Veldhorst, "Single-Electron Occupation in Quantum Dot Arrays at Selectable Plunger Gate Voltage," *Nano Letters*, vol. 23, no. 24, pp. 11 593–11 600, Dec 2023. [Online]. Available: https://doi.org/10.1021/acs.nanolett.3c03349

[96] R. Ruskov, M. Veldhorst, A. S. Dzurak, and C. Tahan, "Electron g-factor of valley states in realistic silicon quantum dots," *Phys. Rev. B*, vol. 98, p. 245424, Dec 2018. [Online]. Available: https://link.aps.org/doi/10.1103/PhysRevB.98.245424

[97] R. Ferdous, K. W. Chan, M. Veldhorst, J. C. C. Hwang, C. H. Yang, H. Sahasrabudhe, G. Klimeck, A. Morello, A. S. Dzurak, and R. Rahman, "Interface-induced spin-orbit interaction in silicon quantum dots and prospects for scalability," *Phys. Rev. B*, vol. 97, p. 241401, Jun 2018. [Online]. Available: https://link.aps.org/doi/10.1103/PhysRevB.97.241401

[98] R. Ferdous, E. Kawakami, P. Scarlino, M. P. Nowak, D. R. Ward, D. E. Savage, M. G. Lagally, S. N. Coppersmith, M. Friesen, M. A. Eriksson, L. M. K. Vandersypen, and R. Rahman, "Valley dependent anisotropic spin splitting in silicon quantum

dots," *npj Quantum Information*, vol. 4, no. 1, p. 26, Jun 2018. [Online]. Available: https://doi.org/10.1038/s41534-018-0075-1

[99] M. O. Nestoklon, L. E. Golub, and E. L. Ivchenko, "Spin and valley-orbit splittings in SiGe/Si heterostructures," *Phys. Rev. B*, vol. 73, p. 235334, Jun 2006. [Online]. Available: https://link.aps.org/doi/10.1103/PhysRevB.73.235334

[100] M. Veldhorst, R. Ruskov, C. H. Yang, J. C. C. Hwang, F. E. Hudson, M. E. Flatté, C. Tahan, K. M. Itoh, A. Morello, and A. S. Dzurak, "Spin-orbit coupling and operation of multivalley spin qubits," *Phys. Rev. B*, vol. 92, p. 201401, Nov 2015. [Online]. Available: https://link.aps.org/doi/10.1103/PhysRevB.92.201401

[101] T. Tanttu, B. Hensen, K. W. Chan, C. H. Yang, W. W. Huang, M. Fogarty, F. Hudson, K. Itoh, D. Culcer, A. Laucht, A. Morello, and A. Dzurak, "Controlling Spin-Orbit Interactions in Silicon Quantum Dots Using Magnetic Field Direction," *Phys. Rev. X*, vol. 9, p. 021028, May 2019. [Online]. Available: https://link.aps.org/doi/10.1103/PhysRevX.9.021028

[102] M. Veldhorst, C. H. Yang, J. C. C. Hwang, W. Huang, J. P. Dehollain, J. T. Muhonen, S. Simmons, A. Laucht, F. E. Hudson, K. M. Itoh, A. Morello, and A. S. Dzurak, "A two-qubit logic gate in silicon," *Nature*, vol. 526, no. 7573, pp. 410–414, Oct 2015. [Online]. Available: https://doi.org/10.1038/nature15263

[103] K. W. Chan, W. Huang, C. H. Yang, J. C. C. Hwang, B. Hensen, T. Tanttu, F. E. Hudson, K. M. Itoh, A. Laucht, A. Morello, and A. S. Dzurak, "Assessment of a Silicon Quantum Dot Spin Qubit Environment via Noise Spectroscopy," *Phys. Rev. Appl.*, vol. 10, p. 044017, Oct 2018. [Online]. Available: https://link.aps.org/doi/10.1103/PhysRevApplied.10.044017

[104] R. Zhao, T. Tanttu, K. Y. Tan, B. Hensen, K. W. Chan, J. C. C. Hwang, R. C. C. Leon, C. H. Yang, W. Gilbert, F. E. Hudson, K. M. Itoh, A. A. Kiselev, T. D. Ladd, A. Morello, A. Laucht, and A. S. Dzurak, "Single-spin qubits in isotopically enriched silicon at low magnetic field," *Nature Communications*, vol. 10, no. 1, p. 5500, Dec 2019. [Online]. Available: https://doi.org/10.1038/s41467-019-13416-7

[105] W. Huang, C. H. Yang, K. W. Chan, T. Tanttu, B. Hensen, R. C. C. Leon, M. A. Fogarty, J. C. C. Hwang, F. E. Hudson, K. M. Itoh, A. Morello, A. Laucht, and A. S. Dzurak, "Fidelity benchmarks for two-qubit gates in silicon," *Nature*, vol. 569, no. 7757, pp. 532–536, May 2019. [Online]. Available: https://doi.org/10.1038/s41586-019-1197-0

[106] P. Harvey-Collard, N. T. Jacobson, C. Bureau-Oxton, R. M. Jock, V. Srinivasa, A. M. Mounce, D. R. Ward, J. M. Anderson, R. P. Manginell, J. R. Wendt, T. Pluym, M. P. Lilly, D. R. Luhman, M. Pioro-Ladrière, and M. S. Carroll, "Spin-orbit Interactions for Singlet-Triplet Qubits in Silicon," *Phys. Rev. Lett.*, vol. 122, p. 217702, May 2019. [Online]. Available: https://link.aps.org/doi/10.1103/PhysRevLett.122.217702

[107] L. Petit, H. G. J. Eenink, M. Russ, W. I. L. Lawrie, N. W. Hendrickx, S. G. J. Philips, J. S. Clarke, L. M. K. Vandersypen, and M. Veldhorst, "Universal quantum logic in hot silicon qubits," *Nature*, vol. 580, no. 7803, pp. 355–359, Apr 2020. [Online]. Available: https://doi.org/10.1038/s41586-020-2170-7

[108] K. W. Chan, H. Sahasrabudhe, W. Huang, Y. Wang, H. C. Yang, M. Veldhorst, J. C. C. Hwang, F. A. Mohiyaddin, F. E. Hudson, K. M. Itoh, A. Saraiva, A. Morello, A. Laucht, R. Rahman, and A. S. Dzurak, "Exchange Coupling in a Linear Chain of Three Quantum-Dot Spin Qubits in Silicon," *Nano Letters*, vol. 21, no. 3, pp. 1517–1522, Feb 2021. [Online]. Available: https://doi.org/10.1021/acs.nanolett.0c04771

[109] A. M. J. Zwerver, T. Krähenmann, T. F. Watson, L. Lampert, H. C. George, R. Pillarisetty, S. A. Bojarski, P. Amin, S. V. Amitonov, J. M. Boter, R. Caudillo, D. Correas-Serrano, J. P. Dehollain, G. Droulers, E. M. Henry, R. Kotlyar, M. Lodari, F. Lüthi, D. J. Michalak, B. K. Mueller, S. Neyens, J. Roberts, N. Samkharadze, G. Zheng, O. K. Zietz, G. Scappucci, M. Veldhorst, L. M. K. Vandersypen, and J. S. Clarke, "Qubits made by advanced semiconductor manufacturing," *Nature Electronics*, vol. 5, no. 3, pp. 184–190, Mar 2022. [Online]. Available: https://doi.org/10.1038/s41928-022-00727-9

[110] W. Gilbert, T. Tanttu, W. H. Lim, M. Feng, J. Y. Huang, J. D. Cifuentes, S. Serrano, P. Y. Mai, R. C. C. Leon, C. C. Escott, K. M. Itoh, N. V. Abrosimov, H.-J. Pohl, M. L. W. Thewalt, F. E. Hudson, A. Morello, A. Laucht, C. H. Yang, A. Saraiva, and A. S. Dzurak, "On-demand electrical control of spin qubits," *Nature Nanotechnology*, vol. 18, no. 2, pp. 131–136, Feb 2023. [Online]. Available: https://doi.org/10.1038/s41565-022-01280-4

[111] R.-Z. Hu, R.-L. Ma, M. Ni, Y. Zhou, N. Chu, W.-Z. Liao, Z.-Z. Kong, G. Cao, G.-L. Wang, H.-O. Li, and G.-P. Guo, "Flopping-mode spin qubit in a Si-MOS quantum dot," *Applied Physics Letters*, vol. 122, no. 13, p. 134002, 03 2023. [Online]. Available: https://doi.org/10.1063/5.0137259

[112] T. Tanttu, W. H. Lim, J. Y. Huang, N. Dumoulin Stuyck, W. Gilbert, R. Y. Su, M. Feng, J. D. Cifuentes, A. E. Seedhouse, S. K. Seritan, C. I. Ostrove, K. M. Rudinger, R. C. C. Leon, W. Huang, C. C. Escott, K. M. Itoh, N. V. Abrosimov, H.-J. Pohl, M. L. W. Thewalt, F. E. Hudson, R. Blume-Kohout, S. D. Bartlett, A. Morello, A. Laucht, C. H. Yang, A. Saraiva, and A. S. Dzurak, "Assessment of the errors of high-fidelity two-qubit gates in silicon quantum dots," *Nature Physics*, Aug 2024. [Online]. Available: https://doi.org/10.1038/s41567-024-02614-w

[113] J. Y. Huang, R. Y. Su, W. H. Lim, M. Feng, B. van Straaten, B. Severin, W. Gilbert, N. Dumoulin Stuyck, T. Tanttu, S. Serrano, J. D. Cifuentes, I. Hansen, A. E. Seedhouse, E. Vahapoglu, R. C. C. Leon, N. V. Abrosimov, H.-J. Pohl, M. L. W. Thewalt, F. E. Hudson, C. C. Escott, N. Ares, S. D. Bartlett, A. Morello, A. Saraiva, A. Laucht, A. S. Dzurak, and C. H. Yang, "High-fidelity spin qubit operation and algorithmic initialization above 1 K," *Nature*, vol. 627, no. 8005, pp. 772–777, Mar 2024. [Online]. Available: https://doi.org/10.1038/s41586-024-07160-2

[114] X. Hu, "Highly tunable ultrafast control of a spin qubit," *Nature Nanotechnology*, vol. 18, no. 2, pp. 100–101, Feb 2023. [Online]. Available: https://doi.org/10.1038/s41565-022-01298-8

[115] M. Lodari, A. Tosato, D. Sabbagh, M. A. Schubert, G. Capellini, A. Sammak, M. Veldhorst, and G. Scappucci, "Light effective hole mass in undoped Ge/SiGe quantum wells," *Phys. Rev. B*, vol. 100, p. 041304, Jul 2019. [Online]. Available: https://link.aps.org/doi/10.1103/PhysRevB.100.041304

[116] P. Stano and D. Loss, "Review of performance metrics of spin qubits in gated semiconducting nanostructures," *Nature Reviews Physics*, vol. 4, no. 10, p. 672–688, Aug. 2022. [Online]. Available: http://dx.doi.org/10.1038/s42254-022-00484-w

[117] W. I. L. Lawrie, N. W. Hendrickx, F. van Riggelen, M. Russ, L. Petit, A. Sammak, G. Scappucci, and M. Veldhorst, "Spin Relaxation Benchmarks and Individual Qubit Addressability for Holes in Quantum Dots," *Nano Letters*, vol. 20, no. 10, pp. 7237–7242, Oct 2020. [Online]. Available: https://doi.org/10.1021/acs.nanolett.0c02589

[118] F. Borsoi, N. W. Hendrickx, V. John, M. Meyer, S. Motz, F. van Riggelen, A. Sammak, S. L. de Snoo, G. Scappucci, and M. Veldhorst, "Shared control of a 16 semiconductor quantum dot crossbar array," *Nature Nanotechnology*, vol. 19, no. 1, pp. 21–27, Jan 2024. [Online]. Available: https://doi.org/10.1038/s41565-023-01491-3

[119] T.-K. Hsiao, P. Cova Fariña, S. D. Oosterhout, D. Jirovec, X. Zhang, C. J. van Diepen, W. I. L. Lawrie, C.-A. Wang, A. Sammak, G. Scappucci, M. Veldhorst, E. Demler, and L. M. K. Vandersypen, "Exciton Transport in a Germanium Quantum Dot Ladder," *Phys. Rev. X*, vol. 14, p. 011048, Mar 2024. [Online]. Available: https://link.aps.org/doi/10.1103/PhysRevX.14.011048

[120] W. I. L. Lawrie, H. G. J. Eenink, N. W. Hendrickx, J. M. Boter, L. Petit, S. V. Amitonov, M. Lodari, B. Paquelet Wuetz, C. Volk, S. G. J. Philips, G. Droulers, N. Kalhor, F. van Riggelen, D. Brousse, A. Sammak, L. M. K. Vandersypen, G. Scappucci, and M. Veldhorst, "Quantum dot arrays in silicon and germanium," *Applied Physics Letters*, vol. 116, no. 8, p. 080501, 2020. [Online]. Available: https://doi.org/10.1063/5.0002013

[121] F. van Riggelen, N. W. Hendrickx, W. I. L. Lawrie, M. Russ, A. Sammak, G. Scappucci, and M. Veldhorst, "A two-dimensional array of single-hole quantum dots," *Applied Physics Letters*, vol. 118, no. 4, p. 044002, 01 2021. [Online]. Available: https://doi.org/10.1063/5.0037330

[122] C.-A. Wang, C. Déprez, H. Tidjani, W. I. L. Lawrie, N. W. Hendrickx, A. Sammak, G. Scappucci, and M. Veldhorst, "Probing resonating valence bonds on a programmable germanium quantum simulator," *npj Quantum Information*, vol. 9, no. 1, p. 58, Jun 2023. [Online]. Available: https://doi.org/10.1038/s41534-023-00727-3

[123] W. I. L. Lawrie, M. Rimbach-Russ, F. v. Riggelen, N. W. Hendrickx, S. L. d. Snoo, A. Sammak, G. Scappucci, J. Helsen, and M. Veldhorst, "Simultaneous single-qubit driving of semiconductor spin qubits at the fault-tolerant threshold," *Nature Communications*, vol. 14, no. 1, p. 3617, Jun 2023. [Online]. Available: https://doi.org/10.1038/s41467-023-39334-3

[124] A. S. Ivlev, H. Tidjani, S. D. Oosterhout, A. Sammak, G. Scappucci, and M. Veldhorst, "Coupled vertical double quantum dots at single-hole occupancy," *Applied Physics Letters*, vol. 125, no. 2, p. 023501, 07 2024. [Online]. Available: https://doi.org/10.1063/5.0198274

[125] X. Zhang, E. Morozova, M. Rimbach-Russ, D. Jirovec, T.-K. Hsiao, P. C. Fariña, C.-A. Wang, S. D. Oosterhout, A. Sammak, G. Scappucci *et al.*, "Universal control of four singlet–triplet qubits," *Nature Nanotechnology*, pp. 1–7, 2024.

[126] N. W. Hendrickx, D. P. Franke, A. Sammak, G. Scappucci, and M. Veldhorst, "Fast two-qubit logic with holes in germanium," *Nature*, vol. 577, no. 7791, pp. 487–491, Jan 2020. [Online]. Available: https://doi.org/10.1038/s41586-019-1919-3

[127] N. W. Hendrickx, L. Massai, M. Mergenthaler, F. J. Schupp, S. Paredes, S. W. Bedell, G. Salis, and A. Fuhrer, "Sweet-spot operation of a germanium hole spin qubit with highly anisotropic noise sensitivity," *Nature Materials*, vol. 23, no. 7, pp. 920–927, Jul 2024. [Online]. Available: https://doi.org/10.1038/s41563-024-01857-5

[128] M. R. M. Atalla, S. Assali, A. Attiaoui, C. Lemieux-Leduc, A. Kumar, S. Abdi, and O. Moutanabbir, "All-Group IV Transferable Membrane Mid-Infrared Photodetectors," *Advanced Functional Materials*, vol. 31, no. 3, p. 2006329, 2021. [Online]. Available: https://onlinelibrary.wiley.com/doi/abs/10.1002/adfm.202006329

[129] M. R. M. Atalla, S. Assali, S. Koelling, A. Attiaoui, and O. Moutanabbir, "Dark current in monolithic extended-SWIR GeSn PIN photodetectors," *Applied Physics Letters*, vol. 122, no. 3, p. 031103, 01 2023. [Online]. Available: https://doi.org/10.1063/5.0124720

[130] D. J. Paul, "8-band $\mathbf{k} \cdot \mathbf{p}$ modeling of the quantum confined Stark effect in Ge quantum wells on Si substrates," *Phys. Rev. B*, vol. 77, p. 155323, Apr 2008. [Online]. Available: https://link.aps.org/doi/10.1103/PhysRevB.77.155323

[131] ——, "8-band $\mathbf{k} \cdot \mathbf{p}$ modelling of mid-infrared intersubband absorption in Ge quantum wells," *Journal of Applied Physics*, vol. 120, no. 4, p. 043103, 2016. [Online]. Available: https://doi.org/10.1063/1.4959259

[132] G. Chang, S. Chang, and S. L. Chuang, "Strain-Balanced Ge_zSn_{1-z}–$Si_xGe_ySn_{1-x-y}$ Multiple-Quantum-Well Lasers," *IEEE Journal of Quantum Electronics*, vol. 46, no. 12, pp. 1813–1820, 2010.

[133] R. K. Hayden, D. K. Maude, L. Eaves, E. C. Valadares, M. Henini, F. W. Sheard, O. H. Hughes, J. C. Portal, and L. Cury, "Probing the hole dispersion curves of a quantum well using resonant magnetotunneling spectroscopy," *Phys. Rev. Lett.*, vol. 66, pp. 1749–1752, Apr 1991. [Online]. Available: https://link.aps.org/doi/10.1103/PhysRevLett.66.1749

[134] R. Winkler, M. Merkler, T. Darnhofer, and U. Rössler, "Theory for the cyclotron resonance of holes in strained asymmetric Ge-SiGe quantum wells," *Phys. Rev. B*, vol. 53, pp. 10 858–10 865, Apr 1996. [Online]. Available: https://link.aps.org/doi/10.1103/PhysRevB.53.10858

[135] C. Kloeffel, M. J. Rančić, and D. Loss, "Direct Rashba spin-orbit interaction in Si and Ge nanowires with different growth directions," *Phys. Rev. B*, vol. 97, p. 235422, Jun 2018. [Online]. Available: https://link.aps.org/doi/10.1103/PhysRevB.97.235422

[136] W. Shockley, "Energy Band Structures in Semiconductors," *Phys. Rev.*, vol. 78, pp. 173–174, Apr 1950. [Online]. Available: https://link.aps.org/doi/10.1103/PhysRev.78.173

[137] G. L. Pearson, J. R. Haynes, and W. Shockley, "Comment on Mobility Anomalies in Germanium," *Phys. Rev.*, vol. 78, pp. 295–296, May 1950. [Online]. Available: https://link.aps.org/doi/10.1103/PhysRev.78.295.2

[138] J. M. Luttinger and W. Kohn, "Motion of Electrons and Holes in Perturbed Periodic Fields," *Phys. Rev.*, vol. 97, pp. 869–883, Feb 1955. [Online]. Available: https://link.aps.org/doi/10.1103/PhysRev.97.869

[139] J. M. Luttinger, "Quantum Theory of Cyclotron Resonance in Semiconductors: General Theory," *Phys. Rev.*, vol. 102, pp. 1030–1041, May 1956. [Online]. Available: https://link.aps.org/doi/10.1103/PhysRev.102.1030

[140] E. O. Kane, "Band structure of indium antimonide," *Journal of Physics and Chemistry of Solids*, vol. 1, no. 4, pp. 249–261, 1957. [Online]. Available: https://www.sciencedirect.com/science/article/pii/0022369757900136

[141] M. Cardona and F. H. Pollak, "Energy-Band Structure of Germanium and Silicon: The $k \cdot p$ Method," *Phys. Rev.*, vol. 142, pp. 530–543, Feb 1966. [Online]. Available: https://link.aps.org/doi/10.1103/PhysRev.142.530

[142] G. Bastard, J. K. Furdyna, and J. Mycielski, "Landau levels and cyclotron resonance in graded mixed semiconductors," *Phys. Rev. B*, vol. 12, pp. 4356–4359, Nov 1975. [Online]. Available: https://link.aps.org/doi/10.1103/PhysRevB.12.4356

[143] M. G. Burt, "An exact formulation of the envelope function method for the determination of electronic states in semiconductor microstructures," *Semiconductor Science and Technology*, vol. 2, no. 7, p. 460, jul 1987. [Online]. Available: https://dx.doi.org/10.1088/0268-1242/2/7/012

[144] ——, "An exact formulation of the envelope function method for the determination of electronic states in semiconductor microstructures," *Semiconductor Science and Technology*, vol. 2, no. 10, p. 701, oct 1987. [Online]. Available: https://dx.doi.org/10.1088/0268-1242/2/10/514

[145] ——, "An exact formulation of the envelope function method for the determination of electronic states in semiconductor microstructures," *Semiconductor Science and Technology*, vol. 3, no. 8, p. 739, aug 1988. [Online]. Available: https://dx.doi.org/10.1088/0268-1242/3/8/003

[146] B. A. Foreman, "Effective-mass Hamiltonian and boundary conditions for the valence bands of semiconductor microstructures," *Phys. Rev. B*, vol. 48, pp. 4964–4967, Aug 1993. [Online]. Available: https://link.aps.org/doi/10.1103/PhysRevB.48.4964

[147] R. G. Veprek, S. Steiger, and B. Witzigmann, "Ellipticity and the spurious solution problem of $\mathbf{k}\cdot\mathbf{p}$ envelope equations," *Phys. Rev. B*, vol. 76, p. 165320, Oct 2007. [Online]. Available: https://link.aps.org/doi/10.1103/PhysRevB.76.165320

[148] B. A. Foreman, "Elimination of spurious solutions from eight-band $\mathbf{k}\cdot\mathbf{p}$ theory," *Phys. Rev. B*, vol. 56, pp. R12 748–R12 751, Nov 1997. [Online]. Available: https://link.aps.org/doi/10.1103/PhysRevB.56.R12748

[149] T. Eißfeller and P. Vogl, "Real-space multiband envelope-function approach without spurious solutions," *Phys. Rev. B*, vol. 84, p. 195122, Nov 2011. [Online]. Available: https://link.aps.org/doi/10.1103/PhysRevB.84.195122

[150] T. Eißfeller, "Theory of the electronic structure of quantum dots in external fields," Ph.D. dissertation, Technische Universitaet Muenchen (Germany), 2012. [Online]. Available: https://www.proquest.com/dissertations-theses/theory-electronic-structure-quantum-dots-external/docview/2193178110/se-2?accountid=40695

[151] L. Voon and M. Willatzen, *The $k\cdot p$ Method: Electronic Properties of Semiconductors*. Springer Berlin Heidelberg, 2009. [Online]. Available: https://books.google.co.cr/books?id=t46OZQrEd8QC

[152] D. Rideau, M. Feraille, L. Ciampolini, M. Minondo, C. Tavernier, H. Jaouen, and A. Ghetti, "Strained Si, Ge, and $Si_{1-x}Ge_x$ alloys modeled with a first-principles-optimized full-zone $\mathbf{k}\cdot\mathbf{p}$ method," *Phys. Rev. B*, vol. 74, p. 195208, Nov 2006. [Online]. Available: https://link.aps.org/doi/10.1103/PhysRevB.74.195208

[153] Z. Song, W. Fan, C. S. Tan, Q. Wang, D. Nam, D. H. Zhang, and G. Sun, "Band structure of $Ge_{1-x}Sn_x$ alloy: a full-zone 30-band $k\cdot p$ model," *New Journal of Physics*, vol. 21, no. 7, p. 073037, Jul 2019. [Online]. Available: http://dx.doi.org/10.1088/1367-2630/ab306f

[154] C. G. Van de Walle, "Band lineups and deformation potentials in the model-solid theory," *Phys. Rev. B*, vol. 39, pp. 1871–1883, Jan 1989. [Online]. Available: https://link.aps.org/doi/10.1103/PhysRevB.39.1871

[155] J. Menéndez and J. Kouvetakis, "Type-I Ge/$Ge_{1-x-y}Si_xSn_y$ strained-layer heterostructures with a direct Ge bandgap," *Applied Physics Letters*, vol. 85, no. 7, pp. 1175–1177, 2004. [Online]. Available: https://doi.org/10.1063/1.1784032

[156] D. J. Dunstan, "Strain and strain relaxation in semiconductors," *Journal of Materials Science: Materials in Electronics*, vol. 8, no. 6, pp. 337–375, Dec 1997. [Online]. Available: https://doi.org/10.1023/A:1018547625106

[157] G. Bir and G. Pikus, *Symmetry and Strain-induced Effects in Semiconductors*. New York: Wiley, 1974. [Online]. Available: https://books.google.ca/books?id=38m2QgAACAAJ

[158] I. Vurgaftman, J. R. Meyer, and L. R. Ram-Mohan, "Band parameters for III–V compound semiconductors and their alloys," *Journal of Applied Physics*, vol. 89, no. 11, pp. 5815–5875, 06 2001. [Online]. Available: https://doi.org/10.1063/1.1368156

[159] R. R. Reeber and K. Wang, "Thermal expansion and lattice parameters of group IV semiconductors," *Materials Chemistry and Physics*, vol. 46, no. 2, pp. 259 – 264, 1996. [Online]. Available: http://www.sciencedirect.com/science/article/pii/S0254058496018081

[160] O. Madelung, Ed., *Semiconductors, Group IV Elements and III-V Compounds*. Springer-Verlag Berlin Heidelberg, 1991.

[161] C. G. Van de Walle and R. M. Martin, "Theoretical calculations of heterojunction discontinuities in the Si/Ge system," *Phys. Rev. B*, vol. 34, pp. 5621–5634, Oct 1986. [Online]. Available: https://link.aps.org/doi/10.1103/PhysRevB.34.5621

[162] P. Lawaetz, "Valence-Band Parameters in Cubic Semiconductors," *Phys. Rev. B*, vol. 4, pp. 3460–3467, Nov 1971. [Online]. Available: https://link.aps.org/doi/10.1103/PhysRevB.4.3460

[163] J. P. Dismukes, L. Ekstrom, and R. J. Paff, "Lattice Parameter and Density in Germanium-Silicon Alloys," *The Journal of Physical Chemistry*, vol. 68, no. 10, pp. 3021–3027, Oct 1964. [Online]. Available: https://doi.org/10.1021/j100792a049

[164] Y. Varshni, "Temperature dependence of the energy gap in semiconductors," *Physica*, vol. 34, no. 1, pp. 149–154, 1967. [Online]. Available: https://www.sciencedirect.com/science/article/pii/0031891467900626

[165] M. P. Polak, P. Scharoch, and R. Kudrawiec, "The electronic band structure of $Ge_{1-x}Sn_x$ in the full composition range: indirect, direct, and inverted gaps regimes, band offsets, and the Burstein–Moss effect," *Journal of Physics D: Applied Physics*, vol. 50, no. 19, p. 195103, apr 2017. [Online]. Available: https://doi.org/10.1088%2F1361-6463%2Faa67bf

[166] M. Bertrand, Q.-M. Thai, J. Chrétien, N. Pauc, J. Aubin, L. Milord, A. Gassenq, J.-M. Hartmann, A. Chelnokov, V. Calvo, and V. Reboud, "Experimental Calibration of Sn-Related Varshni Parameters for High Sn Content GeSn Layers," *Annalen der Physik*, vol. 531, no. 6, p. 1800396, 2019. [Online]. Available: https://onlinelibrary.wiley.com/doi/abs/10.1002/andp.201800396

[167] Y.-H. Li, X. G. Gong, and S.-H. Wei, "Ab initio all-electron calculation of absolute volume deformation potentials of IV-IV, III-V, and II-VI semiconductors: The chemical trends," *Phys. Rev. B*, vol. 73, p. 245206, Jun 2006. [Online]. Available: https://link.aps.org/doi/10.1103/PhysRevB.73.245206

[168] T. Brudevoll, D. S. Citrin, M. Cardona, and N. E. Christensen, "Electronic structure of α-Sn and its dependence on hydrostatic strain," *Phys. Rev. B*, vol. 48, pp. 8629–8635, Sep 1993. [Online]. Available: https://link.aps.org/doi/10.1103/PhysRevB.48.8629

[169] M. Willatzen, L. C. Lew Yan Voon, P. V. Santos, M. Cardona, D. Munzar, and N. E. Christensen, "Theoretical study of band-edge states in Sn_1Ge_n strained-layer superlattices," *Phys. Rev. B*, vol. 52, pp. 5070–5081, Aug 1995. [Online]. Available: https://link.aps.org/doi/10.1103/PhysRevB.52.5070

[170] K. Lu Low, Y. Yang, G. Han, W. Fan, and Y.-C. Yeo, "Electronic band structure and effective mass parameters of Ge1-xSnx alloys," *Journal of Applied Physics*, vol. 112, no. 10, p. 103715, 2012. [Online]. Available: https://doi.org/10.1063/1.4767381

[171] J. Weber and M. I. Alonso, "Near-band-gap photoluminescence of Si-Ge alloys," *Phys. Rev. B*, vol. 40, pp. 5683–5693, Sep 1989. [Online]. Available: https://link.aps.org/doi/10.1103/PhysRevB.40.5683

[172] J. A. Van Vechten, "Quantum Dielectric Theory of Electronegativity in Covalent Systems. I. Electronic Dielectric Constant," *Phys. Rev.*, vol. 182, pp. 891–905, Jun 1969. [Online]. Available: https://link.aps.org/doi/10.1103/PhysRev.182.891

[173] V. R. D'Costa, C. S. Cook, A. G. Birdwell, C. L. Littler, M. Canonico, S. Zollner, J. Kouvetakis, and J. Menéndez, "Optical critical points of thin-film $Ge_{1-y}Sn_y$ alloys: A comparative $Ge_{1-y}Sn_y/Ge_{1-x}Si_x$ study," *Phys. Rev. B*, vol. 73, p. 125207, Mar 2006. [Online]. Available: https://link.aps.org/doi/10.1103/PhysRevB.73.125207

[174] M. G. Burt, "Fundamentals of envelope function theory for electronic states and photonic modes in nanostructures," *Journal of Physics: Condensed Matter*, vol. 11, no. 9, p. 53, mar 1999. [Online]. Available: https://dx.doi.org/10.1088/0953-8984/11/9/002

[175] S. Birner, "Modeling of semiconductor nanostructures and semiconductor-electrolyte interfaces," Ph.D. dissertation, Technische Universitaet Muenchen (Germany), Nov 2011.

[176] J. Li, B. Venitucci, and Y.-M. Niquet, "Hole-phonon interactions in quantum dots: Effects of phonon confinement and encapsulation materials on spin-orbit qubits," *Phys. Rev. B*, vol. 102, p. 075415, Aug 2020. [Online]. Available: https://link.aps.org/doi/10.1103/PhysRevB.102.075415

[177] R. Maurand, X. Jehl, D. Kotekar-Patil, A. Corna, H. Bohuslavskyi, R. Laviéville, L. Hutin, S. Barraud, M. Vinet, M. Sanquer, and S. De Franceschi, "A CMOS silicon spin qubit," *Nature Communications*, vol. 7, no. 1, p. 13575, Nov 2016. [Online]. Available: https://doi.org/10.1038/ncomms13575

[178] H. Watzinger, J. Kukučka, L. Vukušić, F. Gao, T. Wang, F. Schäffler, J.-J. Zhang, and G. Katsaros, "A germanium hole spin qubit," *Nature Communications*, vol. 9, no. 1, p. 3902, Sep 2018. [Online]. Available: https://doi.org/10.1038/s41467-018-06418-4

[179] Y. Hu, F. Kuemmeth, C. M. Lieber, and C. M. Marcus, "Hole spin relaxation in Ge–Si core–shell nanowire qubits," *Nature Nanotechnology*, vol. 7, no. 1, pp. 47–50, Jan 2012. [Online]. Available: https://doi.org/10.1038/nnano.2011.234

[180] C. Kloeffel, M. Trif, and D. Loss, "Strong spin-orbit interaction and helical hole states in Ge/Si nanowires," *Phys. Rev. B*, vol. 84, p. 195314, Nov 2011. [Online]. Available: https://link.aps.org/doi/10.1103/PhysRevB.84.195314

[181] F. Maier, T. Meng, and D. Loss, "Strongly interacting holes in Ge/Si nanowires," *Phys. Rev. B*, vol. 90, p. 155437, Oct 2014. [Online]. Available: https://link.aps.org/doi/10.1103/PhysRevB.90.155437

[182] L. Mao, M. Gong, E. Dumitrescu, S. Tewari, and C. Zhang, "Hole-Doped Semiconductor Nanowire on Top of an *s*-Wave Superconductor: A New and Experimentally Accessible System for Majorana Fermions," *Phys. Rev. Lett.*, vol. 108, p. 177001, Apr 2012. [Online]. Available: https://link.aps.org/doi/10.1103/PhysRevLett.108.177001

[183] F. Maier, J. Klinovaja, and D. Loss, "Majorana fermions in Ge/Si hole nanowires," *Phys. Rev. B*, vol. 90, p. 195421, Nov 2014. [Online]. Available: https://link.aps.org/doi/10.1103/PhysRevB.90.195421

[184] R. M. Lutchyn, E. P. A. M. Bakkers, L. P. Kouwenhoven, P. Krogstrup, C. M. Marcus, and Y. Oreg, "Majorana zero modes in superconductor–semiconductor heterostructures," *Nature Reviews Materials*, vol. 3, no. 5, pp. 52–68, May 2018. [Online]. Available: https://doi.org/10.1038/s41578-018-0003-1

[185] H. Watzinger, C. Kloeffel, L. Vukušić, M. D. Rossell, V. Sessi, J. Kukučka, R. Kirchschlager, E. Lausecker, A. Truhlar, M. Glaser, A. Rastelli, A. Fuhrer, D. Loss, and G. Katsaros, "Heavy-Hole States in Germanium Hut Wires," *Nano Letters*, vol. 16, no. 11, pp. 6879–6885, 2016, pMID: 27656760. [Online]. Available: https://doi.org/10.1021/acs.nanolett.6b02715

[186] O. Moutanabbir, S. Miyamoto, E. E. Haller, and K. M. Itoh, "Transport of Deposited Atoms throughout Strain-Mediated Self-Assembly," *Phys. Rev. Lett.*, vol. 105, p. 026101, Jul 2010. [Online]. Available: https://link.aps.org/doi/10.1103/PhysRevLett.105.026101

[187] S. Miyamoto, O. Moutanabbir, T. Ishikawa, M. Eto, E. E. Haller, K. Sawano, Y. Shiraki, and K. M. Itoh, "Excitonic Aharonov-Bohm effect in isotopically pure ^{70}Ge/Si self-assembled type-II quantum dots," *Phys. Rev. B*, vol. 82, p. 073306, Aug 2010. [Online]. Available: https://link.aps.org/doi/10.1103/PhysRevB.82.073306

[188] D. V. Bulaev and D. Loss, "Electric Dipole Spin Resonance for Heavy Holes in Quantum Dots," *Phys. Rev. Lett.*, vol. 98, p. 097202, Feb 2007. [Online]. Available: https://link.aps.org/doi/10.1103/PhysRevLett.98.097202

[189] Z. Wang, E. Marcellina, A. R. Hamilton, J. H. Cullen, S. Rogge, J. Salfi, and D. Culcer, "Optimal operation points for ultrafast, highly coherent Ge hole spin-orbit qubits," *npj Quantum Information*, vol. 7, no. 1, p. 54, Apr 2021. [Online]. Available: https://doi.org/10.1038/s41534-021-00386-2

[190] N. W. Hendrickx, D. P. Franke, A. Sammak, M. Kouwenhoven, D. Sabbagh, L. Yeoh, R. Li, M. L. V. Tagliaferri, M. Virgilio, G. Capellini, G. Scappucci, and M. Veldhorst, "Gate-controlled quantum dots and superconductivity in planar germanium," *Nature Communications*, vol. 9, no. 1, p. 2835, Jul 2018. [Online]. Available: https://doi.org/10.1038/s41467-018-05299-x

[191] N. W. Hendrickx, W. I. L. Lawrie, L. Petit, A. Sammak, G. Scappucci, and M. Veldhorst, "A single-hole spin qubit," 2019.

[192] F. Vigneau, R. Mizokuchi, D. C. Zanuz, X. Huang, S. Tan, R. Maurand, S. Frolov, A. Sammak, G. Scappucci, F. Lefloch, and S. De Franceschi, "Germanium Quantum-Well Josephson Field-Effect Transistors and Interferometers," *Nano Letters*, vol. 19, no. 2, pp. 1023–1027, Feb 2019. [Online]. Available: https://doi.org/10.1021/acs.nanolett.8b04275

[193] F. Gao, J.-H. Wang, H. Watzinger, H. Hu, M. J. Rančić, J.-Y. Zhang, T. Wang, Y. Yao, G.-L. Wang, J. Kukučka, L. Vukušić, C. Kloeffel, D. Loss, F. Liu, G. Katsaros, and J.-J. Zhang, "Site-Controlled Uniform Ge/Si Hut Wires with Electrically Tunable Spin–Orbit Coupling," *Advanced Materials*, vol. 32, no. 16, p. 1906523, 2020. [Online]. Available: https://onlinelibrary.wiley.com/doi/abs/10.1002/adma.201906523

[194] R. Kotlyar, T. L. Reinecke, M. Bayer, and A. Forchel, "Zeeman spin splittings in semiconductor nanostructures," *Phys. Rev. B*, vol. 63, p. 085310, Feb 2001. [Online]. Available: https://link.aps.org/doi/10.1103/PhysRevB.63.085310

[195] N. J. Traynor, R. J. Warburton, M. J. Snelling, and R. T. Harley, "Highly nonlinear Zeeman splitting of excitons in semiconductor quantum wells," *Phys. Rev. B*, vol. 55, pp. 15 701–15 705, Jun 1997. [Online]. Available: https://link.aps.org/doi/10.1103/PhysRevB.55.15701

[196] M. J. Lawless, R. J. Warburton, R. J. Nicholas, N. J. Pulsford, K. J. Moore, G. Duggan, and K. Woodbridge, "Saddle-point excitons and intraband (Γ-Π) mixing in strained-layer superlattices," *Phys. Rev. B*, vol. 45, pp. 4266–4273, Feb 1992. [Online]. Available: https://link.aps.org/doi/10.1103/PhysRevB.45.4266

[197] R. J. Warburton, R. J. Nicholas, S. Sasaki, N. Miura, and K. Woodbridge, "Superlattice modification of the valence-band spin splitting in $In_xGa_{1-x}As/GaAs$ superlattices up to 45 T," *Phys. Rev. B*, vol. 48, pp. 12 323–12 325, Oct 1993. [Online]. Available: https://link.aps.org/doi/10.1103/PhysRevB.48.12323

[198] V. Jovanov, T. Eissfeller, S. Kapfinger, E. C. Clark, F. Klotz, M. Bichler, J. G. Keizer, P. M. Koenraad, M. S. Brandt, G. Abstreiter, and J. J. Finley, "Highly nonlinear excitonic Zeeman spin splitting in composition-engineered artificial atoms," *Phys. Rev. B*, vol. 85, p. 165433, Apr 2012. [Online]. Available: https://link.aps.org/doi/10.1103/PhysRevB.85.165433

[199] R. Danneau, O. Klochan, W. R. Clarke, L. H. Ho, A. P. Micolich, M. Y. Simmons, A. R. Hamilton, M. Pepper, D. A. Ritchie, and U. Zülicke, "Zeeman Splitting in Ballistic Hole Quantum Wires," *Phys. Rev. Lett.*, vol. 97, p. 026403, Jul 2006. [Online]. Available: https://link.aps.org/doi/10.1103/PhysRevLett.97.026403

[200] M. Kubisa, K. Ryczko, J. Jadczak, L. Bryja, J. Misiewicz, and M. Potemski, "Nonlinear Zeeman Splitting of Holes in Doped GaAs Heterostructures," *Acta Physica Polonica A*, vol. 119, 05 2011.

[201] P. S. Grigoryev, O. A. Yugov, S. A. Eliseev, Y. P. Efimov, V. A. Lovtcius, V. V. Petrov, V. F. Sapega, and I. V. Ignatiev, "Inversion of Zeeman splitting of exciton states in InGaAs quantum wells," *Phys. Rev. B*, vol. 93, p. 205425, May 2016. [Online]. Available: https://link.aps.org/doi/10.1103/PhysRevB.93.205425

[202] F. Fischer, R. Winkler, D. Schuh, M. Bichler, and M. Grayson, "Transport evidence of the lowest Landau-level spin-index anticrossing in (110) GaAs two-dimensional holes," *Phys. Rev. B*, vol. 75, p. 073303, Feb 2007. [Online]. Available: https://link.aps.org/doi/10.1103/PhysRevB.75.073303

[203] P. E. Faria Junior, D. Tedeschi, M. De Luca, B. Scharf, A. Polimeni, and J. Fabian, "Common nonlinear features and spin-orbit coupling effects in the Zeeman splitting of novel wurtzite materials," *Phys. Rev. B*, vol. 99, p. 195205, May 2019. [Online]. Available: https://link.aps.org/doi/10.1103/PhysRevB.99.195205

[204] D. Tedeschi, M. De Luca, P. E. Faria Junior, A. Granados del Águila, Q. Gao, H. H. Tan, B. Scharf, P. C. M. Christianen, C. Jagadish, J. Fabian, and A. Polimeni, "Unusual spin properties of InP wurtzite nanowires revealed by Zeeman splitting spectroscopy," *Phys. Rev. B*, vol. 99, p. 161204, Apr 2019. [Online]. Available: https://link.aps.org/doi/10.1103/PhysRevB.99.161204

[205] W. Bardyszewski and S. P. Łepkowski, "Nonlinear Zeeman splitting of magnetoexcitons in *c*-plane wurtzite GaN-based quantum wells," *Phys. Rev. B*, vol. 90, p. 075302, Aug 2014. [Online]. Available: https://link.aps.org/doi/10.1103/PhysRevB.90.075302

[206] D. A. Broido and L. J. Sham, "Effective masses of holes at GaAs-AlGaAs heterojunctions," *Phys. Rev. B*, vol. 31, pp. 888–892, Jan 1985. [Online]. Available: https://link.aps.org/doi/10.1103/PhysRevB.31.888

[207] U. Ekenberg and M. Altarelli, "Subbands and Landau levels in the two-dimensional hole gas at the GaAs-$Al_xGa_{1-x}As$ interface," *Phys. Rev. B*, vol. 32, pp. 3712–3722, Sep 1985. [Online]. Available: https://link.aps.org/doi/10.1103/PhysRevB.32.3712

[208] R. Moriya, Y. Hoshi, K. Sawano, Y. Shiraki, N. Usami, S. Masubuchi, and T. Machida, "Landau Level Crossing and Anti-crossing of Bilayer Two-dimensional Hole Gas in Ge/SiGe Quantum Well," 09 2013.

[209] C. Engelhardt, D. Többen, M. Aschauer, F. Schäffler, G. Abstreiter, and E. Gornik, "High mobility 2-D hole gases in strained Ge channels on Si substrates studied by magnetotransport and cyclotron resonance," *Solid-State Electronics*, vol. 37, no. 4, pp. 949 – 952, 1994. [Online]. Available: http://www.sciencedirect.com/science/article/pii/0038110194903336

[210] L. A. Terrazos, E. Marcellina, Z. Wang, S. N. Coppersmith, M. Friesen, A. R. Hamilton, X. Hu, B. Koiller, A. L. Saraiva, D. Culcer, and R. B. Capaz, "Theory of hole-spin qubits in strained germanium quantum dots," *Phys. Rev. B*, vol. 103, p. 125201, Mar 2021. [Online]. Available: https://link.aps.org/doi/10.1103/PhysRevB.103.125201

[211] S. Hikami, A. I. Larkin, and Y. Nagaoka, "Spin-Orbit Interaction and Magnetoresistance in the Two Dimensional Random System," *Progress of Theoretical Physics*, vol. 63, no. 2, pp. 707–710, 02 1980. [Online]. Available: https://doi.org/10.1143/PTP.63.707

[212] S. V. Iordanskii, Y. B. Lyanda-Geller, and G. E. Pikus, "Weak localization in quantum wells with spin-orbit interaction," *ZhETF Pis ma Redaktsiiu*, vol. 60, p. 199, 1994.

[213] Y. Fang, P. Philippopoulos, D. Culcer, W. A. Coish, and S. Chesi, "Recent advances in hole-spin qubits," *Materials for Quantum Technology*, vol. 3, no. 1, p. 012003, mar 2023. [Online]. Available: https://dx.doi.org/10.1088/2633-4356/acb87e

[214] D. Jirovec, A. Hofmann, A. Ballabio, P. M. Mutter, G. Tavani, M. Botifoll, A. Crippa, J. Kukucka, O. Sagi, F. Martins, J. Saez-Mollejo, I. Prieto, M. Borovkov, J. Arbiol, D. Chrastina, G. Isella, and G. Katsaros, "A singlet-triplet hole spin qubit in planar Ge," *Nature Materials*, vol. 20, no. 8, pp. 1106–1112, Aug 2021. [Online]. Available: https://doi.org/10.1038/s41563-021-01022-2

[215] O. Moutanabbir, S. Assali, X. Gong, E. O'Reilly, C. A. Broderick, B. Marzban, J. Witzens, W. Du, S.-Q. Yu, A. Chelnokov, D. Buca, and D. Nam, "Monolithic infrared silicon photonics: The rise of (Si)GeSn semiconductors," *Applied Physics Letters*, vol. 118, no. 11, p. 110502, 2021. [Online]. Available: https://doi.org/10.1063/5.0043511

[216] C.-T. Tai, P.-Y. Chiu, C.-Y. Liu, H.-S. Kao, C. T. Harris, T.-M. Lu, C.-T. Hsieh, S.-W. Chang, and J.-Y. Li, "Strain Effects on Rashba Spin-Orbit Coupling of 2D Hole Gases in GeSn/Ge Heterostructures," *Advanced Materials*, vol. 33, no. 26, p. 2007862, 2021. [Online]. Available: https://onlinelibrary.wiley.com/doi/abs/10.1002/adma.202007862

[217] B. M. Ferrari, F. Marcantonio, F. Murphy-Armando, M. Virgilio, and F. Pezzoli, "Quantum spin Hall phase in GeSn heterostructures on silicon," *Phys. Rev. Res.*, vol. 5, p. L022035, May 2023. [Online]. Available: https://link.aps.org/doi/10.1103/PhysRevResearch.5.L022035

[218] G. Fettu, J. E. Sipe, and O. Moutanabbir, "Mid-infrared optical spin injection and coherent control," *Phys. Rev. B*, vol. 107, p. 165202, Apr 2023. [Online]. Available: https://link.aps.org/doi/10.1103/PhysRevB.107.165202

[219] R. People and J. C. Bean, "Calculation of critical layer thickness versus lattice mismatch for Ge_xSi_{1-x}/Si strained-layer heterostructures," *Applied Physics Letters*, vol. 47, no. 3, pp. 322–324, 08 1985. [Online]. Available: https://doi.org/10.1063/1.96206

[220] ——, "Erratum: Calculation of critical layer thickness versus lattice mismatch for Ge_xSi_{1-x}/Si strained-layer heterostructures [Appl. Phys. Lett. 47, 322 (1985)]," *Applied Physics Letters*, vol. 49, no. 4, pp. 229–229, 07 1986. [Online]. Available: https://doi.org/10.1063/1.97637

[221] T. Wimbauer, K. Oettinger, A. L. Efros, B. K. Meyer, and H. Brugger, "Zeeman splitting of the excitonic recombination in $In_xGa_{1-x}As$/GaAs single quantum wells," *Phys. Rev. B*, vol. 50, pp. 8889–8892, Sep 1994. [Online]. Available: https://link.aps.org/doi/10.1103/PhysRevB.50.8889

[222] A. Bogan, S. Studenikin, M. Korkusinski, L. Gaudreau, P. Zawadzki, A. Sachrajda, L. Tracy, J. Reno, and T. Hargett, "Single hole spin relaxation probed by fast single-shot latched charge sensing," *Communications Physics*, vol. 2, no. 1, p. 17, Feb 2019. [Online]. Available: https://doi.org/10.1038/s42005-019-0113-0

[223] D. Q. Wang, O. Klochan, J.-T. Hung, D. Culcer, I. Farrer, D. A. Ritchie, and A. R. Hamilton, "Anisotropic Pauli Spin Blockade of Holes in a GaAs Double Quantum

Dot," *Nano Letters*, vol. 16, no. 12, pp. 7685–7689, Dec 2016. [Online]. Available: https://doi.org/10.1021/acs.nanolett.6b03752

[224] L. Vukušić, J. Kukučka, H. Watzinger, J. M. Milem, F. Schäffler, and G. Katsaros, "Single-Shot Readout of Hole Spins in Ge," *Nano Letters*, vol. 18, no. 11, pp. 7141–7145, Nov 2018. [Online]. Available: https://doi.org/10.1021/acs.nanolett.8b03217

[225] K. Wang, G. Xu, F. Gao, H. Liu, R.-L. Ma, X. Zhang, Z. Wang, G. Cao, T. Wang, J.-J. Zhang, D. Culcer, X. Hu, H.-W. Jiang, H.-O. Li, G.-C. Guo, and G.-P. Guo, "Ultrafast coherent control of a hole spin qubit in a germanium quantum dot," *Nature Communications*, vol. 13, no. 1, p. 206, Jan 2022. [Online]. Available: https://doi.org/10.1038/s41467-021-27880-7

[226] S. Bosco, M. Benito, C. Adelsberger, and D. Loss, "Squeezed hole spin qubits in Ge quantum dots with ultrafast gates at low power," *Phys. Rev. B*, vol. 104, p. 115425, Sep 2021. [Online]. Available: https://link.aps.org/doi/10.1103/PhysRevB.104.115425

[227] J. C. Abadillo-Uriel and M. J. Calderón, "Spin qubit manipulation of acceptor bound states in group IV quantum wells," *New Journal of Physics*, vol. 19, no. 4, p. 043027, apr 2017. [Online]. Available: https://doi.org/10.1088%2F1367-2630%2Faa695f

[228] P. Machnikowski, K. Gawarecki, and L. Cywiński, "Hyperfine interaction for holes in quantum dots: $k \cdot p$ model," *Phys. Rev. B*, vol. 100, p. 085305, Aug 2019. [Online]. Available: https://link.aps.org/doi/10.1103/PhysRevB.100.085305

[229] D. Stange, N. von den Driesch, D. Rainko, C. Schulte-Braucks, S. Wirths, G. Mussler, A. T. Tiedemann, T. Stoica, J. M. Hartmann, Z. Ikonic, S. Mantl, D. Grützmacher, and D. Buca, "Study of GeSn based heterostructures: towards optimized group IV MQW LEDs," *Opt. Express*, vol. 24, no. 2, pp. 1358–1367, Jan 2016. [Online]. Available: http://www.opticsexpress.org/abstract.cfm?URI=oe-24-2-1358

[230] M. R. M. Atalla, S. Assali, S. Koelling, A. Attiaoui, and O. Moutanabbir, "High-Bandwidth Extended-SWIR GeSn Photodetectors on Silicon Achieving Ultrafast Broadband Spectroscopic Response," *ACS Photonics*, vol. 9, no. 4, pp. 1425–1433, 2022. [Online]. Available: https://doi.org/10.1021/acsphotonics.2c00260

[231] D. Ahn and C. Shun-Lien, "Optical gain in a strained-layer quantum-well laser," *IEEE Journal of Quantum Electronics*, vol. 24, no. 12, pp. 2400–2406, 1988.

[232] G. D. Sanders and Y.-C. Chang, "Theory of photoabsorption in modulation-doped semiconductor quantum wells," *Phys. Rev. B*, vol. 35, pp. 1300–1315, Jan 1987. [Online]. Available: https://link.aps.org/doi/10.1103/PhysRevB.35.1300

[233] Y. B. Lyanda-Geller, "Spin-related phenomena in spin 3/2 charge carrier holes systems," *Solid State Communications*, vol. 352, p. 114815, 2022. [Online]. Available: https://www.sciencedirect.com/science/article/pii/S0038109822001521

[234] B. Venitucci and Y.-M. Niquet, "Simple model for electrical hole spin manipulation in semiconductor quantum dots: Impact of dot material and orientation," *Phys. Rev. B*, vol. 99, p. 115317, Mar 2019. [Online]. Available: https://link.aps.org/doi/10.1103/PhysRevB.99.115317

[235] D. V. Bulaev and D. Loss, "Spin relaxation and anticrossing in quantum dots: Rashba versus Dresselhaus spin-orbit coupling," *Phys. Rev. B*, vol. 71, p. 205324, May 2005. [Online]. Available: https://link.aps.org/doi/10.1103/PhysRevB.71.205324

[236] L. M. Woods, T. L. Reinecke, and R. Kotlyar, "Hole spin relaxation in quantum dots," *Phys. Rev. B*, vol. 69, p. 125330, Mar 2004. [Online]. Available: https://link.aps.org/doi/10.1103/PhysRevB.69.125330

[237] D. V. Bulaev and D. Loss, "Spin Relaxation and Decoherence of Holes in Quantum Dots," *Phys. Rev. Lett.*, vol. 95, p. 076805, Aug 2005. [Online]. Available: https://link.aps.org/doi/10.1103/PhysRevLett.95.076805

[238] D. Csontos, P. Brusheim, U. Zülicke, and H. Q. Xu, "Spin-$\frac{3}{2}$ physics of semiconductor hole nanowires: Valence-band mixing and tunable interplay between bulk-material and orbital bound-state spin splittings," *Phys. Rev. B*, vol. 79, p. 155323, Apr 2009. [Online]. Available: https://link.aps.org/doi/10.1103/PhysRevB.79.155323

[239] C. Kloeffel, M. Trif, P. Stano, and D. Loss, "Circuit QED with hole-spin qubits in Ge/Si nanowire quantum dots," *Phys. Rev. B*, vol. 88, p. 241405, Dec 2013. [Online]. Available: https://link.aps.org/doi/10.1103/PhysRevB.88.241405

[240] S. Bosco, B. Hetényi, and D. Loss, "Hole Spin Qubits in Si FinFETs With Fully Tunable Spin-Orbit Coupling and Sweet Spots for Charge Noise," *PRX Quantum*, vol. 2, p. 010348, Mar 2021. [Online]. Available: https://link.aps.org/doi/10.1103/PRXQuantum.2.010348

[241] K. Laubscher, J. D. Sau, and S. Das Sarma, "Majorana zero modes in gate-defined germanium hole nanowires," *Phys. Rev. B*, vol. 109, p. 035433, Jan 2024. [Online]. Available: https://link.aps.org/doi/10.1103/PhysRevB.109.035433

[242] S. D. Liles, F. Martins, D. S. Miserev, A. A. Kiselev, I. D. Thorvaldson, M. J. Rendell, I. K. Jin, F. E. Hudson, M. Veldhorst, K. M. Itoh, O. P. Sushkov, T. D. Ladd, A. S. Dzurak, and A. R. Hamilton, "Electrical control of the g tensor of the first hole in a silicon MOS quantum dot," *Phys. Rev. B*, vol. 104, p. 235303, Dec 2021. [Online]. Available: https://link.aps.org/doi/10.1103/PhysRevB.104.235303

[243] B. Martinez and Y.-M. Niquet, "Variability of Electron and Hole Spin Qubits Due to Interface Roughness and Charge Traps," *Phys. Rev. Appl.*, vol. 17, p. 024022, Feb 2022. [Online]. Available: https://link.aps.org/doi/10.1103/PhysRevApplied.17.024022

[244] T. Andlauer, "Optoelectronic and spin-related properties of semiconductor nanostructures in magnetic fields," Ph.D. dissertation, Technische Universitaet Muenchen (Germany), 2009.

[245] A. Trellakis, A. T. Galick, A. Pacelli, and U. Ravaioli, "Iteration scheme for the solution of the two-dimensional Schrödinger-Poisson equations in quantum structures," *Journal of Applied Physics*, vol. 81, no. 12, pp. 7880–7884, 1997. [Online]. Available: https://doi.org/10.1063/1.365396

[246] L. R. Ram-Mohan, K. H. Yoo, and J. Moussa, "The Schrödinger–Poisson self-consistency in layered quantum semiconductor structures," *Journal of Applied Physics*, vol. 95, no. 6, pp. 3081–3092, 2004. [Online]. Available: https://doi.org/10.1063/1.1649458

APPENDIX A SOLUTION OF THE INFINITE SQUARE WELL PROBLEM IN 6-BAND $k \cdot p$ THEORY

The infinite square well problem is easily solvable within the 6-band $k \cdot p$ framework, where the conduction band contributions are treated perturbatively ($|c\rangle = 0$). The problem consists of diagonalizing the Hamiltonian (3.84) for the subband edge energies E_j^τ and envelope functions $f^{\ell,s,h}(z)$. Since the QW band offsets are assumed infinite, and (3.84) involves only even powers of k_z, all the envelopes must be proportional to the normalized function

$$\varphi_j(z) \equiv \langle z|\varphi_j\rangle = \sqrt{\frac{2}{l_z}} \sin\left(\frac{j\pi z}{l_z}\right). \tag{A.1}$$

η and H levels become

$$|\mathrm{H}\sigma; l\rangle = \left|\frac{3}{2}, \frac{3\sigma}{2}\right\rangle |\varphi_l\rangle\,, \tag{A.2}$$

$$|\eta\sigma; j\rangle = d_{\ell,j} \left|\frac{3}{2}, \frac{\sigma}{2}\right\rangle |\varphi_j\rangle + \sigma d_{s,j} \left|\frac{1}{2}, \frac{\sigma}{2}\right\rangle |\varphi_j\rangle\,, \tag{A.3}$$

with $d_{\ell,j}^2 + d_{s,j}^2 = 1$. Inserting this ansatz into (3.84), and noting that $k_z^2 |\varphi_j\rangle = (j\pi/l_z)^2 |\varphi_j\rangle$ gives one equation for the H levels (already diagonal) and two coupled equations for the η levels. The energies of H levels are

$$E_l^{\mathrm{H}} = \mathfrak{E}_l - 2\mathfrak{e}_l, \tag{A.4}$$

where

$$\mathfrak{E}_j = -\alpha_0\gamma_1 k_j^2 + a_v \mathrm{Tr}\{\varepsilon\}, \tag{A.5}$$

$$\mathfrak{e}_j = -\alpha_0\gamma_2 k_j^2 - \frac{b}{2}\delta\varepsilon, \tag{A.6}$$

$$\tag{A.7}$$

and $k_j^2 = (j\pi/l_z)^2$, $\delta\varepsilon = \varepsilon_{xx} - \varepsilon_{zz}$. The eigenvalue equation for $\eta+$ levels reads

$$\left\{\mathfrak{E}_j + \mathfrak{e}_j - \frac{\Delta_0}{2} + \begin{bmatrix} \mathfrak{e}_j + \Delta_0/2 & \sqrt{8}\mathfrak{e}_j \\ \sqrt{8}\mathfrak{e}_j & -\mathfrak{e}_j - \Delta_0/2 \end{bmatrix}\right\} \begin{bmatrix} d_{\ell,j} \\ d_{s,j} \end{bmatrix} = E_j^{\eta} \begin{bmatrix} d_{\ell,j} \\ d_{s,j} \end{bmatrix} \tag{A.8}$$

which solves into two sets of eigenenergies:

$$E_j^{\pm} = \mathfrak{E}_j + \frac{\Delta_0}{2}\left[x - 1 \pm \sqrt{(1+x)^2 + 8x^2}\right] \tag{A.9}$$

with $x = 2\mathfrak{e}_j/\Delta_0$. Here the "+" superscript refers to LH-like η levels whereas the "−" superscript refers to SO-like levels. To see this, we evaluate $E_j^{\pm}$ in the limit $|x| \ll 1$:

$$E_j^{+} \to \mathfrak{E}_j + 2\mathfrak{e}_j \equiv E_j^{\mathrm{LH}}, \tag{A.10}$$

$$E_j^{-} \to \mathfrak{E}_j - \Delta_0 \equiv E_j^{\mathrm{SO}}. \tag{A.11}$$

Note that $x < 0$ for relaxed, compressively strained or slighly tensile strained wells. For large tensile strain, x can undergo a sign change and become positive. The coefficients $d_{\ell,j}$ and $d_{s,j}$ for the LH-like "+" branch are

$$d_{\ell,j} = -\frac{\sqrt{8}x}{\sqrt{\left(\sqrt{(1+x)^2+8x^2} - x - 1\right)^2 + 8x^2}} = -\mathrm{sgn}(x)(1 - x^2 + \dots), \tag{A.12}$$

$$d_{s,j} = -\frac{\sqrt{(1+x)^2+8x^2} - x - 1}{\sqrt{\left(\sqrt{(1+x)^2+8x^2} - x - 1\right)^2 + 8x^2}} = -\mathrm{sgn}(x)(\sqrt{2}x + \dots), \tag{A.13}$$

where the expansions are accurate for small $|x|$. When SOC is strong ($|x| \ll 1$), the SO component decreases as $1/\Delta_0$ until the level becomes a pure LH subband. On the other hand, for small SOC (large $|x|$), the squared amplitude $d_{\ell,j}^2$ tends to 1/3 for negative x and 2/3 for positive x, and vice-versa for the SO proportion $d_{s,j}^2$.

APPENDIX B SELF-CONSISTENT SOLUTION OF THE COUPLED SCHRÖDINGER-POISSON EQUATIONS

If doping impurities are present within one or more layers of a heterostructure, the Fermi level gets shifted towards either the conduction band or the valence band, depending on the nature of the doping. This shift in the Fermi energy creates a spatial distribution of free charges that generate an electric field V_{ch}. This electric field then modifies the confining potential along the growth direction, which results in different heterostructure energy levels. Since the charge distribution depends on the energy levels in the heterostructure (from Schrödinger's equation) and on the generated electric field V_{ch} (from Poisson's equation), the Schrödinger and Poisson equations must be solved self-consistently. In this section we present the Schrödinger part of the equation system, followed by the Poisson equation, before concluding with the self-consistent procedure to solve both simultaneously.

The Schrödinger equation consists of the eight-band Hamiltonian H_{QW} that was described throughout Chapter 3. Its solution results in energy levels $E_j(\mathbf{k}_\parallel)$ and associated eigenstates $|j\mathbf{k}_\parallel\rangle$:

$$H_{\text{QW}}\,|j\mathbf{k}_\parallel\rangle = E_j(\mathbf{k}_\parallel)\,|j\mathbf{k}_\parallel\rangle\,, \tag{B.1}$$

where j is the subband index. The spatial distribution of charges derives from $E_j(\mathbf{k}_\parallel)$, $|j\mathbf{k}_\parallel\rangle$ and the Fermi energy E_F :

$$n(z) = \sum_{j\in\text{CB}} \frac{1}{(2\pi)^2} \int \mathrm{d}^2\mathbf{k}_\parallel \left|f_{j\mathbf{k}_\parallel}(z)\right|^2 F\left(\frac{E_j(\mathbf{k}_\parallel) - E_F}{k_{\text{B}}T}\right), \tag{B.2a}$$

$$p(z) = \sum_{j\in\text{VB}} \frac{1}{(2\pi)^2} \int \mathrm{d}^2\mathbf{k}_\parallel \left|f_{j\mathbf{k}_\parallel}(z)\right|^2 F\left(-\frac{E_j(\mathbf{k}_\parallel) - E_F}{k_{\text{B}}T}\right), \tag{B.2b}$$

where $F(x) = 1/(e^x + 1)$ is the Fermi-Dirac distribution and

$$\left|f_{j\mathbf{k}_\parallel}(z)\right|^2 = \sum_{\nu\sigma} \left|f^{\nu\sigma}_{j\mathbf{k}_\parallel}(z)\right|^2. \tag{B.3}$$

There is no factor 2 due to spin in (B.2) because it is included in the subband index j. The charge distribution is then given by

$$\rho(z) = e(p(z) - n(z) + N_D^+(z) - N_A^-(z)). \tag{B.4}$$

where $N_D^+(z)$ and $N_A^-(z)$ are the ionized donors and acceptors density. The Fermi energy E_F is chosen such that the whole heterostructure is charge-neutral :

$$\int \mathrm{d}z\, \rho(z; E_F) = 0. \tag{B.5}$$

The Poisson equation establishes the relation between a charge distribution ρ and its associated electric potential ϕ :

$$\frac{\mathrm{d}}{\mathrm{d}z}\epsilon_r(z)\frac{\mathrm{d}}{\mathrm{d}z}\phi = -\frac{\rho}{\epsilon_0}, \tag{B.6}$$

where $\epsilon_r(z)$ is the relative permittivity of the material at position z and ϵ_0 is the permittivity of free space. The relative permittivity of Si [160], Ge [160] and Sn [166] are respectively $\epsilon_r^{\mathrm{Si}} = 11.9$, $\epsilon_r^{\mathrm{Ge}} = 16.0$ and $\epsilon_r^{\mathrm{Sn}} = 24.0$. Given the density ρ from the Schrödinger equation, we can solve for ϕ and obtain the potential energy $V_{\mathrm{ch}} = -e\phi$. The Poisson equation is solved using a Newton-Raphson iteration scheme [244].

The self-consistent solution of both equations is performed by following the procedure in references [245,246]. We first start by solving the Schrödinger part with an initial guess $V_{\mathrm{ch}}^{(0)}$. This results in a first approximation for the Fermi energy and density to be used in Poisson's equation : $\rho^{(1)}$. Numerical instabilities during the Newton-Raphson iterations are prevented by employing a predictor-corrector scheme [245] for the electron and hole densities n and p. For each Newton-Raphson iteration i and corresponding charge redistribution potential $V_{\mathrm{ch}}^{(0,i)}$, the density on the right hand side of Poisson's equation is evaluated from the predictors

$$\tilde{n}(z) = \sum_{j\in\mathrm{CB}} \frac{1}{(2\pi)^2} \int \mathrm{d}^2\mathbf{k}_\parallel \left| f_{j\mathbf{k}_\parallel}(z) \right|^2 F\left(\frac{E_j(\mathbf{k}_\parallel) - E_F + V_{\mathrm{ch}}^{(0)} - V_{\mathrm{ch}}^{(0,i)}}{k_{\mathrm{B}}T} \right), \tag{B.7a}$$

$$\tilde{p}(z) = \sum_{j\in\mathrm{VB}} \frac{1}{(2\pi)^2} \int \mathrm{d}^2\mathbf{k}_\parallel \left| f_{j\mathbf{k}_\parallel}(z) \right|^2 F\left(-\frac{E_j(\mathbf{k}_\parallel) - E_F + V_{\mathrm{ch}}^{(0)} - V_{\mathrm{ch}}^{(0,i)}}{k_{\mathrm{B}}T} \right). \tag{B.7b}$$

Once the Newton-Raphson iterations have converged, we obtain a first approximation for V_{ch}: $V_{\mathrm{ch}}^{(1)}$. This first approximation is then fed back into the Schrödinger part to obtain second approximations for the Fermi energy and density ($\rho^{(2)}$). This whole process is then repeated until V_{ch} and ρ have converged.